# Wave Propagation and Interaction with Damage in Periodic Composite Structures


**Rilwan Kayode Apalowo, M.Eng.**

Thesis submitted to The University of Nottingham
for the degree of Doctor of Philosophy

March 2019

# Abstract

A number of engineering structures such as aircraft fuselages, nuclear reactors, boilers and pressure vessels are subject to severe conditions, during operation, which can endanger the operation and lead to possible catastrophic failure. Such failure consequently has a huge impact on economy and environment. These engineering structures, especially aerospace and automotive structures, generally consist of composite materials due to their excellent mechanical properties. Therefore, there is need to develop numerical tools for constant non-destructive monitoring and assessment of composite structures in order to avoid sudden failure of these engineering components during operation. Various studies have been conducted on wave propagation, and distortion of the wave properties to examine damage/failure within structures. In the first theme of this study, a brief review of the analytical and numerical methodologies for wave propagation and interaction modelling is presented.

The second theme of this study considers two common conditions, namely temperature and pressure, that aerospace and automotive structures are subject to during operation. The first part presents a wave finite element (WFE) methodology for predicting wave propagation properties within periodic layered structures. The computed wave properties are then coupled to the finite element (FE) model of a coupling joint, which bears structural damage, in order to quantify wave interaction with the damage. Second part of the theme considers the impact of temperature on the wave interaction with damage in composite structures. A thermal-mechanical analysis is conducted to experimentally measure mechanical characteristics of a composite layered panel over a wide temperature range. The measured thermomechanical characteristics are applied to study and analyse the effect of temperature on wave propagation and interaction properties within the composite panel. The significance of the panel's glass transition range on the measured and calculated properties is emphasised. In the third part, the developed methodology is extended to incorporate pre-stress effect in wave propagation and interaction with damage within pressurised layered structures. The pre-stress effect is mostly introduced in engineering structures by pressurisation, which is among the severe conditions they are exposed to during operation. Pre-stress impact is anal-

ysed by comparison of results under pressurised and non-pressurised scenarios.

The third theme proposes an inverse wave finite element approach for identifying the geometric and material characteristics of layered composite structures. The non-destructive approach is able to recover the thickness, density, as well as all independent mechanical characteristics such as the tensile and shear moduli for each layer of the composite structure under investigation. It is emphasized that the success of the approach is independent of the employed excitation frequency regime, meaning that both structural dynamics and ultrasound frequency spectra can be employed.

In the fourth theme of this study, a FE based computational scheme for quantifying guided wave interaction with Localised Nonlinear Structural Damage (LNSD) within structures of arbitrary layering and geometric complexity is developed. The computed harmonic wave interaction coefficients are established as indices for structural damage mode identification/classification. Finally, in the fifth theme, a numerical scheme is presented for quantifying wave interaction with structural damage within two-dimensional multilayer composite structures. Wave interaction coefficients for different damage modes and structural parameters are analysed in order to establish an optimum basis for detecting and identifying damage, as well as assessing the orientation and extent of the detected damage.

# Declaration

The work presented in this thesis is the result of my research project as a PhD student at the University of Nottingham and was conducted between October 2015 and March 2019. I declare that the work is my own and has not been submitted for a degree elsewhere.

# Acknowledgements

First and foremost, I thank God for my life! I would also like to thank a number of people who supported me during this PhD study. Their support significantly contributed to the completion of the study.

Firstly, I want to express my sincere gratitude to my supervisors, Dr. Dimitrios Chronopoulos, Prof. Gregor Tanner and Dr. Savvas Triantafyllou for their continuous support, enlightening discussions and patience during this study. They provided me with the necessary guidance throughout. I have learned a lot from their wealth of experience which would be useful in the future. I also wish to thank my internal examiner Prof. Seamus Garvey for his constructive and productive comments and advice during meetings. These have greatly improved the outcome of the work.

My acknowledgements also go to all my friends who contributed to make these years of study enjoyable and pleasant. I would like to appreciate all my colleagues at the Institute for Aerospace Technology and the Composites research group for productive discussions, research collaborations and pleasant moments shared together during these years.

I also thank the University of Nottingham for funding my study through the Faculty of Engineering Research Excellence PhD Scholarship. I express my gratitude to the University for this experience and hope that many more young researchers will have a similar opportunity in the future.

Lastly, particular appreciation goes to my parents, for their continuous support over the years, my darling wife, Muibat, for always being there for me, and my kids, Bilal and Maryam, for being my source of happiness and inspiration. I thank you all!

# Contents

# Nomenclature

| | |
|---|---|
| $\mathbf{a}$ | Wave amplitude |
| $\mathbf{c}$ | Wave scattering coefficients |
| $\mathbf{D}, \mathbb{D}$ | Dynamic stiffness matrix of a substructure and that of the joint |
| $\mathbf{f^e}$ | Vector of forces applied to the coupling joint at its interface with connected substructures |
| $\mathbf{q}, \mathbf{f}$ | Physical displacement and forcing vectors for a substructure |
| $\mathcal{F}$ | Objective function to be minimized |
| $\mathbf{K}, \mathbf{M}, \mathbf{C}$ | Stiffness, mass and damping matrices of a substructure's modelled segment |
| $\mathbb{K}, \mathbb{M}, \mathbb{C}$ | Stiffness, mass and damping matrices of the coupling joint |
| $\mathbf{K}_0$ | Stiffness matrix of an unstressed structure under no pressurisation |
| $\mathbf{K}_\mathrm{p}$ | Pre-stress stiffness matrix of a structure under pressurisation |
| $\boldsymbol{K}_u^e$ | Stiffness matrix of deactivated elements within a damage zone |
| $\mathbf{k}$ | Wavenumber |
| $\mathbf{R}$ | Rotation matrices of the system's substructures |
| $R_T$, $R_T^*$ | Transformation matrix for a substructure's displacement and force vectors |
| $\mathbb{R}_T$, $\mathbb{R}_T^*$ | Transformation matrix for the coupling joint's displacement and force vectors |
| $\mathbf{S}$ | Wave scattering matrix |
| $\mathbf{S}_\mathrm{g}$ | Shape function derivative matrix |
| $\mathbf{S}_\mathrm{m}$ | Cauchy stress tensor |
| $\mathbf{T}$ | Wave propagation transfer matrix |
| $\mathbf{x}(\mathrm{t})$ | Logged signal vector as a function of time |
| $\mathbf{z}$ | Physical displacement vector for the coupling joint |
| $\lambda$ | Propagation constant and eigenvalue of the wave propagation eigenproblem |
| $\boldsymbol{\phi}, \boldsymbol{\Phi}$ | Eigenvector and grouped eigenvector |
| $\boldsymbol{\psi}, \boldsymbol{\Psi}$ | Left eigenvector and grouped left eigenvector |

| | |
|---|---|
| $A, B$ | Expansion coefficients |
| $b, h$ | width and depth of a cross-section |
| $c_p$ | Wave phase velocity |
| $c_g$ | Wave group velocity |
| $\mathrm{E}^1$, $\mathrm{E}^2$ | Loss and storage moduli of a material |
| $\mathrm{E_a}$ | Measured (actual) elastic modulus at respective temperature |
| $\mathrm{E_n}$ | Nominal elastic modulus at ambient temperature |
| $E, G, \nu, \rho$ | Elastic modulus, shear modulus, Poisson's ratio and density of an elastic waveguide |
| $f_0$ | Frequency of the applied excitation |
| $f_{\max}$ | Highest frequency of interest |
| $i$ | Imaginary unit |
| $j$ | Number of DoF on each periodic cross-section of the modelled segment, along the axis in which wave properties are sought |
| $l_e$ | Spatial FE discretization element size |
| $L$ | Length |
| $l, l_{max}$ | Index corresponding to layer number and total number of structural layers |
| $m, m_{max}$ | Index corresponding to each measured frequency and total number of measured frequencies |
| $n_0$ | Number of cycles for the Hanning windowed excitation |
| $\mathcal{O}$ | Big O notation for nonlinear terms approximation |
| $cr$ | propagating wave sorting criterion |
| $p$ | Pressure index |
| $P_0, P$ | Original and reduced stiffness of a structural segment |
| $\mathbb{P}$ | Time averaged power transmission |
| $q_1, q_2$ | Nodal displacements of damage front edges |
| $rf$, $fe$ | Indices denoting wave characteristics obtained through reference measurements and the WFE scheme respectively |
| $\mathrm{R_f}$ | A reduction ratio used in the calculation of temperature-dependent mechanical characteristics |
| $t$ | Time |
| $T$ | Temperature index |
| $t_s$ | Integration time step of the FE transient analysis |
| $U_0$ | Amplitude of applied excitation signal |
| $x, y, z$ | Property in the $x$, $y$ or $z$ direction |
| $\alpha, \epsilon, \alpha_0, \epsilon_0$ | Nonlinear coefficients |

| | |
|---|---|
| $\varepsilon, \mu$ | Wave propagation constants for a substructure and the coupling joint |
| $\eta$ | Structural damping coefficient |
| $\omega$ | Angular frequency |
| $\delta$ | Kronecker delta |
| $\tan\delta$ | Material loss factor, where $\delta$ is the phase lag between the stress and strain of the material |
| $\beta$ | Structural stiffness reduction factor |
| $\lambda_{\min}$ | Shortest wavelength within the bandwidth of the signal |
| $\mathrm{Y}, u, \chi$ | Output, input and scale factor of a dynamic system |
| $\varepsilon_d$ | Cumulative nodal strain of elements within a damage zone |
| $\varepsilon_b$ | Strain between edges of damage front |
| $\varepsilon_{dn}$ | Averaged nodal strain of each element in a damage zone |

## Subscripts

| | |
|---|---|
| $q, \mathrm{f}$ | Displacement and forcing indices |
| $\mathfrak{i}, \mathfrak{n}$ | property of interface and non-interface nodes of the coupling joint with the substructures |
| $J, \mathbb{J}$ | Property of a coupling joint |
| $k$ | Substructure indices |
| $L, R, I$ | Left, right sides and internal DoF indices |
| $LT, IT, RT$ | left top, internal top and right top indices of a modelled segment |
| $LI, I, RI$ | Left internal, internal and right internal indices of a modelled segment |
| $LB, IB, RB$ | Left base, internal base and right base indices of a modelled segment |
| $r, R$ | Node index and total number of nodes in a periodic cross-section of a structural waveguide |
| $n, N$ | Substructure index and total number of substructures existing in the considered system |
| $x, y$ | Direction of wave propagating |
| $\mathrm{w}, W$ | Wave eigenvector index and total number of waves accounted for in a substructure |

## Superscripts

| | |
|---|---|
| $g$ | Global coordinate index |

| | |
|---|---|
| inc, ref | Positive and negative going waves properties |
| $s$ | Periodic segment positioning index |

## Operators

| | |
|---|---|
| $^\top$ | Transpose |
| $^*$ | Hermitian transpose |
| $\dot{}$ | Derivative with respect to time |
| $\ddot{}$ | Second derivative with respect to time |
| $^{-1}$ | Inverse |
| exp | Exponential |
| ln | Natural logarithm |
| $\Re$ | Real operator |
| $\Im$ | Imaginary operator |
| $\|\|$ | Absolute value or modulus |
| $\int$ | Integral |

## Abbreviations

| | |
|---|---|
| BE | Boundary Element |
| CLPT | Classical Laminate Plate Theory |
| CPT | Classical Plate Theory |
| DLT | Discrete Layer Theory |
| DoF | Degree of Freedom |
| DSM | Dynamic Stiffness Matrix |
| ESL | Equivalent Single Layer |
| FD | Finite Difference |
| FE | Finite Element |
| FEM | Finite Element Method |
| FSDT | First Order Shear Deformation Theory |
| HSDT | Higher Order Shear Deformation Theory |
| IWC | Inhomogeneous Wave Correlation |
| LNSD | Localised Nonlinear Structural Damage |
| MAC | Modal Assurance Criterion |
| NDE | Nondestructive Evaluation |
| NDT | Nondestructive Testing |
| PST | Periodic Structure Theory |

| | |
|---|---|
| PSV | Polytec Scanning Vibrometer |
| RM | Receptance Method |
| SEM | Spectral Element Method |
| SFEM | Spectral Finite Element Method |
| SHM | Structural Health Monitoring |
| SLT | Single Layer Theory |
| TFC | Transition Frequency Characterization |
| TMA | Thermal Mechanical Analysis |
| TMM | Transfer Matrix Method |
| WFE | Wave Finite Element |

# List of Figures

# List of Tables

# CHAPTER 1

# Introduction

## 1.1 Motivation

Engineering structures such as aircraft fuselages, nuclear reactors, boilers and pressure vessels are subject to severe conditions, during operation, which can endanger the operation and lead to possible catastrophic failure. Such failure consequently has a huge impact on economy and environment. Mitigation of the risks imposed by a sudden failure of these structures has become an important aspect of Structural Health Monitoring (SHM) in recent years. These engineering structures, especially aerospace and automotive structures, generally consist of composite materials due to their excellent mechanical properties. Advanced composite structures such as chamber core and advanced grid-stiffened structures offer great improvements in weight, strength, damping and acoustic properties [4]. They are however extremely sensitive to defects which are accompanied by the extreme operational conditions they are subject to. Therefore, there is need for constant non-destructive monitoring and assessment of these structures in order to avoid sudden failure during operation.

The dynamic response of a complex system, such as a composite structure, can be modelled using a classical numerical approach such as the Finite Element (FE), Finite Difference (FD) or Boundary Element (BE) method. This can be done with relative ease, high accuracy and low computational cost at low frequency range. However, it becomes difficult, computationally expensive and prone to numerical error within the high frequency range. In order to overcome these difficulties, the wave approach is used to model the dynamic response of the system. The modelling of the wave propagation characteristics along a structure can be used to describe the dynamic behaviour of the structure. This approach is particularly suitable at high frequency range where the vibrational wavelength is relatively small compared to the size of the structure. On the other hand, wave interaction with inhomogeneity within the structure is another

important application of the wave propagation properties. This is specifically for the purpose of monitoring the structure for identification of possible anomalies, such as damage and discontinuities, within the structure. Recent studies have focussed on the propagation and interaction phenomena of wave in engineering structures, but few of which consider in-service conditions of the structures in the analysis. Investigation of interaction mechanism of wave with damage, considering operational conditions the structures are subject to, is an aspect of SHM that still requires great attention. This motivates the need to develop numerical tools for wave propagation and interaction with damage within layered composite structures, and to investigate the impact of operational conditions on the wave interaction properties. Two important conditions, pressure and temperature, are considered in this study. Moreover, a number of composite structures such as plates and shells show periodicity in two directions, i.e., wave properties are periodic and different in two axes of the structures. This motivates the need to extend the wave propagation and interaction methodology to two-dimensional composite layered structures, and establish an optimum basis for detecting and identifying structural damage within the structures.

Structural damage monitoring is pertinent in predicting and/or ensuring operational availability, extended life and viable future performance of structures. Recently, a number of SHM and Nondestructive Testing/Evaluation (NDT/E) methodologies have been developed for detection and assessment of anomalies along structures. These include visual inspection [5], acoustic emission [6, 7], electromagnetic (such as Eddy current [8, 9]) testing, guided and Lamb wave inspection [10, 11], ultrasonic testing [12, 13], vibration and modal analysis [14, 15], radiographic (such as X-ray [16]) testing and so on. Most of these methodologies are based on the application of the wave propagation properties to analyse anomalies along structures. Scattering (reflection and transmission) of waves, which occurs as a result of wave interaction with structural anomalies, as well as wave mode conversion are used for the purpose of analysing the location and extent of the anomalies. Location is assessed through change in mode shape and/or wave speed while anomalies extent is measured as the wave amplitude loss ratio in terms of the reflection or transmission coefficients of the incident waves impinging on the spot of structural anomalies. However, some structural defects, such as infinitesimal sized defects, are difficult to identify at early stage, especially using the linear wave parameters of change in mode shape as well as attenuation. Some of these defects could pose catastrophic effect if not tackled at the early stage. Nonlinear NDE and SHM techniques have been shown to be more reliable in detecting early stage structural defects which are difficult to detect using the conventional NDE and SHM techniques [17, 18]. However, studies on wave interac-

tion with nonlinear damage are found to be limited in the literature. This motivates the development of a numerical methodology for quantifying guided wave interaction with localised nonlinear structural damage within structures of arbitrary layering and geometric complexity.

The versatility in the physical and mechanical properties of composite structures has led to the development of sandwich structures, with tailored properties and a wide range of possible configurations and topologies, to serve specific purposes. However, the identification of the actual physical and mechanical properties of the assembled layers is an aspect of NDE that still requires great attention. Over the past decades, research efforts have been devoted to identify the modal parameters of structural systems. These studies have led to the development of various techniques which include time and frequency domain methods [19–25], Kalman filter methods [26], Bayesian approaches [27–29], vibratory identification techniques [30] and transition frequency characterization techniques [31] to cite a few. However, there is still significant room for further exploration in system identification especially through wave propagation properties of the system. This motivates the need to develop a wave-based methodology for identifying the geometric and mechanical characteristics of each individual layer of layered composite structures.

## 1.2 Literature review

### 1.2.1 Brief historical background of wave propagation in periodic structures

Periodic structures are structures that consist of a number of identical substructure components that are joined together to form a continuous structure. Examples of engineering components exhibiting periodicity properties include satellite panels, railway tracks and aircraft fuselages. Periodic structures can be categorised based on the number of directions in which the substructure components are arranged. One-dimensional (Fig. 1.1b): in which the substructures are arranged in one direction and wave propagation is unidirectional, two-dimensional (Fig. 1.1c): substructures are arranged in two directions and waves propagate in two directions and three-dimensional: substructures are arranged in three directions and waves propagate in three directions. One- and two-dimensional periodic structures are considered within the framework of this study.

Waves propagation in periodic structures dates back to over four centuries ago. As early as 17th century, the first work can be traced to Isaac Newton in his monumental work, the "Principia" [32], in which wave propagation through lumped masses joined by massless springs is considered in order to model the velocity of sound in air and

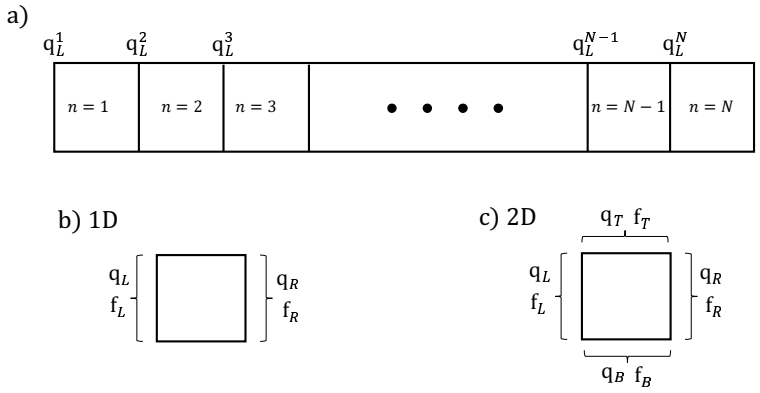


**Figure 1.1:** Forces and displacements on a cell in (b) one-dimensional and (c) two-dimensional periodic structures

the speed of water waves. In the 18th and 19th centuries, various mathematicians and physicists such as Floquet [33], Bernoulli [34], Taylor [35], Euler [36], Lagrange [37] and Cauchy [38] considered various aspects of wave propagation in lumped masses. Of great significant is the work of Floquet [33] in which analytical solutions are obtained for ordinary differential equations with periodic coefficients by transforming the periodic system to a traditional linear system with constant, real coefficients. Until 1887, the systems considered are discrete models of periodic structures composed of lumped masses connected by massless springs.

The continuum model of periodic structure is first formulated in the pioneer work of Rayleigh [39] in which a stretched string, with a periodic and continuous variation of density along its length, undergoing transverse harmonic vibration is considered. After few decades, the next fundamental contribution is the work of Bloch [40] which is based on the Floquet theorem to model wave propagation through crystal lattices and periodic electric filters. General solution for wave propagation, along x direction for instance, in periodic structures is obtained as $u(x) = \mathrm{U}(x)\mathrm{e}^{\mathrm{i}kl}$, where $u$ is the wave function, U is the wave amplitude, $k$ is the wavenumber and $l$ is the length of a periodic cell/segment. Floquet's theorem is further extended by Brillouin [41] to describe the geometric interpretation of wave propagation in periodic media. It is shown that the wavenumber of wave propagating through a periodic media in 3D space exists in irreducible zones popularly known as the Brillouin zone. A summary of the major historical developments in the area of wave propagation in periodic structures are presented in chronological order in Table 1.1.

**Table 1.1:** Major historical developments of wave propagation in periodic structures

| | |
|---|---|
| 6th Century | Pythagoras discovered the mathematical interval of musical sound and vibration of strings |
| 1638 | Galileo discovered the laws of pendulum motion, principles of resonance and factors influencing vibration of strings |
| 1678 | Hooke discovered the law of elasticity, known as the Hooke's law, which forms the basis for static and dynamic behaviour of solid media |
| 1687 | Newton studied wave propagation through lumped masses joined by massless springs in order to model the velocity of sound in air and the speed of water wave |
| 1713 | Taylor established dynamic solution for wave propagation and vibration in stretched strings |
| 1744 | Euler developed dynamic equations for wave propagation in beams and established modal solutions for different boundary conditions of the beam |
| 1755 | Bernoulli developed the principle of superposition for the dynamic behaviour beams and strings |
| 1759 | Lagrange formerly established strings as system of discrete mass particles |
| 1822 | Cauchy developed the dynamical equations of wave motion in solid media using the theory of elasticity |
| 1883 | Floquet developed analytical solutions for ordinary differential equations with periodic coefficients by transforming the periodic system to a traditional linear system with constant, real coefficients |
| 1887 | Rayleigh studied the first continuum model of periodic structure in which a stretched string, with a periodic and continuous variation of density along its length, undergoing transverse harmonic vibration is considered |
| 1929 | Bloch modelled wave propagation through crystal lattices and periodic electric filters. General solution for wave propagation in periodic structures was established |
| 1953 | Brillouin described the geometric interpretation of wave propagation in periodic media and established the Brillouin zone, which is the irreducible zones of wavenumber in 3D space |

Beyond the fundamental works, important developments to analyse increasingly

complicated periodic lattice structures have been observed. Flexural wave motion in one-dimensional periodic beam structures is studied by Cremer and Leilich [42]. Beams with point masses or simple supports at regular intervals are considered. Natural frequencies of a finite periodic beam with arbitrary number of simple supports is studied by Miles [43]. Heckl [44] extends the work to two-dimensional periodic structures in which a rectangular grillage of interconnected uniform periodic beams having both flexural and torsional stiffness is considered. Wave propagation constant is established in terms of the reflection and transmission coefficients of wave impinging through the interface of two infinite beams. Effect of noise induced vibration on stiffened aerospace structures is first studied at the University of Southampton in 1964. This has motivated a series of works concerning wave propagation and interaction in periodic aerospace structures. Mead [45] presents a detailed review of these contributions. These works has led to the eventual development of a number of analytical and numerical techniques and methodologies for the dynamics of periodic layered structures. These methodologies are reviewed in the next section.

### 1.2.2 Review of analysis methods for the dynamics of periodic composite structures

Since the twentieth century, remarkable progress has been made in the design, analysis, and fabrication of composite structures. Several novel composite structures have been designed, fabricated, and investigated for both civil and military applications. Compared to monolithic structures, they have higher strength and stiffness, less weight and are easier and cheaper to fabricate. However, these features are accompanied by increased sound/vibration transmission into the structures [46]. This has made modelling of the dynamic behaviour of composite structures a field of emerging interest in recent years. According to Chronopoulos et al. [47], wave propagation characteristics are a key to decode and model the vibrational behaviour of a structure. Waveguides are highly dispersive due to their geometry rather than just to their material composition. This is why dispersion characteristics, which are the phenomenon in which a wave is separated into its component frequencies, are of great importance in modelling the acoustic or vibrational behaviour of structures.

Composites laminates have been studied using two general theories, the single layer theories, in which layers of a laminate are regarded as an equivalent single layer, and the discrete layer theories, in which each layer of a laminate is considered independently as separate layer.

The *Single Layer Theories* (SLT), otherwise known as the equivalent single layer (ESL) theories, are based on the plane-stress assumption to reduce a 3-D continuum problem

to a 2-D problem. The simplest in the hierarchy of ESL theories is the *Classical Laminate Plate Theory* (CLPT), which is an extension of the *Classical Plate Theory* (CPT) developed by Kirchhoff [48], Love [49] and Timoshenko [50]. In CLPT, composite laminates are plates or thin-shell structures whose stiffness properties may be found by integration of in-plane stress in the normal direction to the laminates surface. CLPT is basically for orthotropic (that is, with principal properties in orthogonal directions) thin plates [51]. Next in the hierarchy of ESL theories is the *First Order Shear Deformation Theory* (FSDT) of plates, which is an extension of the *First Order Theory* developed by Reissner [52] and Mindlin [53] to study transverse waves along plates. FSDT implies a linear displacement variation through the plate thickness. FSDT based methods are developed for calculating improved transverse shear stresses in laminated composite plates [54] and to accommodate higher frequencies [55]. An asymptotic FSDT model for wave dispersion into symmetric flat thick sandwiches structures was first developed by Kurtze and Watters [56]. The first structural FSDT model for an infinite sandwich panel was developed by Dym and Lang [57] which was extended to symmetric sandwiches with an orthotropic core [58]. The ESL theories are limited in analysing thick composite laminates, hence, the need for higher order shear deformation theories. *Higher Order Shear Deformation Theory* (HSDT) is developed based on the same assumptions as the CLPT and FSDT but without the assumption that a straight line normal to the mid-plane before deformation remains straight and normal to the plane even after deformation. HSDT based approaches for calculating dynamic characteristics and shear stresses in relatively thick composite laminates are presented by Ambartsumian [59] for plate deformation analysis, Matsunaga [60] for buckling analysis, Soldatos and Timarci [61] and Sokolinsky and Nutt [62] for dynamic analysis and Swaminathan and Patil [63] for free vibration analysis.

The *Discrete Layer Theory* (DLT), also known as the layerwise theory, is developed to obtain more accurate modelling of composite laminates. In this, each layer of the laminates is modelled as a 3-D solid. Unlike in the ESL theories, continuity is only exhibited through the laminate thickness in the case of the layerwise theories. Hence, transverse stresses are continuous through the laminate thickness but the in-plane stresses may be discontinuous at several points through the thickness. This enables a possible existence of continuous transverse stresses, at the interval of two layers of different materials, and constant shear strains through the thickness of the laminates. These two underlying factors have been applied to study laminated beams [64], two and three layered isotropic plates [65] and laminated plates [66, 67]. The Layerwise approach has also been extensively applied to determine the dynamic response of laminated composite structures [68–70]. However, the computational effort required to obtain the disper-

sion relation of composite laminates using the ESL and the layerwise theory can be enormous at best. This has resulted into the development of various analytical and numerical approaches for modelling the dispersion and wave propagation properties of periodic layered structures. These approaches are reviewed in the next paragraphs.

The *Transfer Matrix Method* (TMM) [71, 72] is based on dividing the structural system into a number of sections where the structural and material characteristics of each section are assumed to be homogeneous. Each section is idealised by a square matrix, known as the transfer matrix, relating the nodal displacements and internal forces of the left and right hand sides of the section. The transfer matrix of the whole structure is then obtained by a direct multiplication of the transfer matrices of the sections. Application of the transfer matrix method has mainly been applied to obtain the dynamic response of various structural systems such as spring-mass structure [71], beam-type periodic structure [73], layered panels [74] and nonlinear periodic beam [75]. TMM solutions can be sought analytically and numerically, where the former give more desirable solution, the latter is prone to poor numerical conditioning [45]. However, the symplectic property of the transfer matrix can be applied to obtain a more accurate numerical solution, as demonstrated by Zhong and Williams [76].

The *Dynamic Stiffness Method* (DSM) is based on the analytical determination of an exact shape function, in the frequency domain, as a solution to the differential equation of motion of the structural system. The structural system is divided (meshed) into a number of elements and the dynamic stiffness matrix, consisting of the mass, stiffness and damping matrices, of each element is obtained. The dynamic stiffness matrix relates the nodal displacements and the internal forces at the nodes of the elements. A global dynamic stiffness matrix is then obtained by assembling the dynamic stiffness matrices of the elements. Some application of this method to study the dynamics of structural systems include prediction of the dynamic characteristics of frame structures [77], 1-D waveguides [78, 79], 2-D plate and shell elements [80, 81], beam and truss structures [82], helical springs [83] and composite structure [84].

The *Receptance Method* (RM), as in the case of the dynamic stiffness method, establishes the receptance matrix, relating the nodal displacements and the internal forces at the nodes of the structural elements. The receptance matrix is obtained as the reciprocal of the dynamic stiffness matrix, which is obtained in the same manner as earlier stated. A periodicity condition, in which the nodal displacements (and internal forces) of the left hand side nodes are related to that of the right hand side nodes of the structural elements, is then applied to the equation of motion of the system in order to obtain a general eigenvalue problem. The solution of this eigenvalue problem gives the propagation constants of the system as a function of frequency. Applications of this method

to dynamics of structural systems include vibration absorption [85], pole placement in solution to structural vibration control problem [86, 87], wave propagation in various structural systems such as periodic beam [88], mono [89] and multi [90] coupled structural systems, layered panels [88]. The mass, stiffness and damping matrices are not required in vibration control analysis by receptance method. This serves as an advantage over the conventional matrix methods as numerical conditioning error, which is mainly as a result of the matrices poor conditioning, would be greatly reduced.

The *Spectral Element Method* (SEM), which is based on the weak/variational formulation of the differential equation of a structural problem, is developed to describe wave propagation characteristics in complicated structures such as a complex system with an assemblage of beam and/or rods. Each beam and/or rod is modelled as a single element and the wave propagation characteristics of the element is studied directly by obtaining the exact dynamic stiffness matrix of the element in the frequency domain. This reduces the number of degrees of freedom required to define the complicated structure thereby reducing computational effort. This can be a significant task by itself. Full description and applications of this method are presented by Doyle [91]. The approach has been applied to study dynamic properties in angle-ply laminates [92], rectangular plate [93], sandwich beam with honeycomb core [94], composite cylindrical shell [95], elastic-piezoelectric beam [96] and laminated composite beam [97]. However, this approach requires new spectral element and consequently new dynamic stiffness matrix be defined for each element (beam and/or rod) in a complex system [98], thereby making it computationally tedious.

Another related approach is the *Spectral Finite Element Method* (SFEM) in which the structural system is discretised using the conventional finite element method, and the dynamic stiffness matrix is determined using another approach such as the Hamiltonian method [99]. Consequently, spectral elements and elements matrices are required in the same manner as in the spectral element method. This approach has been applied to dynamic analysis of various structural systems such as thin-walled structures [100], railway tracks [99], pipe and type [101], layered plates [102] and laminated composite panels [103].

While the spectral element method is more of an analytical method, an alternative and a more general numerical method for solving dynamic problem of continuous structural systems is the *Finite Element Method* (FEM). FEM discretises structural system into a number of finite elements. The number of elements and DOF required to describe the system can become very large, depending on the complexity of the structure, and hence become computationally expensive and poorly conditioned especially at high frequency. To overcome these difficulties, especially that due to large model size, an

alternative wave-based approach known as the wave finite element is recommended.

The *Wave Finite Element* (WFE) method couples the periodic structure theory [104] to FEM. Unlike the spectral element method, there is no need for new element and matrix for each element of the system, and unlike the FEM, the size of the model is generally small even at high frequency. Hence, it is advantageous as it fully utilises commercial finite element analysis packages and existing finite element libraries, and generally computationally inexpensive. The WFE method which contains the assumption of periodicity to be modelled was first introduced by Mead [104]. It was first introduced by Mace et al. [105] to model wave propagation in periodic structures. WFE is extended to two-dimensional structures by Manconi and Mace [106]. It has been applied to a variety of structural situations, such as flat [107], curved [108] and stiffened [109] structures, under free [105, 110], forced [111–113] and simply supported [114] boundary conditions. It has also been applied to obtain wave scattering properties in cylindrical pipes with defects [115], structures with different types of joints [3, 116, 117] and damaged stiffened panels [118, 119]. The approach has recently found applications in predicting the vibroacoustic and dynamic performance of composite panels [120, 121]. The variability of vibroacoustic transmission through layered structures [122] as well as structural identification [2] have been investigated through the same methodology. Based on the advantages of the WFE method over other numerical methods, this research is mostly based on the method.

## 1.3 Aim and objectives

Based on the research motivation highlighted in this chapter, the main aim of this study is to develop computational models for wave propagation and interaction phenomena of the wave with damage in periodic layered structures. The specific objectives of the study are to:

(i) develop a wave based numerical scheme for quantifying wave interaction with damage within one-dimensional layered structures and extend the scheme to structures with periodicity in two directions;

(ii) analyse thermal effect on the wave propagation and interaction properties of layered structures;

(iii) analyse the impact of pressurisation on the wave propagation and interaction properties of pressurised layered structures;

(iv) develop a wave-based approach for identifying the geometric and material characteristics of layered composite structures;

(v) develop a wave based scheme for computing guided wave interaction with non-linear structural damage within structures of arbitrary layering and geometric complexity; and

(vi) establish an optimum basis for detecting and identifying structural damage, as well as assessing the orientation and extent of the damage.

## 1.4 Outline of the thesis

Relevant literature survey is presented in this chapter. The survey presents brief history of wave propagation modelling in periodic structures. It also presents the existing approaches for the computation of wave propagation data in periodic structures. The remainder of the thesis is outlined as follows:

In chapter 2, a numerical scheme for modelling wave propagation, and the interaction of the wave with damage, in periodic structures is presented. A WFE based methodology for predicting wave propagation properties of periodic layered structures is presented in the first part of the chapter. Implementation of structural damage within a periodic structure in the FE model of the structure is presented in the second part. Computation of wave interaction with damage within a defective periodic structure is then presented in the third part. The defective periodic structure is discretized as a system of $N$ substructures coupled though a coupling joint. The WFE computed wave constants for each substructure are coupled to the FE model of the coupling joint, which bears the structural damage, in order to quantify wave interaction with the damage.

In chapter 3, thermal impact on the wave propagation and interaction data in periodic structures is analysed. A thermal mechanical analysis is conducted to experimentally measure mechanical characteristics of a composite layered panel over a broad range of aerospace vehicle's ambient operating temperature. The measured thermo-mechanical characteristics are applied to study and analyse the effect of temperature on the wave propagation and interaction data within the composite panel. Numerical case studies are presented.

In chapter 4, the influence of pre-stressing on the wave propagation and interaction data in pressurised periodic structures is analysed. The developed wave propagation and interaction scheme is extended to incorporate pre-stress effect within pressurised layered structures. Pre-stress impact is analysed by comparison of the results of pressurised and non-pressurised structural case studies.

In chapter 5, an inverse wave finite element approach for identifying the geometric and material characteristics of layered composite structures is proposed. A Hilbert

Transform is employed to measure the time of arrival of the wave pulses along the structure under investigation and subsequently calculate the propagating wavenumbers. Identification objective function is formulated in terms of the structural and material characteristics to be identified. A Newton-like iterative scheme is then employed for minimising the formulated objective function and the mechanical characteristics of each individual layer are obtained through the solution of a system of eigenvalue expressions. Experimental and numerical case studies are presented for validating the presented methodology.

In chapter 6, a FE based computational scheme for quantifying guided wave interaction with nonlinear structural damage within structures of arbitrary layering and geometric complexity is developed. Through-width mode shape of each wave mode propagating within the structure is obtained, and then imposed on the structure in order to compute the wave interaction with nonlinear damage within the structure. Experimental and numerical case studies are presented to validate the developed scheme.

In chapter 7, a numerical scheme is presented for quantifying wave interaction with structural damage within two-dimensional multilayered structures. Numerical case studies are presented for different damage modes and structural parameters in order to establish an optimum basis for detecting and identifying damage, as well as assessing the orientation and extent of the detected damage.

Finally, in chapter 8, the main conclusions of the presented work are drawn, and some ideas on possible prospective work are presented. A list of the publications that resulted from this thesis are also presented.

# CHAPTER 2

# Wave propagation and interaction with damage in periodic structures

## 2.1 Wave propagation in one-dimensional periodic structures

### 2.1.1 Statement of the problem

Elastic wave propagation is considered in the $x$ direction of an arbitrarily layered composite structure. Periodicity condition is hence considered in the $x$ direction. Fig. 2.1 illustrates the FE-modelled periodic segment of the layered composite.

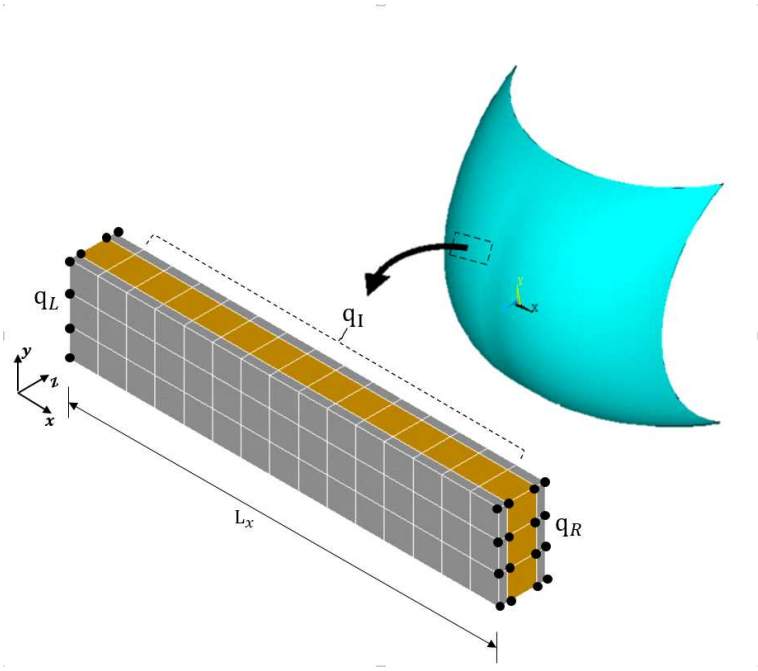


**Figure 2.1:** FE-modelled segment of the composite structure. The left and right sides nodes are bullet marked and the range of internal nodes illustrated

The segment is meshed using a conventional FE software such as ANSYS® or ABAQUS®. The stiffness, mass and damping matrices of the segment **K**, **M** and **C** are extracted using classical FEM algorithm (such as in Appendix A) and are post-processed in MATLAB®. The nodal displacements **q** and forces **f** vectors of the segment are reordered according to a predefined sequence such as

$$\begin{aligned} \mathbf{q} &= \{\mathbf{q}_L \;\; \mathbf{q}_I \;\; \mathbf{q}_R\}^\top \\ \mathbf{f} &= \{\mathbf{f}_L \;\; \mathbf{f}_I \;\; \mathbf{f}_R\}^\top \end{aligned} \tag{2.1.1}$$

where $L$, $R$ and $I$ correspond to its left, right and internal DoF.

### 2.1.2 Formulation of eigenvalue problem

The general equation of motion of the segment can be expressed as

$$\mathbf{M}\ddot{\mathbf{q}} + \mathbf{C}\dot{\mathbf{q}} + \mathbf{K}\mathbf{q} = \mathbf{f} \tag{2.1.2}$$

The problem can be solved using the periodic structure theory coupled to the FE as exhibited in [105]. The time harmonic equation of motion of the segment, assuming uniform and structural damping for all the DoF, can be expressed as

$$\mathbf{D}\mathbf{q} = \mathbf{f} \tag{2.1.3}$$

with the dynamic stiffness matrix **D** expressed as

$$\mathbf{D} = \mathbf{K}(1 + \mathrm{i}\eta) - \omega^2\mathbf{M} \tag{2.1.4}$$

where $\omega$ is the angular frequency and $\eta$ is the structural damping coefficient ($\mathbf{C} = \frac{\eta\mathbf{K}}{\omega}$). Eq. (2.1.3) can be expressed in terms of the left, right and internal DoF of the segment as

$$\begin{bmatrix} \mathbf{D}_{LL} & \mathbf{D}_{LI} & \mathbf{D}_{LR} \\ \mathbf{D}_{IL} & \mathbf{D}_{II} & \mathbf{D}_{IR} \\ \mathbf{D}_{RL} & \mathbf{D}_{RI} & \mathbf{D}_{RR} \end{bmatrix} \begin{Bmatrix} \mathbf{q}_L \\ \mathbf{q}_I \\ \mathbf{q}_R \end{Bmatrix} = \begin{Bmatrix} \mathbf{f}_L \\ \mathbf{f}_I \\ \mathbf{f}_R \end{Bmatrix} \tag{2.1.5}$$

It is assumed that no external forces are applied on the internal nodes, $\mathbf{f}_I = 0$. Applying dynamic condensation on the internal nodes DoF, Eq. (2.1.5) can be expressed as

$$\begin{bmatrix} \mathbf{D}_{11} & \mathbf{D}_{12} \\ \mathbf{D}_{21} & \mathbf{D}_{22} \end{bmatrix} \begin{Bmatrix} \mathbf{q}_L \\ \mathbf{q}_R \end{Bmatrix} = \begin{Bmatrix} \mathbf{f}_L \\ \mathbf{f}_R \end{Bmatrix} \tag{2.1.6}$$

with

$$\begin{aligned} \mathbf{D}_{11} &= \mathbf{D}_{LL} - \mathbf{D}_{LI}\mathbf{D}_{II}^{-1}\mathbf{D}_{IL}, \quad & \mathbf{D}_{12} &= \mathbf{D}_{LR} - \mathbf{D}_{LI}\mathbf{D}_{II}^{-1}\mathbf{D}_{IR} \\ \mathbf{D}_{21} &= \mathbf{D}_{RL} - \mathbf{D}_{RI}\mathbf{D}_{II}^{-1}\mathbf{D}_{IL}, \quad & \mathbf{D}_{22} &= \mathbf{D}_{RR} - \mathbf{D}_{RI}\mathbf{D}_{II}^{-1}\mathbf{D}_{IR} \end{aligned} \tag{2.1.7}$$

For a free wave propagation, the displacement continuity and equilibrium of forces equations at the interface of two consecutive periodic segments $s$ and $s+1$ are expressed as

$$\begin{aligned} \mathbf{q}_L^{s+1} &= \mathbf{q}_R^s \\ \mathbf{f}_L^{s+1} + \mathbf{f}_R^s &= 0 \end{aligned} \tag{2.1.8}$$

Combining Eqs. (2.1.6) and (2.1.8), the displacements and forces of the two consecutive periodic segments can be related as

$$\left\{ \begin{array}{c} \mathbf{q}_L^{s+1} \\ \mathbf{f}_L^{s+1} \end{array} \right\} = \mathbf{T} \left\{ \begin{array}{c} \mathbf{q}_L^{s} \\ \mathbf{f}_L^{s} \end{array} \right\} \tag{2.1.9}$$

where $\mathbf{T}$ is the symplectic transfer matrix expressed as

$$\mathbf{T} = \left[ \begin{array}{cc} -\mathbf{D}_{12}^{-1}\mathbf{D}_{11} & \mathbf{D}_{12}^{-1} \\ -\mathbf{D}_{21} + \mathbf{D}_{22}\mathbf{D}_{12}^{-1}\mathbf{D}_{11} & -\mathbf{D}_{22}\mathbf{D}_{12}^{-1} \end{array} \right]_{[2j\times 2j]} \tag{2.1.10}$$

where $j$ is the number of DoF on each periodic cross-section (along $x$-axis) of the segment.

With wave propagating along the $x$ direction, the unknown propagation constant $\lambda = \mathrm{e}^{-\mathrm{i}kL_x}$, along the axis of propagation, relates the right and left nodal displacements and forces according to Bloch's theorem as

$$\begin{aligned} \mathbf{q}_R^s &= \lambda \mathbf{q}_L^s \\ \mathbf{f}_R^s &= -\lambda \mathbf{f}_L^s \end{aligned} \tag{2.1.11}$$

Substituting Eqs. (2.1.8) and (2.1.11) in Eq. (2.1.9), the free wave propagation is described by the eigenvalue problem

$$\lambda \left\{ \begin{array}{c} \mathbf{q}_L \\ \mathbf{f}_L \end{array} \right\} = \mathbf{T} \left\{ \begin{array}{c} \mathbf{q}_L \\ \mathbf{f}_L \end{array} \right\} \tag{2.1.12}$$

### 2.1.3 Solution of the eigenvalue problem

Solving the eigenproblem (Eq. (2.1.12)) yields eigenvalue $\lambda_{\mathrm{w}}(\omega)$ and eigenvector $\boldsymbol{\phi}_{\mathrm{w}}(\omega) = \left\{ \begin{array}{c} \boldsymbol{\phi}_q \\ \boldsymbol{\phi}_f \end{array} \right\}_{[2j\times 1]}$ solution set for each of the elastic waves propagating along the

structural segment at a specified angular frequency $\omega$. This set gives a comprehensive description of the propagation constant and the mode shape of the wave. Positive (forward) going (with $\lambda^{\text{inc}}$ and $\boldsymbol{\phi}^{\text{inc}}$) and negative (backward) going (with $\lambda^{\text{ref}}$ and $\boldsymbol{\phi}^{\text{ref}}$) waves are also sought through the eigensolution.

The wavenumbers of the waves (at a specified angular frequency) in the positive $k^{\text{inc}}$ and the negative $k^{\text{ref}}$ directions can be determined from the propagation constants as

$$k^{\text{inc}}(\omega) = -\frac{\ln(\lambda^{\text{inc}})}{\mathrm{i}L_x}, \;\; k^{\text{ref}}(\omega) = -\frac{\ln(\lambda^{\text{ref}})}{\mathrm{i}L_x} \tag{2.1.13}$$

Due to the symplectic nature of the transfer matrix, its eigenvalues occur in reciprocal pairs, $\lambda_{\text{w}}^{\text{inc}}$ and $\lambda_{\text{w}}^{\text{ref}} = 1/\lambda_{\text{w}}^{\text{inc}}$ with respective wavenumbers $k_{\text{w}}^{\text{inc}}$ and $k_{\text{w}}^{\text{ref}} = -k_{\text{w}}^{\text{inc}}$, which correspond to positive and negative-going waves [105].

### 2.1.4 Properties of the eigensolution

The solution of the eigenproblem yields a number of waves at each considered angular frequency. However, few of these are propagating waves while the rest are evanescent waves. Generally, propagating waves have very small amplitude change (dissipation) but high oscillation (phase change) while evanescent waves oscillate very slightly but amplitude decays rapidly.

The wavenumber of each wave is obtained in the form

$$k_{\text{w}} = \Re(k_{\text{w}}) + \Im(k_{\text{w}})\mathrm{i} \tag{2.1.14}$$

whose real part indicates the phase change and imaginary part indicates the wave dissipation. As the wave propagates along a waveguide, power flow through the waveguide is obtained as

$$\mathbb{P}_{\text{w}} = \Re(\mathrm{i}\omega \boldsymbol{\phi}_f^{\top} \boldsymbol{\phi}_q)_{\text{w}} \tag{2.1.15}$$

For an undamped structural waveguide, $\Im(k_{\text{w}}) = 0$ and hence $k$ is purely real. Positive going wave along the waveguide is characterised by

$$\begin{gathered} |\lambda_{\text{w}}| \leq 1, \\ \mathbb{P}_{\text{w}} < 0 \;\text{ if }\; |\lambda_{\text{w}}| = 1 \end{gathered} \tag{2.1.16}$$

which states that the amplitude of a positive going wave is either decreasing, towards the direction of propagation, or constant, in the case of waves with no dissipation. The first case, in which no phase change is observed, corresponds to an evanescent wave while the other one, with no dissipation, refers to a propagating wave. That is, the

wavenumber of a propagating wave is purely real while that of an evanescent wave is purely imaginary in an undamped structural waveguide.

For damped structural waveguide, $\Im(k_{\mathrm{w}}) \neq 0$ and hence $k$ is complex. Positive going wave along the waveguide is characterised by

$$|\lambda_{\mathrm{w}}| < 1 \tag{2.1.17}$$

which states that the amplitude of a positive wave along a damped waveguide decreases towards the direction of propagation. The magnitude of $\Im(k_{\mathrm{w}})$ is small compared to that of $\Re(k_{\mathrm{w}})$ for a propagating wave, and otherwise for an evanescent wave within the damped waveguide. This indicates that the propagating wave contains small dissipation (slowly decaying) and the evanescent wave has little phase change (slightly oscillating). Propagating wave along the waveguide is therefore described by

$$\frac{\Re(k_{\mathrm{w}})}{\Im(k_{\mathrm{w}})} > cr \tag{2.1.18}$$

where $cr$ is a positive number. For a layered composite waveguide, the value of $cr$ is generally $\geq 10$.

Properties of the waves constants for undamped and damped waveguides are summarised in Table 2.1.

**Table 2.1:** Wave constants properties of different waves types

| Undamped structural system | | | | | |
|---|---|---|---|---|---|
| direction | wave type | $\Re(k_{\mathrm{w}})$ | $\Im(k_{\mathrm{w}})$ | $\lvert\lambda_{\mathrm{w}}\rvert$ | $\mathbb{P}_{\mathrm{w}}$ |
| positive-going | propagating wave | $> 0$ | $0$ | $1$ | $< 0$ |
| | evanescent wave | $0$ | $< 0$ | $< 1$ | $< 0$ |
| negative-going | propagating wave | $< 0$ | $0$ | $1$ | $> 0$ |
| | evanescent wave | $0$ | $> 0$ | $> 1$ | $> 0$ |

| Damped structural system | | | |
|---|---|---|---|
| direction | wave type | $\Re(k_{\mathrm{w}})/\Im(k_{\mathrm{w}})$ | $\lvert\lambda\rvert$ |
| positive-going | slowly decaying propagating wave | $> cr$ | $< 1$ |
| | slightly oscillatory evanescent wave | $< cr$ | $< 1$ |
| negative-going | slowly decaying propagating wave | $> cr$ | $> 1$ |
| | slightly oscillatory evanescent wave | $< cr$ | $> 1$ |

Wave modes at each considered angular frequency are correlated against the modes at previous frequency in order to sort the wave modes into different wave types. A wave modal assurance criterion (MAC), calculated as

$$MAC = \frac{(\boldsymbol{\phi}^{\top}{}_{\omega 1}\bar{\boldsymbol{\phi}}_{\omega 2})(\boldsymbol{\phi}^{\top}{}_{\omega 2}\bar{\boldsymbol{\phi}}_{\omega 1})}{(\boldsymbol{\phi}^{\top}{}_{\omega 1}\bar{\boldsymbol{\phi}}_{\omega 1})(\boldsymbol{\phi}^{\top}{}_{\omega 2}\bar{\boldsymbol{\phi}}_{\omega 2})} \tag{2.1.19}$$

is used for the correlation. $^{\top}$ and $\bar{}$ are respectively the transpose and conjugate of the vectors, $\boldsymbol{\phi}_{\omega 1}$ is the propagating wave mode to be correlated at present frequency $\omega 2$ and $\boldsymbol{\phi}_{\omega 2}$ is each of the propagating modes already correlated at previous frequency $\omega 1$. A maximum MAC value of 1 indicates a very strong correlation between the two modes while a minimum value of 0 indicates a very weak correlation. During the correlation process, a MAC cut-off value of 1 is first attempted, and if no correlated wave modes are found at this cut-off value, then a lower cut-off value is attempted until the selected wave mode is correlated to a wave type.

### 2.1.5 Normalisation and numerical accuracy

It is useful to obtain the left eigenvector $\boldsymbol{\psi}_{\mathrm{w}}(\omega) = \left\{ \begin{array}{c} \boldsymbol{\psi}_q \\ \boldsymbol{\psi}_f \end{array} \right\}_{[1\times 2j]}$ to improve the accuracy of the wave propagation and interaction analysis. The left eigenvalue problem

$$\lambda_{\mathrm{w}} \left\{ \begin{array}{c} \boldsymbol{\psi}_q \\ \boldsymbol{\psi}_f \end{array} \right\}_{\mathrm{w}} = \left\{ \begin{array}{c} \boldsymbol{\psi}_q \\ \boldsymbol{\psi}_f \end{array} \right\}_{\mathrm{w}} \mathbf{T} \tag{2.1.20}$$

has the same eigenvalues as the right eigenvalue problem (Eq. (2.1.12)). The right and left eigenvectors are orthogonal such that

$$\begin{aligned} \boldsymbol{\psi}_{\mathrm{w}}\boldsymbol{\phi}_{\mathrm{W}} &= 0, \ \ \mathrm{w} \neq \mathrm{W} \\ \boldsymbol{\psi}_{\mathrm{w}}\boldsymbol{\phi}_{\mathrm{W}} &= \delta, \ \ \mathrm{w} = \mathrm{W} \end{aligned} \tag{2.1.21}$$

where $\delta$ is arbitrary.

A useful consequence of this property is that, at a specified frequency, the right eigenvectors can be normalised such that

$$\begin{aligned} \boldsymbol{\psi}_{\mathrm{w}}\boldsymbol{\phi}_{\mathrm{W}} &= 0, \ \ \mathrm{w} \neq \mathrm{W} \\ \boldsymbol{\psi}_{\mathrm{w}}\boldsymbol{\phi}_{\mathrm{W}} &= 1, \ \ \mathrm{w} = \mathrm{W} \end{aligned} \tag{2.1.22}$$

This can be applied to reduce numerical ill-conditioning in the eigensolution.

## 2.2 Finite element modelling of structural damage

Wave interaction with structural damage in layered structures is considered in this study. This section presents the finite element methodologies for some common damage in composite structures. Composite structures are subject to a number of damage modes which range from microscopic fibre faults to large, gross impact damage.

Among these failure modes, notch, crack, delamination and fibre breakage are common failure modes found in composites [123, 124].

In this study, a damaged layered structure is discretized as system of $N$ healthy substructures connected through a damaged coupling joint. FE methods are used to describe the effect of the damage on the mechanical behaviour of the coupling joint. This is implemented in the FE model of the coupling joint. Some of these methods include stiffness reduction, element deletion, duplicate node and kinematics based methods. Descriptions of each of these methods and their applicability are given in the following sections.

### 2.2.1 Stiffness reduction method

It is a known fact that structural defects contribute to a reduction in the overall stiffness properties of the structural segment. In this method, the stiffness loss is incorporated in the FE modelling of the structural segment by multiplying the material property of the structure by a reduction factor $\beta$ as

$$P = \beta P_0, \quad 0 < \beta \leq 1 \tag{2.2.1}$$

where $P$ is the reduced material property, $P_0$ the original magnitude of the property (which can be elastic modulus, shear modulus or density). $\beta$ being the reduction factor, equals unity for a pristine structure. This method is applicable to model cracks and delamination, but it is limited to wave interaction problem where mode conversion is not expected.

### 2.2.2 Element deletion method

This method is mainly applicable for modelling notches such as holes (fibre fractures) and rectangular notches in composites. Here, an element or a number of elements along the axis of the defect is/are deleted from the structure to simulate the effect of the defect. This leads to a reduction in the overall mass and stiffness of the structure. It is one of the simplest FE damage modelling methods as it doesn't require mesh modification.

### 2.2.3 Node duplication method

The node duplication method is applicable for modelling various damage types such as single and multiple delamination and cracks, and fibre breakages.

In this method, nodes along axis of the damage, within the structural segment, are disconnected by adding duplicate nodes, which have the same nodal coordinates but

different nodes numbers, to the nodes being disconnected. Each duplicate node is assigned to an adjacent element such that when a tensile force is applied, the nodes along the damage front are separated. In this respect, if the original nodes are connected to the left side elements, the duplicate nodes will be connected to the elements on the right side.

Illustration examples of this method are presented for 2D and 3D structural segments with through-width damage as presented in Appendix B.

### 2.2.4 Kinematics based method

This approach has a lot of similarities to the node duplication method. It involves enforcing kinematics to the nodes surrounding the damage. The structural segment is segmented into multiple domains along the crack front. The stiffness and mass matrices of each domain are generated and coupled to obtain the overall matrices of the structural segment. More details on the approach can be found in [125]. The method is applicable to model delamination, cracks and fibre breakages.

## 2.3 Wave interaction with damage within a one-dimensional periodic structure

### 2.3.1 Statement of the problem

An arbitrarily layered composite structure containing structural nonlinearity, such as damage, is hereby considered. Periodicity and hence wave propagation are considered in the $x$ direction. The structure is discretized as a system of $N$ healthy substructures connected through a coupling joint, which bears the structural damage/nonlinearity, as shown in Fig. 2.2.

Propagation constants for the waves propagating along each substructure are sought as presented in Sec. 2.1, and interaction of the waves with the damage within the joint is computed in the section. The joint is fully FE modelled in order to implement the structural damage.

### 2.3.2 Formulation of the dynamic stiffness matrix of the joint

The equation of motion for the FE modelled coupling joint can be in general written as

$$\mathbb{M}\ddot{\mathbf{z}} + \mathbb{C}\dot{\mathbf{z}} + \mathbb{K}\mathbf{z} = \mathbf{f}^{\mathbf{e}} \tag{2.3.1}$$

with the frequency dependent dynamic stiffness matrix (DSM) of the joint expressed as

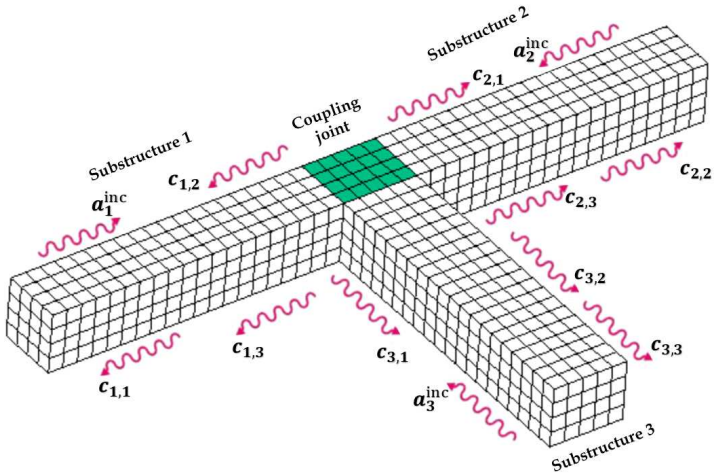


**Figure 2.2:** Wave propagation in one-dimensional structural system consisting of substructures connected through a joint. Waves having amplitudes $\mathbf{a}_n^{\text{inc}}$ impinging on the joint from the $n$th substructure will give rise to waves of reflection coefficients $\mathbf{c}_{n,n}$ in the $n$th substructure and waves of transmission coefficients $\mathbf{c}_{k,n}$ in the $k$th substructure

$$\mathbb{D} = \mathbb{K} + i\omega\mathbb{C} - \omega^2\mathbb{M} \tag{2.3.2}$$

where $\mathbb{K}, \mathbb{C}$ and $\mathbb{M}$ are stiffness, damping and mass matrices of the coupling joint, $\mathbf{z}$ is the physical displacement vector of the coupling joint and $\mathbf{f_e}$ is the set of elastic forces applied to the coupling joint at its interface with connected substructure. It is assumed that all connected substructure are considered to be purely elastic. As a result of this and similar to the substructure, the DSM of the joint can be partitioned with regards to the interface $\mathbb{i}$ and non-interface $\mathbb{n}$ DoF of the joint with the substructure as

$$\begin{bmatrix} \mathbb{D}_{\mathbb{i}\mathbb{i}} & \mathbb{D}_{\mathbb{i}\mathbb{n}} \\ \mathbb{D}_{\mathbb{n}\mathbb{i}} & \mathbb{D}_{\mathbb{n}\mathbb{n}} \end{bmatrix} \begin{Bmatrix} \mathbf{z}_{\mathbb{i}} \\ \mathbf{z}_{\mathbb{n}} \end{Bmatrix} = \begin{Bmatrix} \mathbf{f}_{\mathbb{i}}^{\mathbf{e}} \\ \mathbf{f}_{\mathbb{n}}^{\mathbf{e}} \end{Bmatrix} \tag{2.3.3}$$

It is assumed that no force is applied at the non-interface nodes of the joint, i.e. $\mathbf{f}_{\mathbb{n}}^{\mathbf{e}} = \mathbf{0}$. Applying dynamic condensation on the non-interface DoF, Eq. (2.3.3) can be expressed as

$$\mathbb{D}_{\mathbb{J}}\mathbf{z}_{\mathbb{i}} = \mathbf{f}_{\mathbb{i}}^{\mathbf{e}} \tag{2.3.4}$$

with the DSM of the joint expressed as

$$\mathbb{D}_{\mathbb{J}} = [\mathbb{D}_{\mathbb{i}\mathbb{i}} - \mathbb{D}_{\mathbb{i}\mathbb{n}}\mathbb{D}_{\mathbb{n}\mathbb{n}}^{-1}\mathbb{D}_{\mathbb{n}\mathbb{i}}]_{[jN\times jN]} \tag{2.3.5}$$

at a specified angular frequency.

### 2.3.3 Calculation of the wave interaction scattering coefficients

Each supported wavemode w with w $\in [1 \cdots W]$ for substructure $n$ with $n \in [1 \cdots N]$, at a specified angular frequency, can be grouped as

$$\begin{aligned}
\mathbf{\Phi}^{\text{inc}}_{n,q} &= \begin{bmatrix} \boldsymbol{\phi}^{\text{inc}}_{q,1} & \boldsymbol{\phi}^{\text{inc}}_{q,2} & \cdots & \boldsymbol{\phi}^{\text{inc}}_{q,W} \end{bmatrix}_{[j\times W]} \\
\mathbf{\Phi}^{\text{inc}}_{n,f} &= \begin{bmatrix} \boldsymbol{\phi}^{\text{inc}}_{f,1} & \boldsymbol{\phi}^{\text{inc}}_{f,2} & \cdots & \boldsymbol{\phi}^{\text{inc}}_{f,W} \end{bmatrix}_{[j\times W]} \\
\mathbf{\Phi}^{\text{ref}}_{n,q} &= \begin{bmatrix} \boldsymbol{\phi}^{\text{ref}}_{q,1} & \boldsymbol{\phi}^{\text{ref}}_{q,2} & \cdots & \boldsymbol{\phi}^{\text{ref}}_{q,W} \end{bmatrix}_{[j\times W]} \\
\mathbf{\Phi}^{\text{ref}}_{n,f} &= \begin{bmatrix} \boldsymbol{\phi}^{\text{ref}}_{f,1} & \boldsymbol{\phi}^{\text{ref}}_{f,2} & \cdots & \boldsymbol{\phi}^{\text{ref}}_{f,W} \end{bmatrix}_{[j\times W]}
\end{aligned} \tag{2.3.6}$$

The wavemodes of the entire substructures in the system, at a specified frequency, can then be grouped as

$$\mathbf{\Phi}^{\text{inc}}_{q}(\omega, k_y) = \begin{bmatrix} \mathbf{\Phi}^{\text{inc}}_{1,q} & \mathbf{0} & \cdots & \mathbf{0} \\ \mathbf{0} & \mathbf{\Phi}^{\text{inc}}_{2,q} & \cdots & \mathbf{0} \\ \cdots & \cdots & \cdots & \cdots \\ \mathbf{0} & \mathbf{0} & \cdots & \mathbf{\Phi}^{\text{inc}}_{N,q} \end{bmatrix}_{[jN\times WN]} \tag{2.3.7}$$

with respective expressions for $\mathbf{\Phi}^{\text{inc}}_{f}$, $\mathbf{\Phi}^{\text{ref}}_{q}$, and $\mathbf{\Phi}^{\text{ref}}_{f}$.

For each substructure, a local coordinate system is defined such that the substructure's axis is directed towards the joint as shown in Fig. 2.2. A rotation matrix $\mathbf{R_n}$ is defined, which transforms the DoF of each substructure from the local to the global coordinates of the system. The wavemodes of the substructures are transformed into global coordinates as

$$\mathbf{\Phi}^{\text{g,inc}}_{q} = \mathbf{R}\mathbf{\Phi}^{\text{inc}}_{q} \tag{2.3.8}$$

with respective similar expressions for $\mathbf{\Phi}^{\text{g,inc}}_{f}$, $\mathbf{\Phi}^{\text{g,ref}}_{q}$ and $\mathbf{\Phi}^{\text{g,ref}}_{f}$. Superscript g denotes the global coordinates index and $\mathbf{R}$ represents the rotation matrices of the system's substructures, grouped in a block diagonal matrix as

$$\mathbf{R} = \begin{bmatrix} \mathbf{R}_1 & \mathbf{0} & \cdots & \mathbf{0} \\ \mathbf{0} & \mathbf{R}_2 & \cdots & \mathbf{0} \\ \cdots & \cdots & \cdots & \cdots \\ \mathbf{0} & \mathbf{0} & \cdots & \mathbf{R}_N \end{bmatrix}_{[jN\times jN]} \tag{2.3.9}$$

The equilibrium of forces at the coupling joint interfaces with the substructures is expressed as

$$\mathbf{f}_{\mathbb{i}}^{\mathbf{e}} - \mathbf{R}\mathbf{f} = 0 \tag{2.3.10}$$

where $\mathbf{f}$ is the set of forces applied by the substructures at the interfaces.

The continuity conditions at the interfaces give

$$\mathbf{z}_{\mathbb{i}} = \mathbf{R}\mathbf{q} \tag{2.3.11}$$

with

$$\mathbf{q} = \begin{bmatrix} \mathbf{q}_1 & \mathbf{q}_2 & \cdots \mathbf{q}_N \end{bmatrix}^{\top}_{[jN\times 1]} \tag{2.3.12}$$

As shown in Fig. 2.2, waves of amplitudes $\mathbf{a}_n^{\text{inc}}$ are impinging on the coupling joint from the $n$th substructure. These give rise to reflected waves of amplitudes $\mathbf{a}_n^{\text{ref}}$ in the $n$th substructure and transmitted waves of amplitudes $\mathbf{a}_k^{\text{ref}}$ in the $k$th substructure (and vice versa). The reflected and transmitted waves amplitudes are related to the reflection $\mathbf{c}_{n,n}$ and transmission $\mathbf{c}_{k,n}$ coefficients of the scattered waves as

$$\begin{aligned} \mathbf{a}_n^{\text{ref}} &= \mathbf{c}_{n,n}\mathbf{a}_n^{\text{inc}} \\ \mathbf{a}_k^{\text{ref}} &= \mathbf{c}_{k,n}\mathbf{a}_n^{\text{inc}} \end{aligned} \tag{2.3.13}$$

Hence, the incident waves amplitudes can be related to the amplitudes of the scattered waves as

$$\mathbf{a}^{\text{ref}} = \mathbf{S}\mathbf{a}^{\text{inc}} \tag{2.3.14}$$

where ${\mathbf{a}^{\text{inc}}}_{[WN\times 1]}$ is the vector containing the amplitudes of the incident waves moving towards the coupling joint and ${\mathbf{a}^{\text{ref}}}_{[WN\times 1]}$ the vector containing the amplitudes of the reflected and transmitted scattered waves. The wave scattering matrix $\mathbf{S}$ whose diagonal and off-diagonal elements respectively represent the reflection and transmission coefficients of the scattered waves can be expressed in the form

$$\mathbf{S} = \begin{bmatrix} \mathbf{c}_{1,1} & \cdots & \mathbf{c}_{1,W} & \cdots & \mathbf{c}_{1,WN} \\ \cdots & \cdots & \cdots & \cdots & \cdots \\ \mathbf{c}_{W,1} & \cdots & \mathbf{c}_{W,W} & \cdots & \mathbf{c}_{W,WN} \\ \cdots & \cdots & \cdots & \cdots & \cdots \\ \mathbf{c}_{WN,1} & \cdots & \mathbf{c}_{WN,W} & \cdots & \mathbf{c}_{WN,WN} \end{bmatrix}_{[WN\times WN]} \tag{2.3.15}$$

In order to calculate the scattering matrix, an expression is defined for the motion in the substructures between the physical domain, where the motion is described in terms of $\mathbf{q}$ and $\mathbf{f}$ and the wave domain, where the motion is described in terms of waves of

amplitudes $\mathbf{a}^{\text{inc}}$ and $\mathbf{a}^{\text{ref}}$ travelling in the positive and negative directions respectively as

$$\begin{aligned} \mathbf{q}_n &= \boldsymbol{\Phi}_{n,q}^{\text{inc}} \mathbf{a}_n^{\text{inc}} + \boldsymbol{\Phi}_{n,q}^{\text{ref}} \mathbf{a}_n^{\text{ref}} \\ \mathbf{f}_n &= \boldsymbol{\Phi}_{n,f}^{\text{inc}} \mathbf{a}_n^{\text{inc}} + \boldsymbol{\Phi}_{n,f}^{\text{ref}} \mathbf{a}_n^{\text{ref}} \end{aligned} \tag{2.3.16}$$

and by concatenating the corresponding vectors and matrices, the general expressions for $\mathbf{q}$ and $\mathbf{f}$ for the system's substructures can be expressed as

$$\begin{aligned} \mathbf{q} &= \boldsymbol{\Phi}_{q}^{\text{inc}} \mathbf{a}^{\text{inc}} + \boldsymbol{\Phi}_{q}^{\text{ref}} \mathbf{a}^{\text{ref}} \\ \mathbf{f} &= \boldsymbol{\Phi}_{f}^{\text{inc}} \mathbf{a}^{\text{inc}} + \boldsymbol{\Phi}_{f}^{\text{ref}} \mathbf{a}^{\text{ref}} \end{aligned} \tag{2.3.17}$$

Substituting Eq. 2.3.4 into the equilibrium equation (Eq. 2.3.10) and the continuity equation (Eq. 2.3.11) into the resulting expression gives

$$\mathbb{D}_{\mathbb{J}} \mathbf{R} \mathbf{q} = \mathbf{R} \mathbf{f} \tag{2.3.18}$$

Also Substituting Eqs. 2.3.8 and 2.3.17 into Eq. 2.3.18 and express the resulting equation in the form of Eq. 2.3.14 gives the wave interaction scattering matrix as

$$\boldsymbol{S}(\omega) = -[\boldsymbol{\Phi}_{f}^{\text{g,ref}} - \mathbb{D}_{\mathbb{J}} \boldsymbol{\Phi}_{q}^{\text{g,ref}}]^{-1} [\boldsymbol{\Phi}_{f}^{\text{g,inc}} - \mathbb{D}_{\mathbb{J}} \boldsymbol{\Phi}_{q}^{\text{g,inc}}] \tag{2.3.19}$$

for a specified angular frequency.

# CHAPTER 3

# Thermal impact on wave interaction with damage in periodic composite structures

## 3.1 Introduction

Composite structures are being increasingly used in many industrial fields, such as aerospace and military, due to their versatile physical and mechanical properties. However, aerospace and automotive structures operate within varying temperature range, which is typically from -100°C to +200°C for launch vehicles and from -60°C to +50°C for aircraft and automobile structures. Despite their versatility, composite structures may exhibit a great variety of structural failure modes for which they must be thoroughly inspected in order to ensure continuous usage and structural integrity. These modes, which include delamination, notch, fibre breakage, matrix crack and debonding, occur mainly as a result of loads during service and inaccuracies during manufacturing. Aeronautics industries spend approximately 27% of an average modern aircraft's lifecycle cost on offline inspection and repair of the structural failures [126]. Therefore, the non-destructive damage detection and evaluation is of paramount importance for monitoring the condition and residual life estimation of in-service aerospace structures. Of particular interest is thermal-dependent damage detection in composite layered structures.

Thermomechanical behaviour of laminated structures has been conducted on various topics. In Lee et al. [127], the elastodynamic response of a polymeric laminate subjected to a discrete range of temperatures at a constant relative humidity is studied, with damping and dynamic longitudinal elastic modulus presented as a function of temperature dependent. In Barker and Vangerko [128, 129], the temperature-

dependent elastic constant and dynamic shear properties of an epoxy resin and its carbon fibre reinforced composite are presented. More recently, the effect of high temperatures on the thermomechanical response of various composite structures, such as multi-layered plates and shells [130], glass epoxy composites [131, 132] and carbon fibre epoxy composites [133, 134], has been extensively assessed. Moreover, temperature-dependent wave-based detection of structural damage has been an extensive field of study over the recent years. In Konstantinidis et al. [135, 136], baseline subtraction approach is used to predict temperature effect on guided wave signal and to optimally enhance the long-term stability of the signal. The approach is extended in Clarke et al. [137, 138] to reduce the number of baseline measurements to be used. Pitch-catch approach is used to numerically predict and experimentally measure the effect of [139] as well as moderately [140] and extremely [141] elevated temperature on the Lamb wave response in sandwich panels and aluminium plates, respectively. This is extended in di Scalea and Salamone [142] to cover a wider range of temperature in a large frequency range. Semi-analytical finite element (SAFE) model is developed in Marzani and Salamone [143] to predict guided wave response under varying temperature in plate. More recently, co-integration technique is developed to control the effect of varying temperature in damage detection of structure based on spectral lines analysis [144, 145], wavelet decomposition [146] and direct Lamb wave responses [147]. However, FE-based computational scheme is quite limited in this field of research and the investigation of thermal effect on wave interaction within complex and arbitrarily layered composite structures is almost in-existent in the open literature.

Wave-based damage detection methods are based on calculating wave scattering (reflection and transmission) coefficients from wave interaction with inhomogeneity within structural waveguides. It has been shown that a fraction (known as reflection coefficient) of an incident wave will be reflected due to an interaction with inhomogeneity within a medium. Structural inhomogeneity can be in the form of joint; such as point and finite joint [148], beam connection [149], plate and stiffened rib connection [150], angled joint [151], curved junction [152], T-junction [153] and L-junction [3, 154], or in the form of damage; such as crack [155] and delamination [156] within the structure.

Calculation of the wave scattering coefficients have been exhibited using various numerical methods, among which the WFE method [105] is one of the most efficient computational methods. The method has been applied to calculate wave scattering properties of various structural joints [3, 157–159]. However, application of this method can be extended to wave scattering from damage within layered structures. Evaluation of the service conditions the structures are subject to, will be a significant contribution

towards non-destructive damage detection of the structures.

Hence, the main contribution of this chapter is to evaluate the effect of temperature on wave propagation and the interaction of the wave with damage in periodic composite structures. The temperature-dependent mechanical properties of a layered composite panel consisting of a honeycomb core sandwiched between carbon epoxy facesheets are experimentally calculated using a thermal mechanical analysis. These are applied to compute temperature-dependent wave scattering from damage within the composite panel in order to evaluate thermal effects on the scattering coefficients.

## 3.2 Measurement of Temperature Dependent Mechanical characteristics

A Thermal Mechanical Analysis (TMA) device is used to measure the temperature dependent mechanical characteristics of a sandwich panel comprising of a carbon epoxy facesheet and a quasi-isotropic honeycomb core, which absorbs and adheres to the resin in which the facesheet is impregnated. In the polymerisation process, the resin serves as the facesheet matrix as well as the binding agent. The nominal mechanical characteristics of the composite panel's constituents at an ambient temperature of $20°C$ are shown in Table 3.1.

**Table 3.1:** Nominal mechanical properties of a sandwich composite panel at $20°C$

| Carbon Epoxy | Honeycomb foam |
|---|---|
| $E = 54$ GPa | $E_x = 85$ MPa |
| $\rho = 1410$ kg/m$^3$ | $E_y = 85$ MPa |
| $\nu = 0.09$ | $\rho = 48$ kg/m$^3$ |
| | $\nu_{xy} = 0.23$ |
| | $G_{yz} = 44$ MPa |
| | $G_{xz} = 44$ MPa |

Measurements are made at a temperature range of -5°C to 150°C and then extrapolated for the results of temperatures up to -100°C by assuming smooth quadratic expansion of the curves. This extrapolation is done to capture the lower limits of the operating temperature range of the composite panel as an aerospace structure. Such extrapolation is generally acceptable for composite materials having no significant transition (such as crystallisation) in their metallography structure at low temperature range (such as those below -5°C).

Temperature dependent elastic modulus of the facesheet material is measured us-

**Figure 3.1:** Configuration of the segment of the facesheet under traction test in the TMA device

ing the TMA device by subjecting the segment of the facesheet to an initial longitudinal traction test (Fig. 3.1) before imposing a 1 Hz excitation as displacement to the segment. The corresponding material loss factor is determined as $\tan\delta = E^1/E^2$, where $\delta$ is the phase lag between the stress and strain, $E^1$ the loss modulus and $E^2$ the storage modulus of the material. A reduction ratio, $R_f$, calculated as $R_f = E_a/E_n$ is determined at each temperature of the measured elastic modulus, with $E_a$ the measured (actual) values at respective temperature and $E_n$ the nominal value at ambient temperature as given in Table 3.1. This is used to calculate the actual values of other mechanical characteristics of the material as $E_a = R_f \times E_n$ at each corresponding temperature using the nominal value of each of the mechanical characteristics.

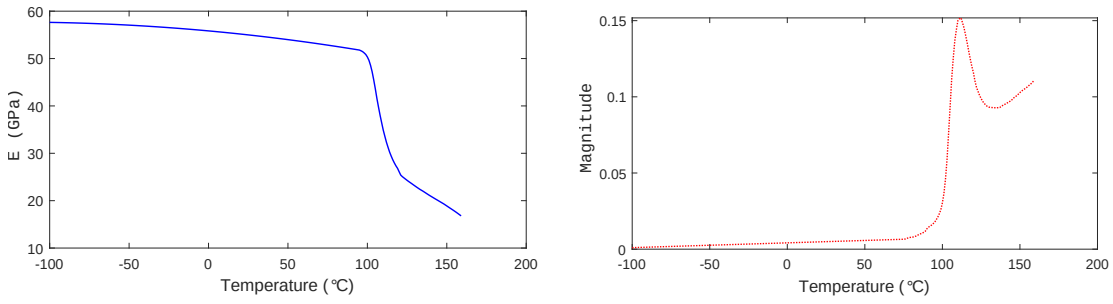


**(a)** Elastic modulus **(b)** Loss factor

**Figure 3.2:** Experimentally measured temperature dependent elastic modulus (-) and the corresponding material loss factor ($\cdots$) for the facesheet material

The results of the experimental measurements and the corresponding material loss

factor are presented in Fig. 3.2. The measured elastic modulus decreases while the corresponding material loss factor increases slightly with temperature until $110^{\circ}C$, where the glass transition of the resin occurs. There is a drastic increase of the loss factor to the peak level at this temperature range. Beyond this temperature, the elastic modulus decreases rapidly with temperature while the loss factor decreases, then start increasing again due to the high viscosity of the resin at this temperature.

**Figure 3.3:** Configuration of the segment of the core under shear deformation in the TMA device

On the other hand, temperature dependent shear modulus of the honeycomb core is measured using the TMA machine by subjecting the segment of the core to shear deformation as shown in the configuration in Fig. 3.3. In order to avoid any influence of the elasticity of the facesheet on the shear deformation of the core's segment, a steel sheet layer is attached onto it to increase its rigidity. Similar calculations, as described in the Elastic's modulus measurement, are carried out to determine the shear modulus and the corresponding material loss ratios of the quasi-isotropic honeycomb core.

The results of the temperature dependent shear modulus measurements and the corresponding material loss factor are presented in Fig. 3.4. Results measured in this case show similar trend as in the case of the facesheet material.

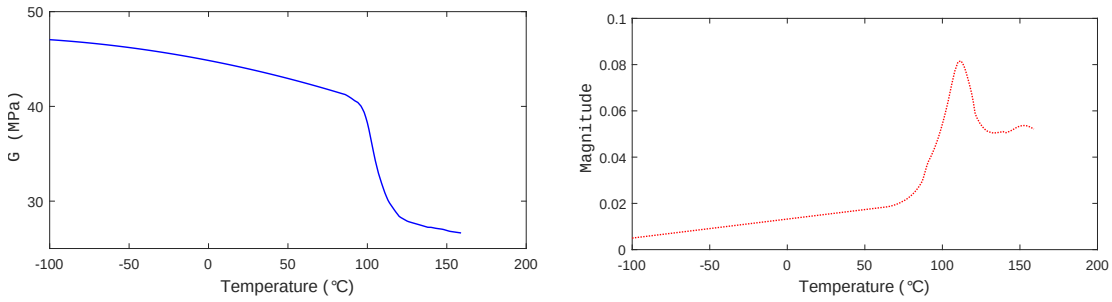


**(a)** Shear modulus **(b)** Loss factor

**Figure 3.4:** Experimentally measured temperature dependent shear modulus (-) and the corresponding material loss factor (· · · ) for the honeycomb core material

## 3.3 Temperature dependent wave characteristics in periodic layered structures

### 3.3.1 Temperature dependent wave propagation constants

Temperature dependent wave propagation along an arbitrarily layered sandwich panel, which is periodic in the $x$ direction, is considered. Wave motion is considered along the $x$ direction. Following the wave propagation analysis presented in Sec. 2.1.2, the free wave propagation along the panel can be defined by the eigenvalue problem

$$\lambda \begin{Bmatrix} \mathbf{q}_L \\ \mathbf{f}_L \end{Bmatrix} = \mathbf{T} \begin{Bmatrix} \mathbf{q}_L \\ \mathbf{f}_L \end{Bmatrix} \tag{3.3.1}$$

whose solution yields eigenvalue $\lambda_{\mathrm{w}}(\omega, T)$ and wavenumber

$$k_{\mathrm{w}}(\omega, T) = -\frac{\ln(\lambda_{\mathrm{w}})}{\mathrm{i}L_x} \tag{3.3.2}$$

for each of the elastic waves propagating along the structural waveguide at a specified angular frequency $\omega$ and temperature.

### 3.3.2 Temperature dependent wave interaction with damage

The layered panel can contain structural discontinuity such as damage. In order to compute interaction scattering coefficients of the propagating wave interaction with the damage, the panel is discretized (Fig. 3.5) into a system of two healthy substructures coupled through a damaged joint, which bears the damage. Temperature dependent interaction scattering coefficients is hereby considered. Following the wave interaction analysis presented in Sec. 2.3, the interaction scattering coefficients matrix can be expressed as

$$S(\omega, T) = -[\mathbf{\Phi}_f^{\text{g,ref}} - \mathbb{D}_{\mathbb{J}}\mathbf{\Phi}_q^{\text{g,ref}}]^{-1}[\mathbf{\Phi}_f^{\text{g,inc}} - \mathbb{D}_{\mathbb{J}}\mathbf{\Phi}_q^{\text{g,inc}}] \tag{3.3.3}$$

for a specified angular frequency and temperature.

## 3.4 Case studies

Thermal impact on the wave characteristics of the layered composite panel, whose temperature dependent mechanical properties are measured as presented in Sec. 3.2, is now considered. The damaged panel ($L_1 = L_2 = 0.12$mm, $L_J = 0.005$mm) is defined as a system of two healthy substructures coupled through a damaged joint as shown in Fig. 3.5. The panel's cross-section ($b = 0.006$ mm and $h = 0.012$ mm) is made up of a core $h_c = 0.01$ mm sandwiched between upper and lower skins $h_s = 0.001$ mm. Calculations are made over temperature range of -100°C to 150°C and angular frequency range of 0.1 kHz to 120 kHz. FE modelling is done in ANSYS®. The layered panel is meshed using SOLID185 elements each of length 0.001 mm.

### 3.4.1 Temperature Dependent Wave Properties

Thermal impact on the wave propagation constants is analysed by applying the measured temperature dependent mechanical properties in computation of the wave constants. A periodic segment, of length 0.001 (along $x$ direction), of each substructure is modelled. A total of 72 elements, 6 for the each skin and 60 for the core, are required to model each substructure. Eqs. (3.3.1) and (3.3.2) are solved to obtain the wave constants as a function of temperature and angular frequency.

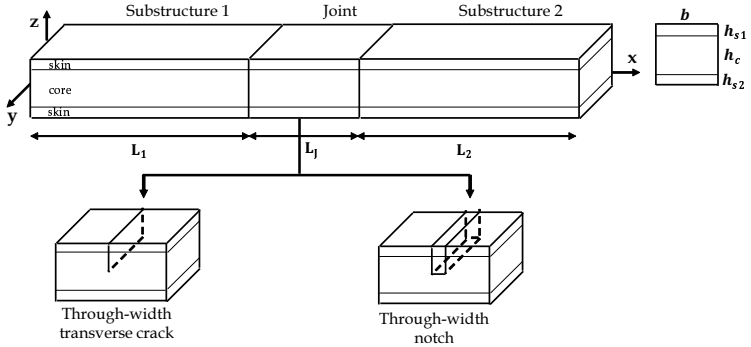


**Figure 3.5:** Sandwich panel defined as two healthy substructures coupled through a damaged joint

Temperature dependent dispersion curves of the propagating waves along the panel are presented in Figs. 3.6 and 3.7. Four wave modes, in-plane and out-of-plane bending waves, torsional and longitudinal waves, exist within frequency range below

10 kHz. Beyond this limit, higher order of the modes cut on. The number of additional waves obtained and their cut-on frequencies depend on temperature as shown in Fig. 3.6. At 25°$C$, there are five additional waves with cut-on frequencies of about 10 kHz, 18 kHz, 25 kHz, 75 kHz and 90 kHz respectively, while there are seven additional waves at 150°$C$, with cut-on frequencies of about 10 kHz, 12 kHz, 22 kHz, 68 kHz, 78 kHz, 102 kHz and 109 kHz respectively.

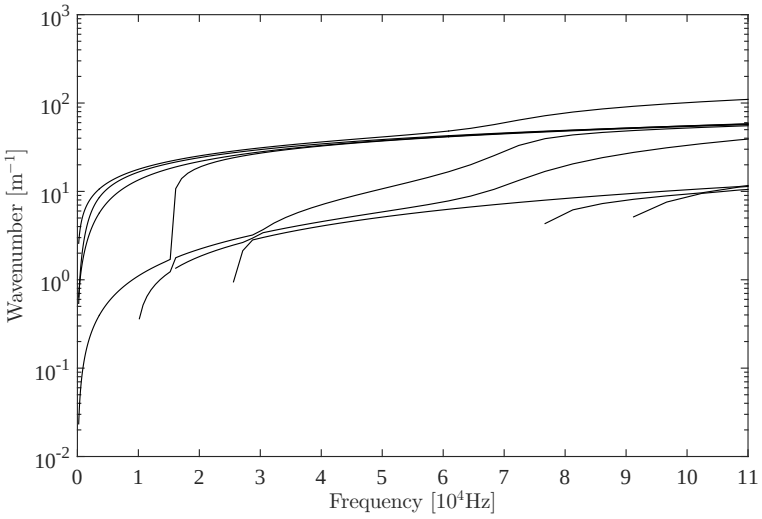


**(a)** 25°$C$

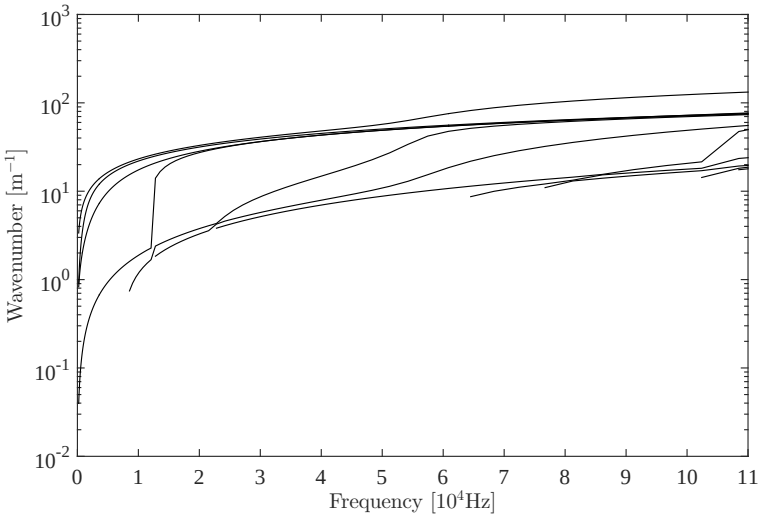


**(b)** 150°$C$

**Figure 3.6:** Dispersion relations for waves in the composite panel at 25°$C$ and 150°$C$

Thermal effect on the dispersion property is further analysed using the dispersion curves for the torsional wave at various temperatures. Little change in wavenumber is observed between -100°C and 90°C, whereas a significant change of about 30% is recorded between 90°C and 110°C, and beyond 110°C, the wavenumber increases at a steady rate. It therefore follows that the propagation constants of the panel becomes

more significant within and beyond its glass transition temperature range (90°C to 110°C). This behaviour is similar to the trend observed for the mechanical properties of the panel.

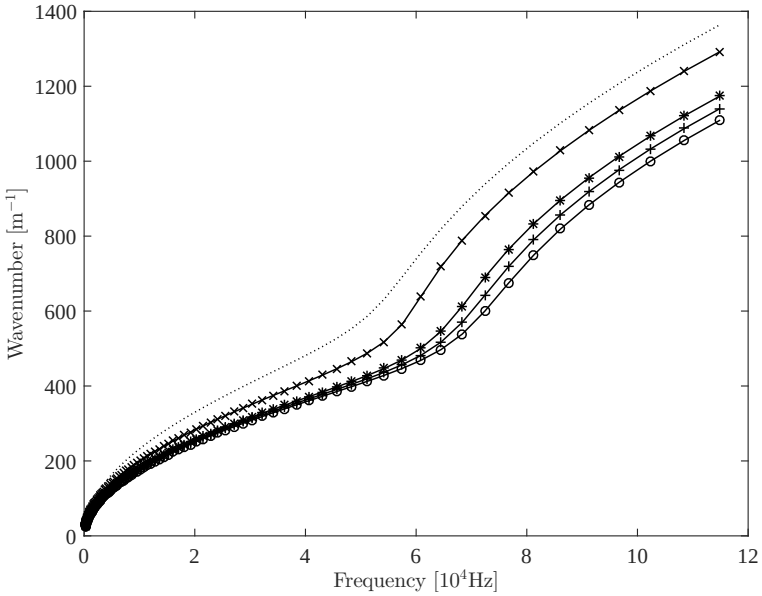


**Figure 3.7:** Dispersion relations for torsional wave in the composite panel at -100°*C* (o), 25°*C* (+), 90°*C* (*), 110°*C* (x) and 150°*C* ($\cdots$)

### 3.4.2 Temperature Dependent Wave Scattering Coefficients

Thermal impact on the wave interaction with damage is analysed by applying the measured temperature dependent mechanical properties in computation of the interaction scattering coefficients. The wave constants (eigenvectors) for both substructures are coupled to that of the joint in order to obtain the wave interaction scattering coefficients (refer to Sec. 2.3 for detail). The interaction characteristics are studied for different damage types, namely notch and crack as shown in Fig. 3.5. The notch and crack are implemented using the element deletion and the node duplication methods (Sec. 2.2) respectively. The joint is fully-FE modelled in order to implement the respective damage. Eq. (3.3.3) is solved to for the wave interaction scattering coefficients as a function of temperature and angular frequency.

#### 3.4.2.1 Interaction with crack

Wave scattering from a 5 mm deep crack within the panel's joint, as shown in Fig. 3.5, is considered. The crack is situated at length 2 mm within the 5 mm long joint, and runs transversely through the breadth of the joint. A total of 360 elements, 30 for each skin and 300 for the core, are required to model the joint.

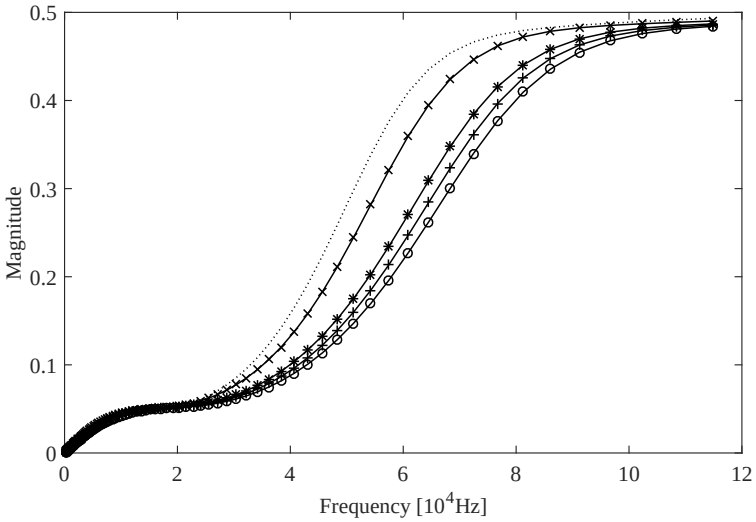


**Figure 3.8:** Temperature dependent reflection coefficient magnitude of the flexural wave from a crack within the panel at -100°$C$ (o), 25°$C$ (+), 90°$C$ (*), 110°$C$ (x) and 150°$C$ ($\cdots$)

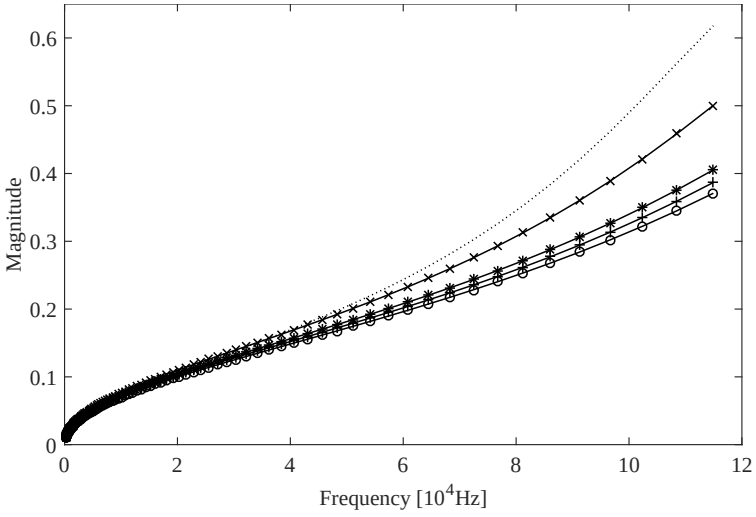


**Figure 3.9:** The temperature dependent reflection coefficient magnitude of the torsional wave from a crack within the panel at -100°$C$ (o), 25°$C$ (+), 90°$C$ (*), 110°$C$ (x) and 150°$C$ ($\cdots$)

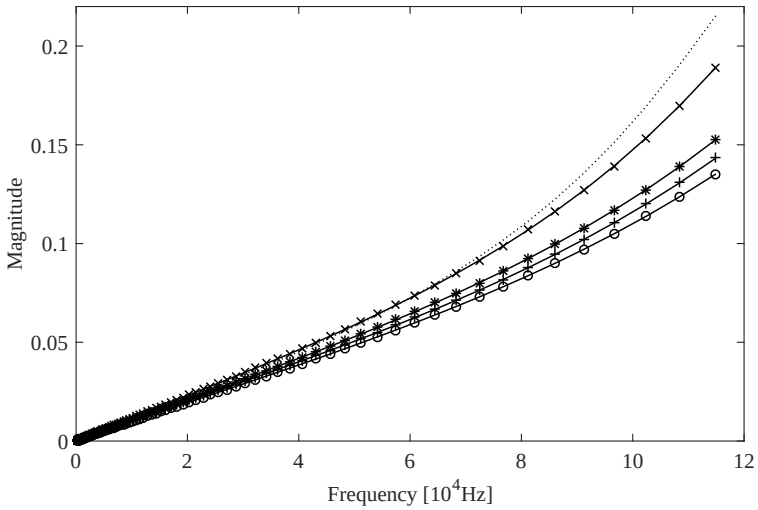


**Figure 3.10:** The temperature dependent reflection coefficient magnitude of the axial wave from a crack within the panel at -100°$C$ (o), 25°$C$ (+), 90°$C$ (*), 110°$C$ (x) and 150°$C$ ($\cdots$)

Results of the bending, torsional and longitudinal waves reflection coefficients (from crack) as a function of angular frequency and temperature are presented in Figs. 3.8, 3.9 and 3.10 respectively. The reflection coefficients of the axial and torsional waves show more sensitivity to change in temperature at higher frequencies in the range above 60 kHz, while that of the bending wave shows significant difference only in the range between 25 kHz and 85 kHz but little difference outside the range. The effect of temperature on the reflection coefficient below, within and after the glass transition temperature varies significantly. Below the glass transition temperature, there exist a slight increase in the reflection coefficients of all the wave types with a maximum increase of about 10% per 50°$C$ change in temperature. Above the glass transition temperature, a considerable amount of increment is observed with respect to temperature change with an observed increase of about 28% per 50°$C$ temperature change.

#### 3.4.2.2 Interaction with notch

Wave scattering from a 1 mm wide and 5 mm deep notch within the panel's joint, as shown in Fig. 3.5, is considered. The notch is situated between lengths 2 mm and 3 mm within the 5 mm long joint, and runs transversely through the breadth of the joint. Upon the implementation of the notch, a total of 330 elements, 24 for upper skin, 30 for lower skin and 276 for the core, are required to model the joint.

Results of the bending, torsional and longitudinal waves reflection coefficients (from notch) as a function of angular frequency and temperature are presented in Figs. 3.8, 3.9 and 3.10 respectively. Wave reflection coefficients from a notch within

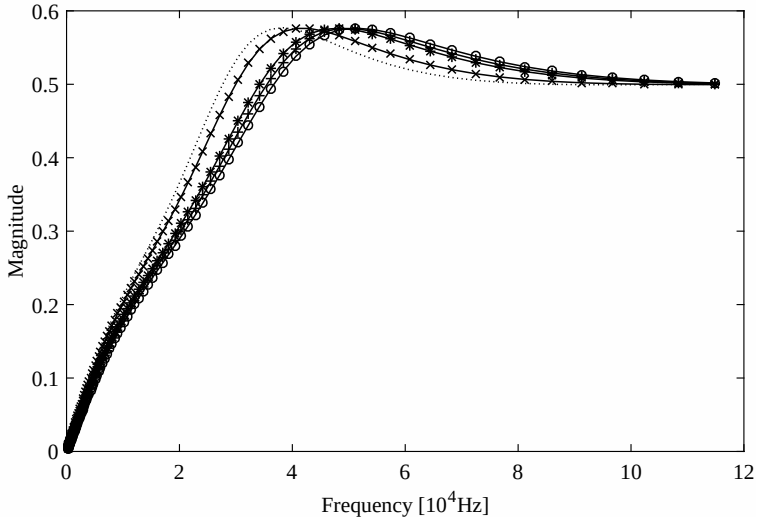


**Figure 3.11:** The temperature dependent reflection coefficient magnitude of the flexural wave from a notch within the panel at -100°$C$ (o), 25°$C$ (+), 90°$C$ (*), 110°$C$ (x) and 150°$C$ ($\cdots$)

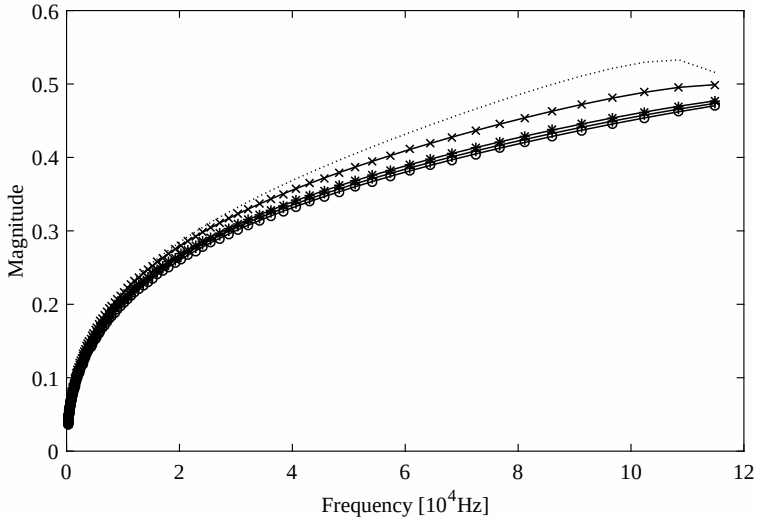


**Figure 3.12:** The temperature dependent reflection coefficient magnitude of the torsional wave from a notch within the panel at -100°$C$ (o), 25°$C$ (+), 90°$C$ (*), 110°$C$ (x) and 150°$C$ ($\cdots$)

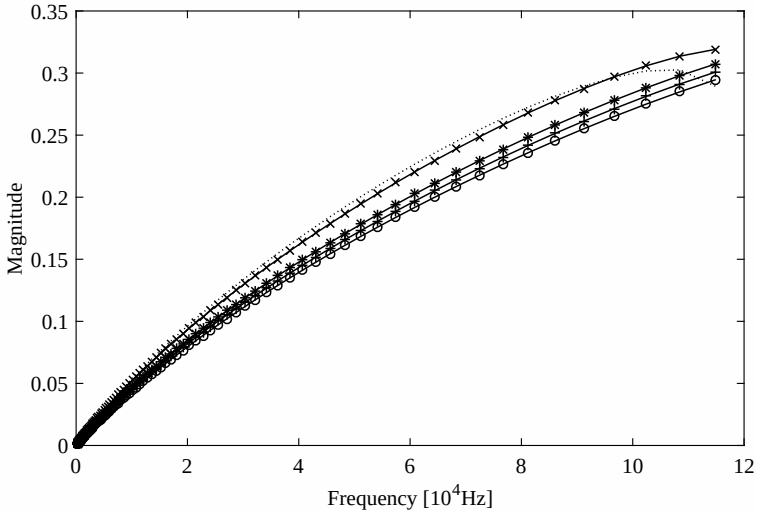


**Figure 3.13:** The temperature dependent reflection coefficient magnitude of the axial wave from a notch within the panel at -100°*C* (o), 25°*C* (+), 90°*C* (*), 110°*C* (x) and 150°*C* ($\cdots$)

the panel follow similar trend as that of the crack, especially with regards to the glass transition range. Generally, the significance of the glass transition temperature range on the scattering properties of the panel is quite similar to that obtained for the panel's thermomechanical characteristics and wave propagation constants.

## 3.5 Conclusions

Thermal impact on the wave propagation constants and the wave interaction scattering properties of a quasi-isotropic sandwich panel is presented in this study. The panel is made of two materials, a carbon epoxy facesheet, impregnated in the resin and draped over the mould, and a quasi-isotropic honeycomb core. The thermomechanical characteristics of each of these materials are separately measured experimentally within temperature range of -100°C to 150°C. A large divergence is observed in the trend of the measured properties, within and above the glass transition temperature range of the resin.

Wave propagation constants, and the scattering coefficients of the wave interaction with damage within the panel are obtained using the developed FE-based scheme. The measured thermomechanical characteristics are used to analyse thermal impact on the wave characteristics. Similar to the experimental results, the predicted wave propagation and interaction properties exhibit significant difference in their results within the glass transition temperature range. It can be concluded that temperature, especially at glass transition range, is a significant factor that should be taken into consideration in the design process of aerospace material in order to improve its wave response perfor-

mance.

# CHAPTER 4

# Pre-stress impact on wave interaction with damage in pressurised composite structures

## 4.1 Introduction

Composite structures are increasingly used in modern aerospace and automobile industries due to their well-known benefits. However, they exhibit a wide range of structural failure modes for which the structures have to be frequently and thoroughly inspected in order to ensure continuous structural integrity. The use of 'offline' structural inspection techniques currently leads to a massive reduction of the aircraft's availability and significant financial losses for the operator. The non-destructive detection and evaluation of damage in industrial structural components during service is of pertinent importance for ensuring continuous usage of the components.

Ultrasonic wave distortion during propagation in structural media has been studied as early as in Worlton [160]. It has been demonstrated that ultrasonic waves can be successfully employed in non-destructive detection of structural defects [161–163]. Generally, non-destructive approaches can be classified into matrix formulation and wave propagation techniques. The wave propagation techniques strongly rely on the calculation of dispersion curves and wave interaction reflection and transmission coefficients to inspect and evaluate structural media. They can be further categorised into two steps, namely response and modal steps [164]. The former measures wave scattering from defects within structures, while the latter determines wave dispersion characteristics such as velocities and wavenumber. These techniques have been successfully demonstrated in various structural media such as truss [165, 166], beams [167], 3-D solid media [168] and composite structures [169]. It has also been applied to calculate

wave interaction coefficients from structural joints such as curved [91], spring-type [170], welded [126], adhesive [171], angled [172] and liquid-coupled joints [173].

FE based wave propagation NDE technique for periodic structures was first introduced in Mead [104]. It was shown that wave dispersion characteristics within the layered media can be accurately predicted for a wide frequency range by solving an eigenvalue problem for the wave propagation constants. The work was extended to 2-D media in Langley [174]. The WFE method was applied in Mace et al. [105] to facilitate the post-processing of the eigenvalue problem solutions and the improvement of the computational efficiency of the method was presented in Waki et al. [175]. The method is considered as an expansion of Bloch's theorem and its main assumption being the periodicity of the structure to be modelled. It couples the periodic structure theory to the FE method by modelling only a small periodic segment of the structure, thereby saving a whole lot of computational cost and time. The method has been successfully implemented in various structural configurations for predicting the vibroacoustic and dynamic performance of aerospace structures.

Aerospace structures are necessarily pre-stressed by pressurisation at altitudes above 3000 m above the sea level to protect crew and passengers [176] by enabling breathing. This is done by applying pressure load on the structure so as to counteract oxygen deprivation (inside the cabin) by constantly pumping outside air into the cabin. Owing to this, it is essential to consider the impact of pre-stressing on damage detection of aerospace structures.

Hence, the contribution of the work hereby presented is to investigate wave propagation and interaction of the wave with damage within layered structures, and examine the effect of pre-stressing on the wave propagation and interaction properties. The structure is pre-stressed by subjecting it to a uniformly distributed surface pressure. The pre-stress effect is evaluated by comparing the wave response (dispersion and scattering properties) of the pressurised state to that of non-pressurised state.

## 4.2 Stiffness property of a pressurised structure

Pressure-containing structures, such as pressure vessels and airplane cabins, are subjected to internal pressure which induces equal tensile stresses on the internal walls of the structures as shown in Fig. 4.1. These stresses include circumferential stress $\sigma_\theta$, axial stress $\sigma_z$ and radial stress $\sigma_r$. The latter equals zero in a thin-walled vessel. However, when the structures are subjected to external pressure, compressive stresses will be induced on the walls instead of tensile stresses. Generally, the stresses are in static equilibrium which implies that the stresses around the wall have a resultant which

balances the pressure differences normal to the wall surface.

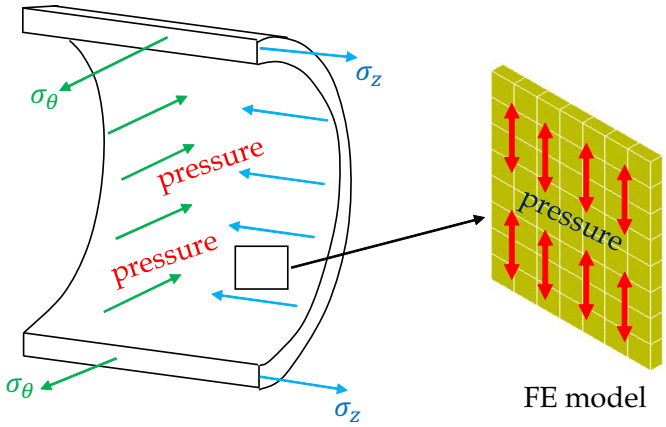


**Figure 4.1:** Internal pressurisation of a pressure-containing structure and the equivalent FE model

In this work, the pre-stress effect from stresses arising from an internal pressure applied on the wall of a pressure-containing structure is considered. The pre-stress effect is studied on wave propagation and interaction properties of the structure.

Consider an arbitrarily layered composite structure internally pressurised as shown in Fig. 4.1. The pre-stress effect as a result of the applied pressure is accounted for by adding a pre-stress stiffness matrix, $\mathbf{K}_\mathrm{p}$, to the original (unstressed) stiffness matrix, $\mathbf{K}_0$, of the structure.

The pre-stress stiffness matrix is dependent on the geometry, displacement field and the state of stress of each structural element [177]. For 3D elements, which are used in this study, the pre-stress stiffness matrix is given as [178]

$$\mathbf{K}_\mathrm{p} = \iiint \mathbf{S}_\mathrm{g}^\top \mathbf{S}_\mathrm{m} \mathbf{S}_\mathrm{g} \, \mathrm{d}x\mathrm{d}y\mathrm{d}z \tag{4.2.1}$$

where $\mathbf{S}_\mathrm{g}$ is the shape function derivative matrix, $\mathbf{S}_\mathrm{m}$ is the Cauchy stress tensor and $[\bullet]^\top$ is a transpose. Hence, the total stiffness matrix of the pre-stressed system is given as

$$\mathbf{K} = \mathbf{K}_0 + \mathbf{K}_\mathrm{p} \tag{4.2.2}$$

Evidently, $\mathbf{K}$ equals to $\mathbf{K}_0$ under no pressurisation scenario.

## 4.3 Wave characteristics of pressurised layered structures

In the general case, a pressurised structural system consisting of $N$ healthy periodic substructures connected through a coupling joint as shown in Fig. 4.2 is considered. The coupling joint could exhibit arbitrarily complex mechanical behaviour such as

damage, geometric or material inconsistencies and is fully FE modelled. Each waveguide can be of different and arbitrary layering and can also support a number ($W$) of propagating waves at a given frequency and pressure.

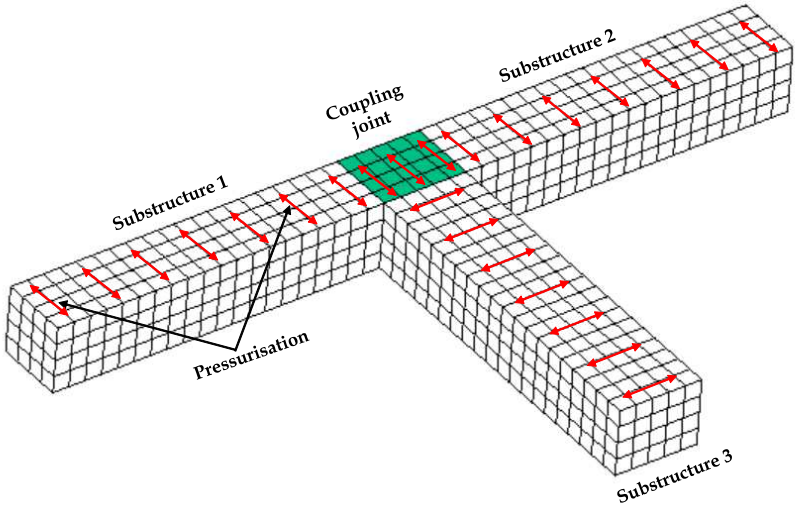


**Figure 4.2:** Pressurised structural system consisting of $N$ periodic substructures connected through a coupling joint

Waves having amplitudes $\mathbf{a}_n^{\text{inc}}$ impinging on the joint from the $n$th substructure will give rise to waves of reflection coefficients $\mathbf{c}_{n,n}$ in the $n$th substructure and waves of transmission coefficients $\mathbf{c}_{k,n}$ in the $k$th substructure. Pre-stress effect on the interaction scattering coefficients is considered.

### 4.3.1 Wave propagation constants of pressurised layered structures

The propagation constants of the waves in each pressurised substructure are sought through the wave propagation analysis presented in Sec. 2.1.2. Following the analysis, wave propagation along the system can be defined by the eigenvalue problem

$$\lambda \begin{Bmatrix} \mathbf{q}_L \\ \mathbf{f}_L \end{Bmatrix} = \mathbf{T} \begin{Bmatrix} \mathbf{q}_L \\ \mathbf{f}_L \end{Bmatrix} \tag{4.3.1}$$

whose solution yields eigenvalue $\lambda_{\text{w}}(\omega, p)$ and wavenumber

$$k_{\text{w}}(\omega, p) = -\frac{\ln(\lambda_{\text{w}})}{\text{i}\text{L}_x} \tag{4.3.2}$$

for each of the elastic waves propagating along the pressurised substructure at a specified angular frequency $\omega$ and pressure.

### 4.3.2 Wave interaction with damage within pressurised layered structures

Scattering coefficients of wave interaction with damage within the joint is sought through the wave interaction analysis presented in Sec. 2.3. Following the analysis, the interaction scattering coefficients matrix can be expressed as

$$\boldsymbol{S}(\omega, p) = -[\boldsymbol{\Phi}_f^{\mathrm{g,ref}} - \mathbb{D}_{\mathbb{J}}\boldsymbol{\Phi}_q^{\mathrm{g,ref}}]^{-1}[\boldsymbol{\Phi}_f^{\mathrm{g,inc}} - \mathbb{D}_{\mathbb{J}}\boldsymbol{\Phi}_q^{\mathrm{g,inc}}] \tag{4.3.3}$$

for a specified angular frequency and pressure.

## 4.4 Case studies

This section presents case studies to demonstrate the application of the developed methodology. The case studies are divided into two; validation and test case studies. The validation case is presented for a model whose experimental wave characteristics can be obtained. The experimental results are compared to the numerically predicted results in order to illustrate the validity of the presented methodology. The test cases present the application of the proposed scheme in computing waves propagation constants and quantifying waves interaction with damage within pressurised layered structures. The effect of pre-stress (due to pressurisation) on these waves properties is also examined. In all cases, finite element size is chosen to ensure that mesh density is fine enough to represent the structure accurately at a reasonable computational cost. All properties and dimensions are in SI units, unless otherwise stated.

**Table 4.1:** Mechanical properties of the materials used for the case studies presented in Sec. 4.4

| | Material I | Material II | Material III | Material IV |
|---|---|---|---|---|
| $\rho$ | 7850 kg/m$^3$ | 2700 kg/m$^3$ | 3500 kg/m$^3$ | 50 kg/m$^3$ |
| $E_x$ | 210 GPa | 68 GPa | 54 GPa | 70 GPa |
| $E_y$ | - | 68 GPa | 54 GPa | - |
| $E_z$ | - | 40 GPa | 54 GPa | - |
| $\nu_{xy}$ | 0.25 | 0.3 | 0.3 | 0.3 |
| $\nu_{yz}$ | - | 0.334 | 0.3 | - |
| $\nu_{xz}$ | - | 0.334 | 0.3 | - |
| $G_{xy}$ | - | 3.6 GPa | 2.8 GPa | - |
| $G_{yz}$ | - | 1.2 GPa | 1.0 GPa | - |
| $G_{xz}$ | - | 1.2 GPa | 1.0 GPa | - |

### 4.4.1 Experimental validation case study

A notched plate of thickness 2d $= 0.003$ and length $L = 0.6$ is considered. The plate has uniform area throughout its cross sections and is made of mild steel whose material properties are presented in Table 4.1 as Material I.

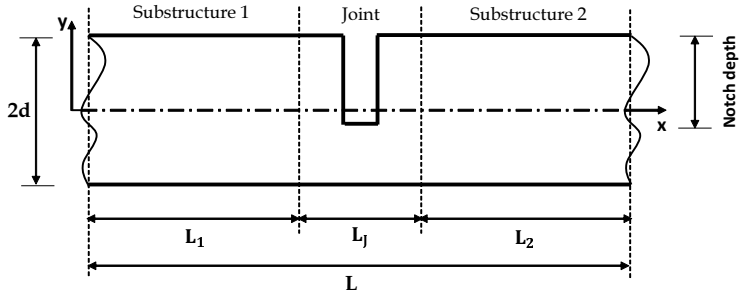


**Figure 4.3:** Schematic illustration of a notched plate discretised as a system of two healthy substructures connected through a notched coupling joint

Experimental measurements, for wave reflection coefficients in the configuration shown in Fig. 4.3, are presented in [1]. Model parameters used for the experimental measurements are chosen to match those presented hereby.

Based on the presented methodology, the plate is discretised as a system of two pristine substructures ($L_1 = L_2 = 0.295$) connected through a notched coupling joint ($L_J = 0.01$) as shown in Fig. 4.3. The plane strain condition is assumed. ANSYS is used to model a periodic segment (of length $\Delta = 0.001$) of each substructure with PLANE 182 FEs of element size 0.001 each. Similar element size used for the substructures is repeated for the coupling joint. Waves reflection coefficients are obtained by solving Eq. (4.3.3). Reflections from notches, of depths 0.0005, 0.001 and 0.002, which are respectively 17%, 33% and 67% of the plate thickness are considered. A uniform notch width of 0.0005 is used in all cases. The notches are modelled using the element deletion approach presented in Sec. 2.2.

In practice, the wave reflection calculation can be made by a full FE transient simulation. A windowed tone burst signal is applied as time-dependent harmonic displacement boundary conditions (of excitation frequency $\omega$) at one of the extreme cross-sections of the plate. In this case, the entire plate is modelled as one plate instead of a system of substructures and coupling joint as in the case of the presented methodology.

Results obtained through the presented methodology are compared with that of the full FE transient simulation and the experimental measurements presented in [1].

Good agreement is observed among the results as shown in Fig. 4.4. It is also worthwhile to state that the developed methodology is more efficient (than the full FE approach) for predicting wave scattering (reflection and transmission) from damage

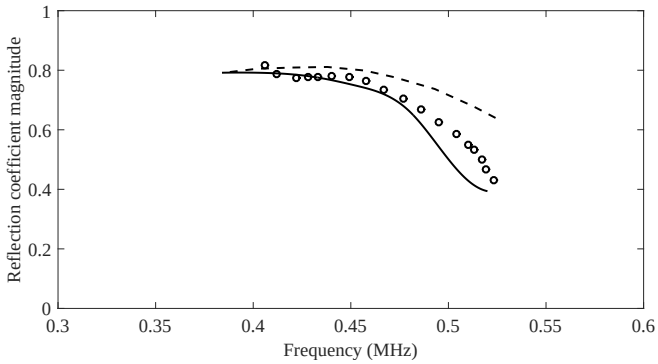


**(a)** 67% notch depth

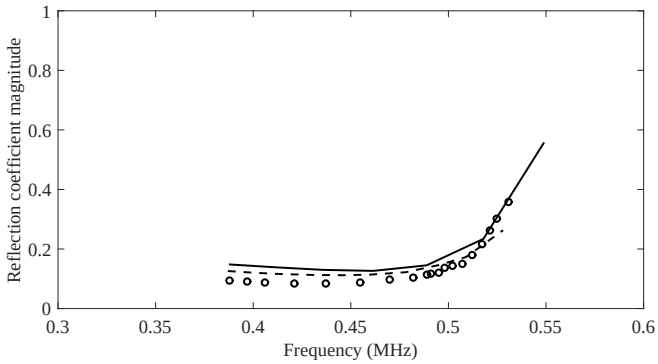


**(b)** 33% notch depth

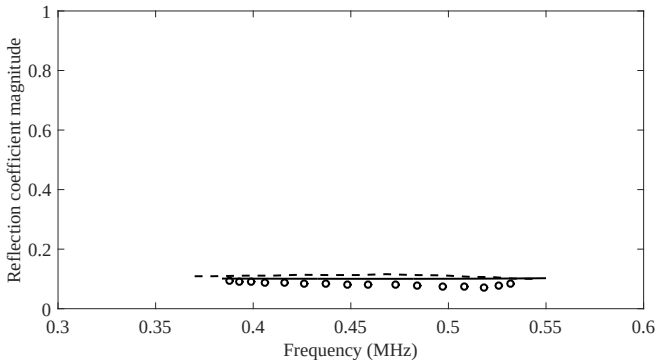


**(c)** 17% notch depth

**Figure 4.4:** Comparison of the wave reflection coefficients from notch of varying depths: Presented methodology (-), Full FE predictions (- -) and Experimental measurements (○) in [1]

within structural waveguides for the following noted reasons. First, model size and computational time. FE mesh of the plate consists of 7,200 elements and 15,626 DoFs in the full FE model against a total of 144 elements (12 for each substructure and 120 for the joint) and 390 DoFs in the presented model. Solving the full FE model requires a computational time of about 105 minutes compared to that of the presented methodology which is solved under 5 minutes. Therefore, a great deal of computational time and hence cost is saved by the presented approach. Another noted point is in terms of the complexity of the structural system. Full FE model mostly assume plane strain condition in order to simplify and reduce model size of a structural system. In this manner, some propagating waves especially those along the suppressed axis might not be captured. However, the presented approach can be applied for analysing wave interaction in complex structural systems (such as composite structures and structural networks) with low computational size and cost.

### 4.4.2 Test case studies

#### 4.4.2.1 Transversely-isotropic laminated beam

A cracked transversely-isotropic laminate having a uniform cross-sectional area ($b = 0.01$ and $h = 0.005$) is considered. The beam is defined as a system of two pristine beams ($L_1 = L_2 = 0.2$) connected through a cracked beam ($L_J = 0.004$) as shown in Fig. 4.5. Each beam comprises five layers of glass-epoxy whose material properties are presented in Table 4.1 as Material II.

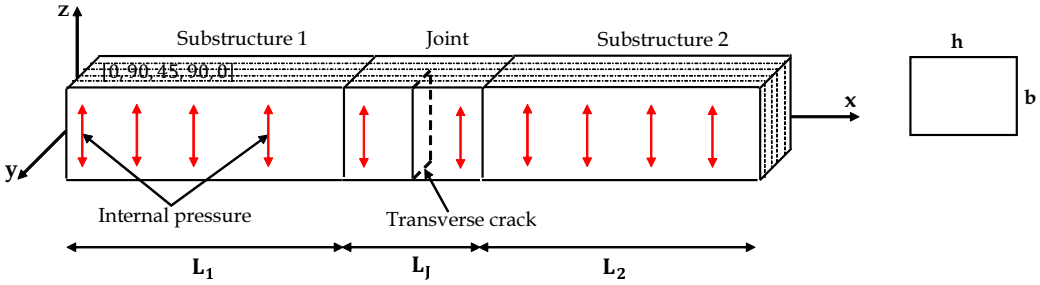


**Figure 4.5:** Schematic illustration of a pressurised transversely-isotropic laminated beam

A segment (of length $\Delta = 0.001$) of each substructure is modelled in ANSYS with 40 SOLID185 FEs of length 0.001. Using similar element size, the coupling joint is modelled with 160 finite elements. The crack within the joint is modelled using the node duplication approach (Sec. 2.2). Two crack scenarios, of depths 0.001 and 0.002, are considered. These are respectively equivalent to 20% and 40% of the total depth of the beam. The cracks are through-width and located at mid length of the joint.

Each beam is pre-stressed with uniform internal pressure. The pressure is applied across the surfaces of the three internal layers of the laminated beam as shown in Fig. 4.5. Five different pressure scenarios are considered; non-pressurised case and pressurised cases with applied pressure $p = 0.1$ GPa, 0.5 GPa, 1.0 GPa and 1.5 GPa.

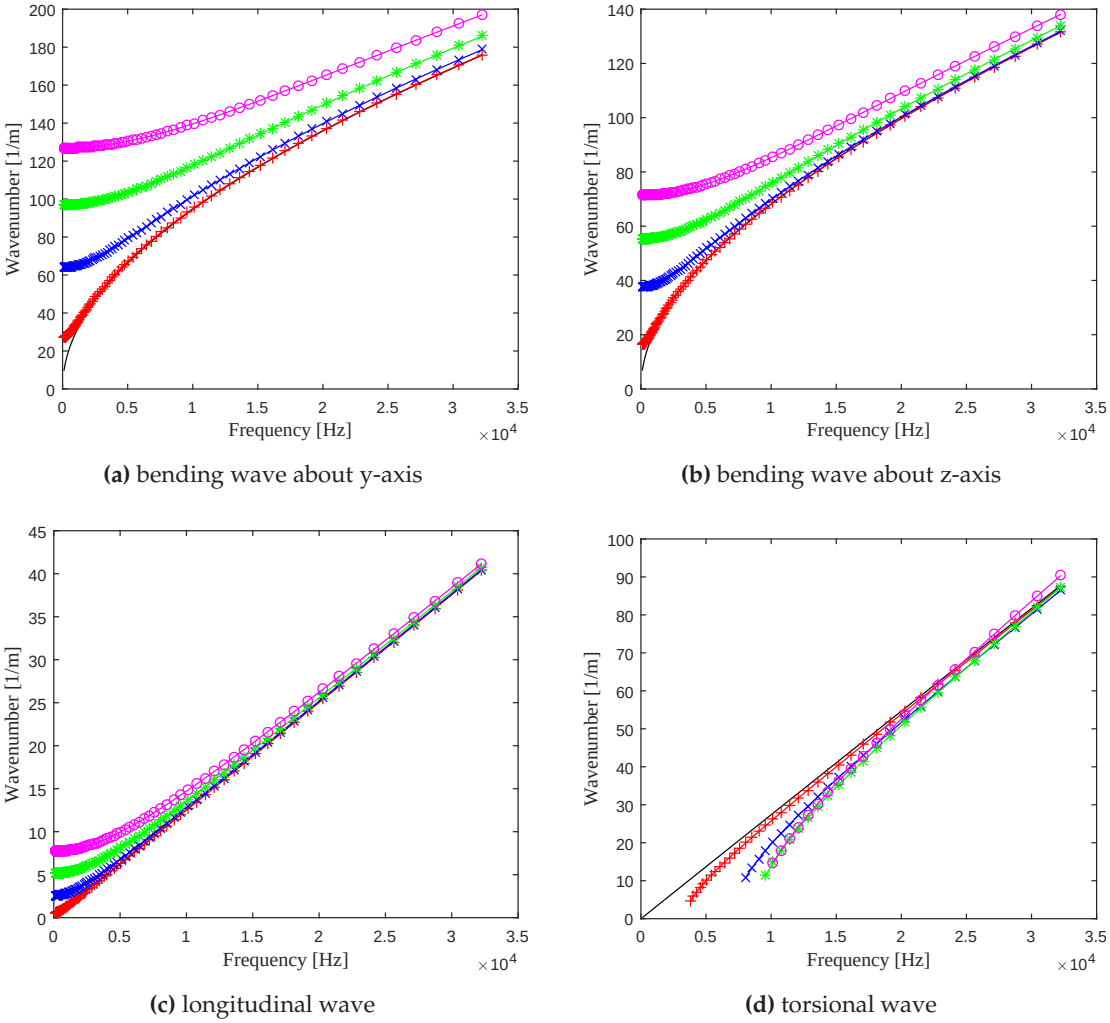


**(a)** bending wave about y-axis

**(b)** bending wave about z-axis

**(c)** longitudinal wave

**(d)** torsional wave

**Figure 4.6:** Dispersion curves for the transversely-isotropic cracked beam: non-pressurised (-), internal pressure $p = 0.1$ GPa (-+), 0.5 GPa (-x), 1.0 GPa (-*) and 1.5 GPa (-o)

Dispersion curves for the beam are obtained by solving Eq. (4.3.2) within frequency range $\omega = [1.0 \times 10^2 - 3.3 \times 10^4]$ Hz and the specified pressure. The dispersion curves are presented in Fig. 4.6. Four propagating modes at each frequency are obtained for the non-pressurised waveguide. For the pressurised waveguide, there are three propagating modes (y-axis bending wave, z-axis bending wave and longitudinal wave) at low frequency range. Fourth mode (torsional wave) cuts on at $\omega = 3.8 \times 10^3$ Hz, $8.1 \times 10^3$ Hz, $9.6 \times 10^3$ Hz and $1.0 \times 10^4$ Hz in the 0.1 GPa, 0.5 GPa, 1.0 GPa and 1.5 GPa

pressurised waveguides respectively. In the low frequency range, the wavenumbers of the pressurised waveguide are significantly different compared to the non-pressurised one. An average difference of about 32% per 0.1 GPa is observed for the bending waves at low frequency range. Differences of about 20% and 11% are observed for the longitudinal and torsional wavenumbers within the frequency range. Increase in the wavenumbers can be attributed to reduction in loss factor of the waveguide due to an increase in strain energy as a result of the applied pressure. The difference in wavenumbers (of the non-pressurised and pressurised waveguides) diminishes gradually as the frequency gets higher.

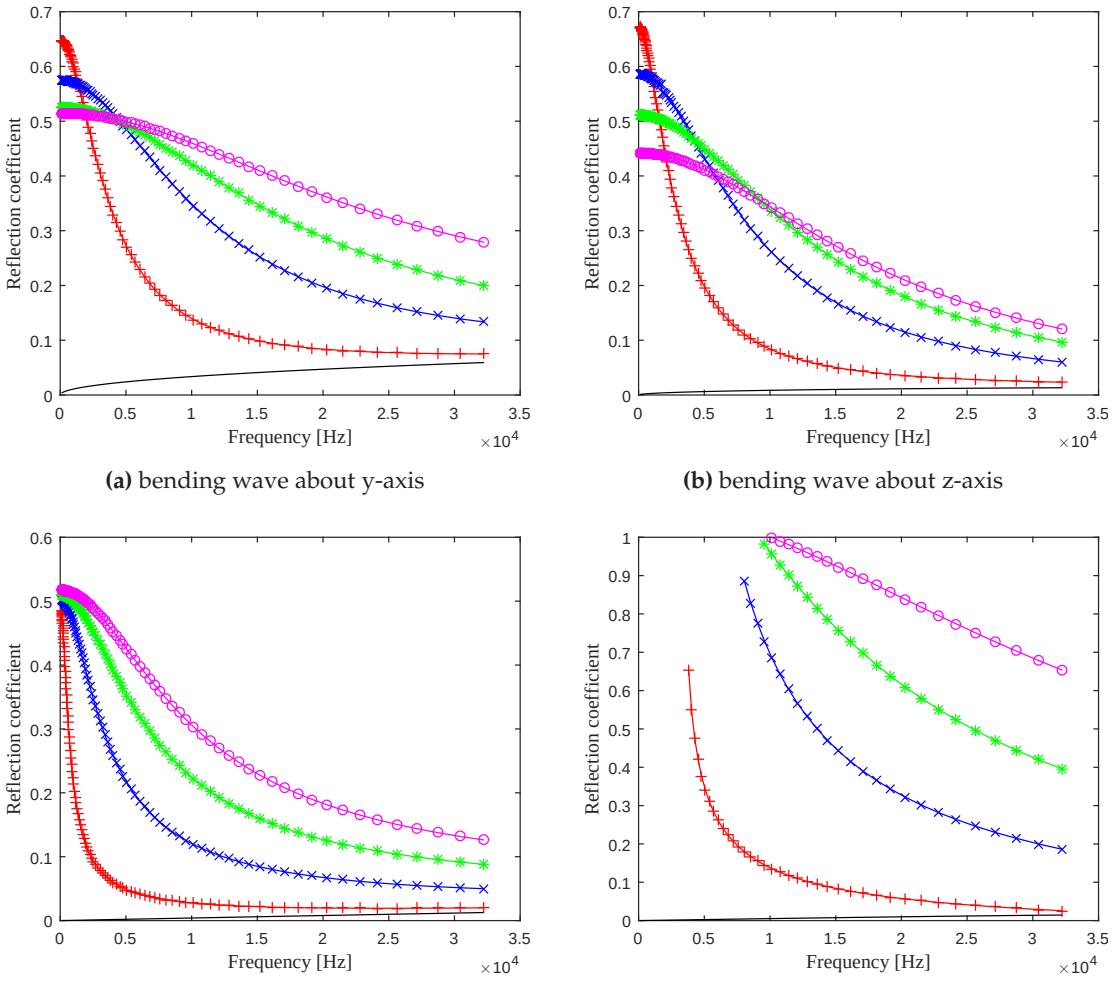


**(a)** bending wave about y-axis

**(b)** bending wave about z-axis

**(c)** longitudinal wave

**(d)** torsional wave

**Figure 4.7:** Wave reflection coefficients for the transversely-isotropic laminate with 20% depth crack: non-pressurised (-), internal pressure $p = 0.1$ GPa (-+), 0.5 GPa (-x), 1.0 GPa (-*) and 1.5 GPa (-o)

Eq. (4.3.3) is solved for the wave interaction coefficients from the cracked coupling joint. Reflection coefficients for the 20% and the 40% depth cracks are presented in Figs.

(4.7) and (4.8) respectively. As observed from the results, the magnitude of the wave reflection coefficient increases with depth of crack.

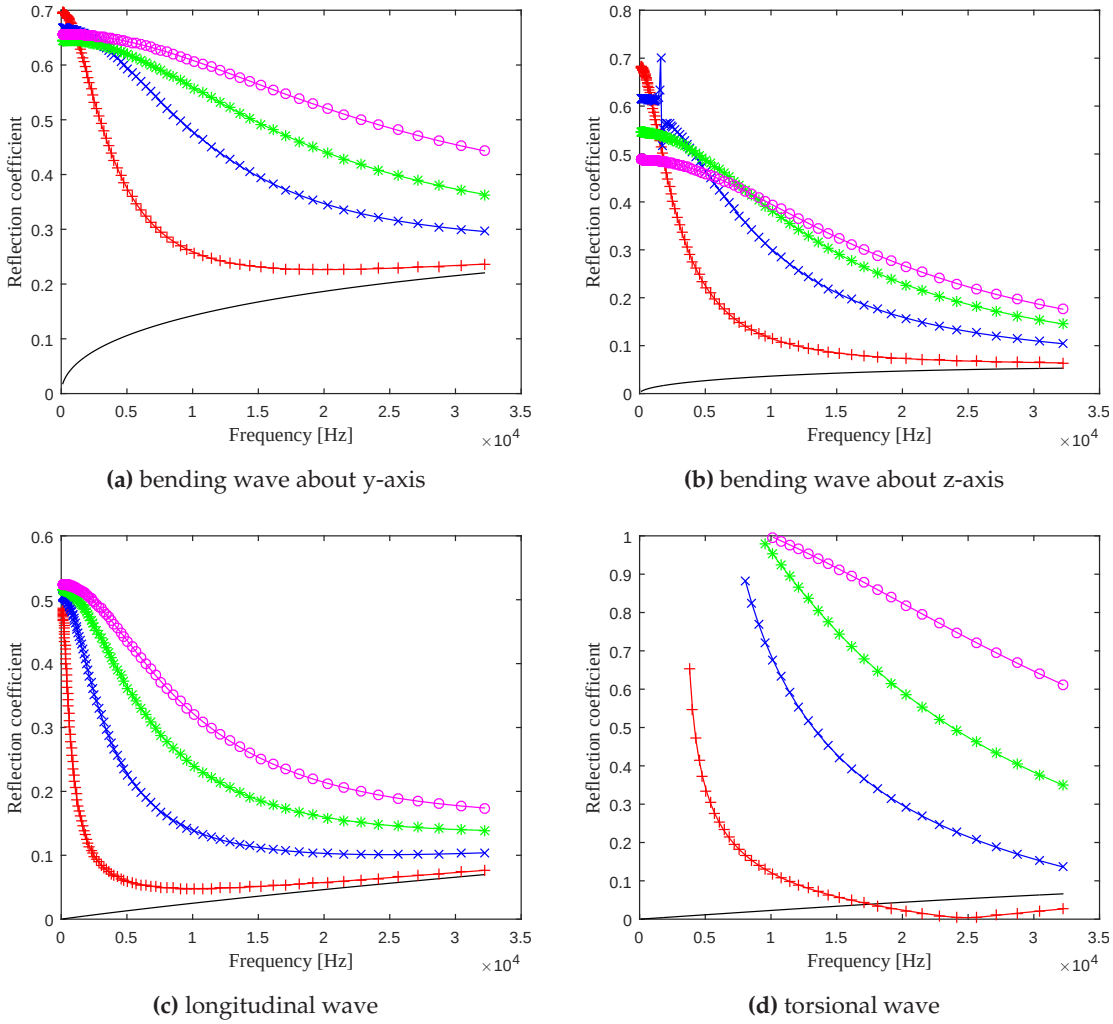


**(a)** bending wave about y-axis

**(b)** bending wave about z-axis

**(c)** longitudinal wave

**(d)** torsional wave

**Figure 4.8:** Wave reflection coefficients for the transversely-isotropic laminate with 40% depth crack: non-pressurised (-), internal pressure $p = 0.1$ GPa (-+), 0.5 GPa (-x), 1.0 GPa (-*) and 1.5 GPa (-o)

With respect to applied pressure, it can be observed that the wave reflection coefficient magnitude increases with an increase in the magnitude of applied pressure. Average increments of about 45%, 20%, 25% and 90% per 0.1 GPa are respectively observed for the y-axis bending wave, the z-axis bending wave, the longitudinal and the torsional wave.

Consequently from the presented results, magnitudes of wave constants and interaction coefficients are generally boosted by applied pressure. This can therefore be used to detect micro structural defects which may not be easily detected under non-pressurisation scenario. Application of pre-stressing (through pressurisation) as

a damage detection method is further examined using a sandwich laminate with micro delamination as presented in next section.

#### 4.4.2.2 Sandwich beam

A delaminated sandwich beam is considered. The asymmetric sandwich beam consists of carbon epoxy facesheets ($h_{s1} = 0.002$, $h_{s2} = 0.001$) and an isotropic core ($h_c = 0.01$). The material properties of the facesheets and the core are presented in Table 4.1 as Materials III and IV respectively. The beam's cross-section ($b = 0.005$, $h = 0.013$) is constant throughout and is fixed at both ends.

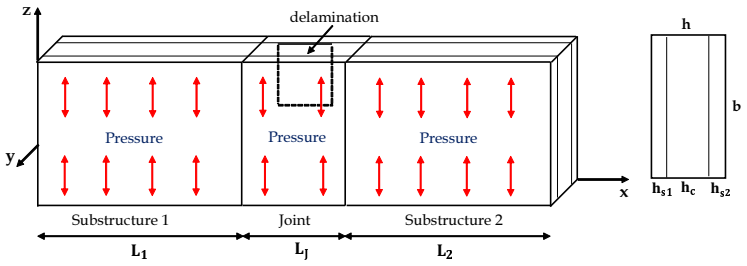


**Figure 4.9:** Schematic representation of a pressurised sandwich beam

The delaminated beam is discretised as two healthy beams ($L_1 = L_2 = 0.2$) coupled through a delaminated joint ($L_J = 0.004$) as shown in Fig. 4.9. The beams are modelled in ANSYS using SOLID185 elements. Cubed sized elements of length 0.001 are used to model the facesheets, while elements of size $0.001 \times 0.002 \times 0.001$ are employed for modelling the core. As a result, 40 FEs are used for a periodic segment (of length $\Delta = 0.001$) of each substructure and 160 elements for the coupling joint.

Interlaminar delamination, along the interface of the upper facesheet and the core, is considered. Two delamination scenarios (20% and 40% of the beam width) are examined. They are both of length 0.002 (symmetrically located about the mid length of the joint).

As in the previous example, each beam is pre-stressed using uniform internal pressure. The pressure is applied across the surfaces of the sandwich core as shown in Fig. 4.9. Six different pressure scenarios are examined; one with no pressure applied and the rest with applied pressure of 0.1 GPa, 0.2 GPa, 0.3 GPa, 0.4 GPa and 0.5 GPa per $(0.001 \times 0.002)$ cross sectional area.

Eq. (4.3.2) is solved for the dispersion curves of the sandwich beam. Four propagating waves are obtained, with the remaining waves being nearfield waves. The dispersion curves of the propagating waves as a function of frequency are presented in Fig. 4.10. The curves are presented for each of the seven pressure scenarios. For the pressurised waveguide, a smooth, nearly linear behaviour (with regards to the

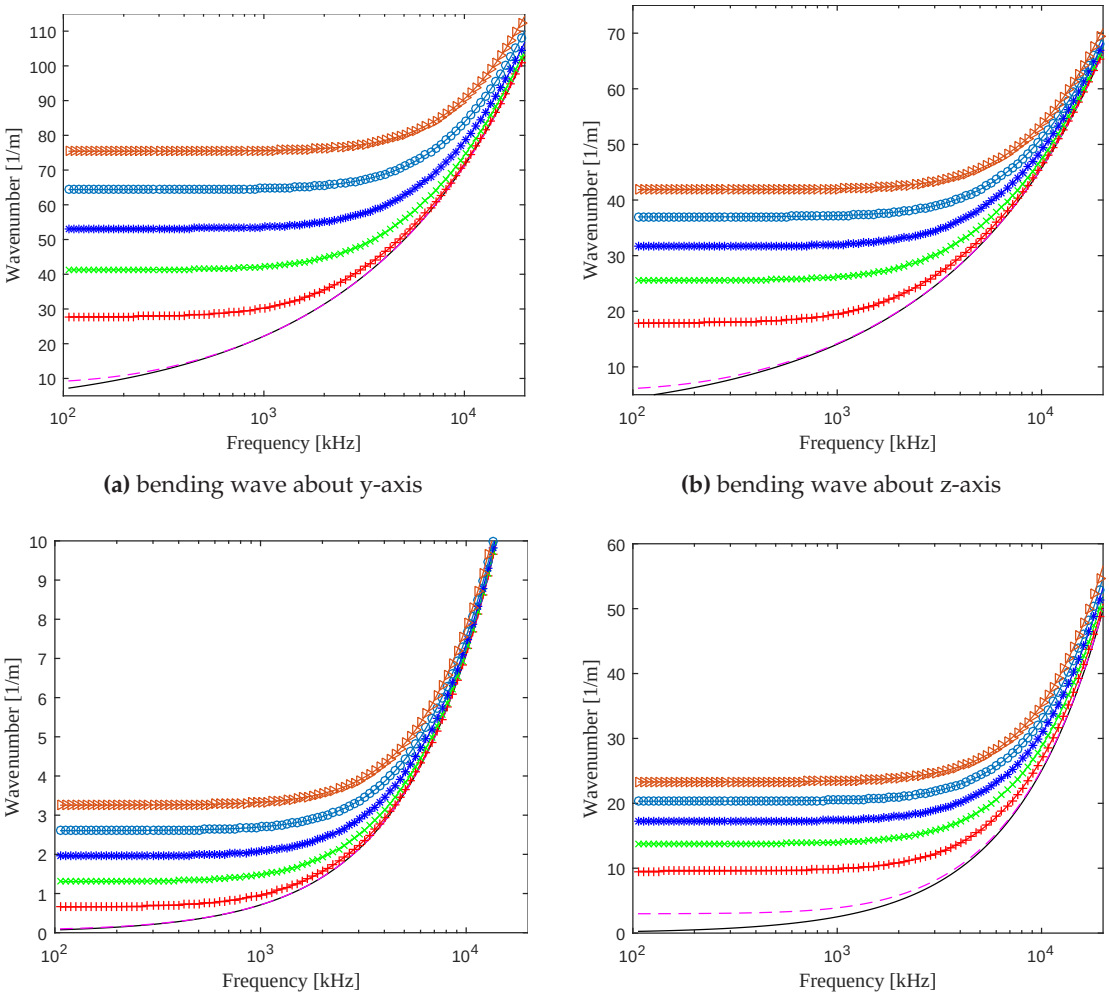


**(a)** bending wave about y-axis

**(b)** bending wave about z-axis

**(c)** longitudinal wave

**(d)** torsional wave

**Figure 4.10:** Dispersion curves for the sandwich beam: non-pressurised (-), pressure $p = 0.01$ GPa (- -), 0.1 GPa (-+), 0.2 GPa (-x), 0.3 GPa (-*), 0.4 GPa (-o) and 0.5 GPa (->)

wavenumbers) is observed as a function of frequency. This is observed up until a certain frequency, then a rapid rise takes place. This behaviour is similar for all the pressure scenarios. However, the frequency at which the rapid rise is observed varies with the applied pressure. It is observed at about 1.0 kHz, 1.6 kHz, 2.2 kHz, 2.8 kHz and 3.4 kHz respectively in the 0.1 GPa, 0.2 GPa, 0.3 GPa, 0.4 GPa and 0.5 GPa pressurised waveguides. There is also a steady increase in the wavenumbers as a function of applied pressure. An average increase of about 27% per 0.1 GPa is observed at each frequency in the low frequency range. It should be noted that the differences are normalised as frequency gets higher and tend to become equal irrespective of the magnitude of pressure applied.

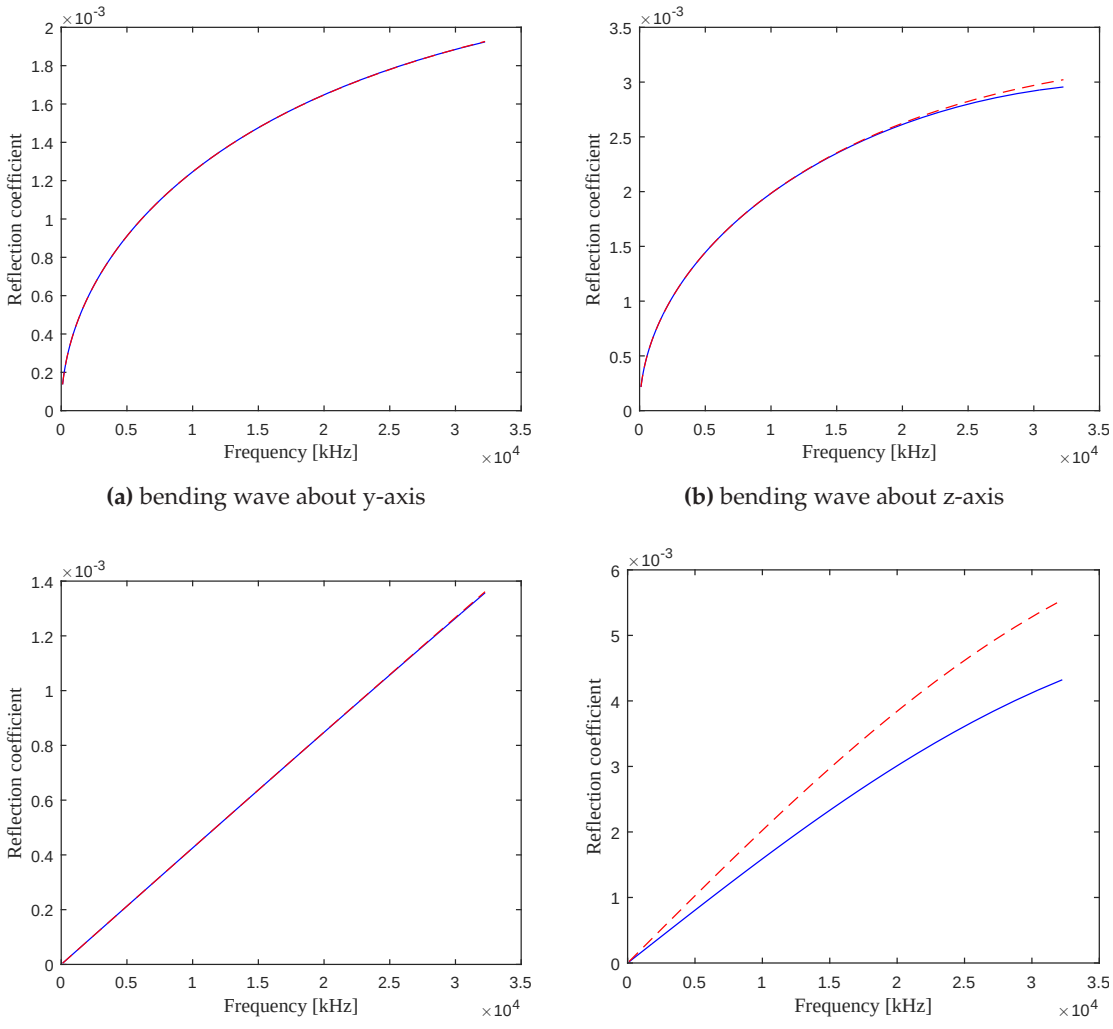


**(a)** bending wave about y-axis

**(b)** bending wave about z-axis

**(c)** longitudinal wave

**(d)** torsional wave

**Figure 4.11:** Wave reflection coefficient magnitude from the 20% (-) and the 40% (- -) widths delaminations in the non-pressurised sandwich beam

Eq. (4.3.3) is solved for the wave reflections coefficients from the delamination. Fig.

4.11 presents the coefficient magnitudes of wave reflections from the 20% and the 40% widths delaminations in the non-pressurised sandwich beam. Due to the minute severity of the considered delaminations, little reflection magnitudes are obtained within the considered frequency range. It can also be seen that negligible differences are observed between both delamination scenarios for all propagating wave types.

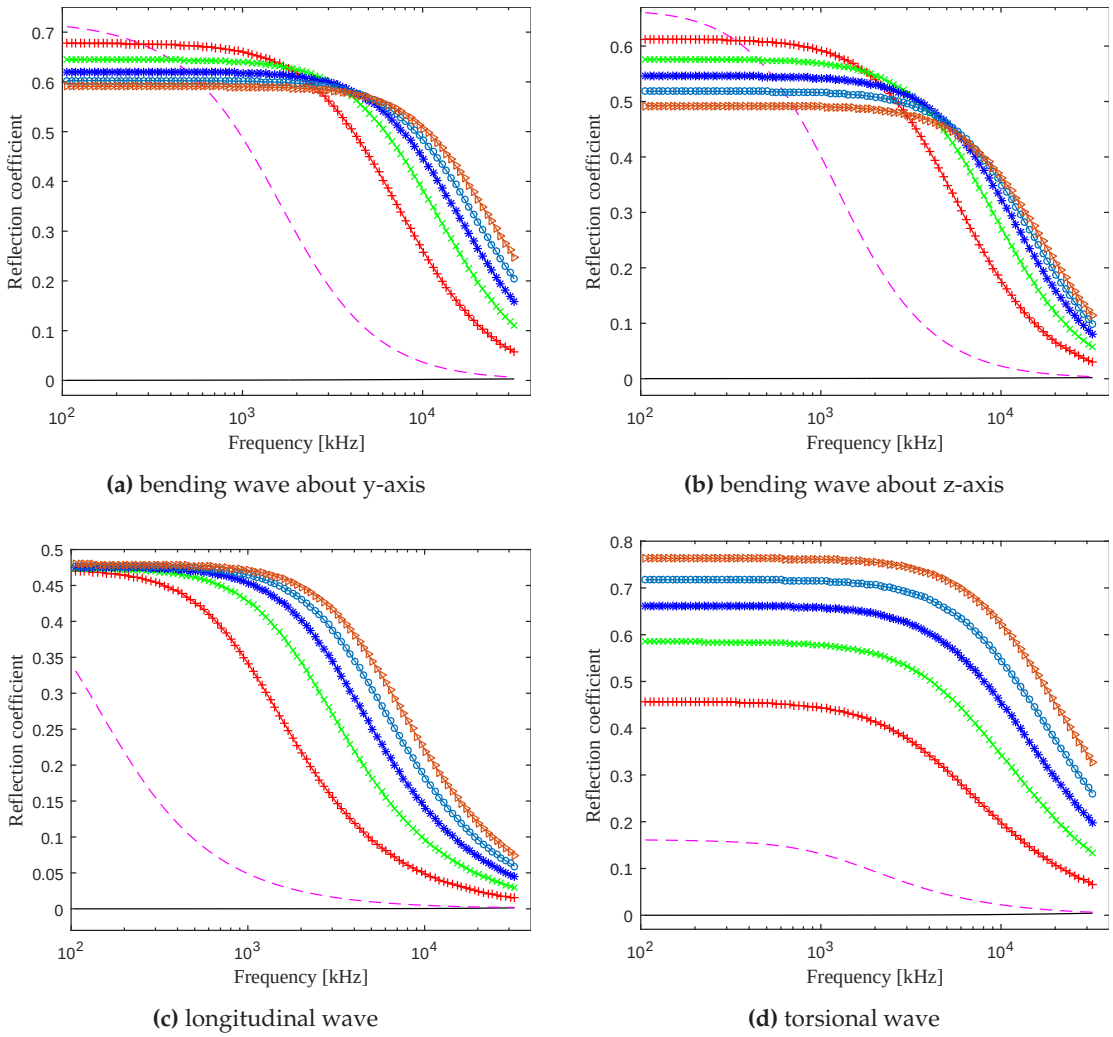


**(a)** bending wave about y-axis

**(b)** bending wave about z-axis

**(c)** longitudinal wave

**(d)** torsional wave

**Figure 4.12:** Wave reflection coefficient magnitude from 20% (-) width delamination within the sandwich beam: non-pressurised (-), pressure $p = 0.01$ GPa (--), 0.1 GPa (-+), 0.2 GPa (-x), 0.3 GPa (-*), 0.4 GPa (-o) and 0.5 GPa (->)

The reflection coefficients magnitude becomes greatly significant in the pressurised system as shown in Fig. 4.12. Compared to the non-pressurised system, there is an average change of about 50-70% in the low frequency range and of about 10-25% in the high frequency range. This can be explained by the fact that structural pre-stressing brings about a change in the loss factor of the structure. In general, this consequently affects the magnitude of wave propagation properties.

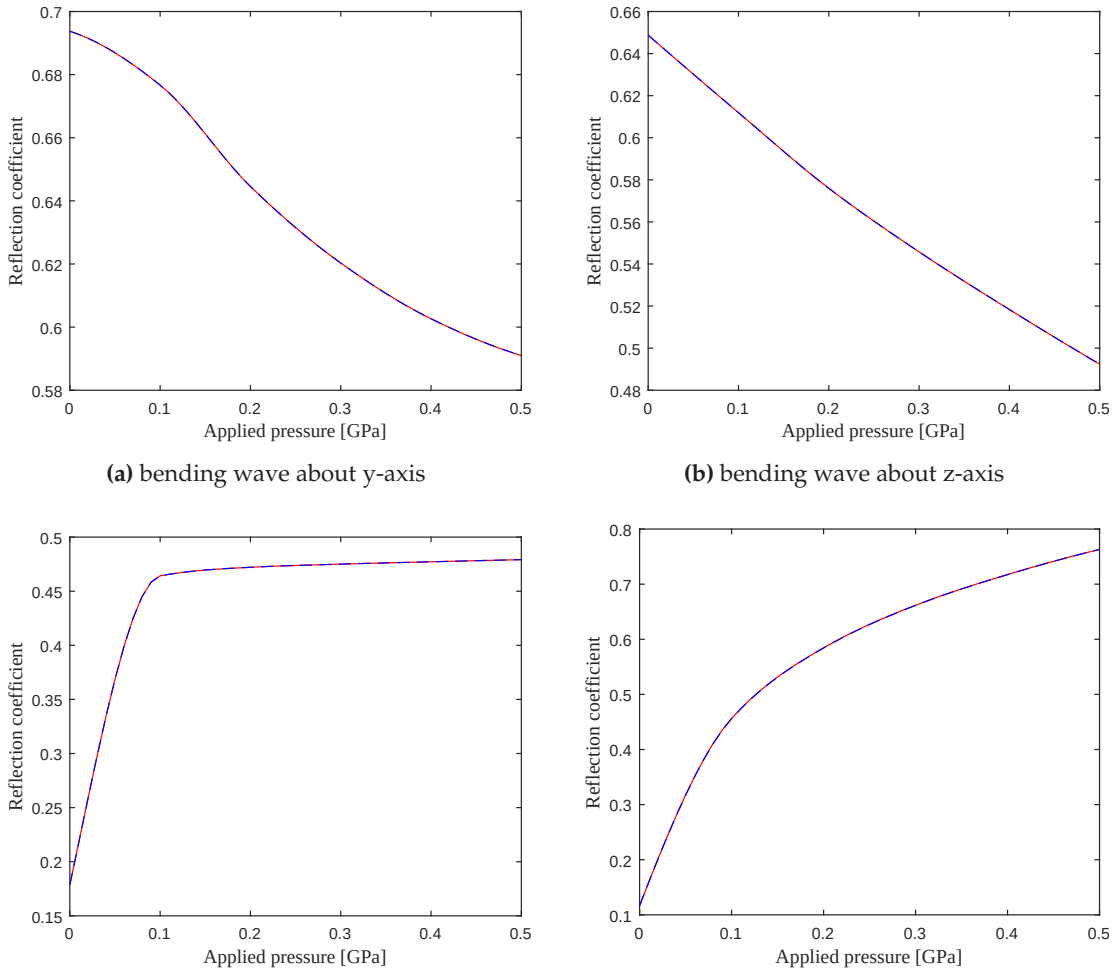


**(a)** bending wave about y-axis

**(b)** bending wave about z-axis

**(c)** longitudinal wave

**(d)** torsional wave

**Figure 4.13:** Wave reflection coefficient magnitude at 0.2 kHz for the pressurised sandwich beam as a function of applied pressure: 20% (-) width delamination, 40% (- -) width delamination.

As a function of frequency, the reflection magnitudes are constant over the low frequency range, then reduce slowly over the mid frequency range before reducing rapidly over the high frequency range. This behaviour is similar for all wave types and at each applied pressure.

Variation of the reflection coefficient magnitudes as a function of applied pressure is extensively examined at different frequency within each of the identified frequency ranges i.e. at which coefficient magnitude is constant (e.g. 0.2 kHz), slightly reduces (e.g. 0.8 kHz) and rapidly reduces (e.g. 6.4 kHz) with respect to frequency.

At 0.2 kHz (Fig. 4.13), there is a proportional reduction of about 28% per 0.1 GPa in the reflection coefficient of the y-axis bending wave. Similar trend is observed for the z-axis bending wave. An average increment of about 30% per 0.1 GPa is observed for the torsional wave while a slight steady increment of about 2% per 0.1 GPa is observed

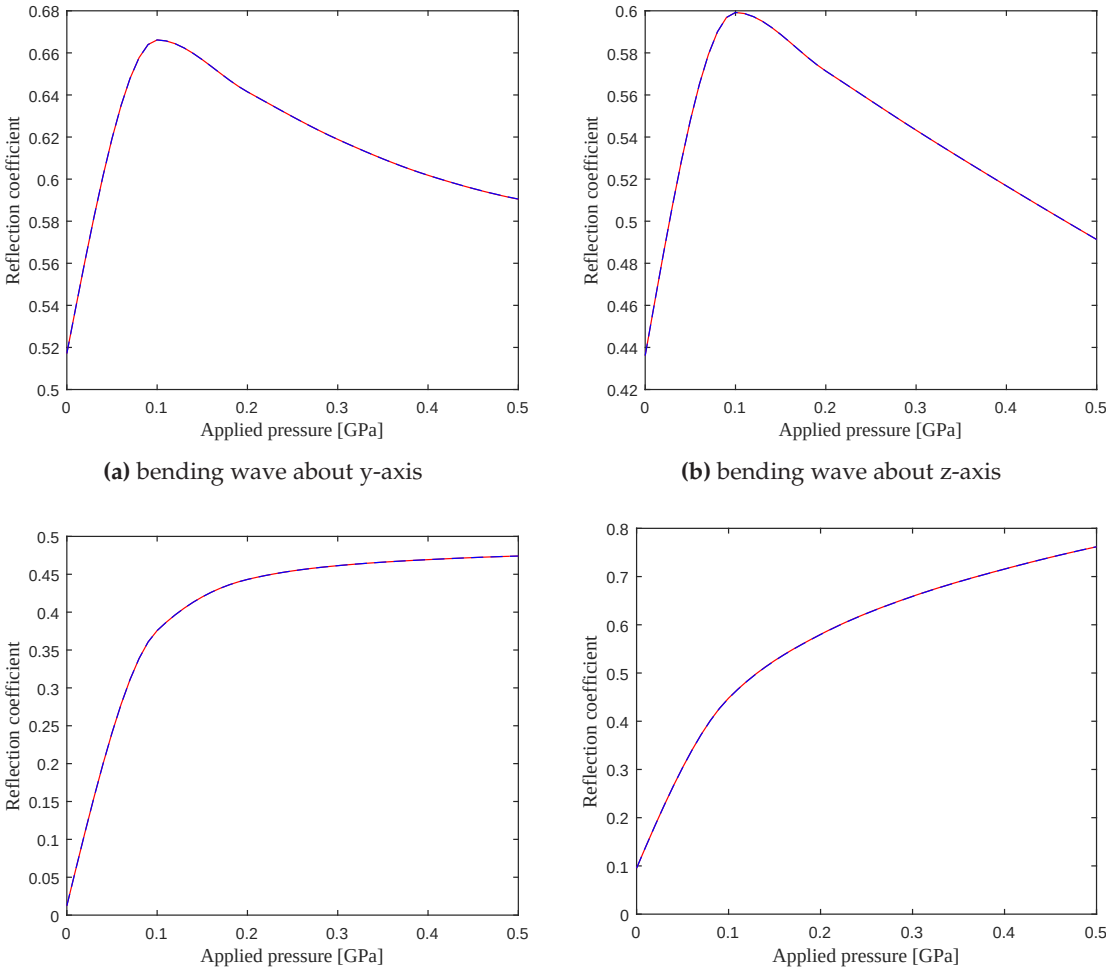


**(a)** bending wave about y-axis

**(b)** bending wave about z-axis

**(c)** longitudinal wave

**(d)** torsional wave

**Figure 4.14:** Wave reflection coefficient magnitude at 0.8 kHz for the pressurised sandwich beam as a function of applied pressure: 20% (-) width delamination, 40% (- -) width delamination.

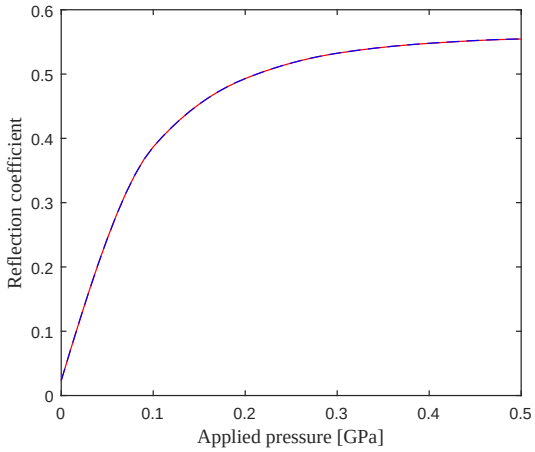


**(a)** bending wave about y-axis

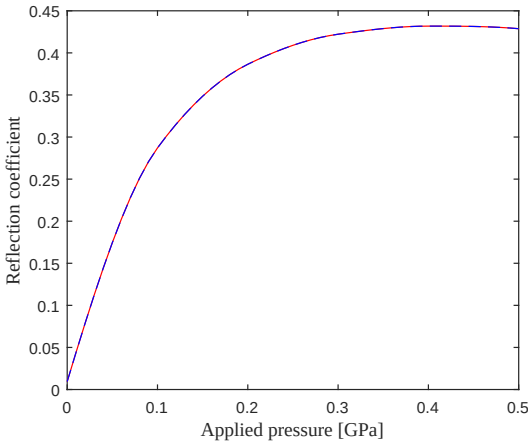


**(b)** bending wave about z-axis

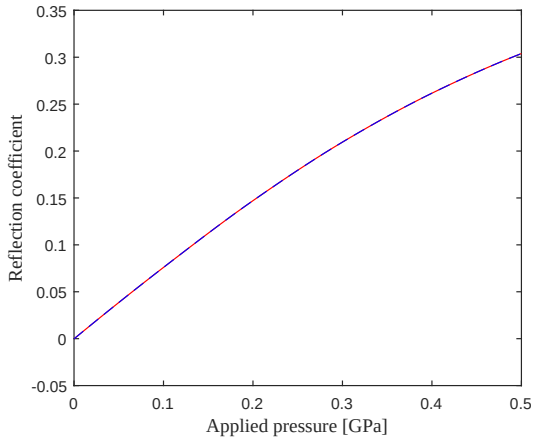


**(c)** longitudinal wave

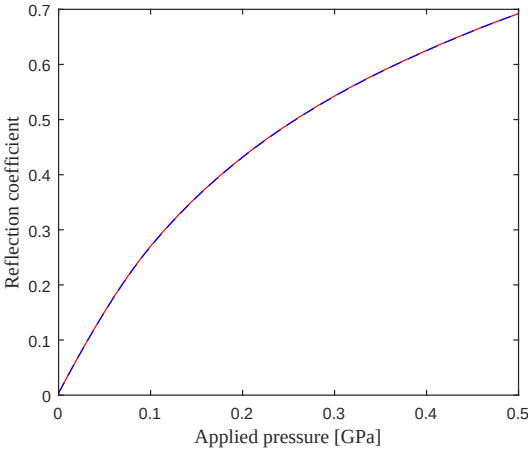


**(d)** torsional wave

**Figure 4.15:** Wave reflection coefficient magnitude at 6.4 kHz for the pressurised sandwich beam as a function of applied pressure: 20% (-) width delamination, 40% (- -) width delamination.

for the longitudinal wave.

At 0.8 kHz (Fig. 4.14), the reflection magnitudes of the x- and y-axes bending waves increase with the applied pressure up to 1 GPa. Beyond this pressure, reduction in the magnitudes is observed. Longitudinal and torsional waves both show similar trends. There is an increase in their coefficient magnitudes with respect to applied pressure. Increment obtained for the torsional wave is however more than that of the longitudinal wave.

Unlike at 0.2 kHz and 0.8 kHz, the reflection coefficient magnitudes of the bending waves at 6.4 kHz (Fig. 4.15) increase with respect to the applied pressure. The longitudinal and the torsional waves maintain similar trend as in 0.2 kHz and 0.8 kHz.

Similar to the non-pressurised system, it is noted that there is no significant difference observed in the reflection coefficients (with respect to frequency and applied pressure) of the 20% width delamination compared to that of the 40% width delamination.

## 4.5 Conclusions

Pre-stress effect on the wave interaction with damage within pressurised layered structures is hereby examined. A FE-based methodology for quantifying wave interaction with damage within pressurised layered structures is presented. The scheme can be applied to pressurised structures of arbitrary complexity, layering and material characteristics as FE discretisation is employed. The scheme discretises pressurised defective waveguide into a system of two pristine waveguides connected through a defective coupling joint. The wave propagation properties within the pristine waveguides are coupled to a damage within the joint in order to compute the wave scattering coefficients for each propagating wave mode in the system. The pre-stress effect on the scattering coefficients is examined. The principal outcome of the work can be summarised as follows:

(i) The presented approach is validated with experimental measurements and full FE transient response predictions. Very good agreement is observed.

(ii) The approach is able to predict the dispersion properties of an arbitrarily complex structure as well as the scattering coefficients of wave interaction with damage within pressurised structures.

(iii) The approach also successfully examined the effect of pre-stress on the wave properties of pressurised structures. It was shown that pressurisation can be used to detect micro defects which may be too small to detect under no pressurisation.

# CHAPTER 5

# Structural identification scheme for periodic layered structures

## 5.1 Introduction

Wide usage of composites has led to the development of new composite structures with tailored properties and a wide range of configurations and topologies. However, the non-destructive verification of the actual mechanical properties of the assembled layered structure remains an open engineering challenge. System identification has been applied extensively in the field of structural dynamics and it has been proven to be useful in the analysis of the dynamic behaviour of the structure. In the context of structural dynamics, system identification generally includes modal-parameter identification by extracting the modal data of a structural system such as its natural frequencies, damping ratio and mode shapes as well as physical-parameter identification by extracting useful information related to stiffness, mass and damping. Over the past decade, various system identification approaches, such as stochastic subspace identification method [179], extended Kalman filter method [26] and Bayesian approach [27], have been proposed.

The cited system identification approaches are generally based on the measurement of structural vibration information. A number of research contributions have demonstrated that wave propagation properties are more sensitive to structural parameters than other structural responses. Therefore, consistent efforts have been directed to extract systems' structural conditions using wave propagation information over the past decade [126, 180]. Though some efforts [181, 182] have been devoted to obtain model parameters through wave propagation, they have not resulted in full-fledged applications. Therefore, there is still significant room for further exploration in system identification by integrating mathematical models of wave propagation.

The propagation of guided waves in sandwich structures has indeed been the subject of intense research in the recent years. Traditional analytical methods typically employed for modelling wave propagation in monolayers can only correctly capture the wave characteristics in the low frequency range for thick structures. In contrast, FE-based wave methods assume a full 3D displacement field and are therefore capable of capturing the entirety of wave motion types in the waveguide under investigation in a very accurate and efficient manner.

The contribution of the work presented in this chapter is to develop a comprehensive methodology coupling periodic structure theory to FE in order to identify the geometric and mechanical characteristics of each individual layer of layered composite structures.

## 5.2 Statement of the problem

An arbitrarily layered composite structure (Fig. 5.1), periodic in the $x$ direction, is considered. The structure is arbitrarily complex and consists of an arbitrary number of layers which may be isotropic or anisotropic. Some of its structural characteristics, which include thickness, density and other material characteristics of each layer, are assumed to be unknown.

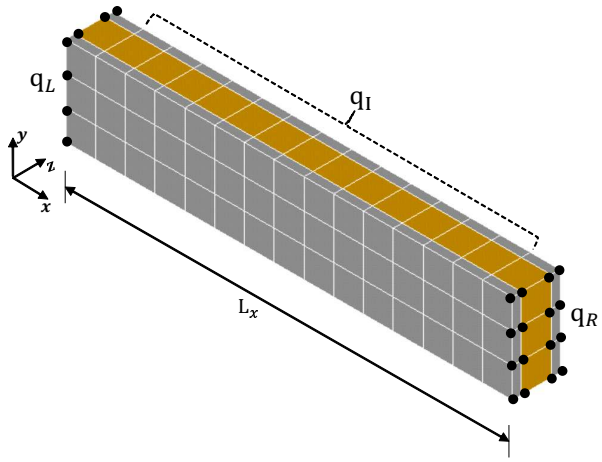


**Figure 5.1:** An arbitrarily layered composite structure, periodic in the $x$ direction. The left and right sides nodes are bullet marked and the range of internal nodes illustrated

Through the methodology presented, wave propagation data of the structure are sought and the acquired wave data are employed to obtain the identifiable properties of the layered structures. The identification scheme therefore involves; calculation of reference wave data within a layered structure and application of the wave data to obtain the unknown properties of the structure.

## 5.3 Reference wave data calculation

The required wave data to be employed in the structural identification scheme include the wave velocities and wavenumbers of waves propagating within the structure under investigation. These data are measured by exciting the structure at an extreme end and computing its response at any node. A number of approaches [183] can be employed for exciting and measuring specific wave signal within composite structures. These include piezoelectric actuation [184], non-contact laser actuation [185] and shaker and accelerometer actuation.

Piezoelectric actuation is employed. It is assumed that the excitation frequencies of the wave packages are known and can be maintained within a certain spectrum. A sufficiently fine discretisation (at least 6-10 elements per wavelength) is employed for numerical accuracy. The excitation signals are quasi-monochromatic burst of amplitude $U_0$, centred around frequency $f_0$ and involving a number of $n_0$ cycles. To avoid frequency leakage, a proper signal windowing technique should be employed. On that note, Hanning window is employed. Input signals are windowed so that the signal is defined by

$$u(t) = \begin{cases} U_0 \sin\left(\dfrac{\pi f_0 t}{n_0}\right) \sin\left(2\pi f_0 t\right), & 0 \leq t \leq \dfrac{n_0}{f_0} \\ 0, & t > \dfrac{n_0}{f_0} \end{cases} \tag{5.3.1}$$

An illustration of the configuration for obtaining the reference wave data is presented in Fig.5.2. The waveguide is excited with a specified signal of frequency $f_0$ at a location $x = x_0$. The signal is monitored at location $x = x_1$, after which the signal has travelled over a distance of $L = x_1 - x_0$. Once the experimental or numerical signal measurements are logged, the wavenumbers and group velocities of the excited waves can be determined. The process is repeated for each target excitation frequency.

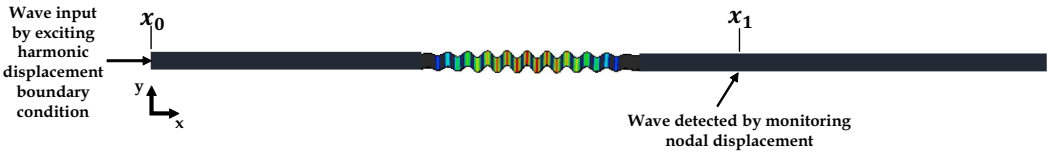


**Figure 5.2:** Illustration of the configuration for obtaining the reference wave data. Piezoelectric actuation is employed for exciting the waveguide and computing its response

Time histories of the signal are registered at the excitation and monitoring locations. The maximum amplitudes of the acquired time history signals $\mathbf{x}(t)$ are obtained from the Hilbert Transforms $H[\mathbf{x}(t)]$ of the signals in the time domain. Hilbert Transform

$H[\mathbf{x}(t)]$ of the acquired time history signal $\mathbf{x}(t)$ is used to evaluate the main attributes of $\mathbf{x}$(t). The signal envelope is determined at excitation, $x_0$ and arrival, $x_1$ while the time delay is defined by the time difference between the maximal amplitudes of the envelopes. The total Time of Flight (ToF) of the wave signal from the point of excitation to the monitoring point is measured as the time difference $t(x_1) - t(x_0)$ between the maximum amplitudes of the excited and the monitored signal envelopes. Then the wavenumber of the wave package is straightforward to obtain as

$$k = \frac{\omega}{c_p} \tag{5.3.2}$$

where the phase velocity of the signal $c_p$ can be obtained from its ToF and propagation distance $L$. It is noted that the phase velocity for a non-dispersive wave is equal to its group velocity.

## 5.4 Comparative wave data calculation

The propagation wave data for the elastic waves travelling within the layered structure can be sought through a wave FE (WFE) scheme as described in Sec. 2.1. It is noted that analytical multilayer modelling techniques [69] have also shown to successfully predict the broadband wave properties for layered structures, however the WFE method is hereby preferred thanks to its versatility (different numbers of layers and complex material properties are straightforward to take into account, with no need of altering the modelling approach).

Since the excitation frequency is known and controlled, an unlimited number of eigenvalues (for the same wave) can be extracted for the corresponding number of excitation frequencies. This is done by solving the eigenproblem of Eq. (2.1.12) at each considered frequency. Each resulting $\mathrm{w_{th}}$ eigenvalue $\lambda_{\mathrm{w}}$ can be expressed as

$$\lambda_{\mathrm{w},fe} = \mathrm{e}^{-\mathrm{i}k_{\mathrm{w},fe}L_x} \tag{5.4.1}$$

and the corresponding wavenumber $k_{\mathrm{w}}$ can be given by

$$k_{\mathrm{w},fe} = \frac{\ln \lambda_{\mathrm{w},fe}}{-\mathrm{i}L_x} \tag{5.4.2}$$

which can be directly compared to the reference wavenumber values $k_{\mathrm{w},rf}$. $rf$ and $fe$ are indices denoting the reference and the WFE wave characteristics respectively.

## 5.5 Formulation of the identification objective function

The objective function of the identification process to be minimized is obtained through a least squares approach as

$$\mathcal{F}(\mathbf{p}) = \sum_{m=1}^{m_{max}} \left( k_{m,rf} - k_{m,fe} \right)^2 \tag{5.5.1}$$

where $k_{m,rf}$ and $k_{m,fe}$ are respectively the reference and the WFE-calculated wavenumbers at frequency $\omega_m$ for the same wave type, while $\mathbf{p}$ is the vector of parameters to be identified. In the general case, $\mathbf{p}$ is expressed as

$$\mathbf{p} = \left\{ \; E_{x,1} E_{y,1} E_{z,1} v_{xy,1} v_{xz,1} v_{yz,1} G_{xy,1} G_{xz,1} G_{yz,1} h_1 \rho_{m,1} \cdots \rho_{m,l_{max}} \; \right\}^\top \tag{5.5.2}$$

for layers $l \in [1, l_{max}]$. $m_{max}$ is the total number of reference eigenvalues which can be used in the identification procedure. It is obvious that the minimum required $m_{max}$ equals to the number of parameters to be identified. However results for additional frequencies will generally improve the precision of the identification process, but an excessive $m_{max}$ is undesired, as for each computation of $\mathcal{F}$, an equivalent number of eigenproblems needs to be solved.

## 5.6 Post-processing the identification objective function

In order to accelerate the Newton-like structural identification scheme, the first (or even the second) gradient of the objective function $\frac{\partial \mathcal{F}}{\partial \beta_i}$ may be provided for each sought structural property $\beta_i$ as

$$\frac{\partial \mathcal{F}}{\partial \beta_i} = \sum_{m=1}^{m_{max}} \left( 2 k_{m,fe} \frac{\partial k_{m,fe}}{\partial \beta_i} - 2 k_{m,rf} \frac{\partial k_{m,fe}}{\partial \beta_i} \right) \tag{5.6.1}$$

It is noted that the set of parameters may be considered to have constrained values (e.g. $\beta_i \in [\beta_{i,min}, \beta_{i,max}]$), for practical reasons. In order to compute the gradient of the wavenumber values $\frac{\partial k_{m,fe}}{\partial \beta_i}$, an expression of the mass and stiffness matrices directly as a function of the material and geometric characteristics of each layer is greatly practical, as derived in Appendix C. By employing the symbolic expressions for the mass and stiffness derivatives $\frac{\partial \mathbf{M}}{\partial \beta_i}$, $\frac{\partial \mathbf{K}}{\partial \beta_i}$ the wavenumber sensitivity $\frac{\partial k_{m,fe}}{\partial \beta_i}$ can be computed as in [186].

The constrained minimization problem can be implemented within standard mathematics software and nonlinear optimization algorithms (such as *fmincon* in MATLAB) can be employed in order to compute the optimal parameter vector $\mathbf{p}$ that minimizes

$\mathcal{F}(\mathbf{p})$ and corresponds to the identified structural properties. It is stressed that due to the existence of several local minima in $\mathcal{F}$, a global search algorithm is employed during the solution process. The minimum of the encountered solutions is retained as the global set of acquired structural characteristics.

The generic iterative procedure of the post-processing identification process is presented in Algorithm 1.

**Algorithm 1** Newton-like iterative scheme for identifying the parameters of a layered structure

1: Input measured reference wave characteristics. Determine total number of local minima to be investigated and evaluated. Define identification criterion for objective function $\mathcal{F}$
2: $i \leftarrow 1$ Input structural parameters for initial design to be evaluated
3: Substitute new set of structural parameters in symbolic expressions of $\mathbf{M}$, $\mathbf{K}$, $\frac{\partial \mathbf{K}}{\partial \beta_i}$, $\frac{\partial \mathbf{M}}{\partial \beta_i}$ and formulate the corresponding matrices for the periodic unit cell of the layered design under investigation
4: Solve the eigenproblem of Eq. (2.1.12) for design $i$. Compute WFE wave velocities and wavenumbers
5: Compute $\mathcal{F}$ and the sensitivity values $\frac{\partial \mathcal{F}}{\partial \beta_i}$ for each structural parameter $\beta_i$ to be recovered
6: **if** $\mathrm{d}\mathcal{F} <$ Solution convergence criterion **then**
7: Solution corresponds to a local minimum
8: **if** $\mathcal{F} <$ Identification criterion **then**
9: Solution corresponds to global identification solution and process can end
10: **else**
11: Radically alter the structural parameters and go to Step 3
12: **end if**
13: **else**
14: Use $\frac{\partial \mathcal{F}}{\partial \beta_i}$ in order to alter structural parameters for converging towards a local minimum. $i \leftarrow i + 1$ (next solution step). Go to Step 3
15: **end if**

## 5.7 Case studies

The presented scheme is validated in this Section through numerical and experimental results. It is shown that when clear wavenumber measurements are obtained, the approach can be exceptionally accurate. Moreover, the procedure can be applied within

a rational amount of time (especially if only one or two structural parameters are to be sought) using conventional low-cost computing equipment.

### 5.7.1 Numerical validation of the identification scheme

#### 5.7.1.1 Monolayer case study

The first numerical case study attempts to identify the thickness, density and elastic modulus of a monolayer structure whose properties are exhibited under Structure I in Table 5.1. The monolayer structure is modelled using 3D solid elements in ANSYS®. A Hanning windowed longitudinal pressure wave excitation (of $n_0$=9 cycles) is numerically imposed at an extreme cross section of the modelled structure. A general representation of the measurement process is depicted in Fig.5.3).

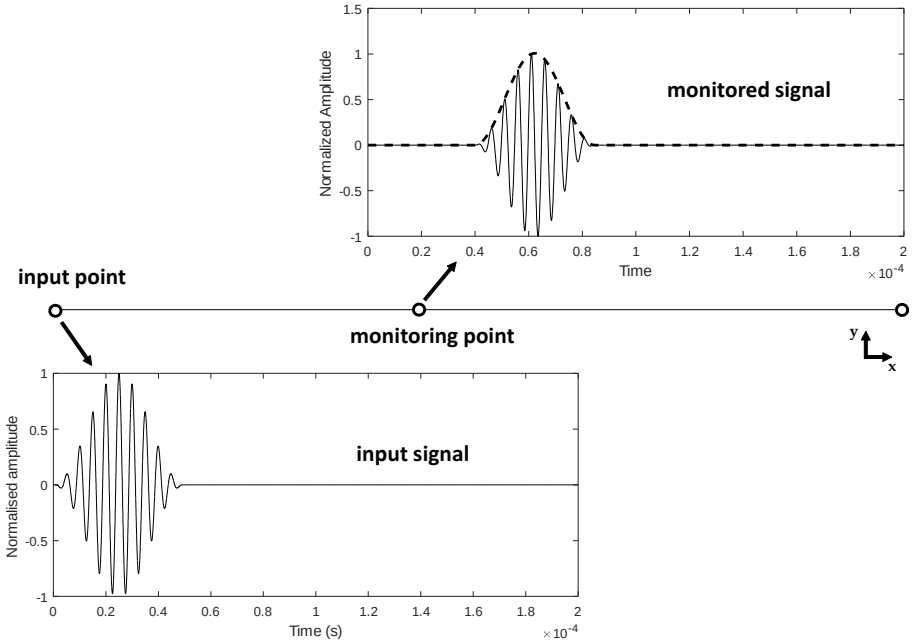


**Figure 5.3:** General representation of the ToF measurements. The pulse input is generated using an excitation device at the input point while the time delay is measured at the monitoring point. Note that better results are obtained when no edge reflections are interfering with the registered pulse

The propagating waveform along the monolayer structure is presented in Fig.5.4 for six different excitation frequencies. As expected, negligible dispersion occurs for all six pulses, thanks to the high number of cycles $n_0$ employed for the Hanning window process, as well as to the non-dispersive nature of longitudinal waves. It is clear that the absence of reflected and converted waves at high frequencies allows a reliable determination of the wave envelope characteristics.

Six wavenumber measurements are recovered for the six different frequencies, from

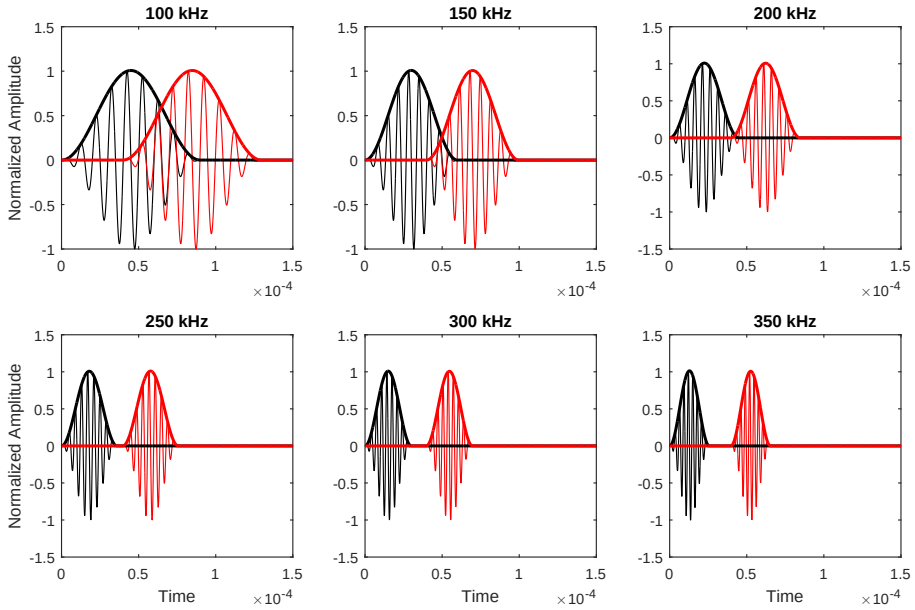


**Figure 5.4:** Time acquisition at $x = 0$ (black curves) and $x = 3$cm (red curves) with the wave envelopes depicted in the monolayer structure. The number of cycles is $n_0$=9. The ToF is measured at the maximal amplitude of Hilbert transform (solid lines) signal

100 kHz to 350 kHz with a step of 50 kHz. The reference wave characteristics related to the recovered wavenumber values are presented in Fig. 5.5. These are retained for comparison with the WFE obtained results for the same wave type which will form the objective function of the identification problem. The same process is repeated for a flexural wave propagating within the monolayer structure with the results also presented in Fig. 5.5.

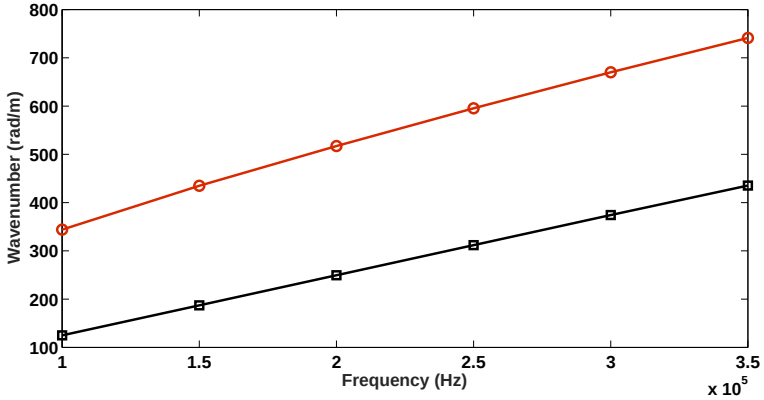


**Figure 5.5:** Reference wavenumber values obtained through a numerical solution of the full FE model for a monolayer structure: Results for longitudinal wave (□) and flexural wave (◯)

Once the reference wave characteristics $k_{m,rf}$ are established, the objective function $\mathcal{F}$ can be established as a function of the structural properties to be identified $E$, $\rho$

and $h$. The WFE wave characteristics, to be compared with the reference ones, are obtained through the eigenproblem solutions of Eq. (5.4.2). An identification criterion equal to 10 is employed (suggesting that any local minimum with a value less than that would be considered as a solution). The minimization process is completed in 58 iterations each of which lasted approximately 8 s, resulting in a total computation time of 460 s on a conventional PC device. This suggests that employing dedicated optimization software and high-performance computing equipment would radically reduce the amount of processing time. The final value of the objective function when longitudinal wave measurements are employed is of the order of $10^{-1}$. The second best identified solution give an objective function value at the order of $10^{1}$, therefore confirming the optimality of the result. The identified parameters are exhibited in Table 5.1 and are in excellent agreement with the ones initially used in the full FE model (maximum divergence is considerably less than 1%). The result therefore validates the accuracy and robustness of the proposed scheme.

#### 5.7.1.2 Layered composite case study

A similar process is followed for extending the calculations to a layered composite structural configuration. The properties for each layer of the sandwich structure are given as Structure II (lower facesheet), Structure III (core layer) and Structure IV (upper facesheet) in Table 5.1. Once again, a longitudinal as well as a flexural wave excitation is imposed at an extreme cross-section of the modelled structure. A Hanning window is applied at all pulses with $n_0$=9. The results for six different excitation frequencies are presented in Fig. 5.6.

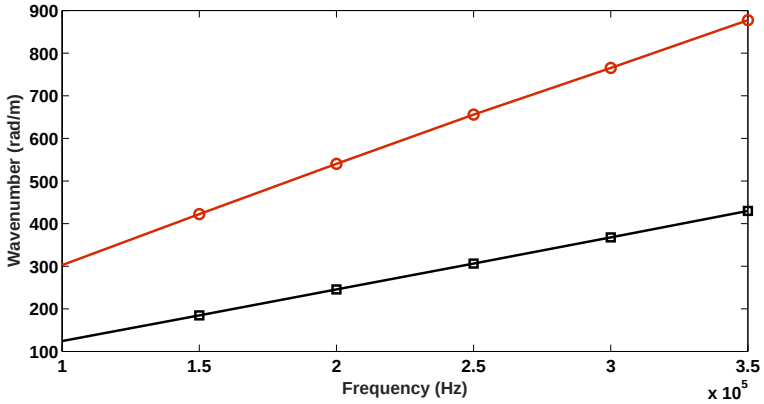


**Figure 5.6:** Reference wavenumber values obtained through a numerical solution of the full FE model for the multilayer structure. Results for longitudinal wave (□) and flexural wave (◯)

In order to find out the maximum number of parameters that can be identified within a reasonable amount of time for the multilayer structure, identification proce-

dure is run for three, four, five and six unknown parameters. The WFE wave characteristics, to be compared with the reference ones, are obtained through the eigenproblem solutions of Eq. (5.4.2). The identification criterion is again set equal to 10. It is observed that the processes with five and six unknown parameters never converged to a satisfactory value of the objective function after about 18,000 s of post-processing time (5 hrs). This is due to the existence of an important number of local minima that needed to be investigated by the *fmincon* algorithm. None of the derived local solutions however had a value close to zero.

The identification process did converge when four parameters were considered unknown ($\rho_{II}$, $G_{xz,III}$, $E_{x,IV}$ and $h_{IV}$) with the corresponding indices taken as in Table 5.1. The minimization process converged after 137 iterations each of which lasted approximately 14 s, resulting in a total computation time of 1950 s on a PC device. The properties identified through the results corresponding to the longitudinal wave are again presented in Table 5.1. Very good agreement exists between the recovered values and the ones initially injected in the full FE model (maximum divergence again not greater that 1%), while the final value of the objective function is equal to 5.34. It is evident that incorrect wavenumber measurements will radically increase the value of the calculated objective function, therefore leading to a non-convergent problem.

**Table 5.1:** Properties of numerically modelled structural layers and identified characteristics through the presented identification scheme

| Structure I | Structure II | Structure III | Structure IV |
|---|---|---|---|
| $\rho = 7850$ kg/m$^3$ | $\rho = 3500$ kg/m$^3$ | $\rho = 150$ kg/m$^3$ | $\rho = 3500$ kg/m$^3$ |
| $h = 1$ mm | $h = 0.5$ mm | $h = 5$ mm | $h = 1$ mm |
| $E = 170$ GPa | $E_x = 150$ GPa | $E_x = 95$ MPa | $E_x = 150$ GPa |
| - | $E_y = 85$ GPa | $E_y = 95$ MPa | $E_y = 85$ GPa |
| - | $E_z = 85$ GPa | $E_z = 150$ MPa | $E_z = 85$ GPa |
| $v = 0.29$ | $v_{xy} = 0.15$ | $v_{xy} = 0.3$ | $v_{xy} = 0.15$ |
| - | $v_{xz} = 0.1$ | $v_{xz} = 0.23$ | $v_{xz} = 0.1$ |
| - | $v_{yz} = 0.1$ | $v_{yz} = 0.3$ | $v_{yz} = 0.1$ |
| - | $G_{xy} = 15$ GPa | $G_{xy} = 20$ MPa | $G_{xy} = 15$ GPa |
| - | $G_{yz} = 23$ GPa | $G_{yz} = 55$ MPa | $G_{yz} = 23$ GPa |
| - | $G_{xz} = 15$ GPa | $G_{xz} = 35$ MPa | $G_{xz} = 15$ GPa |
| Identified structural characteristics | | | |
| $\rho = 7857.43$ kg/m$^3$ | $\rho = 3474.8$ kg/m$^3$ | $G_{xz} = 35.44$ MPa | $h = 1.0038$ mm |
| $h = 0.9973$ mm | - | - | $E_x = 148.91$ GPa |
| $E = 174.32$ GPa | - | - | - |

### 5.7.2 Experimental validation of the identification scheme

An experimental approach is employed in this section in order to further extend the validation of the presented structural identification scheme. The proposed scheme is applied to a sandwich structure, and results are compared with the ones obtained in Droz et al. [31] from Inhomogeneous Wave Correlation (IWC) method, static experiments and the Transition Frequency Characterization (TFC) method.

The structure is a rectangular sandwich plate measuring 60 cm $\times$ 288 cm, placed in a horizontal position as depicted in Fig. 5.7. The constitutive materials are a 10 mm-thick Nomex honeycomb core involving a 3.2 mm cell size, while propagation is considered in the W-direction. The sandwich's skins are 0.6 mm-thick Hexforce with multi-axial, carbon-reinforced fibres. The density of the skins given by the manufacturer is $\rho_s = 1451\,\text{kg.m}^{-3}$ and the core's density is $\rho_c = 99\,\text{kg.m}^{-3}$.

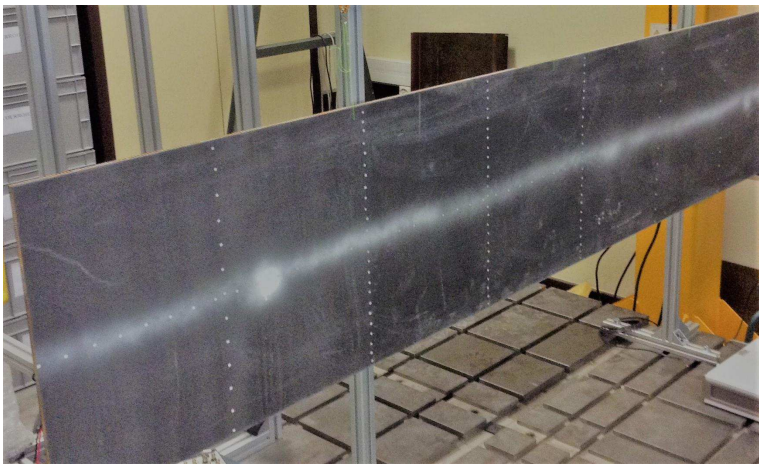

**Figure 5.7:** Photo of the structure used to retrieve experimental wavenumbers [2]

Structural response is measured using a Polytec Scanning Vibrometer (PSV) and is transmitted to the acquisition system in order to compute the structural impedance at various points of the panel. The panel was excited using a shaker, controlled by the Polytec acquisition system and adhered to the structure through a force sensor. The shaker is used to produce the harmonic excitation at the edge of the plate while the laser vibrometer is used to measure normal displacement field at the surface, along a 50 cm line of 66 points.

Static measurements conducted on the layered structure provides the following mechanical characteristics for the elastic modulus of the skins and the shear modulus of the core along the investigated direction:

$$E_{\text{manuf}} = 70\,\text{GPa} \quad \text{and} \quad G_{\text{manuf}} \in [30 - 38]\,\text{MPa}$$

The IWC method [31] is employed to estimate the flexural wavenumbers in the

plate. The frequency range of interest spans 0 and 4000 Hz. The phase velocities obtained by the IWC method are shown in Fig.5.8.

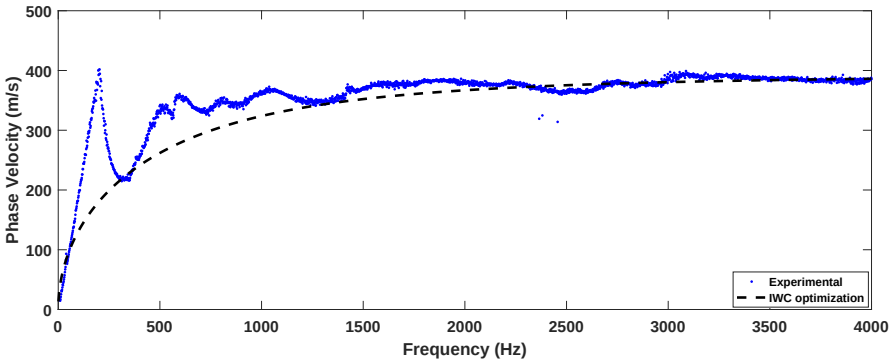


**Figure 5.8:** Flexural phase velocities obtained in the main direction of the plate. Inaccurate results are usually expected in the low frequencies for the IWC method. The convergence however increases with frequency, providing approximated material properties and a good correlation with analytical results

Material properties, for the elastic modulus of the skins and the shear modulus of the core, obtained from the IWC characterization [31] are:

$$E_{\text{IWC}} = 62\,\text{GPa} \quad \text{and} \quad G_{\text{IWC}} = 37.8\,\text{MPa}$$

The TFC method is similarly employed to obtain the flexural wave characteristics in the plate. Pulse generation at frequency $f_n$ involves at least 10 cycles to limit dispersion effects occurring at these frequencies and is controlled by the PSV Laser using a triggering procedure. The response is measured at 1 m from the source for a selected number of frequencies between 500 Hz and 1500 Hz. The time signals are averaged at least 30 times to reduce experimental noise. Noteworthy, the group velocity can also be derived from measured phase velocities and wavenumbers. Measured pulses are presented in Fig. 5.9 for 6 different frequencies close to the transition bandwidth 880 Hz.

Material properties, for the elastic modulus of the skins and the shear modulus of the core, obtained by the TFC method [31] are:

$$E_{\text{TFC}} = 69.8\,\text{GPa} \quad \text{and} \quad G_{\text{TFC}} = 36.5\,\text{MPa}$$

The proposed identification scheme is now applied to estimate the two mechanical characteristics. The Newton-like minimization scheme, depicted in Fig. 5.10 and detailed in Algorithm 1, is programmed and executed using the experimentally obtained flexural wavenumbers as the reference wavenumbers. The structural parameters to be identified are the elastic modulus of the skins and the shear modulus of the core in the

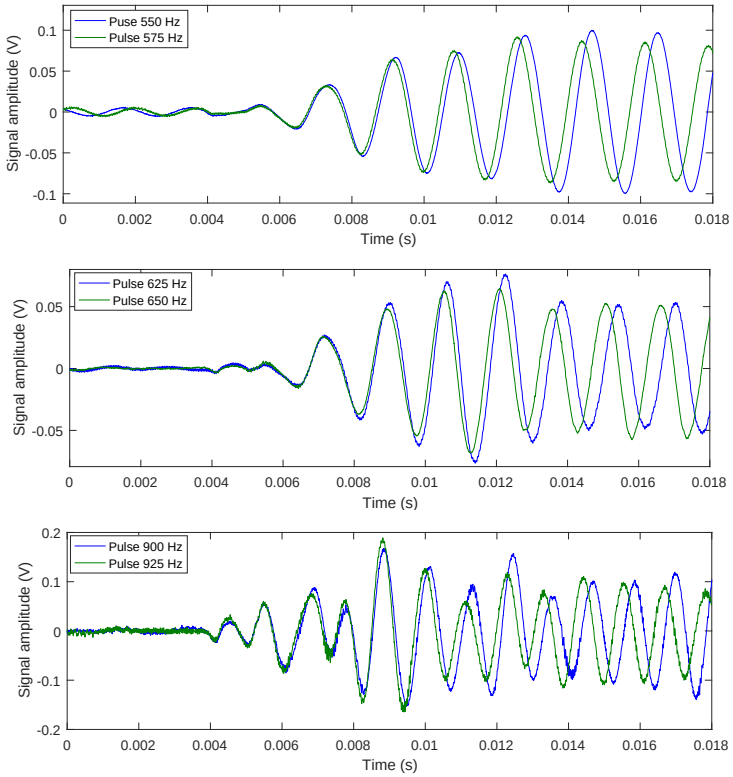


**Figure 5.9:** Measured pulse signals at acquisition point

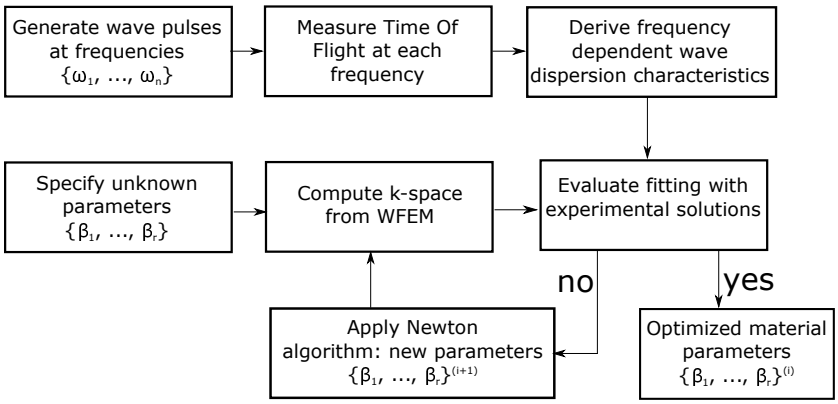


**Figure 5.10:** Experimental procedure for the WFE-based model updating strategy

direction of wave propagation. A new design is therefore generated after each iteration, taking into account the first derivative of $\mathcal{F}$. After converging to a minimum of $\mathcal{F}$, the final value of the objective function is compared to the identification criterion. If the identification condition is not satisfied, a drastically altered design is evaluated by the iterative algorithm. The WFE-obtained wavenumbers, to be compared with the reference ones, are obtained through the eigenproblem solutions of Eq. (5.4.2). An identification criterion equal to 10 is employed while the minimization process converged in 91 iterations each of which lasted approximately 14 s, resulting in a total computation time of 1274 s on a conventional PC device.

The identified elastic modulus for the skins of the laminate and the shear modulus of the honeycomb core in the direction under investigation are computed as:

$$E_{\text{WFE}} = 69.5\,\text{GPa} \quad \text{and} \quad G_{\text{WFE}} = 37.1\,\text{MPa}$$

which are both in very good agreement with the values provided by the static measurements, the IWC and the TFC methods, therefore experimentally validating the exhibited computational scheme.

## 5.8 Conclusions

In this work, a new structural identification technique, based on FE modelling and the properties of propagating waves in layered structures, is developed and applied. The principal contribution the work is a robust numerical NDE procedure for recovering effective structural parameters of arbitrarily complex, layered structures. The contributions can be summarised as

(i) The method is able to extract layer characteristics including thickness, density, elastic and shear moduli and is robust enough to be applied in a broadband frequency range. Case studies elaborating on both ultrasonic as well as low frequency ranges are presented. In the ultrasonic range the wave characteristics are straightforward to extract through the measured wave envelopes, while in the low frequency regime dedicated techniques such as the IWC approach can be employed.

(ii) The exhibited scheme is validated through comparison with experimental results as well as through full FE transient response predictions. Excellent agreement is observed for the identified structural parameters.

(iii) It is emphasized that the proposed wave-based method has significant advantages compared to modal identification approaches. More precisely the accuracy

of the structural parameters is not altered by the presence of uncertain boundaries since the data is obtained locally, through single-shot measurements. This is a considerable advantage compared to a number of stationary and other existing methods, since it can then be applied in situ and without requiring additional sampling of the structure. The use of unlimited and user-selected excitation frequencies can effectively increase the number of parameters to be identified through the inverse wave modelling, resulting in a significant increase of the method's robustness in a broadband frequency sense.

# CHAPTER 6

# Wave interaction with nonlinear damage and generation of harmonics in composite structures

## 6.1 Introduction

Linear ultrasonic wave techniques have been widely developed for monitoring the condition and residual life estimation of in-service composite structures. However, these techniques are generally limited to relatively large defects but much less sensitive to micro and nonlinear defects. Therefore there is a need to develop nonlinear acousto-ultrasonic technique which will detect and evaluate nonlinear incipient defects in composite structures efficiently and reliably.

As early as in Breazeale and Thompson [187], wave distortion and generation of higher harmonics during wave propagation in nonlinear medium have been considered. A numerical model for wave interaction with nonlinear coupling is first presented in Vakakis [188]. Harmonic generation in nonlinear wave interaction has hence been greatly deployed for detecting contact-type defects (such as breathing cracks) as well as distributed deterioration (e.g. fatigue) in structural waveguides [163, 189]. Numerical modelling of nonlinear wave interaction with an interface of rough surfaces in contact is studied in Pecorari [190]. An alternative approach to nonlinear ultrasonic techniques is presented in Croxford et al. [191] to investigate the non-collinear mixing of bulk shear waves for the purpose of measuring and eliminating nonlinearities in the system. Rayleigh waves are used in Kawashima et al. [192] to detect surface cracks and nonlinear longitudinal waves in Soshu and Toshihiko [193] to evaluate closed cracks. An analytical scheme for modelling multi-modal wave interaction with damage is presented in Giurgiutiu et al. [194]. Reflection of compression and Rayleigh waves when

impinging at the edge of an elastic plate is studied numerically in Autrusson et al. [195]. A coupled linear and nonlinear FE approach is developed in Fierro et al. [196] to investigate wave interaction with damage in solid media. Recently, corrosion damage imaging using wave tomography method based on ultrasonic guided waves is reported in Ciampa et al. [197]. A pitch-catch FE based approach was developed in Shen and Giurgiutiu [198] to investigate nonlinearity introduced by breathing cracks. Despite the reported attempts to capture wave interaction with localised structural nonlinearities and damage, there is currently limited computational scheme for predicting these quantities in composite structures of arbitrary layering and geometric complexity.

FE-based nonlinear wave interaction has been studied numerically using unilateral contact laws. These laws are available in commercial FE packages and have been used to study nonlinear wave interaction with delamination [199], breathing [198] and buried [200] cracks. However, in Shen and Giurgiutiu [198], multi-mode guided wave is excited at the transmitter sensor. These modes may have not been fully separated when being received at the receiver sensor, especially when the sensor is close to the damage zone. Hence, this may lead to modes overlapping (mix-mode effect). Also in [200], it was presented that the wave frequency spectrum of the wave packet corresponding to the incident wave (in the nonlinear interaction with a crack) is nonlinear, i.e. contains harmonics. Physically, this is expected to be purely linear (such as in [199, 201]) because the incident wave has not come into contact with the nonlinear damage at that stage. Generation of harmonics is only valid for the new wave packet formed from the interaction phenomenon. Lastly, most of the reported work did not consider quantification of the harmonic reflection/transmission coefficients of the nonlinear wave-damage interaction phenomenon. These facts give rise to the objective of the work presented hereby.

The main contribution of the work presented in this chapter is the development of a generic WFE based computational scheme for computing wave interaction with localised nonlinear structural damage (LNSD) in arbitrarily layered composite structures. It is also aimed at establishing the computed harmonic wave interaction coefficients as a damage mode identification tool. More specifically, through-thickness mode-shapes of the guided waves propagating along structures of arbitrary layering and geometric complexities are obtained through a wave finite element method. In order to generate a specific guided mode, the WFE obtained through-thickness amplitudes relating to the eigen-properties of each mode are applied in a time domain FE calculation. The approach presents a significant advantage in specific mode excitation without mix-mode effect. The clapping mechanism of the LNSD is modelled using an element birth and death criterion. Two generic damage orientations, namely crack

(vertical orientation) and delamination (horizontal orientation), are considered in this study. The guided wave propagates and interacts with the LNSD along the structure, and harmonic reflection coefficients are obtained from the interaction phenomenon. The calculated harmonic reflection coefficients are applied as indices for detecting presence of LNSD and to study the dependence of the interaction coefficients on the LNSD severity. Further analysis is also made into identification/classification of structural damage type based on their wave interaction coefficients magnitudes.

## 6.2 Statement of the problem

Wave propagation is considered in the $x$ direction of an arbitrarily layered composite structure, periodic in the $x$ direction. In general case, plane strain condition is assumed in the $z$ direction and the structure can exhibit structural nonlinearity, such as nonlinear/clapping damage as shown in Fig. 6.1.

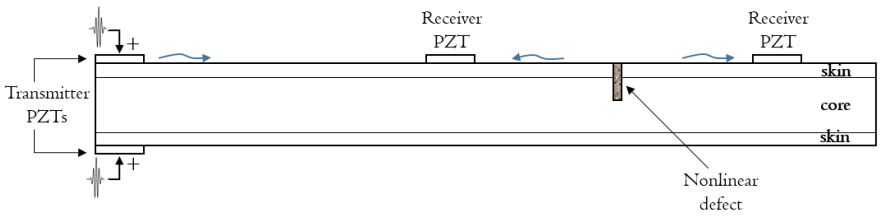


**Figure 6.1:** Arbitrarily layered composite structure containing structural defect exhibiting nonlinear mechanical behaviour. Imposed wave signal is received after interaction with the nonlinear defect

The wave propagation constants at each periodic cross-section of the structure are obtained through the WFE scheme, as presented in Sec. 2.1, by solving the eigenvalue problem in Eq. (2.1.12). The WFE-computed mode shape of a specific wave at the left extreme cross-section of the plate is piezoelectrically generated, as a voltage tone burst signal of the wave, and imposed on the extreme cross-section as shown in Fig. 6.1. Quantification of the wave signal interaction with the nonlinear damage is hereby considered.

## 6.3 Nonlinear structural damage modelling

### 6.3.1 Harmonics generation through contact acoustic nonlinearity

Contact acoustic nonlinearity (CAN) is generated when a propagating wave interacts with nonlinear/micro damage within a structural medium. This leads to a clapping mechanism of the damage being activated during the interaction. The clapping mecha-

nism, during which the damage opens and closes alternatively, leads to the generation of sub and higher harmonics of the wave. Hence, the general output function of a dynamic system, consisting of the sub and higher order terms, can be expressed as

$$\mathrm{Y}(u) = \chi u + \alpha\chi u^2 + \epsilon\chi u^3 + \cdots + \alpha_0\chi u^{1/2} + \epsilon_0\chi u^{1/3} + \cdots \tag{6.3.1}$$

where $\chi$ is the scale scale factor of the dynamic system. The input function, $u$, of the system can be expressed in harmonic form as

$$u(\omega) = u_0 \mathrm{e}^{\mathrm{i}\omega t} \tag{6.3.2}$$

Substituting Eq. (6.3.2) into Eq. (6.3.1) gives the harmonic output function of the system as

$$\mathrm{Y}(u) = A_1 u(\omega) + A_2 u(2\omega) + A_3 u(3\omega) + \mathcal{O}(4\omega) + B_1 u(\omega/2) + B_2 u(\omega/3) + \mathcal{O}(\omega/4) \tag{6.3.3}$$

This shows that the output function of a nonlinear dynamic system contains fundamental ($\omega$), sub ($\omega/2$, $\omega/3$, $\omega/4\cdots$) and higher ($2\omega$, $3\omega$, $4\omega\cdots$) harmonics whereas the input function contains only the fundamental harmonic. Hence, wave interaction with nonlinear damage is expected to generate interaction scattering coefficients not only at fundamental frequency but also at sub and higher harmonic frequencies. This feature is highly essential in accessing nonlinearity within structural systems. As will be demonstrated in later sections, it is also essential for damage detection and identification.

### 6.3.2 Element birth/death criterion for modelling clapping mechanism of nonlinear damage

As earlier stated, the clapping mechanism of a nonlinear damage within a structural medium is based on the CAN phenomenon generated from an interaction of the damage with a wave propagating through the medium.

The clapping mechanism involves an asynchronous opening or closing of the damage as the wave travels through it. The damage closes during the compressional phase of the wave, and opens during the tensile phase as shown in Fig. 6.2.

In CAN, compressive stress strengthens the contact between interface surfaces of the defect while tensile stress weakens it. Hence, the compressional phase of the wave penetrates the defect and closes it while the tensile part does otherwise.

The clapping mechanism of the damage is implemented in an element birth/death criterion. In the criterion, elements within the damage zone are deactivated (damage

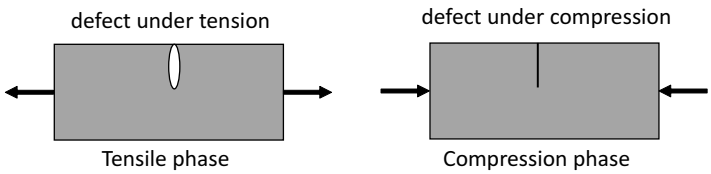


**Figure 6.2:** Acoustic mechanism in a contact-type damage: the damage opens under tension and closes when in compression

opens) when their cumulative strains are positive (i.e. when undergoing tension) and reactivated (damage closes) when negative (i.e. when undergoing compression).

It should be noted that when elements are deactivated, they are not removed or deleted from the structural model, but rather made insignificant in the model. Hence, during this stage, the material stiffness of the deactivated finite elements is reduced by a severe reduction factor [178]. This leads to an updated stiffness matrix in order to accommodate reduction in stiffness properties of the medium. As structural matrices (mass, stiffness or damping) are an assemblage of constituent elements matrices, the stiffness matrix of the affected elements is updated as

$$\boldsymbol{K}_u^e = \beta \boldsymbol{K} \tag{6.3.4}$$

where $\boldsymbol{K}$ is the original stiffness matrix of the elements when active (alive), $\boldsymbol{K}_u^e$ is the updated stiffness matrix of the elements when deactivated (dead) and $\beta$ is the stiffness reduction factor (equals $10^{-6}$ by default or a user defined value, typically $\ll 1$). On the other hand, the mass matrix of the deactivated elements are set to zero to remove their effect from the entire model.

As earlier stated, deactivation of the elements within the damage zone depends on the cumulative strain value of the elements. The cumulative strain of the damage zone elements, as illustrated in Figure 6.3, are determined as

$$\begin{aligned} \varepsilon_d &= \sum_{n=1}^{N} \varepsilon_{dn} \\ \varepsilon_b &= q_2 - q_1 \end{aligned} \tag{6.3.5}$$

with all strain values measured along the axis of wave propagation.

The iterative procedure of the elements birth/death criterion for nonlinear wave interaction modelling is summarised in the pseudocode presented in Algorithm 1.

The algorithm presents the routine through which the elements within the damage zone are systematically made active or inactive during the nonlinear transient analysis. After each solution step, the cumulative strains ($\varepsilon_d, \varepsilon_b$) of the damage zone elements are calculated (Eq. 6.3.5). The elements are made inactive if the magnitudes of the strains

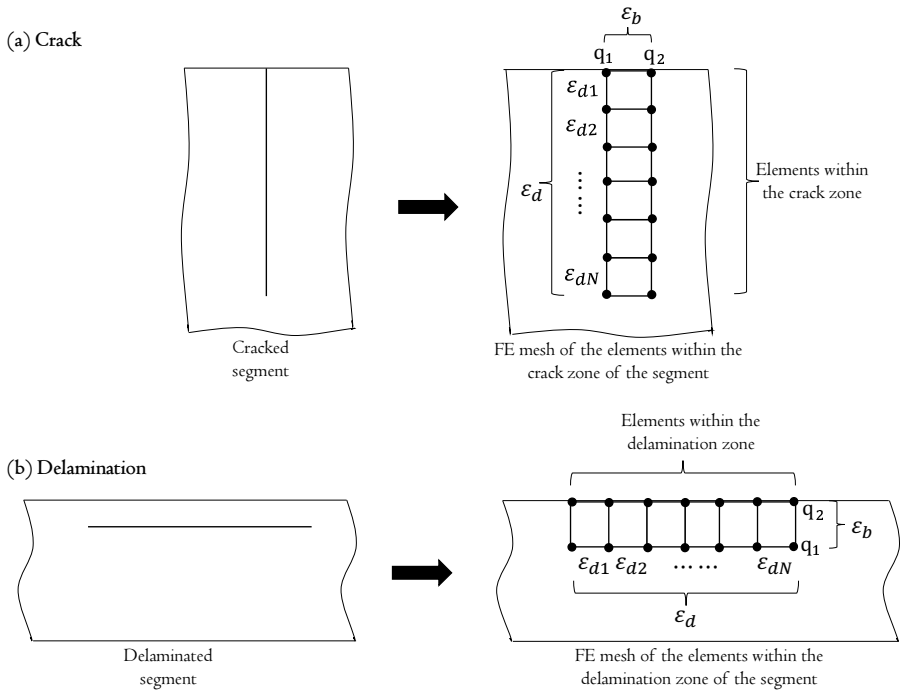


**Figure 6.3:** Configuration of the element birth/death criterion for damage clapping mechanism: (a) Crack (b) Delamination. (Not to scale)

**Algorithm 2** Iterative procedure of the element birth/death criterion for damage clapping mechanism

1: Build the model, apply load and constraints and determine solution parameters
2: $i \leftarrow 1$ (first solution step)
3: Solve the model for solution step $i$
4: Determine $\varepsilon_d$ and $\varepsilon_b$
5: **if** $\varepsilon_d < 0 \cap \varepsilon_b < 0$ **then**
6: Reactivate the damage zone elements if presently deactivated
7: **else**
8: Deactivate the damage zone elements if presently active
9: **end if**
10: **if** $i \leq m$ (where $m$ equals number of solution steps) **then**
11: $i \leftarrow i + 1$ (next solution step)
12: Go to step 3
13: **else**
14: End of iteration
15: **end if**

are positive (i.e. under tension) or active if the strain values are negative (i.e. under compression). This iteration is repeated for every load step of the analysis.

## 6.4 Finite element wave interaction modelling

Consider wave propagation in the $x$ direction along an arbitrarily layered composite structure in which plane strain condition is assumed in the $z$ direction. Interaction of the wave with nonlinear damage within the structure is hereby presented, using the element birth/death criterion to implement the clapping mechanism of the damage.

Each supported wavemode w with $\mathrm{w} \in [1 \cdots \mathrm{W}]$, at a specified angular frequency, can be grouped into displacement and force components as

$$\begin{aligned}
\boldsymbol{\Phi}_{q}^{\mathrm{inc}} &= \left[ \begin{array}{cccc} \boldsymbol{\phi}_{q,1}^{\mathrm{inc}} & \boldsymbol{\phi}_{q,2}^{\mathrm{inc}} & \cdots & \boldsymbol{\phi}_{q,W}^{\mathrm{inc}} \end{array} \right]_{[j \times W]} \\
\boldsymbol{\Phi}_{f}^{\mathrm{inc}} &= \left[ \begin{array}{cccc} \boldsymbol{\phi}_{f,1}^{\mathrm{inc}} & \boldsymbol{\phi}_{f,2}^{\mathrm{inc}} & \cdots & \boldsymbol{\phi}_{f,W}^{\mathrm{inc}} \end{array} \right]_{[j \times W]} \\
\boldsymbol{\Phi}_{q}^{\mathrm{ref}} &= \left[ \begin{array}{cccc} \boldsymbol{\phi}_{q,1}^{\mathrm{ref}} & \boldsymbol{\phi}_{q,2}^{\mathrm{ref}} & \cdots & \boldsymbol{\phi}_{q,W}^{\mathrm{ref}} \end{array} \right]_{[j \times W]} \\
\boldsymbol{\Phi}_{f}^{\mathrm{ref}} &= \left[ \begin{array}{cccc} \boldsymbol{\phi}_{f,1}^{\mathrm{ref}} & \boldsymbol{\phi}_{f,2}^{\mathrm{ref}} & \cdots & \boldsymbol{\phi}_{f,W}^{\mathrm{ref}} \end{array} \right]_{[j \times W]}
\end{aligned} \tag{6.4.1}$$

The displacement eigenvectors of each positive going elastic wave $\boldsymbol{\phi}_{q,\mathrm{w}}^{\mathrm{inc}}$ can be further grouped as

$$\boldsymbol{\phi}_{q,\mathrm{w}}^{\mathrm{inc}} = \left\{ \begin{array}{cccccccc} q_{1,x} & q_{1,y} & q_{2,x} & q_{2,y} & \cdots & q_{r,x} & q_{r,y} \end{array} \right\}^{\mathsf{T}} \tag{6.4.2}$$

with $q_{r,x}$ and $q_{r,y}$ the in-plane ($x$-axis) and the out-of-plane ($y$-axis) displacement components of node $r$ where $r \in [1 \cdots R]$. $R$ is the number of nodes along a periodic cross-section of the structural waveguide. Hence, the displacement vectors of each propagating wave, in the in-plane $\boldsymbol{\phi}_{q,\mathrm{w}x}^{\mathrm{inc}}$ and out-of-plane $\boldsymbol{\phi}_{q,\mathrm{w}y}^{\mathrm{inc}}$ directions, can be extracted from Eqs. (6.4.1) and (6.4.2).

FE quantification of wave interaction with nonlinear damage within the layered composite plate is conducted using piezo-electrically generated ultrasonic wave. PZT wafer transducers are bonded to the plate as shown in Fig. 6.1. The wafers and the plate are assumed to be of infinite dimension in the $z$ direction (plane strain condition). ANSYS 14.0 is used for the FE calculations. 2-D 4-node PLANE182 (for the plate) and PLANE13 (for the PZTs) elements are chosen due to their plane strain capability in modelling structural solids. The elements have two DoFs in each node; displacements in $x$ and $y$ directions.

In order to generate ultrasonic wave of a specific mode and avoid mix-mode effect, the transmitter PZTs are excited, employing the WFE computed displacement of the

mode being excited, at one extreme cross-section of the waveguide. This will suppress other modes within the waveguide. The wave is excited as a time-dependent harmonic voltage boundary condition (of excitation frequency $\omega$).

Generally, in this study, the in-plane mode $\boldsymbol{\phi}^{\text{inc}}_{q,\text{w}x}$ is applied to generate a longitudinal wave motion. The excitation signal is a 20 V peak-to-peak Hanning windowed toneburst consisting of five cycles at center frequency of $f_0 = 100$ kHz. The time dependent harmonic voltage (with $\omega = 2\pi f_0$) is given as

$$V(t) = \begin{cases} \phi^{\text{inc}}_{q,\text{w}x} \sin(\omega t) \cdot (0.5 - 0.5\cos(\frac{\omega t}{5}), & t \leq \frac{10\pi}{\omega} \\ 0, & t > \frac{10\pi}{\omega} \end{cases} \tag{6.4.3}$$

Spatial (element size) and temporal (integration time step) resolutions of the FE model are chosen, to ensure solution convergence while ensuring the model computational size is relatively reasonable, as

$$t_s = \frac{1}{20 f_{\text{max}}}; \qquad l_e = \frac{\lambda_{\text{min}}}{20} \tag{6.4.4}$$

Element size, $l_e$, is chosen to ensure that the FE discretization has at least 20 nodes per minimum wavelength. This discretisation is sufficiently adequate to avoid spatial aliasing and ensure the accuracy of higher harmonics [202]. The smaller the integration time step $t_s$, the better the accuracy of the numerical result. However, too small $t_s$ requires high calculation time and hence increases computational cost excessively. Therefore the Newmark integration time scheme is employed to strike a compromise between the time step and the computational size using 20 points per cycle of the highest frequency of interest [202].

After each solution step of the transient analysis, decision is made to decide whether to deactivate or reactivate the elements within the damage zone. The decision is based on the outcome of the element birth/death criterion presented in Algorithm 2.

## 6.5 Case studies

### 6.5.1 Experimental validation

The computational scheme exhibited in this study is applied in a cracked plate shown in Fig. 6.4. The plate, which is made of aluminium (whose material properties are presented in Table 6.1), is 1.2 m long, 0.7 m wide and 0.001 m thick. The fatigue crack is produced by machining a notch at 0.7 m from the left edge of the plate and runs transversely through the plate's width. The plate is then subjected to cyclic loading under a loading machine until a fatigue crack is developed at the notch site. A range

of cracks of different widths and depths are studied. The crack widths considered are within the range of 0.5 and 5.0 of the plate thickness at depths of 25% and 50% of the plate thickness.

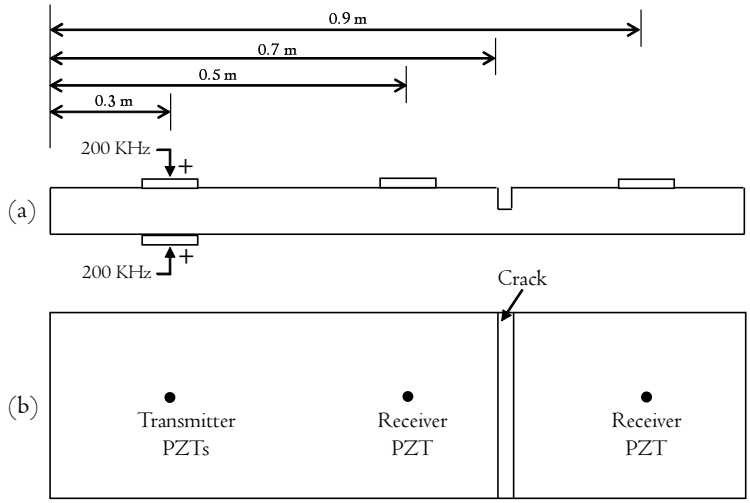


**Figure 6.4:** Schematic representation of the cracked plate set-up: (a) front view; (b) plan view

**Table 6.1:** Material properties of the materials used for the case studies presented in Sec. 6.5

| | Aluminium | Mild steel | Glass fibre |
|---|---|---|---|
| $\rho$ | 2600 kg/m$^3$ | 7800 kg/m$^3$ | 1400 kg/m$^3$ |
| $E_x$ | 68.95 GPa | 208 GPa | 45 GPa |
| $E_y$ | - | - | 16 GPa |
| $E_z$ | - | - | 16 GPa |
| $\nu_{xy}$ | 0.3 | 0.3 | 0.28 |
| $\nu_{yz}$ | - | - | 0.4 |
| $\nu_{xz}$ | - | - | 0.28 |
| $G_{xy}$ | - | - | 5.83 GPa |
| $G_{yz}$ | - | - | 5.79 GPa |
| $G_{xz}$ | - | - | 5.83 GPa |

In order to validate the presented scheme, the results derived through the scheme are compared against those obtained through experimental measurements and those of the WFE-FE methodology presented in [3].

The test rig set-up for the experimental measurements is shown in Fig. 6.5. At a given frequency, there exist at least two Lamb modes propagating through an aluminium plate [203]. However, single mode excitation and monitoring make wave

interaction measurement easier and more accurate without mixed-mode effect. Due to its simple and non-dispersive characteristics at low frequencies, the set-up is designed with the aim of exciting and receiving only symmetric Lamb wave mode. This is achieved by sticking two piezoelectric transducers (referred to as the transmitter PZT) on the double surface at the excitation point, with the two actuators having same coordinates as shown in Fig. 6.4. Exciting these two transmitter PZTs with the same input signal, symmetric mode will be generated, while the antisymmetric mode will be suppressed. Similar approach can be applied to excite only antisymmetric mode, but with the directions of the input signals in opposite sense to each other. Two additional piezoelectric transducers (referred to as the receiver PZT) are bonded on the plate at 0.5 m and 0.9 m to respectively receive the reflected and transmitted wave signals from the crack.

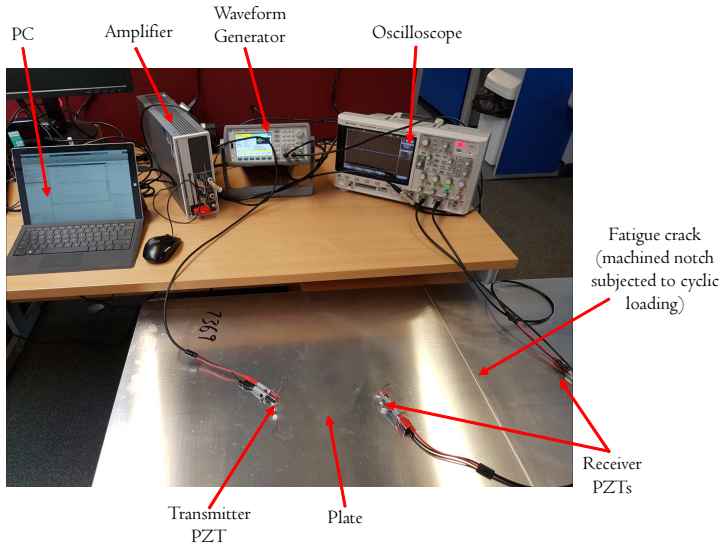


**Figure 6.5:** Assembly of the experimental configuration

The set-up system is composed of a dual channel Keysight 33512B arbitrary waveform generator, a Tabor 9200A high-voltage amplifier, with a gain factor of 40 dB, a DSOX2014A digital storage oscilloscope of sampling frequency 9.6 MHz and a PC. Circular radial mode piezoelectric transducers (Steminc part number: SMD07T02R412WL) are chosen to excite and register the guided waves. Each measurement correspond to average of 32 tests in order to reduce the system noise. Using the waveform generator, a 10 V peak-to-peak 5-cycle Hanning window modulated tone-burst voltage signal is generated and applied to the two transmitter PZTs. The centre frequency of the excitation tone-burst is 200 kHz. Upon the excitation, elastic waves are generated by the transmitter transducers and sent through the plate. The voltage output of the travelling waves are measured at the receiver PZT using the

oscilloscope. The PZT to the left side of the damage measures the reflected signal from the damage, while that to the right side of the damage measures the transmitted signal. The received signal is amplified and input to the oscilloscope for digital capture and display on the PC.

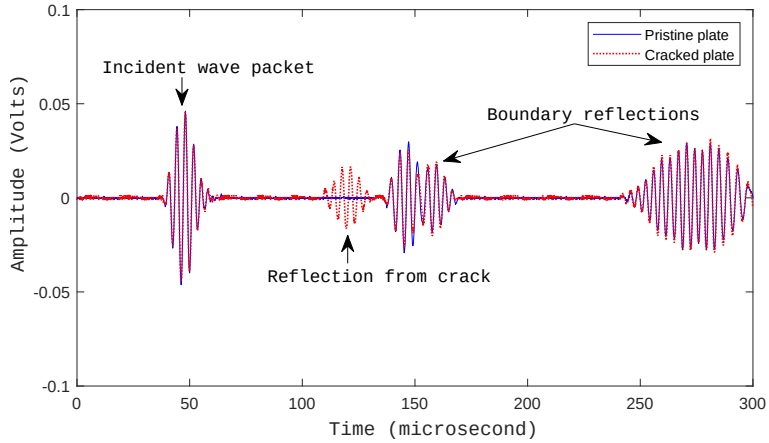


**Figure 6.6:** Superimposed experimental time record for pristine (-) and cracked (. . . ) plates. Crack is 0.5 mm deep and 2.5 mm wide

The waveform of the reflected output signal after interaction with the fatigue crack in the plate is presented in Fig. 6.6. The crack in this case is 0.5 mm deep and 2.5 mm wide. The output signal waveform is superimposed with that measured from the damage free (pristine) plate. It can be observed from Fig. 6.6 that, compared with the pristine plate waveform history, there exist a new wave packet generated in the damage plate waveform history. It therefore follows that the new signal packet is generated by an interaction of the travelling wave with the crack. Another evident difference is that the damaged plate signal has a slight phase shift and amplitude drop which can be attributed to energy leakage during generation of the new signal packet.

FFT of the measured responses is conducted to obtain the frequency spectral of the output signals. Unwanted signals such as the edge reflections are gated out during the FFT analysis. The wave reflection coefficient is therefore calculated by dividing the frequency spectrum of the reflected signal by that of the incident signal.

The superimposed results of the presented approach, experimental measurements and WFE-FE methodology [3] are shown in Fig. 6.7. The results present wave reflection coefficients, at fundamental frequency, as a function of the crack width for crack depths of 25% and 50% of the plate thickness. The crack width axis is normalised to the plate thickness, so that the results may be applied equally to other thicknesses of the plate provided that the frequency-thickness of 200 kHz-mm is also maintained. The reflection coefficient magnitude in each case increases with respect to the crack width until the crack has reached a width of about 3.0 of the plate thickness. Beyond this level, the

coefficient magnitude decreases with respect to the crack width until it tends towards zero value, and then increases again in a sinusoidal-like fashion.

As shown in Fig. 6.7, results obtained by the presented scheme agree very well with the experimental measurements with a maximum difference of about 6%. Compared with the WFE-FE predictions, the difference rises to about 18%. This difference can be attributed to energy leakage to higher harmonics in the nonlinear analysis. It should be noted that the WFE-FE model is a linear wave interaction analysis with no leakage of energy to harmonics generation. Hence, the difference.

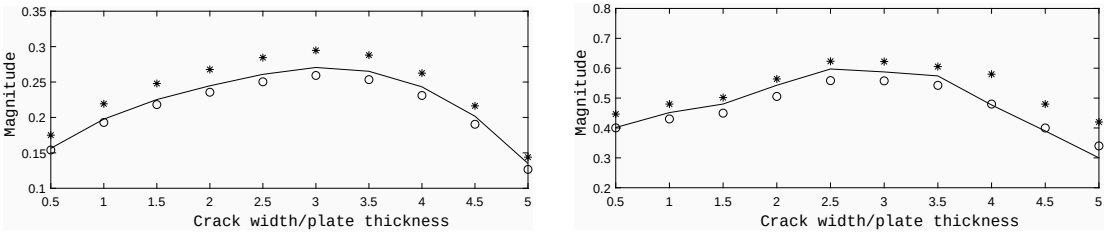


**(a)** 25% crack depth/plate thickness **(b)** 50% crack depth/plate thickness

**Figure 6.7:** Wave reflection coefficients from the crack as a function of the crack width/plate thickness: Current scheme (o), Experimental measurements (-), WFE-FE methodology [3] (*)

### 6.5.2 Numerical case studies

The capability of the presented methodology for computing wave interaction with nonlinear damage is exhibited in this section. Two different nonlinear damage cases, namely crack and delamination, are considered. In each case, pristine plate, plate with linear damage and plate with nonlinear damage are all considered in order to distinguish wave interaction phenomenon in each scenario of structural condition. Response of each failure mode to the interaction phenomenon is also being studied and analysed.

#### 6.5.2.1 Description and boundary condition of the model

A sandwich composite plate of thickness 2 mm and length $l_p = 1000$ mm is considered as shown in Fig. 6.8. The viscoelastic sandwich plate is made of a glass fibre core sandwiched between isotropic skins. The material properties of the plate's constituents are presented in Table 6.1). The thickness of the core $h_c = 1.6$ mm while that of each skin $h_s = 0.2$ mm. Piezoelectric sensors, each of length 7 mm and thickness 0.2 mm, are bonded on the plate as shown in Fig. 6.8. Material properties of the piezoelectric are presented in Table 6.2).

FE calculations are performed in two-dimensional domain using rectangular plane

**Table 6.2:** Material properties of the piezoelectric sensor used for the case studies presented in Sec. 6.5.2

| Parameter | Value | Unit |
|---|---|---|
| Density | $\rho = 7750$ | $\mathrm{kg/m^3}$ |
| Loss tangent | $\tan\delta = 0.02$ | - |
| Elastic flexibility | $S_{11} = S_{33} = 16.4$ | $10^{-12}\ \mathrm{m^2/N}$ |
| | $S_{22} = 18.8$ | |
| | $S_{12} = S_{21} = -7.22$ | |
| | $S_{13} = S_{31} = -5.74$ | |
| | $S_{23} = S_{32} = -7.22$ | |
| | $S_{44} = S_{55} = 47.5$ | |
| | $S_{66} = 44.3$ | |
| Piezoelectric strain coefficients | $d_{21} = -1.71$ | $10^{-10}\ \mathrm{m/V}$ |
| | $d_{22} = 3.74$ | |
| | $d_{23} = -1.71$ | |
| | $d_{14} = 5.84$ | |
| | $d_{35} = 5.84$ | |
| Electric permittivity | $\varepsilon_{11} = 2.12$ | $10^{-8}\ \mathrm{F/m}$ |
| | $\varepsilon_{22} = 1.75$ | |
| | $\varepsilon_{33} = 2.12$ | |

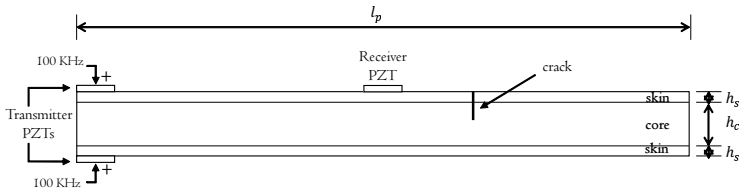


**(a)** Plate with crack

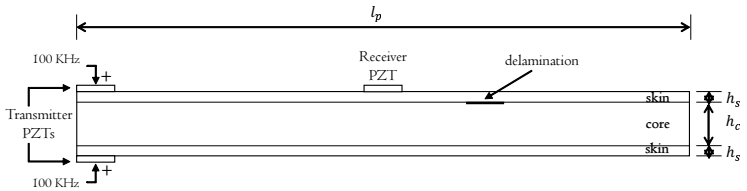


**(b)** Plate with delamination

**Figure 6.8:** FE modelling configuration for sandwich plate with (a) crack and (b) delamination

strain elements. Eq. (2.1.12) is solved for the wave propagation constants. Two propagating waves, longitudinal (symmetric mode) and bending (antisymmetric mode), are obtained. The WFE calculated displacement mode shapes of the propagating waves in the in-plane and out-of-plane directions are presented in Fig. 6.9.

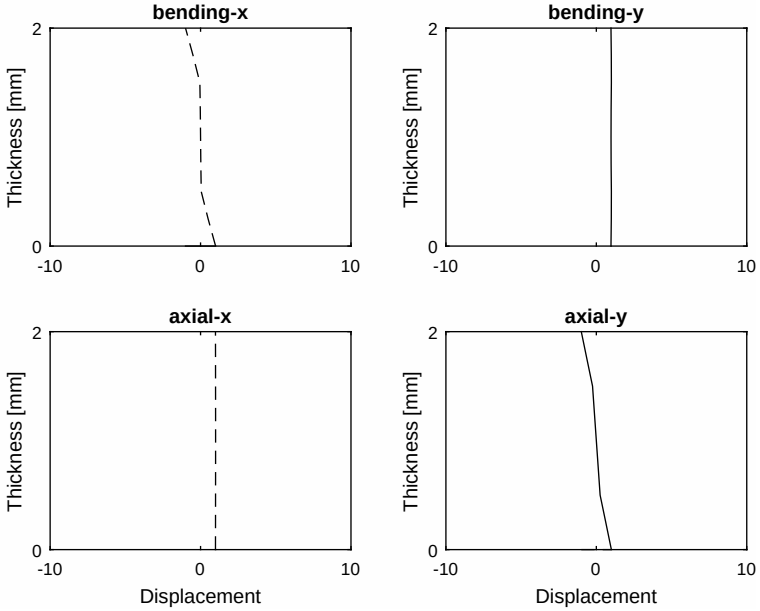


**Figure 6.9:** Mode shapes of the propagating waves in the sandwich plate at 100 kHz; left column: in-plane, right column: out-of-plane.

#### 6.5.2.2 Pristine plate

The plate in its undamaged state is first considered as a baseline for other conditions of the plate to be considered.

Fig. 6.10 presents the calculated time history of the signal, obtained at the receiver PZT, for the undamaged plate. As observed, there exist a single wavelet in the predicted response which suggests that the wave interact with no form of damage/discontinuities during propagation along the plate. The frequency spectrum (as shown in Figs. 6.12 and 6.16) of the wavelet also gives only the fundamental frequency component which ascertain the absence of any form of nonlinearity in the pristine plate.

#### 6.5.2.3 Interaction with crack

In order to exhibit the effect of crack severity on the wave interaction phenomenon, interaction coefficients are obtained as a function of the crack depths. Crack depths considered include 0.2, 0.4, 0.6, 0.8, 1.0, 1.2, 1.4 and 1.6 (all in millimetre). These correspond to 0.1 to 0.8 of the plate thickness. The crack severity is scaled to normalise the crack depth to the plate thickness, so that the results obtained can be applied equally

to other thicknesses of the plate provided that the frequency-thickness of 200 kHz-mm is satisfied.

In each case, the crack is situated at 600 mm from the transmitter PZT, and reflection from the crack-damage interaction is received at the receiver PZT located 100 mm away from the crack. The configuration is as shown in Fig. 6.8a.

As earlier informed, calculations are made for plate with linear crack and plate with nonlinear crack in order to distinguish wave interaction phenomenon in each scenario of structural condition.

#### 6.5.2.3.1 Interaction with linear crack

Guided wave interaction with linear crack within the sandwich plate is considered in this section. In this case, the crack opens throughout the calculation window. That is, elements within the crack zone are deactivated/dead throughout.

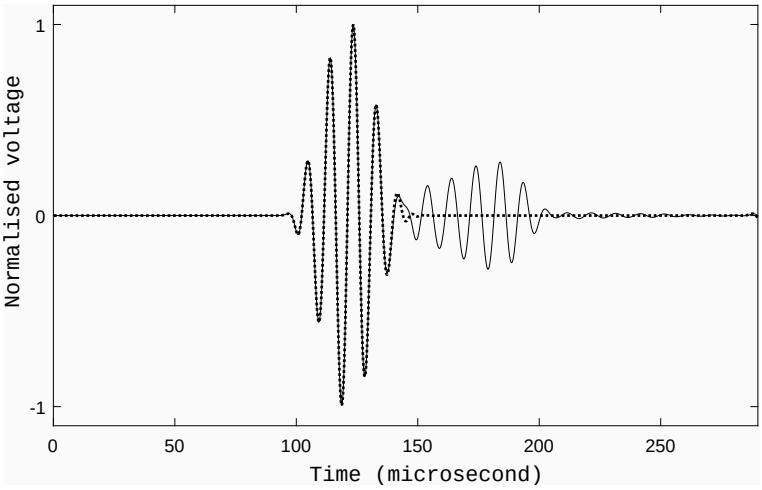


**Figure 6.10:** Superimposed time history predictions for the pristine plate ($\cdots$) and the plate with linear crack (-)

The time domain response of the plate with linear crack is presented in Fig. 6.10. Compared to the pristine plate, there exist two wavelets; the incident wavelet and the wavelet reflected from the wave-crack interaction phenomenon. The presence of the reflected wavelet is an indication of damage, in the structural waveguide, which interact with the wave during propagation. This confirms the capability of the developed scheme in detecting structural damage.

Fig. 6.12 presents the frequency spectral for the incident wavelet (Fig. 6.12a), when the reflected wavelet ($t \geq 145\ \mu s$) is gated out, and for the reflected wavelet (Fig. 6.12b), when the incident wavelet ($t \leq 145\ \mu s$) is gated out. However, as in the pristine plate, there exist spectrum component for only the fundamental frequency for both the incident and the reflected wavelets. The absence of harmonics signifies an absence of

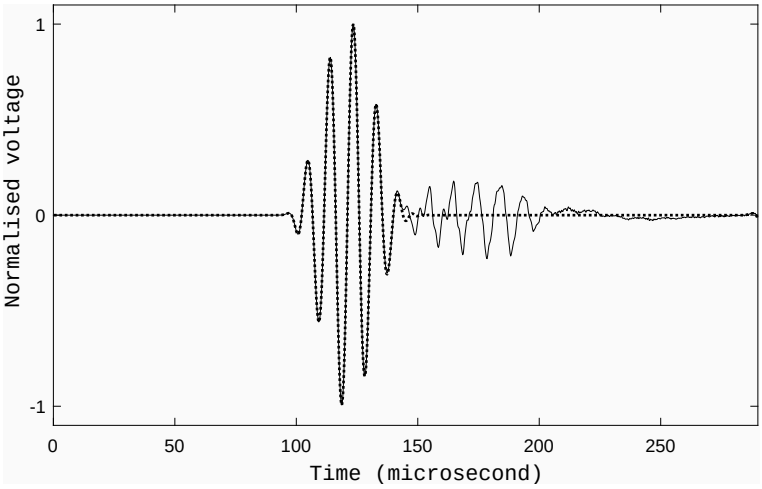


**Figure 6.11:** Superimposed time history predictions for the pristine plate (· · · ) and the plate with nonlinear crack (-)

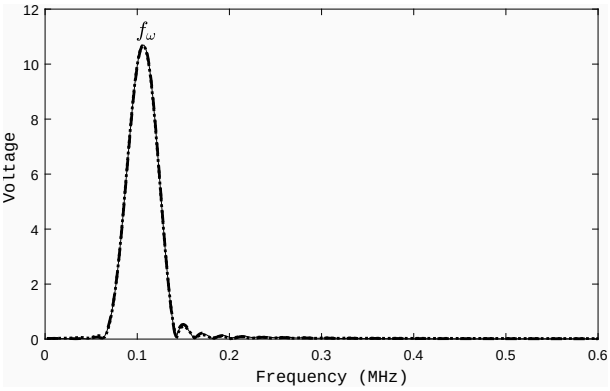


**(a)** Incident signal

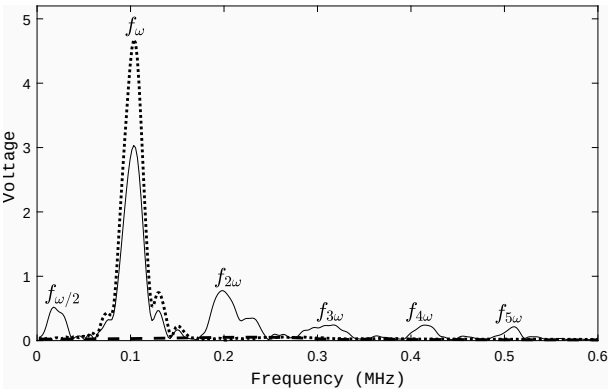


**(b)** Reflected signal

**Figure 6.12:** Superimposed frequency spectral of the incident and the reflected wavelets: pristine plate (- -); plate with linear crack (· · · ); plate with nonlinear crack (-)

nonlinearity in the waveguide with linear crack.

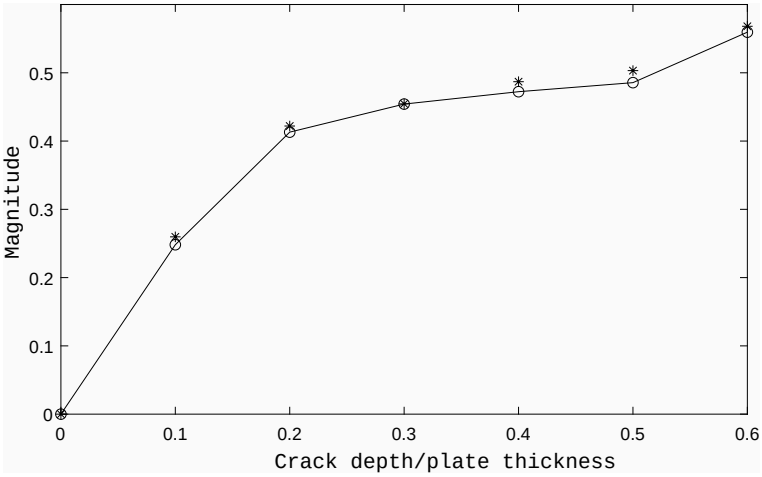


**Figure 6.13:** Wave interaction reflection coefficients for the plate with linear crack: present methodology (-o); computation as in [3] ($*$)

The wave interaction reflection coefficient is estimated by dividing the reflected response signal by the incident response signal. Fig. 6.13 presents the reflection coefficients for the damage interaction in the linear domain. In order to further validate the presented methodology, the results presented are compared against the approach presented in [3] for a sandwich plate with linear structural crack. Excellent agreement is observed for the wave interaction coefficients obtained by both methodologies.

#### 6.5.2.3.2 Interaction with nonlinear crack

Guided wave interaction with clapping (nonlinear) crack within the sandwich plate is considered in this section. In this case, the crack opens and closes under tension and compression respectively.

The time history of the response obtained for the plate with nonlinear crack at crack depth 0.3 of the plate thickness is presented in Fig. 6.11. Similar to the linear crack case, the response signal contains two wavelets; incident and reflected packets. But unlike the linear case, the reflected wave packet shows distortion along its path. This is due to contact acoustic nonlinearity within the waveguide.

Fig. 6.12 shows the frequency spectral for the incident wavelet (Fig. 6.12a) and the reflected wavelet (Fig. 6.12b) when the reflected and incident wavelets are respectively gated out. Compared to the linear case, the nonlinear wave interaction gives not only the fundamental frequency spectrum components but also sub and higher harmonic components up to the fifth harmonic. The presence of harmonic components is a significant indication of the presence of nonlinearity in the system. It should be noted that the amplitude of the spectrum at fundamental frequency is lower in the nonlinear case

compared to the linear case. This is as a result energy leaking to higher harmonics in the nonlinear case. It should also be noted that the spectrum of the incident wave is purely linear (even for the nonlinear case), i.e. no generation of harmonics. This is as expected because the wave has not interacted with the nonlinear crack at that stage.

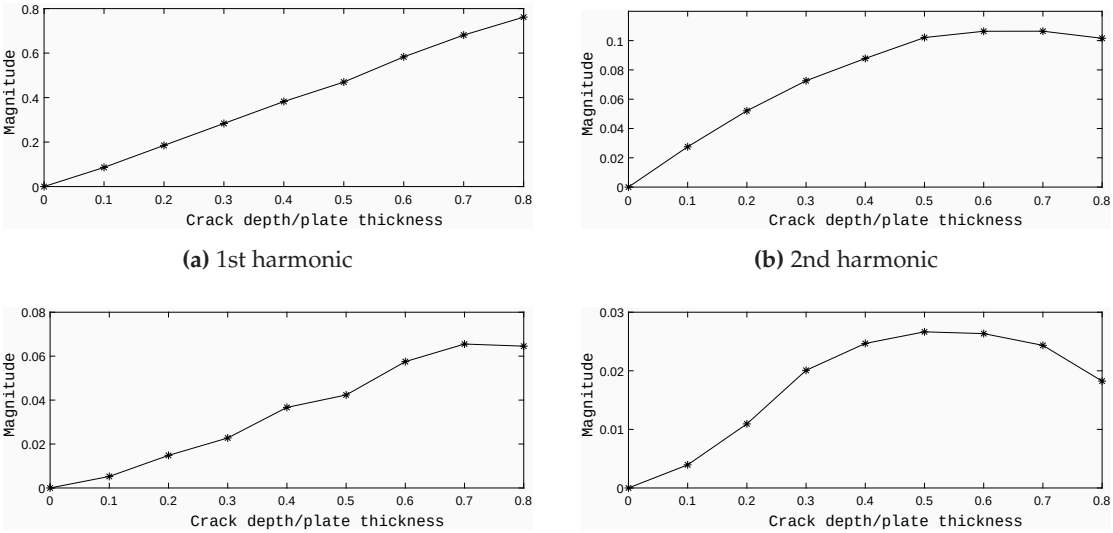


**(a)** 1st harmonic **(b)** 2nd harmonic

**(c)** 3rd harmonic **(d)** 4th harmonic

**Figure 6.14:** Wave interaction reflection coefficients for the plate with nonlinear crack at different harmonic frequencies

The results of the fundamental and higher harmonic wave reflection coefficients as a function of the crack severity are presented in Fig. 6.14.

As expected, due to energy dissipation of the wave to generate higher harmonics, it is observed that the reflection coefficients reduces as the harmonic frequency increases. Reflection coefficient of about 0.76 is obtained at the fundamental harmonic, compared to 0.11, 0.066 and 0.027 obtained at the second, third and fourth harmonics respectively.

Except at fundamental frequency where the trend is almost linear with respect to the crack severity, the dependence of the reflection coefficient on the crack severity follows a quarter-sinusoidal profile. In each case, the reflection coefficient increases with the crack severity until about a crack severity of 0.7 of the plate thickness where the reflection coefficient starts reducing against the crack severity. The outcome of the wave reflection coefficient relationship with crack severity can, in principle, be used as an indicator for early monitoring and detection of a crack. This outcome can also be used to measure the span of a crack.

#### 6.5.2.4 Interaction with delamination

In this case, interaction of guided wave with skin-core delamination is considered. Calculations are made for plate with linear crack and plate with nonlinear crack in order

to distinguish wave interaction phenomenon in each scenario of structural condition.

In order to exhibit the effect of the delamination severity on the wave interaction phenomenon, interaction coefficients are obtained as a function of the delamination widths. Delamination widths of 0.2, 0.4, 0.6, 0.8, 1.0, 1.2, 1.4 and 1.6 (all in millimetre) are considered. These correspond to 0.1 to 0.8 of the plate thickness. The delamination severity is scaled to normalise the delamination width to the plate thickness, so that the results obtained can be applied equally to other thicknesses of the plate provided that the frequency-thickness of 200 kHz-mm is satisfied.

In each case, the delamination is situated at 600 mm from the transmitter PZT, and reflection from the guided wave interaction with the delamination is received at the receiver PZT located 100 mm away from the delamination. The configuration is as shown in Fig. 6.8b.

It should be noted that similar parameters and configurations used in the crack case are used in this case. This is done in order to directly compare and contrast results in both cases and exhibit the developed methodology as a damage identification tool.

#### 6.5.2.4.1 Interaction with linear delamination

Guided wave interaction with linear delamination within the sandwich plate is considered in this section. As a linear analysis, the plate remains delaminated throughout the calculation window.

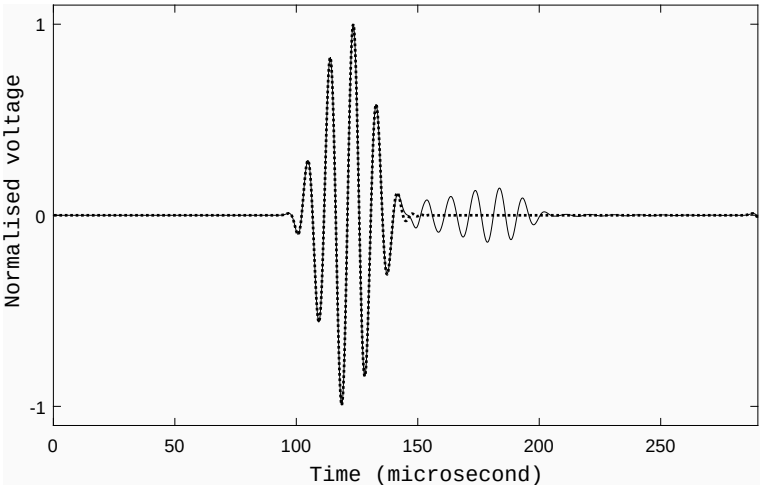


**Figure 6.15:** Superimposed time history predictions for the pristine plate (· · ·) and the plate with linear delamination (-)

Fig. 6.15 presents the time domain response of the guided wave interaction with linear delamination within the plate superimposed with the time history obtained for the pristine plate.

The pristine plate response contains only the incident wavelet while the plate with

linear delamination contains incident and reflected wavelets. The presence of the reflected wavelet is an indication of damage, in the structural waveguide, which interact with the guided wave during propagation. This establish the application of the developed scheme for damage detection.

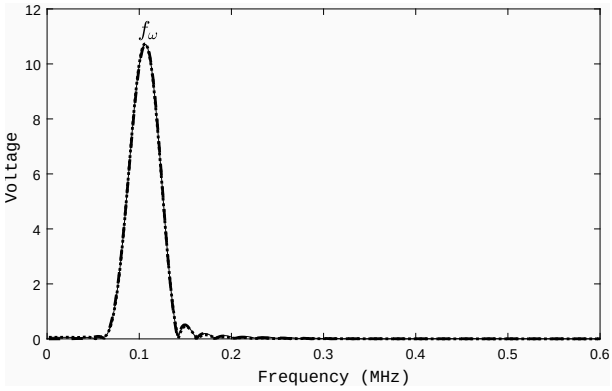


**(a)** Incident signal

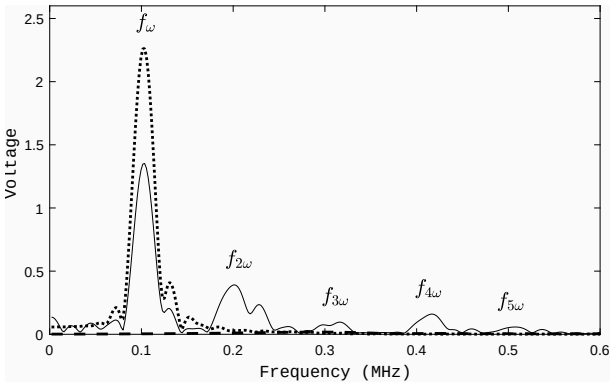


**(b)** Reflected signal

**Figure 6.16:** Superimposed frequency spectral of the incident and the reflected wavelets: pristine plate (- -); plate with linear delamination ($\cdots$); plate with nonlinear delamination (-)

The frequency spectrum of the incident wavelet, in the time history (Fig. 6.15) of the plate with linear delamination, when the reflected wavelet ($t \geq 145\ \mu s$) is gated out is shown Fig. 6.16a. As expected, the incident wave spectrum of the pristine plate and that of the plate with linear delamination are equal. The frequency spectrum of the reflected wavelet when the incident wavelet ($t \leq 145\ \mu s$) is gated out is shown in Fig. 6.16b. As observed, there exist spectrum component for only the fundamental harmonic. The absence of higher harmonics confirms the absence of nonlinearity in the plate with linear delamination.

#### 6.5.2.4.2 Interaction with nonlinear delamination

Guided wave interaction with nonlinear delamination within the sandwich plate is considered in this section. Based on the developed scheme, the clapping delamination opens and closes under tension and compression respectively.

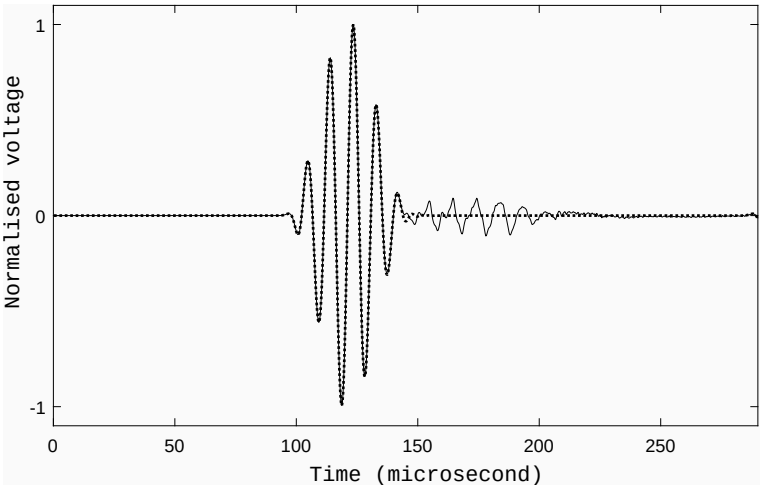


**Figure 6.17:** Superimposed time history predictions for the pristine plate ($\cdots$) and the plate with nonlinear delamination (-)

The time history of the response obtained for the plate with nonlinear delamination at delamination width 0.3 of the plate thickness is presented in Fig. 6.17. It is superimposed with the time history of the response obtained for the pristine plate.

Similar to the response obtained for the plate with linear delamination, the response contains two wave packets; incident and reflected packets. But unlike the linear case, the reflected wave packet of the nonlinear case shows distortion along its path. This is due to contact acoustic nonlinearity within the nonlinear system. The presence of the distorted reflected wave package is an indication of not just a damage but a nonlinear damage in the structural waveguide.

The frequency spectrum of the incident wave package and that of the reflected wave package, when the reflected ($t \geq 145\ \mu s$) and incident ($t \leq 145\ \mu s$) wave packages are respectively gated out, are presented in Fig. 6.16 for the sandwich plate with nonlinear delamination. The results presented are superimposed with that of the pristine plate and the plate with linear delamination. As observed from the presented results, the frequency spectrum of the incident wave equals to those obtained for the pristine plate as well as the plate with linear delamination. It should be noted that the spectrum is purely linear, i.e. no generation of harmonics is observed. This is because the wave has not interacted with the nonlinear delamination at that stage. However, the frequency spectrum of the reflected wave generates harmonic components up to the fifth harmonics. The presence of harmonic components in the frequency spectrum is a significant

indication of the presence of nonlinearity in the system. It should also be noted that the amplitude of the spectrum component at fundamental frequency is lower in the nonlinear case compared to the linear case. This is as a result energy leaking to higher harmonics in the nonlinear case.

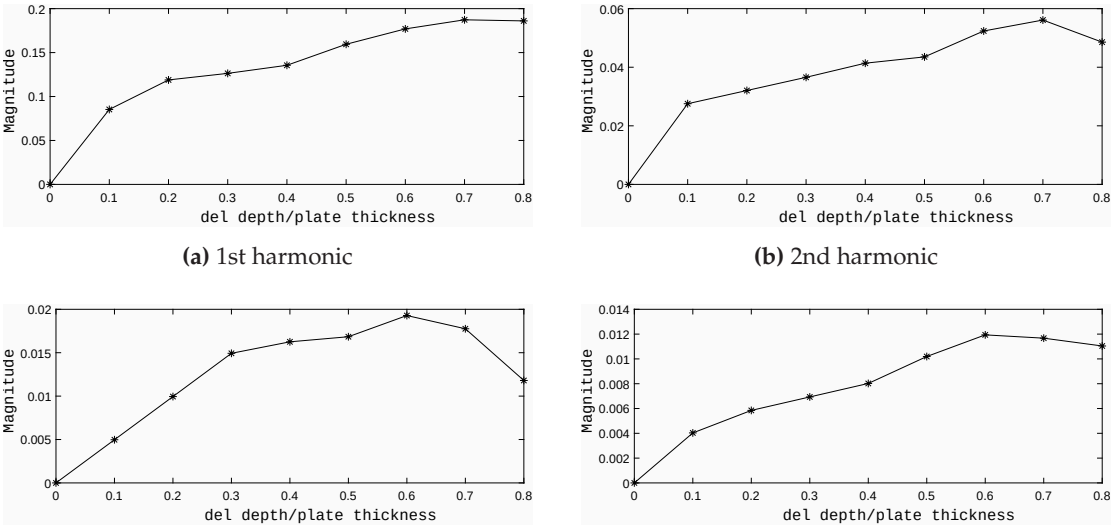


**(a)** 1st harmonic

**(b)** 2nd harmonic

**(c)** 3rd harmonic

**(d)** 4th harmonic

**Figure 6.18:** Wave interaction reflection coefficients for the sandwich plate with nonlinear delamination at different harmonic frequencies

The results of the harmonic wave reflection coefficients, generated for the guided wave interaction with nonlinear delamination in the sandwich plate, as a function of the delamination severity are presented in Fig. 6.18.

As expected, due to energy dissipation of the wave to generate higher harmonics, it is observed that the reflection coefficients reduces as the harmonic frequency increases. Reflection coefficient of about 0.19 is obtained at the fundamental harmonic, compared to 0.056, 0.019 and 0.012 obtained at the second, third and fourth harmonics respectively. In relation to the delamination width severity, the reflection coefficient follows a quarter-sinusoidal profile. In each case, the reflection coefficient increases with the delamination severity until delamination of an average width of 0.7 of the plate thickness where the reflection coefficient starts reducing against the delamination severity. The outcome of the wave reflection coefficient relationship with delamination severity could, in principle, be used as an indicator for early monitoring and detection of a delamination. This outcome could also be used to measure the span of a delamination.

Having demonstrated the application of the developed scheme in detecting LNSD of different modes, it is essential to exhibit the applicability of the scheme in classifying/identifying the damage modes using the calculated harmonic reflection coefficients. Two modes (of different orientations) of the most common localised damage

modes in periodic structures are considered; crack and delamination.

As presented and discussed above, the harmonic reflection coefficients of both damage modes follow similar relationship with respect to the span of the damage. However, as observed from the results, the reflection coefficient magnitudes are obviously different at various harmonic frequencies generated. Peak reflection coefficient magnitude of about 0.76 is obtained for the guided wave interaction with crack at fundamental harmonic compared to 0.19 obtained for interaction with delamination. Similarly, 0.11, 0.066 and 0.027 are obtained at second, third and fourth harmonics respectively for interaction with crack compared to 0.056, 0.019 and 0.012 respectively obtained for interaction with delamination. These depict an average difference of about 62% between the results obtained for the wave interaction with crack and that of delamination. Based on these outcomes, it is evident that the developed methodology can be applied to detect and quantify nonlinear structural damage in composite structures and classify them into specific mode type.

## 6.6 Conclusions

A WFE-based computational scheme for analysing and quantifying wave interaction with nonlinear damage in composite structure is presented in this chapter. The scheme can be applied to structures of arbitrary complexity, layering and material characteristics as an FE discretisation is employed. The scheme applies the WFE computed wave modes as time-dependent harmonic boundary conditions, using transient piezoelectrically generated ultrasonic wave, on the plate and is able to compute the generation of wave harmonics for each excited wave. The principal contributions of the work can be summarised as

(i) The presented scheme successfully models nonlinear damage using an element birth and death criterion in a commercial FE software.

(ii) The scheme is able to impose specific guided wave mode without a mix-mode effect due to the WFE-obtained mode displacement being employed.

(iii) The scheme successfully models wave propagation and interaction with nonlinear damage within a structural medium. As demonstrated through the obtained incident and reflected wave packets, the property of the wave remains linear until interaction with the nonlinearity within the medium. Upon interaction with the nonlinear damage, wave property becomes nonlinear with generation of harmonic reflected wave packets.

(iv) The scheme is also able to compute sub and super harmonic reflection coefficients for the guided wave interaction with nonlinear structural damage. Results obtained through the developed methodology are validated with experimental measurements and results presented in open literature for guided wave interaction with damage. Good agreement is obtained among the results.

(v) The dependence of the wave interaction coefficients on the severity of the nonlinear damage is analysed using crack and delamination as case studies.

(vi) The application of the developed scheme in classifying and identifying the detected damage mode using the quantified harmonic reflection coefficients is also demonstrated.

# CHAPTER 7

# Wave propagation and interaction with damage in two-dimensional periodic multilayered structures

## 7.1 Introduction

Advancements in computational tools development has resulted in significant increase in the application of model-based approaches to detect, analyse and classify damage in structures. Implementing a suitable modelling technique for this purpose has hence become an important aspect of Structural Health Monitoring (SHM). The FEM is one of the most commonly employed modelling techniques. However, to detect small sized damage, especially at high frequency, a very fine mesh density is needed which results in a very large sized model. This makes FEM computationally expensive for this purpose. Wave-based modelling techniques are computationally affordable, especially for simple structures, because they require low computational resources. Thus, they are preferred for problems where FEM becomes computationally large. For arbitrarily complex structures, such as composite structures or structural networks, a WFE approach is introduced in Mead [104], Mace et al. [105].

WFE method has shown great efficiency and versatility in its applications to various structural problems. However, very few of these applications considered two-dimensional structures. Wave propagation in two-dimensional structures using the WFE method is introduced in Manconi and Mace [106]. It is extended in Mitrou et al. [116], using the hybrid WFE-FE approach [3], to compute wave scattering from different joints in a coupled monolayered structures. In order to implement localised damage and compute wave scattering from the damage, the coupled structures have to be multilayered. This prompted the essence of the work hereby presented.

The contribution of the work presented in this chapter is development of a WFE based numerical scheme for quantifying wave interaction with localised structural damage within two-dimensional multi-layer composite structures having arbitrary layering, complexities and material characteristics. The scheme discretises a damaged structural medium into a system of $N$ healthy substructures (waveguides) connected through a joint which bears the localised structural damage/discontinuity. Wave propagation constants along different directions of the substructures are sought by combining periodic structure theory with the FE method. The damaged joint is modelled using a standard FE approach, ensuring joint-substructures mesh conformity. This is coupled to the obtained wave propagation constants in order to determine scattering coefficients of the wave interaction with damage in different propagation directions of the structure. Wave interaction coefficients for different damage modes and parameters are analysed in order to establish an optimum basis for detecting and identifying damage, as well as assessing the orientation and extent of the damage.

## 7.2 Wave propagation in two-dimensional composite structure

### 7.2.1 Statement of the problem

Elastic wave propagation is considered in the $x$ and $y$ directions of an arbitrarily layered composite structure. Periodicity condition is hence considered in the $x$ and $y$ directions. A segment of the structure is modelled, using a commercial FE software, as shown in Fig. 7.1.

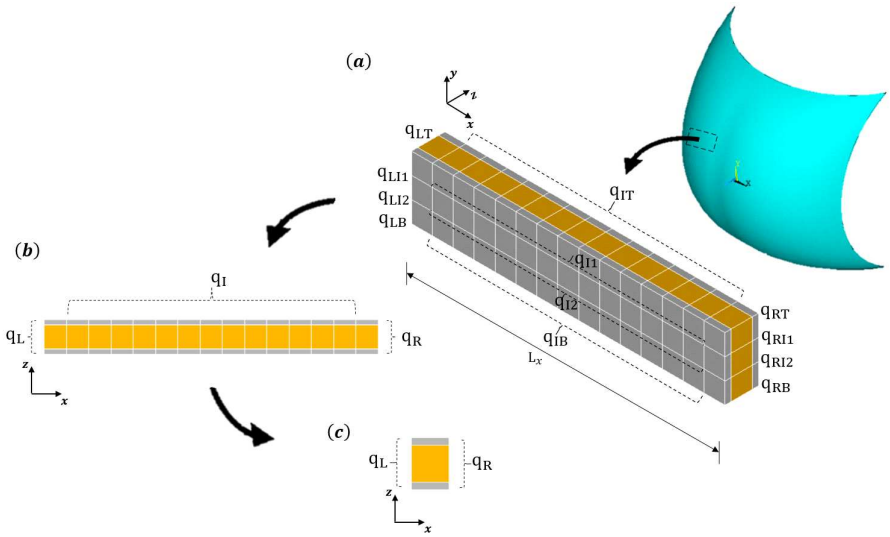


**Figure 7.1:** FE-modelled periodic segment of an arbitrarily layered two-dimensional composite structure

The stiffness, mass and damping matrices of the segment **K**, **M** and **C** are extracted

using classical FEM algorithm as presented in Appendix A. The nodal displacements $\mathbf{q}$ and forces vectors $\mathbf{f}$ are reordered according to a predefined sequence such as

$$\begin{aligned}\mathbf{q} &= \{\mathbf{q}_{LT}\ \mathbf{q}_{IT}\ \mathbf{q}_{RT}\ \mathbf{q}_{LI1}\ \mathbf{q}_{I1}\ \mathbf{q}_{RI1}\ \mathbf{q}_{LI2}\ \mathbf{q}_{I2}\ \mathbf{q}_{RI2}\ \mathbf{q}_{LB}\ \mathbf{q}_{IB}\ \mathbf{q}_{RB}\}^\top \\ \mathbf{f} &= \{\mathbf{f}_{LT}\ \mathbf{f}_{IT}\ \mathbf{f}_{RT}\ \mathbf{f}_{LI1}\ \mathbf{f}_{I1}\ \mathbf{f}_{RI1}\ \mathbf{f}_{LI2}\ \mathbf{f}_{I2}\ \mathbf{f}_{RI2}\ \mathbf{f}_{LB}\ \mathbf{f}_{IB}\ \mathbf{f}_{RB}\}^\top\end{aligned} \tag{7.2.1}$$

where $I$ corresponds to internal, $LI$, $RI$ the interface edge, $IT$, $IB$ the interface top and base and $LT$, $RT$, $LB$, $RB$ the interface corner indices.

### 7.2.2 PST formulation of the segment's equation of motion

The time harmonic equation of motion of the modelled segment, assuming uniform and structural damping for all the DoFs, can be written as

$$[\mathbf{K} + \mathrm{i}\omega\mathbf{C} - \omega^2\mathbf{M}]\mathbf{q} = \mathbf{f} \tag{7.2.2}$$

where $\omega$ is the angular frequency and $\mathbf{f}$ is the nodal forces vector. The DSM can then be expressed as

$$\mathbf{D} = \mathbf{K}(1 + \mathrm{i}\eta) - \omega^2\mathbf{M} \tag{7.2.3}$$

where $\eta$ is the structural damping coefficient ($\mathbf{C} = \frac{\eta\mathbf{K}}{\omega}$). The equation of motion (Eq. (7.2.2)) is therefore expressed as

$$\mathbf{D}\mathbf{q} = \mathbf{f} \tag{7.2.4}$$

A practical procedure for extracting the wave propagation characteristics of the segment is injecting a set of assumed propagation constants $\varepsilon_x$ or $\varepsilon_y$. The set of these constants can be chosen in relation to the direction of propagation towards which the wavenumbers are to be sought and according to the desired resolution of the wavenumber curves. In this study, propagation constants are injected along $y$ axis and propagation characteristics are sought along $x$ axis by transforming Eq. (7.2.4) into a standard eigenvalue problem with $x$ as the direction of wave propagation.

Applying the Bloch's theorem under the assumption of a time harmonic response, the displacements at each periodic edge along the axis of wave injection ($y$ axis) can be expressed as a function of the displacements at one edge. Using the edge with indices $LB$, $IB$ and $RB$ as the edge of reference, then

$$\begin{aligned}\mathbf{q}_{LT} &= \mathrm{e}^{-\mathrm{i}\varepsilon_y}\mathbf{q}_{LB},\ \ \mathbf{q}_{IT} = \mathrm{e}^{-\mathrm{i}\varepsilon_y}\mathbf{q}_{IB},\ \ \mathbf{q}_{RT} = \mathrm{e}^{-\mathrm{i}\varepsilon_y}\mathbf{q}_{RB} \\ \mathbf{q}_{LI1} &= \mathrm{e}^{-\mathrm{i}\frac{2}{3}\varepsilon_y}\mathbf{q}_{LB},\ \ \mathbf{q}_{I1} = \mathrm{e}^{-\mathrm{i}\frac{2}{3}\varepsilon_y}\mathbf{q}_{IB},\ \ \mathbf{q}_{RI1} = \mathrm{e}^{-\mathrm{i}\frac{2}{3}\varepsilon_y}\mathbf{q}_{RB} \\ \mathbf{q}_{LI2} &= \mathrm{e}^{-\mathrm{i}\frac{1}{3}\varepsilon_y}\mathbf{q}_{LB},\ \ \mathbf{q}_{I2} = \mathrm{e}^{-\mathrm{i}\frac{1}{3}\varepsilon_y}\mathbf{q}_{IB},\ \ \mathbf{q}_{RI2} = \mathrm{e}^{-\mathrm{i}\frac{1}{3}\varepsilon_y}\mathbf{q}_{RB}\end{aligned} \tag{7.2.5}$$

Using same theorem, the corresponding force vectors can be expressed as

$$\begin{aligned} \mathbf{f}_{LT} =& \mathrm{e}^{-\mathrm{i}\varepsilon_y}\mathbf{f}_{LB},\ \ \mathbf{f}_{IT} =\mathrm{e}^{-\mathrm{i}\varepsilon_y}\mathbf{f}_{IB},\ \ \mathbf{f}_{RT} =\mathrm{e}^{-\mathrm{i}\varepsilon_y}\mathbf{f}_{RB} \\ \mathbf{f}_{LI1} =& \mathrm{e}^{-\mathrm{i}\frac{2}{3}\varepsilon_y}\mathbf{f}_{LB},\ \ \mathbf{f}_{I1} =\mathrm{e}^{-\mathrm{i}\frac{2}{3}\varepsilon_y}\mathbf{f}_{IB},\ \ \mathbf{f}_{RI1} =\mathrm{e}^{-\mathrm{i}\frac{2}{3}\varepsilon_y}\mathbf{f}_{RB} \\ \mathbf{f}_{LI2} =& \mathrm{e}^{-\mathrm{i}\frac{1}{3}\varepsilon_y}\mathbf{f}_{LB},\ \ \mathbf{f}_{I2} =\mathrm{e}^{-\mathrm{i}\frac{1}{3}\varepsilon_y}\mathbf{f}_{IB},\ \ \mathbf{f}_{RI2} =\mathrm{e}^{-\mathrm{i}\frac{1}{3}\varepsilon_y}\mathbf{f}_{RB} \end{aligned} \tag{7.2.6}$$

where

$$\varepsilon_y = k_y L_y \tag{7.2.7}$$

Expressing Eq. (7.2.5) in tensorial form gives

$$\mathbf{q} = \mathbf{R}_T \left\{\mathbf{q}_{LB}\ \ \mathbf{q}_{IB}\ \ \mathbf{q}_{RB}\right\}^\top \tag{7.2.8}$$

where

$$\mathbf{R}_T = \begin{bmatrix} \lambda_y\mathbf{I} & \mathbf{0} & \mathbf{0} \\ \mathbf{0} & \lambda_y\mathbf{I} & \mathbf{0} \\ \mathbf{0} & \mathbf{0} & \lambda_y\mathbf{I} \\ \lambda_y^{\frac{2}{3}}\mathbf{I} & \mathbf{0} & \mathbf{0} \\ \mathbf{0} & \lambda_y^{\frac{2}{3}}\mathbf{I} & \mathbf{0} \\ \mathbf{0} & \mathbf{0} & \lambda_y^{\frac{2}{3}}\mathbf{I} \\ \lambda_y^{\frac{1}{3}}\mathbf{I} & \mathbf{0} & \mathbf{0} \\ \mathbf{0} & \lambda_y^{\frac{1}{3}}\mathbf{I} & \mathbf{0} \\ \mathbf{0} & \mathbf{0} & \lambda_y^{\frac{1}{3}}\mathbf{I} \\ \mathbf{I} & \mathbf{0} & \mathbf{0} \\ \mathbf{0} & \mathbf{I} & \mathbf{0} \\ \mathbf{0} & \mathbf{0} & \mathbf{I} \end{bmatrix} \tag{7.2.9}$$

with

$$\lambda_y = \mathrm{e}^{-\mathrm{i}\varepsilon_y} \tag{7.2.10}$$

$\mathbf{R}_T$ is the transformation matrix for expressing the displacements at each periodic edge as a function of the displacements at the reference edge.

Assuming equilibrium along the reference edge, Eq. (7.2.6) can also be expressed in tensorial form as

$$\mathbf{R}_T^*\ \ \mathbf{f} = \left\{\mathbf{f}_{LB}\ \ \mathbf{f}_{IB}\ \ \mathbf{f}_{RB}\right\}^\top \tag{7.2.11}$$

where $\mathbf{R}_T^*$, which is a Hermitian transpose of $\mathbf{R}_T$, is the transformation matrix for the forces vector.

Substituting Eqs. (7.2.8) and (7.2.11) into Eq. (7.2.4) gives a reformulated standard equation of motion as

$$[\mathbf{R}_T^* \mathbf{K} \mathbf{R}_T + \mathrm{i}\omega \mathbf{R}_T^* \mathbf{C} \mathbf{R}_T - \omega^2 \mathbf{R}_T^* \mathbf{M} \mathbf{R}_T] \begin{Bmatrix} \mathbf{q}_{LB} \\ \mathbf{q}_{IB} \\ \mathbf{q}_{RB} \end{Bmatrix} = \begin{Bmatrix} \mathbf{f}_{LB} \\ \mathbf{f}_{IB} \\ \mathbf{f}_{RB} \end{Bmatrix} \tag{7.2.12}$$

The modelled periodic segment, as shown in Fig. 7.1, has three periodic segments along the axis of wave injection (i.e. $y$ axis). Generally, for a periodic segment with $n$ periodic layers along the axis of wave injection, the transformation matrix is expressed as

$$\mathbf{R}_T = \begin{bmatrix} \lambda_y^{\frac{n}{n}}\mathbf{I} & \mathbf{0} & \mathbf{0} \\ \mathbf{0} & \lambda_y^{\frac{n}{n}}\mathbf{I} & \mathbf{0} \\ \mathbf{0} & \mathbf{0} & \lambda_y^{\frac{n}{n}}\mathbf{I} \\ \lambda_y^{\frac{n-1}{n}}\mathbf{I} & \mathbf{0} & \mathbf{0} \\ \mathbf{0} & \lambda_y^{\frac{n-1}{n}}\mathbf{I} & \mathbf{0} \\ \mathbf{0} & \mathbf{0} & \lambda_y^{\frac{n-1}{n}}\mathbf{I} \\ \lambda_y^{\frac{n-2}{n}}\mathbf{I} & \mathbf{0} & \mathbf{0} \\ \mathbf{0} & \lambda_y^{\frac{n-2}{n}}\mathbf{I} & \mathbf{0} \\ \mathbf{0} & \mathbf{0} & \lambda_y^{\frac{n-2}{n}}\mathbf{I} \\ \vdots & \ddots & \vdots \\ \lambda_y^{\frac{0}{n}}\mathbf{I} & \mathbf{0} & \mathbf{0} \\ \mathbf{0} & \lambda_y^{\frac{0}{n}}\mathbf{I} & \mathbf{0} \\ \mathbf{0} & \mathbf{0} & \lambda_y^{\frac{0}{n}}\mathbf{I} \end{bmatrix} \tag{7.2.13}$$

### 7.2.3 Formulation of eigenvalue problem

The standard eigenvalue relation for the equation of motion (Eq. 7.2.12) is hereby formulated using a WFE approach which couples the periodic structure theory with the FE method.

In Eq. (7.2.12), $x$ is the direction along which propagation characteristics are sought when wave properties along $y$ are known and imposed as earlier stated. Hence, the DSM of the segment can be partitioned with regard to its left $LB$ (denoted as $L$), right $RB$ (denoted as $R$) and internal $IB$ (denoted as $I$) DoF as

$$\begin{bmatrix} \mathbf{D}_{LL} & \mathbf{D}_{LI} & \mathbf{D}_{LR} \\ \mathbf{D}_{IL} & \mathbf{D}_{II} & \mathbf{D}_{IR} \\ \mathbf{D}_{RL} & \mathbf{D}_{RI} & \mathbf{D}_{RR} \end{bmatrix} \begin{Bmatrix} \mathbf{q}_L \\ \mathbf{q}_I \\ \mathbf{q}_R \end{Bmatrix} = \begin{Bmatrix} \mathbf{f}_L \\ \mathbf{f}_I \\ \mathbf{f}_R \end{Bmatrix} \tag{7.2.14}$$

It is assumed that no external forces are applied on the internal nodes, $\mathbf{f}_I = \mathbf{0}$. Applying dynamic condensation technique on the internal nodes DoF, Eq. (7.2.14) can be expressed as

$$\begin{bmatrix} \mathbf{D}_{11} & \mathbf{D}_{12} \\ \mathbf{D}_{21} & \mathbf{D}_{22} \end{bmatrix} \begin{Bmatrix} \mathbf{q}_L \\ \mathbf{q}_R \end{Bmatrix} = \begin{Bmatrix} \mathbf{f}_L \\ \mathbf{f}_R \end{Bmatrix} \tag{7.2.15}$$

with

$$\begin{aligned} \mathbf{D}_{11} &= \mathbf{D}_{LL} - \mathbf{D}_{LI}\mathbf{D}_{II}^{-1}\mathbf{D}_{IL}, \quad & \mathbf{D}_{12} &= \mathbf{D}_{LR} - \mathbf{D}_{LI}\mathbf{D}_{II}^{-1}\mathbf{D}_{IR} \\ \mathbf{D}_{21} &= \mathbf{D}_{RL} - \mathbf{D}_{RI}\mathbf{D}_{II}^{-1}\mathbf{D}_{IL}, \quad & \mathbf{D}_{22} &= \mathbf{D}_{RR} - \mathbf{D}_{RI}\mathbf{D}_{II}^{-1}\mathbf{D}_{IR} \end{aligned} \tag{7.2.16}$$

As earlier stated, it is assumed that no external forces are applied on the segment. As a result of this, the displacement continuity and equilibrium of forces equations at the interface of two consecutive periodic segments $s$ and $s+1$ are given as

$$\begin{aligned} \mathbf{q}_L^{s+1} &= \mathbf{q}_R^s \\ \mathbf{f}_L^{s+1} &= -\mathbf{f}_R^s \end{aligned} \tag{7.2.17}$$

Combining Eqs. (2.1.8) and (7.2.17), the relation of the displacements and forces of the two consecutive periodic segments can be expressed in the form

$$\begin{Bmatrix} \mathbf{q}_L^{s+1} \\ \mathbf{f}_L^{s+1} \end{Bmatrix} = \mathbf{T} \begin{Bmatrix} \mathbf{q}_L^s \\ \mathbf{f}_L^s \end{Bmatrix} \tag{7.2.18}$$

and the expression of the symplectic transfer matrix $\mathbf{T}$ is defined as

$$\mathbf{T} = \begin{bmatrix} -\mathbf{D}_{12}^{-1}\mathbf{D}_{11} & \mathbf{D}_{12}^{-1} \\ -\mathbf{D}_{21} + \mathbf{D}_{22}\mathbf{D}_{12}^{-1}\mathbf{D}_{11} & -\mathbf{D}_{22}\mathbf{D}_{12}^{-1} \end{bmatrix}_{[j \times j]} \tag{7.2.19}$$

where $j$ is the number of DoF on each periodic cross-section of the waveguide's segment.

As previously stated, propagation characteristics along $y$ direction are assumed known. The unknown propagation constant along $x$ direction $\lambda_x = \mathrm{e}^{-\mathrm{i}k_x L_x}$ relates the right and left nodal displacements and forces according to Bloch's theorem as

$$\begin{aligned} \mathbf{q}_R^s &= \lambda_x \mathbf{q}_L^s \\ \mathbf{f}_R^s &= -\lambda_x \mathbf{f}_L^s \end{aligned} \tag{7.2.20}$$

Substituting Eqs. (7.2.17) and (7.2.20) in Eq. (7.2.18), the free wave propagation is described by the eigenproblem

$$\lambda_x \begin{Bmatrix} \mathbf{q}_L \\ \mathbf{f}_L \end{Bmatrix} = \mathbf{T} \begin{Bmatrix} \mathbf{q}_L \\ \mathbf{f}_L \end{Bmatrix} \tag{7.2.21}$$

whose eigenvalues $\lambda_x(\omega, k_y)$ and eigenvectors $\boldsymbol{\phi}(\omega, k_y) = \begin{Bmatrix} \boldsymbol{\phi}_q \\ \boldsymbol{\phi}_f \end{Bmatrix}_{[j\times 1]}$ solution sets provide a comprehensive description of the propagation constants and the wave mode shapes for each of the elastic waves propagating in the structural waveguide at a specified angular frequency, $\omega$ and wavenumber along $y$, $k_y$. Both positive going (with $\lambda_x^{\text{inc}}$ and $\boldsymbol{\phi}^{\text{inc}}$) and negative going (with $\lambda_x^{\text{ref}}$ and $\boldsymbol{\phi}^{\text{ref}}$) waves are sought through the eigensolution. Positive going waves are characterised [105] by

$$\begin{gathered} |\lambda_x^{\text{inc}}| \leq 1, \\ \Re(\mathrm{i}\omega \boldsymbol{\phi}_f^{\text{inc}\top} \boldsymbol{\phi}_q^{\text{inc}}) < 0, \text{ if } |\lambda_x^{\text{inc}}| = 1 \end{gathered} \tag{7.2.22}$$

which states that when a wave is propagating in the positive $x$ direction, its amplitude should be decreasing, or that if its amplitude is constant (in the case of propagating waves with no attenuation), then there is time average power transmission in the positive direction. Then the wavenumbers of the waves (at a specified angular frequency and $k_y$) in the positive $k_x^{\text{inc}}$ and the negative $k_x^{\text{ref}}$ directions can be determined from the propagation constants as

$$\begin{aligned} k_x^{\text{inc}}(\omega, k_y) &= -\frac{\ln(\lambda_x^{\text{inc}})}{\mathrm{i}L_x} \\ k_x^{\text{ref}}(\omega, k_y) &= -\frac{\ln(\lambda_x^{\text{ref}})}{\mathrm{i}L_x} \end{aligned} \tag{7.2.23}$$

## 7.3 Wave interaction with damage within two-dimensional periodic structure

### 7.3.1 Statement of the problem

An arbitrarily layered two-dimensional periodic structure containing structural nonlinearity, such as damage, is hereby considered. Periodicity and hence wave propagation are considered in the $x$ and $y$ directions. The structure is discretized as a system of $N$ healthy substructures connected through a coupling joint, which bears the structural damage/nonlinearity, as shown in Fig. 7.2. Propagation constants for the waves propagating along each substructure are sought as presented in Sec. 7.2, and interaction of

the waves with the damage within the joint is computed in the section. The joint is fully FE modelled in order to implement the structural damage.

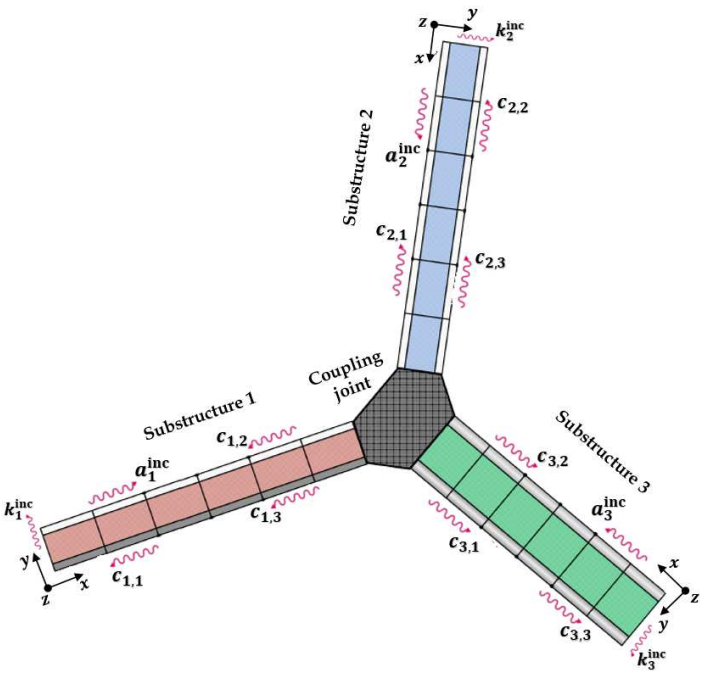


**Figure 7.2:** Wave propagation in two-dimensional structural system consisting of substructures connected through a joint. A positive going wave, of wave constant $\mathbf{k}_n^{\text{inc}}$, propagating along the $y$-axis in the $n$th substructure gives rise to incident wave, of amplitude $\mathbf{a}_n^{\text{inc}}$ along the $x$-axis, impinging on the joint from the $n$th substructure. This will give rise to reflected wave of coefficient $\mathbf{c}_{n,n}$ in the $n$th substructure and transmitted wave of coefficient $\mathbf{c}_{k,n}$ in the $k$th substructure

Each substructure can be different and hence can support a different number of propagating waves, $W$, at a given $\omega$ and $k_y$. However the cross-sections at the interface of each substructure and the coupling joint must be similar as shown in Fig. 7.2.

### 7.3.2 PST formulation of the coupling joint's equation of motion

Consider a typical coupling joint along which a wave propagates in the $x$ and $y$ directions. The PST formulation of the joint's fully FE-modelled segment is presented in Fig. 7.3.

The equation of motion for the fully FE-modelled coupling joint can be expressed as

$$\mathbb{M}\ddot{\mathbf{z}} + \mathbb{C}\dot{\mathbf{z}} + \mathbb{K}\mathbf{z} = \mathbf{f}^{\mathbf{e}} \tag{7.3.1}$$

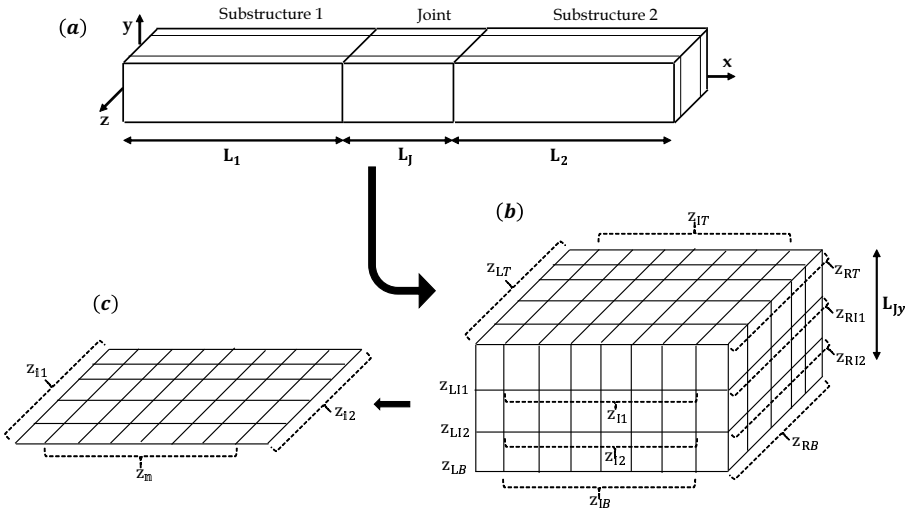


**Figure 7.3:** PST formulation of a typical fully FE-modelled coupling joint

where $\mathbb{K}, \mathbb{C}$ and $\mathbb{M}$ are stiffness, damping and mass matrices of the coupling joint. $\mathbf{z}$ is the physical displacement vector of the coupling joint and $\mathbf{f^e}$ is the set of elastic forces applied to the coupling joint at its interface with connected waveguides.

Propagation constants are injected along the $y$ axis and propagation characteristics are sought along the $x$ direction. Hence, displacements and forces vectors are expressed as function of the displacements and forces at a chosen reference edge along the $y$ axis. The edge with indices $LB$, $IB$ and $RB$ is used as the reference edge. The segment's displacements are expressed as

$$\begin{aligned}
\mathbf{z}_{LT} &= \mathrm{e}^{-\mathrm{i}\mu_y}\mathbf{z}_{LB}, \;\; \mathbf{z}_{IT} = \mathrm{e}^{-\mathrm{i}\mu_y}\mathbf{z}_{IB}, \;\; \mathbf{z}_{RT} = \mathrm{e}^{-\mathrm{i}\mu_y}\mathbf{z}_{RB} \\
\mathbf{z}_{LI1} &= \mathrm{e}^{-\mathrm{i}\frac{2}{3}\mu_y}\mathbf{z}_{LB}, \;\; \mathbf{z}_{I1} = \mathrm{e}^{-\mathrm{i}\frac{2}{3}\mu_y}\mathbf{z}_{IB}, \;\; \mathbf{z}_{RI1} = \mathrm{e}^{-\mathrm{i}\frac{2}{3}\mu_y}\mathbf{z}_{RB} \\
\mathbf{z}_{LI2} &= \mathrm{e}^{-\mathrm{i}\frac{1}{3}\mu_y}\mathbf{z}_{LB}, \;\; \mathbf{z}_{I2} = \mathrm{e}^{-\mathrm{i}\frac{1}{3}\mu_y}\mathbf{z}_{IB}, \;\; \mathbf{z}_{RI2} = \mathrm{e}^{-\mathrm{i}\frac{1}{3}\mu_y}\mathbf{z}_{RB}
\end{aligned} \tag{7.3.2}$$

and forces expressed as

$$\begin{aligned}
\mathbf{f}^{\mathbf{e}}_{LT} &= \mathrm{e}^{-\mathrm{i}\mu_y}\mathbf{f}^{\mathbf{e}}_{LB}, \;\; \mathbf{f}^{\mathbf{e}}_{IT} = \mathrm{e}^{-\mathrm{i}\mu_y}\mathbf{f}^{\mathbf{e}}_{IB}, \;\; \mathbf{f}^{\mathbf{e}}_{RT} = \mathrm{e}^{-\mathrm{i}\mu_y}\mathbf{f}^{\mathbf{e}}_{RB} \\
\mathbf{f}^{\mathbf{e}}_{LI1} &= \mathrm{e}^{-\mathrm{i}\frac{2}{3}\mu_y}\mathbf{f}^{\mathbf{e}}_{LB}, \;\; \mathbf{f}^{\mathbf{e}}_{I1} = \mathrm{e}^{-\mathrm{i}\frac{2}{3}\mu_y}\mathbf{f}^{\mathbf{e}}_{IB}, \;\; \mathbf{f}^{\mathbf{e}}_{RI1} = \mathrm{e}^{-\mathrm{i}\frac{2}{3}\mu_y}\mathbf{f}^{\mathbf{e}}_{RB} \\
\mathbf{f}^{\mathbf{e}}_{LI2} &= \mathrm{e}^{-\mathrm{i}\frac{1}{3}\mu_y}\mathbf{f}^{\mathbf{e}}_{LB}, \;\; \mathbf{f}^{\mathbf{e}}_{I2} = \mathrm{e}^{-\mathrm{i}\frac{1}{3}\mu_y}\mathbf{f}^{\mathbf{e}}_{IB}, \;\; \mathbf{f}^{\mathbf{e}}_{RI2} = \mathrm{e}^{-\mathrm{i}\frac{1}{3}\mu_y}\mathbf{f}^{\mathbf{e}}_{RB}
\end{aligned} \tag{7.3.3}$$

with

$$\mu_y = k_y L_{Jy} \tag{7.3.4}$$

Expressing Eqs. (7.3.2) and (7.3.3) in tensorial forms gives

$$\begin{aligned}
\mathbf{z} &= \mathbb{R}_T \left\{ \mathbf{z}_{LB} \;\; \mathbf{z}_{IB} \;\; \mathbf{z}_{RB} \right\}^\top \\
\mathbb{R}_T^* \;\; \mathbf{f^e} &= \left\{ \mathbf{f}^{\mathbf{e}}_{LB} \;\; \mathbf{f}^{\mathbf{e}}_{IB} \;\; \mathbf{f}^{\mathbf{e}}_{RB} \right\}^\top
\end{aligned} \tag{7.3.5}$$

where $\mathbb{R}_T$ is the transformation matrix for the displacements and $\mathbb{R}_T^*$, which is the Hermitian of $\mathbb{R}_T$, is the transformation matrix for the forces. Generally, for a coupling joint of $n$ periodic layers along the axis of wave injection ($y$ axis in this case), the transformation matrix based on the predefined sequence (Fig. 7.3) can be expressed as

$$\mathbf{R}_T = \begin{bmatrix} \gamma_y^{\frac{n}{n}}\mathbf{I} & \mathbf{0} & \mathbf{0} \\ \mathbf{0} & \gamma_y^{\frac{n}{n}}\mathbf{I} & \mathbf{0} \\ \mathbf{0} & \mathbf{0} & \gamma_y^{\frac{n}{n}}\mathbf{I} \\ \gamma_y^{\frac{n-1}{n}}\mathbf{I} & \mathbf{0} & \mathbf{0} \\ \mathbf{0} & \gamma_y^{\frac{n-1}{n}}\mathbf{I} & \mathbf{0} \\ \mathbf{0} & \mathbf{0} & \gamma_y^{\frac{n-1}{n}}\mathbf{I} \\ \gamma_y^{\frac{n-2}{n}}\mathbf{I} & \mathbf{0} & \mathbf{0} \\ \mathbf{0} & \gamma_y^{\frac{n-2}{n}}\mathbf{I} & \mathbf{0} \\ \mathbf{0} & \mathbf{0} & \gamma_y^{\frac{n-2}{n}}\mathbf{I} \\ \vdots & \ddots & \vdots \\ \gamma_y^{\frac{0}{n}}\mathbf{I} & \mathbf{0} & \mathbf{0} \\ \mathbf{0} & \gamma_y^{\frac{0}{n}}\mathbf{I} & \mathbf{0} \\ \mathbf{0} & \mathbf{0} & \gamma_y^{\frac{0}{n}}\mathbf{I} \end{bmatrix} \tag{7.3.6}$$

with

$$\gamma_y = \mathrm{e}^{-\mathrm{i}\mu_y} \tag{7.3.7}$$

Substituting Eq. (7.3.5) into Eq. (7.3.1) gives a reformulated equation of motion for the joint as

$$[\mathbb{R}_T^*\mathbb{K}\mathbb{R}_T + \mathrm{i}\omega\mathbb{R}_T^*\mathbb{C}\mathbb{R}_T - \omega^2\mathbb{R}_T^*\mathbb{M}\mathbb{R}_T] \begin{Bmatrix} \mathbf{z}_{LB} \\ \mathbf{z}_{IB} \\ \mathbf{z}_{RB} \end{Bmatrix} = \begin{Bmatrix} \mathbf{f^e}_{LB} \\ \mathbf{f^e}_{IB} \\ \mathbf{f^e}_{RB} \end{Bmatrix} \tag{7.3.8}$$

In the reformulated equation of motion, the segment is partitioned with regards to its left $LB$, right $RB$ and internal $IB$ DoF which are denoted as i1, i2 and n as shown in Fig. 7.3. The $\omega$ and $k_y$ dependent DSM of the joint can then be expressed as

$$\mathbb{D} = \mathbb{R}_T^*\mathbb{K}\mathbb{R}_T + \mathrm{i}\omega\mathbb{R}_T^*\mathbb{C}\mathbb{R}_T - \omega^2\mathbb{R}_T^*\mathbb{M}\mathbb{R}_T \tag{7.3.9}$$

It is assumed that all connected waveguides are considered to be purely elastic and that no external force is applied at the non-interface nodes of the joint. As a result of this, the DSM of the joint is partitioned with regards to the interface (i1 and i2 as shown

in Fig. 7.3) DoF, denoted as $\mathbb{i}$, and non-interface DoF, denoted as $\mathbb{n}$, of the joint with the waveguides as

$$\begin{bmatrix} \mathbb{D}_{\mathbb{ii}} & \mathbb{D}_{\mathbb{in}} \\ \mathbb{D}_{\mathbb{ni}} & \mathbb{D}_{\mathbb{nn}} \end{bmatrix} \begin{Bmatrix} \mathbf{z}_{\mathbb{i}} \\ \mathbf{z}_{\mathbb{n}} \end{Bmatrix} = \begin{Bmatrix} \mathbf{f}^{\mathbf{e}}_{\mathbb{i}} \\ \mathbf{f}^{\mathbf{e}}_{\mathbb{n}} \end{Bmatrix} \tag{7.3.10}$$

Applying dynamic condensation on the non-interface DoF ($\mathbf{f}^{\mathbf{e}}_{\mathbb{n}} = \mathbf{0}$), Eq. (7.3.10) can be expressed as

$$\mathbb{D}_{\mathbb{J}} \mathbf{z}_{\mathbb{i}} = \mathbf{f}^{\mathbf{e}}_{\mathbb{i}} \tag{7.3.11}$$

with the DSM of the joint expressed as

$$\mathbb{D}_{\mathbb{J}} = [\mathbb{D}_{\mathbb{ii}} - \mathbb{D}_{\mathbb{in}} \mathbb{D}^{-1}_{\mathbb{nn}} \mathbb{D}_{\mathbb{ni}}]_{[jN/2 \times jN/2]} \tag{7.3.12}$$

at a specified $\omega$ and $k_y$.

### 7.3.3 Calculation of the wave interaction scattering coefficients

Each supported wavemode w with $\mathrm{w} \in [1 \cdots \mathrm{W}]$ for substructure $n$ with $n \in [1 \cdots N]$ can be grouped as

$$\begin{aligned} \boldsymbol{\Phi}^{\mathrm{inc}}_{n,q} &= \begin{bmatrix} \boldsymbol{\phi}^{\mathrm{inc}}_{q,1} & \boldsymbol{\phi}^{\mathrm{inc}}_{q,2} & \cdots & \boldsymbol{\phi}^{\mathrm{inc}}_{q,W} \end{bmatrix}_{[j/2 \times W]} \\ \boldsymbol{\Phi}^{\mathrm{inc}}_{n,f} &= \begin{bmatrix} \boldsymbol{\phi}^{\mathrm{inc}}_{f,1} & \boldsymbol{\phi}^{\mathrm{inc}}_{f,2} & \cdots & \boldsymbol{\phi}^{\mathrm{inc}}_{f,W} \end{bmatrix}_{[j/2 \times W]} \\ \boldsymbol{\Phi}^{\mathrm{ref}}_{n,q} &= \begin{bmatrix} \boldsymbol{\phi}^{\mathrm{ref}}_{q,1} & \boldsymbol{\phi}^{\mathrm{ref}}_{q,2} & \cdots & \boldsymbol{\phi}^{\mathrm{ref}}_{q,W} \end{bmatrix}_{[j/2 \times W]} \\ \boldsymbol{\Phi}^{\mathrm{ref}}_{n,f} &= \begin{bmatrix} \boldsymbol{\phi}^{\mathrm{ref}}_{f,1} & \boldsymbol{\phi}^{\mathrm{ref}}_{f,2} & \cdots & \boldsymbol{\phi}^{\mathrm{ref}}_{f,W} \end{bmatrix}_{[j/2 \times W]} \end{aligned} \tag{7.3.13}$$

at a specified $\omega$ and $k_y$.

The analysis for the calculation of wave interaction scattering coefficients is similar to that of one-dimensional structure presented in Sec. 2.3.3. As presented in Sec. 2.3.3, the wave interaction scattering matrix, whose diagonal and off-diagonal elements respectively represent the reflection and transmission coefficients, is calculated as

$$S(\omega, k_y) = -[\boldsymbol{\Phi}^{\mathrm{g,ref}}_{f} - \mathbb{D}_{\mathbb{J}} \boldsymbol{\Phi}^{\mathrm{g,ref}}_{q}]^{-1} [\boldsymbol{\Phi}^{\mathrm{g,inc}}_{f} - \mathbb{D}_{\mathbb{J}} \boldsymbol{\Phi}^{\mathrm{g,inc}}_{q}] \tag{7.3.14}$$

at a specified angular frequency, $\omega$, and imposed wave constant along $y$, $k_y$. $\boldsymbol{\Phi}^{\mathrm{g,inc}}_{q}$ is computed as presented in Eq. 2.3.8 with respective similar expressions for $\boldsymbol{\Phi}^{\mathrm{g,inc}}_{f}$, $\boldsymbol{\Phi}^{\mathrm{g,ref}}_{q}$ and $\boldsymbol{\Phi}^{\mathrm{g,ref}}_{f}$.

## 7.4 Case studies

This section presents numerical case studies to demonstrate the validity and applicability of the developed methodology. The case examples are divided into two parts, namely validation and test case studies. In the first part, structural model whose wave dispersion and scattering properties can easily be obtained theoretically is presented. The theoretical results are compared to the numerical results obtained through the presented scheme in order to demonstrate the validity of the scheme. The second part, test case studies, presents the application of the scheme to quantify wave interaction with defects in damaged layered structures, and characterise damage types based on calculated wave interaction coefficients.

In all the example cases, FE mesh size of a structural segment is chosen based on the theoretical dispersion curves for the segment. This is to ensure that the mesh density is fine enough to represent the structure accurately at a reasonable computational time. In each case, a damaged structural system is discretized as a system of two healthy substructures connected through a coupling joint, within which the damage is implemented. Wave propagation constants along each substructure are obtained by solving Eq. (7.2.21) while the scattering coefficients for the wave interaction with the damage are computed through Eq. (7.3.14). All segments are meshed using ANSYS® software package. All properties and dimensions are in SI units, unless otherwise stated.

**Table 7.1:** Mechanical properties of the materials used for the case studies presented in Sec. 7.4

| | Aluminium | Glass Epoxy I | Glass Epoxy II | Honeycomb foam |
|---|---|---|---|---|
| $\rho$ | 2600 kg/m$^3$ | 2000 kg/m$^3$ | 2000 kg/m$^3$ | 110 kg/m$^3$ |
| $E_x$ | 70 GPa | 45.6 GPa | 54 GPa | 180 MPa |
| $E_y$ | - | 16.2 GPa | 54 GPa | - |
| $E_z$ | - | 16.2 GPa | 48 GPa | - |
| $\nu_{xy}$ | 0.278 | 0.3 | 0.06 | 0.28 |
| $\nu_{yz}$ | - | 0.4 | 0.313 | - |
| $\nu_{xz}$ | - | 0.278 | 0.313 | - |
| $G_{xy}$ | - | 5.83 GPa | 3.16 GPa | - |
| $G_{yz}$ | - | 5.79 GPa | 1.78 GPa | - |
| $G_{xz}$ | - | 5.83 GPa | 1.78 GPa | - |

### 7.4.1 Validation case studies

The presented computational scheme is hereby validated using a cracked aluminium beam system consisting of two healthy substructures connected through a coupling joint, which bears the damage (such as in Fig. 7.8). The three waveguides in the system can in general have different material characteristics. However in this case they are assumed to be made of aluminium with material properties given in Table 7.1. The entire beam has a uniform cross section with $L_1 = L_2 = 0.2$, $L_J = 0.05$, $b = 0.001$ and $h = 0.003$.

The beam supports longitudinal, torsional and bending waves whose respective wavenumbers $k_l$, $k_t$ and $k_b$ can be obtained analytically as

$$\begin{aligned} k_l &= \omega\sqrt{\frac{\rho(1-\nu^2)}{E}} \\ k_t &= \omega\sqrt{\frac{\rho}{G}} \\ k_b &= \sqrt{\omega}\sqrt[4]{\frac{\rho h}{D}} \end{aligned} \tag{7.4.1}$$

where $G = E/2(1+\nu)$ is the shear modulus and $D = Eh^3/12(1-\nu^2)$ is the bending stiffness of the beam.

For a given imposed wave along $y$-axis, $k_y$ and at a specified $\omega$, the analytical wavenumber of each wave type along $x$-direction can be obtained as

$$k_x^2(\omega, k_y) = k^2 - k_y^2 \tag{7.4.2}$$

The analytical wave reflection and transmission coefficients of the wave interaction with the crack is obtained as in [91, 204]. The crack within the coupling joint is modelled using the stiffness reduction method with reduction factors ranging from $\beta = 0.09$ to 0.01. This corresponds to damage severity ratio ranging from 0.1 to 0.9 respectively.

The problem is solved by the presented computational scheme. Each waveguide is modelled using SOLID185 finite element of length $\Delta = 0.001$. In order to validate the scheme, the results obtained by the scheme are compared against the analytical results.

Results for the dispersion curves using both approaches are presented in Figs. 7.4 and 7.5. Excellent agreement is observed, which establishes the validity of the scheme. Fig. 7.4 presents dispersion curves in the ($\omega$,$k_x$) plane for different imposed wave values. For imposed wave $k_y = 0$, every wave cuts on at angular frequency $\omega = 0$ as expected. This is equivalent to one dimensional wave propagating with waves propagating only in the x-direction. Cut on frequencies of the waves are observed to increase as $k_y$ value increases. Fig. 7.5 presents dispersion curves in the ($k_x$,$k_y$) plane for different angular frequency values. As observed, the contour curves are independent of

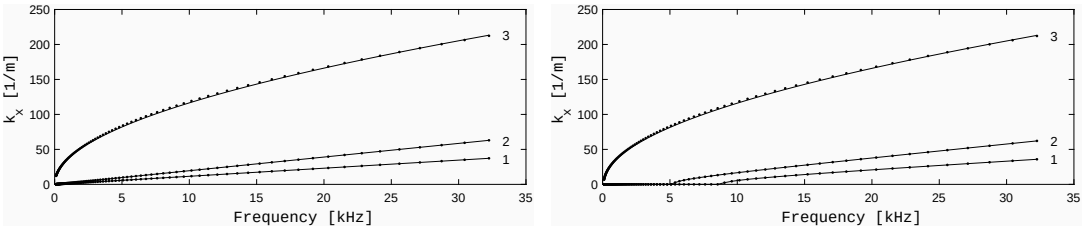


**(a)** at $k_y = 0m^{-1}$ **(b)** at $k_y = 10m^{-1}$

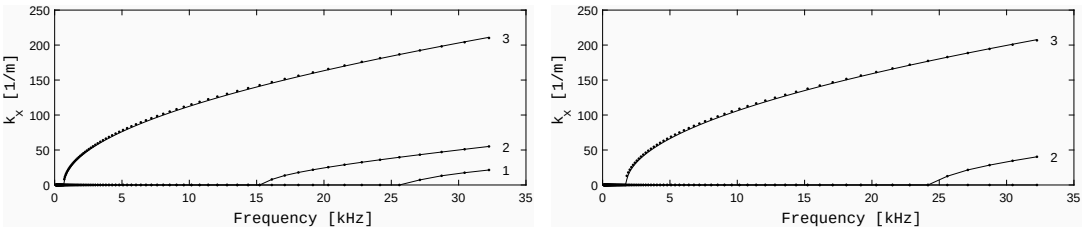


**(c)** at $k_y = 30m^{-1}$ **(d)** at $k_y = 50m^{-1}$

**Figure 7.4:** Dispersion curves for the beam: bending (3), torsional (2) and longitudinal (1) modes. Present methodology (-), Euler-Bernoulli analytical results (. . . )

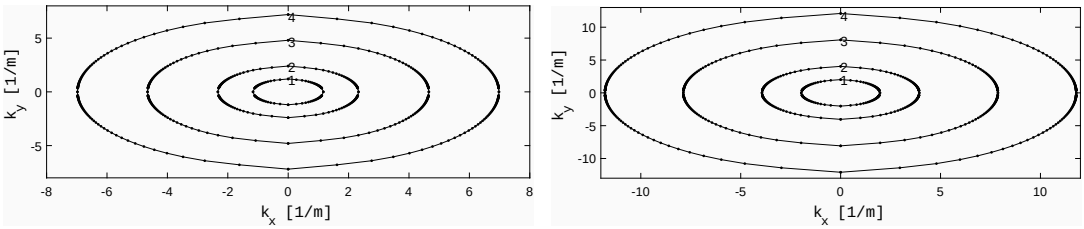


**(a)** longitudinal wave **(b)** torsional wave

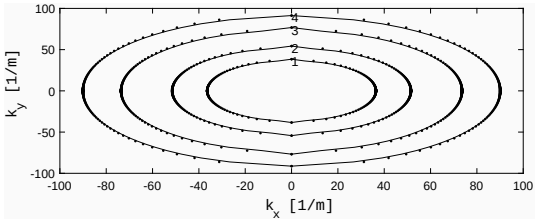


**(c)** bending wave

**Figure 7.5:** $k_x$ vs $k_y$ for the beam, at different frequencies: 1kHz (1), 2kHz (2), 3kHz (3) and 4kHz (4). Present methodology (-), Euler-Bernoulli analytical results (. . . )

propagation direction. This is due to the isotropic nature of the beam under consideration, in which it is expected that material properties will be independent of direction.

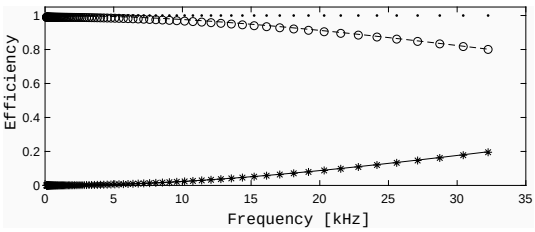


**(a)** longitudinal wave

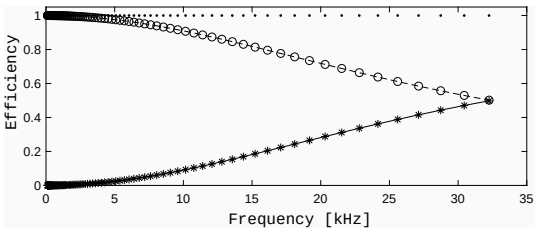


**(b)** torsional wave

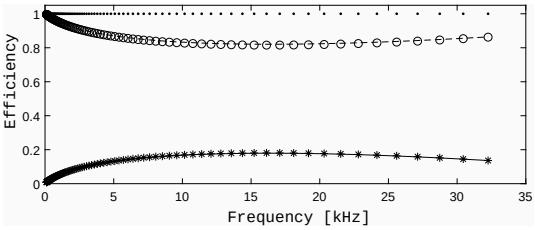


**(c)** bending wave

**Figure 7.6:** Reflection and transmission efficiencies of the wave interaction with damage within the beam's coupling joint. Present methodology: reflection (-), transmission (- -). Analytical results: reflection (*), transmission (o). Conservation of energy (. . . )

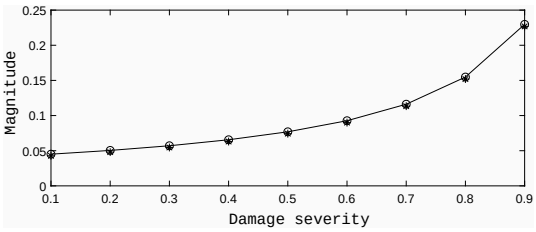


**(a)** longitudinal wave

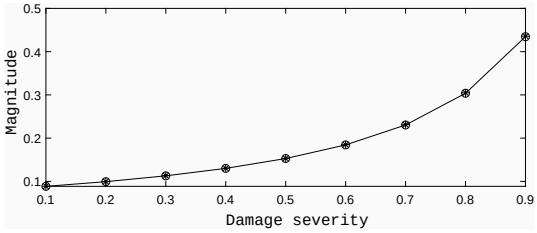


**(b)** torsional wave

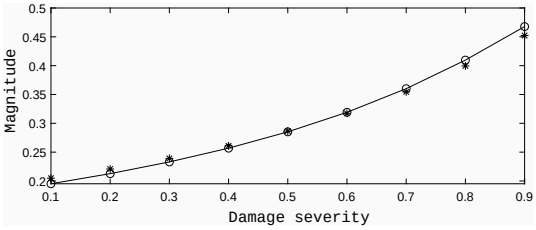


**(c)** bending wave

**Figure 7.7:** Reflection coefficient of the wave interaction with damage within the beam's coupling joint. Present methodology (-o), Analytical results (*)

Figs. 7.6 and 7.7 present the reflection and transmission efficiencies, for the wave interaction with the damage within the beam, obtained as the square of the reflection

and transmission coefficients. Excellent agreement is observed between the analytical results [91, 204] and that of the present scheme. As a conservation of energy, the reflection and transmission efficiencies of a wave propagating through an undamped system should sum up to unity. This is observed in both sets of results presented in Fig. 7.6. Fig. 7.7 presents the dependence of the reflection coefficients on damage severity. It is observed that the coefficient magnitude increases as the damage becomes more severe.

### 7.4.2 Test case studies

#### 7.4.2.1 Orthotropic beam

An arbitrarily layered two-dimensional orthotropic beam having a uniform cross-sectional area ($b = 0.01$ and $h = 0.01$) is considered. The beam is defined as a system of two healthy substructures ($L_1 = L_2 = 0.2$) connected through a damaged coupling joint ($L_J = 0.01$) as shown in Fig. 7.8. Each waveguide comprises ten layers of glass-epoxy composite material whose material properties are presented in Table 7.1 as glass epoxy I.

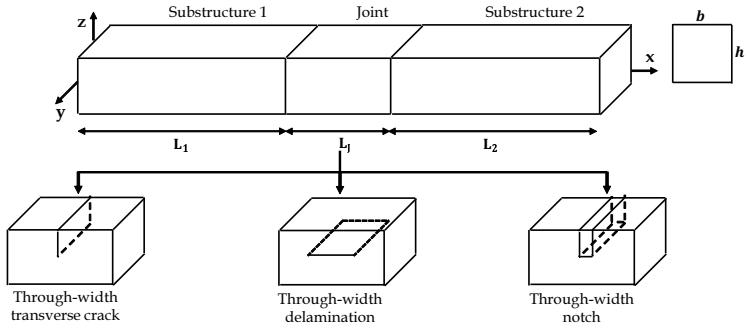


**Figure 7.8:** Two-dimensional orthotropic beam defined as two healthy substructures coupled through a damaged joint

A segment (of length $\Delta = 0.001$) of each substructure is modelled with 100 SOLID185 FEs, each of length 0.001. Dispersion curves are obtained within frequency range $\omega = [1.0 \times 10^2 - 6.0 \times 10^4]$ Hz. Three propagating modes are obtained within this range. The dispersion curves for the waves, in the ($\omega$,$k_x$) axis at $k_y$ = 10 m$^{-1}$ and ($k_y$,$k_x$) axis at $\omega$= 50 kHz, are presented in Fig. 7.9.

As expected, being an orthotropic beam, the dispersion property of the beam depends on the propagation direction of the waves. As shown in Fig. 7.9, it is observed that the cut-on frequency of a wave propagating in the x direction greatly depends on the imposed wavenumber in the y direction, $k_y$. The higher the value of $k_y$, the higher the cut-on frequencies of the propagating waves. It is also observed that at a given frequency, the wavenumber $k_x$ of a wave propagating along x direction reduces with

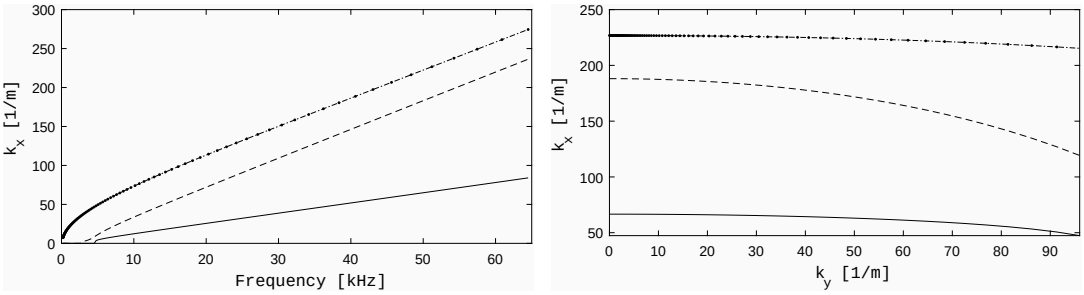


**(a)** ($\omega$,$k_x$) plane for $k_y$ = 12 m$^{-1}$ **(b)** ($k_y$,$k_x$) plane for $\omega$ = 50 kHz

**Figure 7.9:** Dispersion curves of the two-dimensional orthotropic beam: bending mode (-.), torsional mode (- -) and longitudinal mode (-)

increase in $k_y$.

Interaction characteristics of the wave interaction with damage within the coupling joint are studied for different damage modes, as presented in the next sections. Dependence of the interaction scattering coefficients on the severities of the damage modes are analysed in order to establish optimal parameters for detecting and identifying the damage modes in the beam.

In each case, the coupling joint is modelled using similar element size as the substructures. Hence, the coupling joint is modelled with 1000 SOLID185 FEs. Damage parameters depend on the damage mode being analysed as presented in next sections. Generally, notches are modelled using the element deletion method while cracks and delaminations are modelled using the node duplication approach (Sec. 2.2).

#### 7.4.2.1.1 Dependence of wave interaction coefficient on crack within the orthotropic beam

In this case, wave reflection from zero-width crack within the beam's coupling joint, as shown in Fig. 7.8, is considered. The crack is situated at mid length of the joint, and runs transversely through the breadth of the joint. In order to analyse the dependence of the wave reflection coefficient on the severity of the crack, several crack depths are considered. Crack depths within the range [0.001 - 0.009] m, which correspond to ratios [0.1 - 0.9] of the beam's thickness ($h$), are analysed.

Fig. 7.10 shows the variations of the bending wave reflection coefficient with frequency and $k_y$ for different crack depths. With respect to frequency, the reflection coefficient have a minimum, beyond which the reflection coefficient increases with frequency and before which it decreases. The frequency bandwidth, at which the reflection coefficient reaches a minimum increases inversely with the crack depth. That is, lower depth crack will exhibit wider bandwidth. On the other hand, the reflection coef-

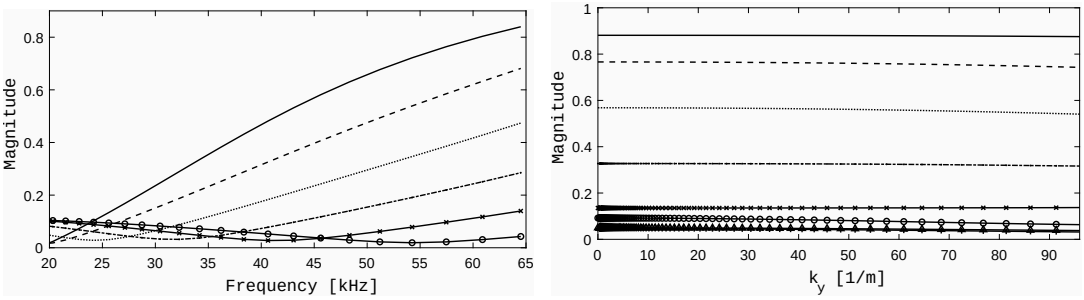


**(a)** w.r.t $\omega$ **(b)** w.r.t. $k_y$

**Figure 7.10:** Bending wave reflection coefficient from the cracked orthotropic beam. Crack severity ratios: 0.4 (-o), 0.5 (-x), 0.6 (-.), 0.7 (. . . ), 0.8 (- -) and 0.9 (-)

ficient changes very slightly with respect to $k_y$ for the various crack depths. This trend is analogous to that obtained for the bending wave's dispersion curve $k_x$ versus $k_y$ as shown in Fig. 7.9.

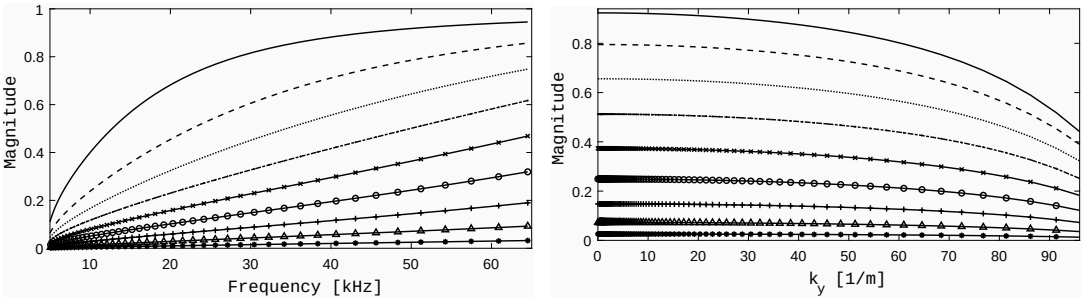


**(a)** w.r.t $\omega$ **(b)** w.r.t. $k_y$

**Figure 7.11:** Longitudinal wave reflection coefficient from the cracked orthotropic beam. Crack severity ratios: 0.1 (-*), 0.2 (-Δ), 0.3 (-+), 0.4 (-o), 0.5 (-x), 0.6 (-.), 0.7 (. . . ), 0.8 (- -) and 0.9 (-)

Fig. 7.11 presents the longitudinal wave reflection coefficient as a function of frequency and $k_y$ at various crack depths. In relation to frequency, the reflection coefficient magnitude increases steadily, though not linear especially for deeper crack, until it becomes plateaued. On the other hand, with respect to $k_y$, the reflection magnitude decreases very slightly over low to mid $k_y$ range, then reduces rapidly towards zero. This is also in similar fashion to the trend obtained for the longitudinal wavenumber against $k_y$ (7.9).

#### 7.4.2.1.2 Dependence of wave interaction coefficient on notch within the orthotropic beam

In this case, wave reflection from 1 mm wide notch within the beam's coupling joint, as shown in Fig. 7.8, is considered. The notch is situated at mid length of the joint, and

runs transversely through the breadth of the joint. In order to analyse the dependence of the wave reflection coefficient on the severity of the notch, notch depths, within the range [0.001 - 0.009] m, which correspond to ratios [0.1 - 0.9] of the beam's thickness are analysed.

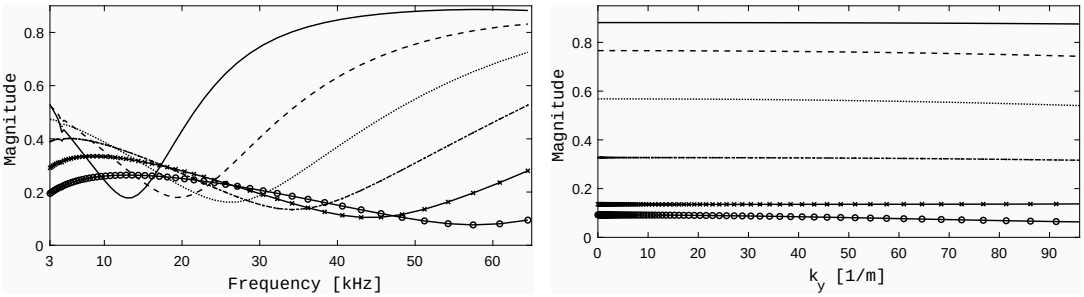


**(a)** w.r.t $\omega$ **(b)** w.r.t. $k_y$

**Figure 7.12:** Bending wave reflection coefficient from the orthotropic laminate with notch, for various severity ratios of the notch 0.1 (-*), 0.2 (-Δ), 0.3 (-+), 0.4 (-o), 0.5 (-x), 0.6 (-.), 0.7 (. . . ), 0.8 (- -) and 0.9 (-)

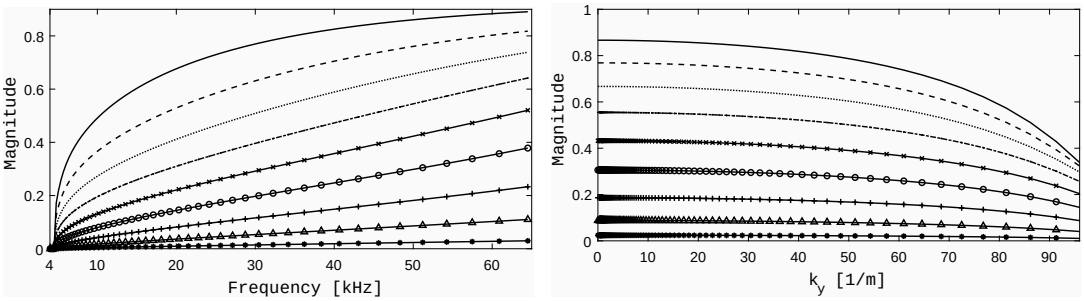


**(a)** w.r.t $\omega$ **(b)** w.r.t. $k_y$

**Figure 7.13:** Longitudinal wave reflection coefficient from the orthotropic laminate with notch, for various severity ratios of the notch 0.1 (-*), 0.2 (-Δ), 0.3 (-+), 0.4 (-o), 0.5 (-x), 0.6 (-.), 0.7 (. . . ), 0.8 (- -) and 0.9 (-)

Reflection coefficient results with respect to frequency and $k_y$ for different notch depths are presented in Figs. 7.12 and 7.13. With respect to frequency, the reflection coefficient of the bending wave has a minimum, beyond which the reflection coefficient increases with frequency and before which it decreases. The frequency at which the reflection coefficient reaches a minimum increases inversely with the crack depth. The reflection coefficient of the longitudinal wave increases steadily until it becomes plateaued. With respect to $k_y$, reflection coefficient of the bending wave changes very slightly with respect to $k_y$ for the various crack depths while that of the longitudinal wave decreases very slightly over low to mid $k_y$ range, then reduces rapidly towards zero.

#### 7.4.2.1.3 Dependence of wave interaction coefficient on delamination within the orthotropic beam

Wave reflection from interlaminar delamination within the beam's coupling joint (Fig. 7.8) is considered in this case. The delamination is situated at mid layer (between the fifth and sixth plies) of the joint, and runs transversely through the breadth of the joint. Delamination widths in the range [0.001 - 0.009] m are considered. These correspond to ratios [0.1 - 0.9] of the beam's thickness.

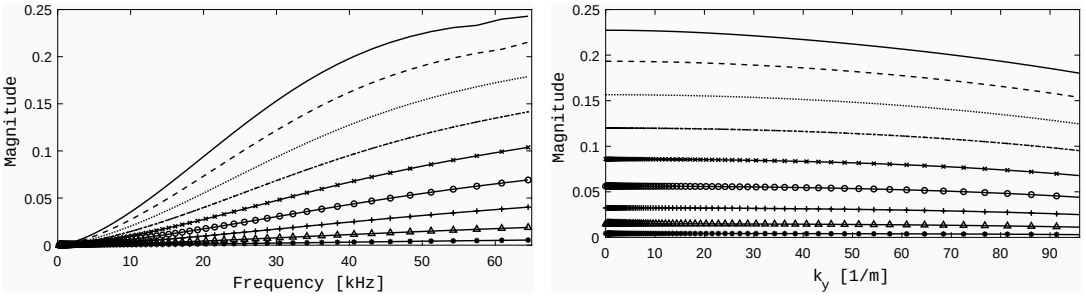


**(a)** w.r.t $\omega$ **(b)** w.r.t. $k_y$

**Figure 7.14:** Bending wave reflection coefficient from the orthotropic laminate with interlaminar delamination, for various severity ratios of the delamination 0.1 (-*), 0.2 (-Δ), 0.3 (-+), 0.4 (-o), 0.5 (-x), 0.6 (-.), 0.7 (. . . ), 0.8 (- -) and 0.9 (-)

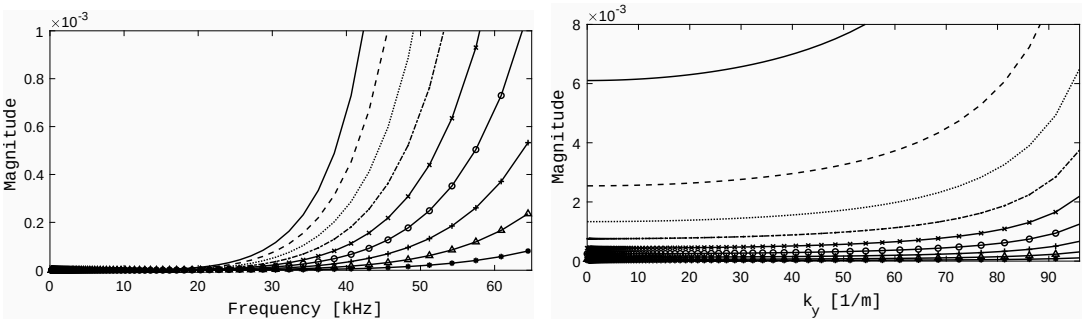


**(a)** w.r.t $\omega$ **(b)** w.r.t. $k_y$

**Figure 7.15:** Longitudinal wave reflection coefficient from the orthotropic laminate with interlaminar delamination, for various severity ratios of the delamination 0.1 (-*), 0.2 (-Δ), 0.3 (-+), 0.4 (-o), 0.5 (-x), 0.6 (-.), 0.7 (. . . ), 0.8 (- -) and 0.9 (-)

Reflection coefficient results with respect to angular frequency as well as $k_y$ for different notch depths are presented in Figs. 7.14 and 7.15. With respect to angular frequency, reflection coefficient of the bending wave increases until it becomes plateaued. Reflection coefficient of the longitudinal wave also increases with angular frequency,

but slightly. With respect to $k_y$, reflection coefficient of the bending wave decreases slightly over low to mid $k_y$ range, then, beyond this range, reduces rapidly. The reflection coefficient of the longitudinal wave increases very slightly until high $k_y$ range, then increases more significantly.

#### 7.4.2.1.4 Comparison of wave interaction coefficient for the different damage modes within the orthotropic beam

Having computed wave interaction characteristics for different damage modes within the orthotropic beam, it is essential to evaluate the sensitivity of each damage mode to wave reflection in order to establish optimal parameter for detecting and identifying damage mode based on their wave interaction properties.

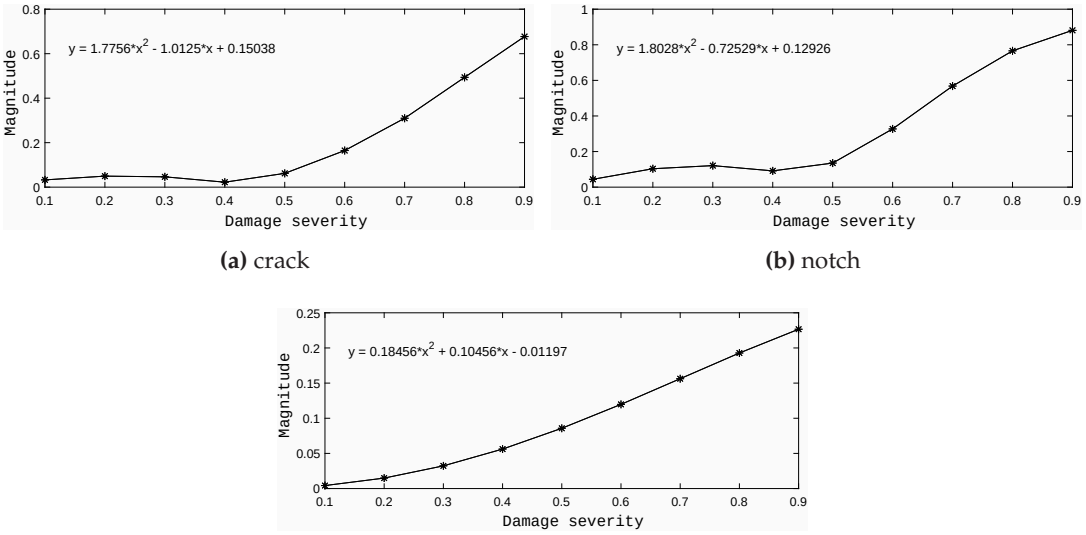


**(a)** crack **(b)** notch

**(c)** interlaminar delamination

**Figure 7.16:** Bending wave reflection coefficient as a function of damage severity (for different damage modes) within the orthotropic beam

Figs. 7.16 and 7.17 present wave reflection coefficient against damage severity for the various damage modes considered above. As observed, crack and notch are more sensitive to reflection compared to delamination. However, the sensitivity of the delamination to bending wave reflection is higher compared to that of longitudinal wave reflection. Though, reflection coefficient from crack and notch are both highly significant for the two wave modes, it can be observed that reflection from both damage modes are observed to be more significant for the longitudinal wave compared to the bending wave. Also, at each damage severity, reflection from the crack is higher than that of the notch by about 5%.

From these observations, it therefore follows that bending wave is the proper wave

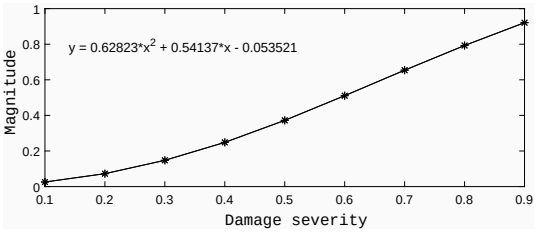


**(a)** crack

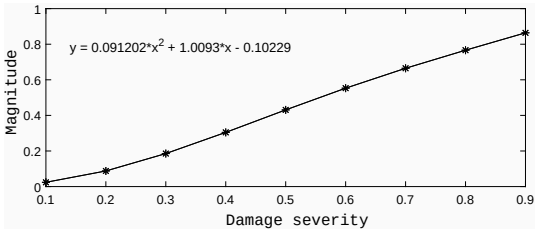


**(b)** notch

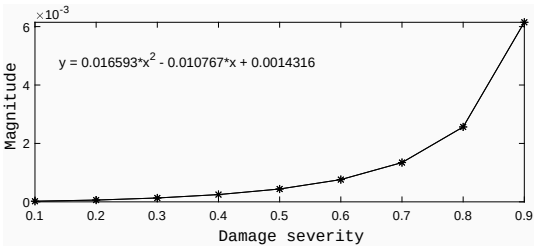


**(c)** interlaminar delamination

**Figure 7.17:** Longitudinal wave reflection coefficient as a function of damage severity (for different damage modes) within the orthotropic beam

mode to detect interlaminar delamination within the carbon epoxy beam while either bending or longitudinal is good for detecting crack and notch within the beam though longitudinal mode is more recommended based on the results. Applying the trend equations indicated on the Figures, wave interaction scattering coefficient from a specific damage mode within the beam can be calculated. The trend can also be applied to identify specific damage mode based on the scattering coefficient obtained from wave interaction with the damage.

#### 7.4.2.2 Sandwich laminate

A two-dimensional sandwich laminate (Fig. 7.18) having a uniform cross-sectional area ($b = 0.01$ and $h = 0.01$) is considered. The upper and lower skin laminae ($h_{s1} = h_{s2} = 0.001$) each consists of one orthotropic layer of glass-epoxy and the core ($h_c = 0.008$) consists of eight layers of honeycomb foam material. The material properties of the glass-epoxy and the honeycomb core are presented in Table 7.1 as glass epoxy II and honeycomb foam respectively.

The damaged laminate system is discretised as a system of two healthy substructures ($L_1 = L_2 = 0.2$) connected through a damaged joint ($L_J = 0.01$) as shown in Fig. 7.18.

A segment (of length $\Delta = 0.001$) of each waveguide is modelled with 100 SOLID185 FEs (10 for each skin and 80 for the core) using elements of size 0.001. Dispersion curves for the laminate are obtained within frequency range $\omega = [1.0 \times 10^2 - 6.0 \times 10^4]$ Hz.

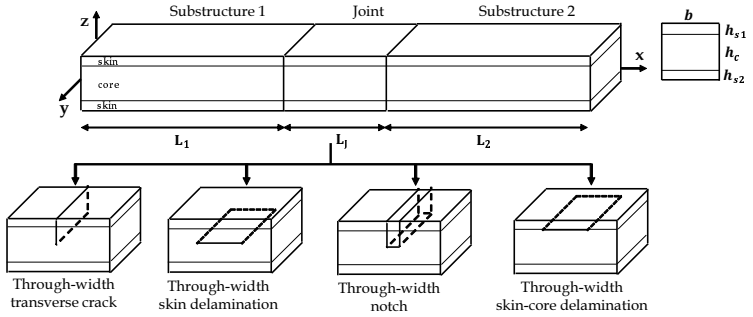


**Figure 7.18:** Two-dimensional sandwich laminate defined as two healthy substructures connected through a damaged joint

Three propagating modes are obtained within the frequency range. The dispersion curves for the waves, in the ($\omega$,$k_x$) axis at $k_y$ = 2 m$^{-1}$ and ($k_y$,$k_x$) axis at $\omega$= 30 kHz, are presented in Fig. 7.19.

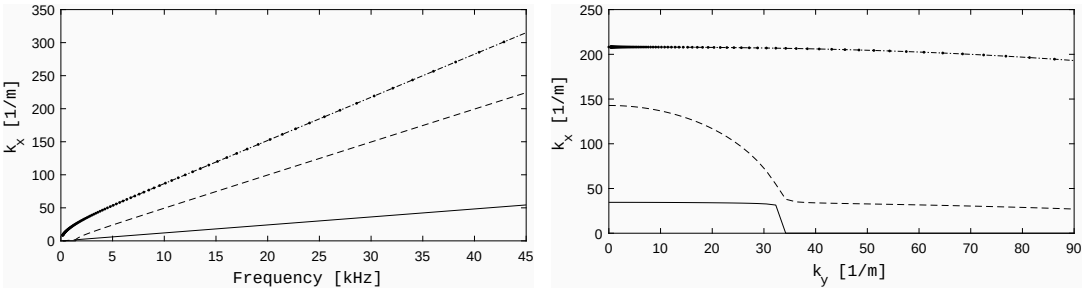


**(a)** ($\omega$,$k_x$) plane **(b)** ($k_y$,$k_x$) plane

**Figure 7.19:** Dispersion curves for the two-dimensional sandwich laminate: bending mode (-.), torsional mode (- -) and longitudinal mode (-)

As in the case of the orthotropic beam, the dispersion property of the sandwich laminate depends on the propagation direction of the waves. As shown in Fig. 7.9, it is observed that the cut-on frequency of a wave propagating in the x direction greatly depends on the imposed wavenumber in the y direction, $k_y$. The higher the imposed $k_y$, the higher the cut-on frequencies of the waves. It is also observed that at a given frequency, the wavenumbers of the waves propagating along x direction reduce with respect to $k_y$.

Interaction characteristics of the wave interaction with damage within the coupling joint are studied for different damage modes, as presented in the next sections. Dependence of the interaction scattering coefficients on the severities of the damage modes are analysed in order to establish optimal parameters for detecting and identifying the damage modes in the laminate.

In each damage mode case, the coupling joint is modelled with similar element size used for the substructures. Hence, the joint consists of 1000 SOLID185 FEs. As

presented in next sections, damage parameters depends on the damage mode being analysed. Generally, notches are modelled using the element deletion method while cracks and delaminations are modelled using the node duplication approach (Sec. 2.2).

#### 7.4.2.2.1 Dependence of wave interaction coefficient on crack within the sandwich laminate

In this case, wave reflection from zero-width crack within the laminate's coupling joint, as shown in Fig. 7.18, is considered. The crack is situated at mid length of the joint, and runs transversely through the breadth of the joint. In order to analyse the dependence of the wave reflection coefficient on the severity of the crack, several crack depths are considered. Crack depths within the range [0.001 - 0.009] m, which correspond to ratios [0.1 - 0.9] of the laminate's thickness, are analysed. Variations of the bending and longitudinal waves reflection coefficients with angular frequency and $k_y$ for different crack depths are presented in Figs. 7.20 and 7.21.

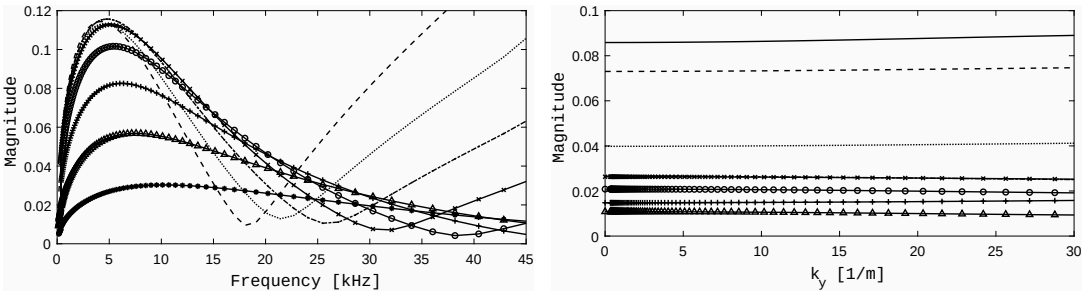


**(a)** w.r.t $\omega$ **(b)** w.r.t. $k_y$

**Figure 7.20:** Bending wave reflection coefficient from the crack within the sandwich laminate, for various severity ratios of the crack 0.1 (-*), 0.2 (-Δ), 0.3 (-+), 0.4 (-o), 0.5 (-x), 0.6 (-.), 0.7 (. . . ), 0.8 (- -) and 0.9 (-)

With respect to angular frequency, the bending wave reflection coefficient exhibits a sinusoidal-type of relationship. The reflection coefficient increases to a maximum then reduces to a minimum, then increases back to a maximum and so on. Generally, the reflection coefficient, at a given frequency, increases linearly with the crack severity. The longitudinal wave reflection coefficient generally increases with respect to angular frequency. At a given frequency, it directly increases with regards to the crack severity.

In relation to $k_y$, the bending wave reflection coefficient changes very slightly until a considerably higher value of $k_y$. At a given value of $k_y$, the reflection coefficient varies directly with the severity of the crack. Similar variation is observed for the longitudinal wave reflection coefficient. However, at a given value of $k_y$, the change in the wave reflection magnitude, per 0.1 change in the crack severity ratio, is more uni-

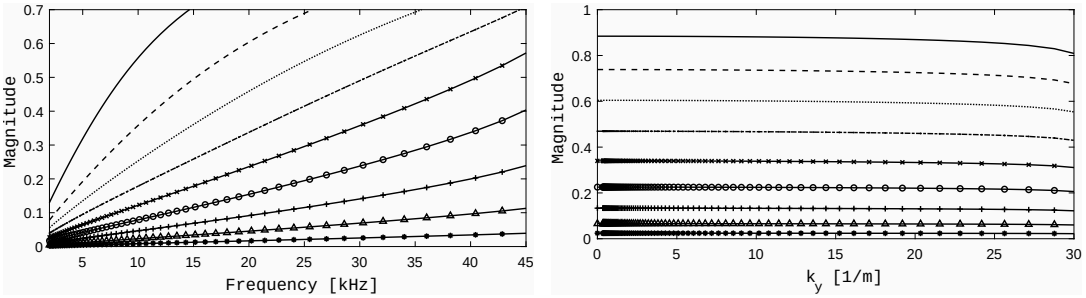


**(a)** w.r.t $\omega$ **(b)** w.r.t. $k_y$

**Figure 7.21:** Longitudinal wave reflection coefficient from the crack within the sandwich laminate, for various severity ratios of the crack 0.1 (-*), 0.2 (-Δ), 0.3 (-+), 0.4 (-o), 0.5 (-x), 0.6 (-.), 0.7 (. . . ), 0.8 (- -) and 0.9 (-)

form in the longitudinal wave compared to the bending wave. For the longitudinal wave, a uniform average change of about 0.1 is observed. While an average change of about 0.005 and 0.02, are observed for the bending wave at low and high severity range respectively.

#### 7.4.2.2.2 Dependence of wave interaction coefficient on notch within the sandwich laminate

In this case, wave reflection from 1 mm wide notch within the laminate's coupling joint, as shown in Fig. 7.18, is considered. The notch is situated at mid length of the joint, and runs transversely through the breadth of the joint. In order to analyse the dependence of the wave reflection coefficient on the severity of the notch, notch depths, within the range [0.001 - 0.009] m, which correspond to ratios [0.1 - 0.9] of the laminate's thickness are analysed.

Variations of the bending and longitudinal waves reflection coefficients with frequency and $k_y$ for different notch severity ratios are presented in Figs. 7.22 and 7.23.

As a function of frequency, bending wave reflection from the notch exhibits a sinusoidal-type of relationship while longitudinal wave reflection generally increases as frequency increases. At a given angular frequency, the bending wave reflection coefficient varies directly with notch severity. Similar trend is observed for the longitudinal wave reflection.

With respect to $k_y$, reflection coefficients of the waves change very slightly until a considerably higher value of $k_y$. At a given value of $k_y$, the reflection coefficient of both wave modes varies directly with the severity of the notch. However, there is an average of 0.1 increase in the longitudinal wave reflection coefficient per 0.1 change of the notch severity ratio. Changes in the bending wave reflection coefficient per 0.1 change of the

notch severity ratio is not uniform; an average change of about 0.02 is observed at low severity ratio while an average change of about 0.25 is observed at higher severity ratio.

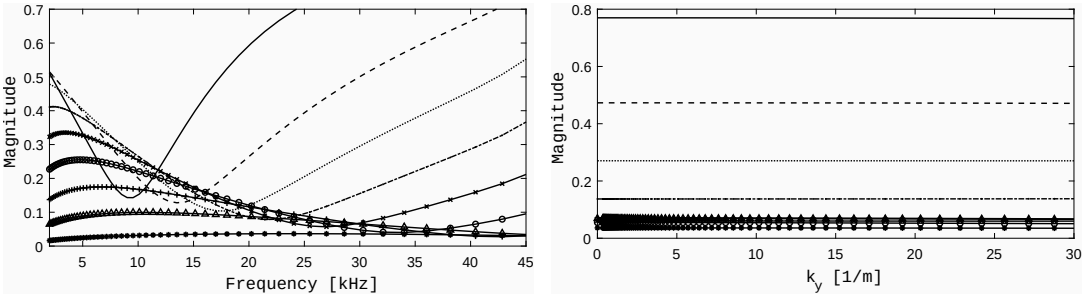


**(a)** w.r.t $\omega$ **(b)** w.r.t. $k_y$

**Figure 7.22:** Bending wave reflection coefficient from the notch within the sandwich laminate, for various severity ratios of the notch 0.1 (-*), 0.2 (-Δ), 0.3 (-+), 0.4 (-o), 0.5 (-x), 0.6 (-.), 0.7 (. . . ), 0.8 (- -) and 0.9 (-)

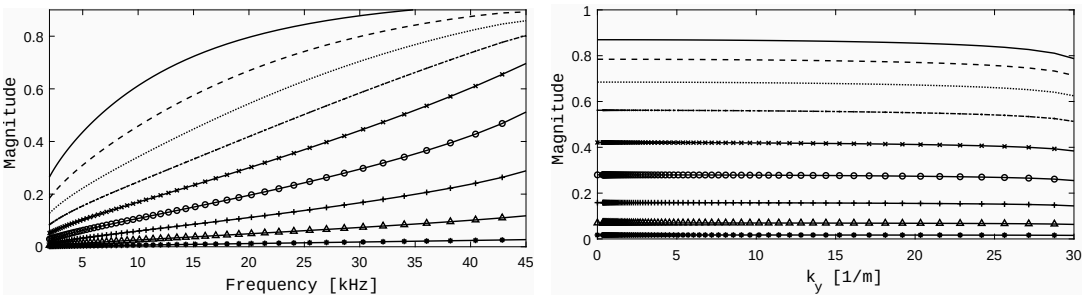


**(a)** w.r.t $\omega$ **(b)** w.r.t. $k_y$

**Figure 7.23:** Longitudinal wave reflection coefficient from the notch within the sandwich laminate, for various severity ratios of the notch 0.1 (-*), 0.2 (-Δ), 0.3 (-+), 0.4 (-o), 0.5 (-x), 0.6 (-.), 0.7 (. . . ), 0.8 (- -) and 0.9 (-)

#### 7.4.2.2.3 Dependence of wave interaction coefficient on skin-core interlaminar delamination within the sandwich laminate

Wave reflection from skin-core interlaminar delamination within the laminate's coupling joint, as shown in Fig. 7.18, is considered in this case. The delamination, situated at the skin-core interface, runs transversely through the breadth of the joint. In order to analyse the dependence of the wave reflection coefficient on the severity of the delamination, several lengths are considered. Delamination lengths within the range [0.001 - 0.009] m, which correspond to ratios [0.1 - 0.9] of the laminate's thickness, are analysed. Variations of the bending and longitudinal waves reflection coefficients with frequency and $k_y$ for different skin-core delamination severities are presented in Figs. 7.24 and 7.25.

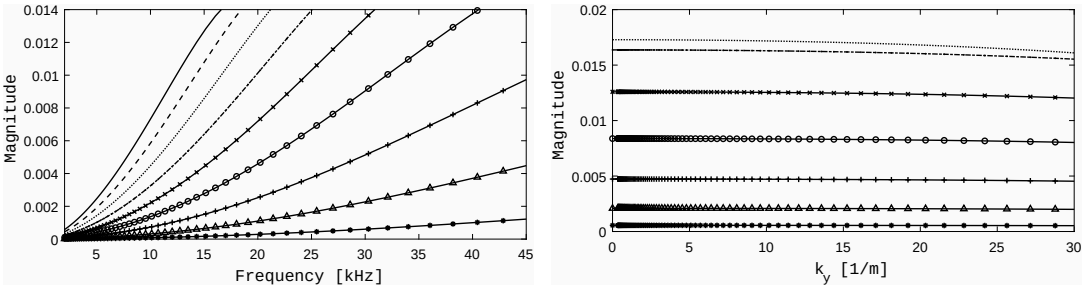


**(a)** w.r.t $\omega$ **(b)** w.r.t. $k_y$

**Figure 7.24:** Bending wave reflection coefficient from the skin-core interlaminar delamination within sandwich laminate, for various severity ratios of the delamination 0.1 (-*), 0.2 (-Δ), 0.3 (-+), 0.4 (-o), 0.5 (-x), 0.6 (-.), 0.7 (. . . ), 0.8 (- -) and 0.9 (-)

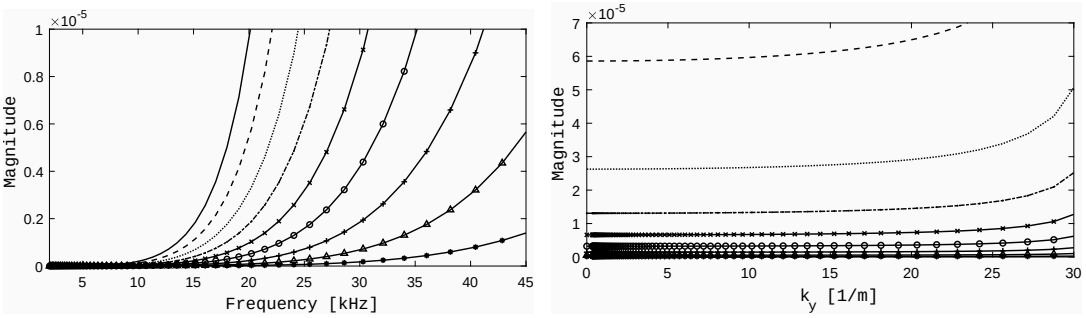


**(a)** w.r.t $\omega$ **(b)** w.r.t. $k_y$

**Figure 7.25:** Longitudinal wave reflection coefficient from the skin-core interlaminar delamination within sandwich laminate, for various severity ratios of the delamination 0.1 (-*), 0.2 (-Δ), 0.3 (-+), 0.4 (-o), 0.5 (-x), 0.6 (-.), 0.7 (. . . ), 0.8 (- -) and 0.9 (-)

With respect to angular frequency, reflection coefficient of the bending wave increases as frequency increases. Reflection coefficient of the longitudinal wave also increases with angular frequency, but slightly. With respect to $k_y$, reflection coefficient of the bending wave changes very slightly over the considered $k_y$ range. Reflection coefficient of the longitudinal wave increases very slightly until high $k_y$ range, then increases more significantly. Generally, reflection coefficient of the waves increases with increase in the delamination severity ratio.

#### 7.4.2.2.4 Dependence of wave interaction coefficient on core interlaminar delamination within the sandwich laminate

Wave reflection from core interlaminar delamination within the laminate's coupling joint, as shown in Fig. 7.18, is considered in this case. The delamination, situated at the mid-height of the joint, runs transversely through the breadth of the joint. In order to analyse the dependence of the wave reflection coefficient on the severity of the delamination, several lengths are considered. Delamination lengths within the range [0.001 - 0.009] m, which correspond to ratios [0.1 - 0.9] of the laminate's thickness, are analysed. Variations of the bending and longitudinal waves reflection coefficients with frequency as well as with $k_y$ for different core delamination severities are presented in Figs. 7.26 and 7.27.

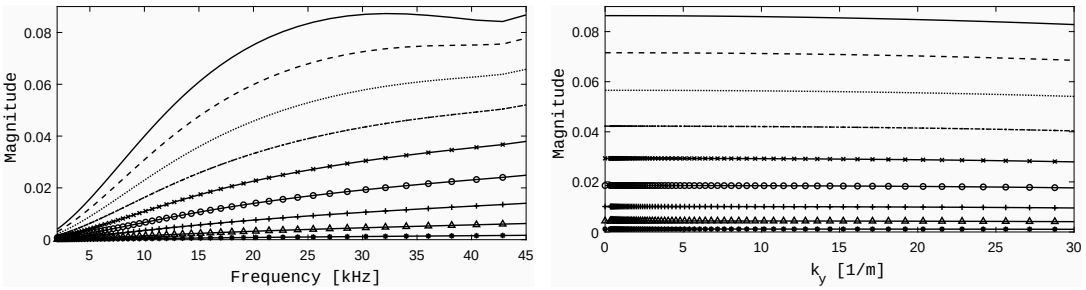


**(a)** w.r.t $\omega$ **(b)** w.r.t. $k_y$

**Figure 7.26:** Bending wave reflection coefficient from the core interlaminar delamination within the sandwich laminate, for various severity ratios of the delamination 0.1 (-*), 0.2 (-Δ), 0.3 (-+), 0.4 (-o), 0.5 (-x), 0.6 (-.), 0.7 (. . . ), 0.8 (- -) and 0.9 (-)

Results obtained follow similar trend as the skin-core delamination. However, the reflection coefficient magnitude are higher in this case.

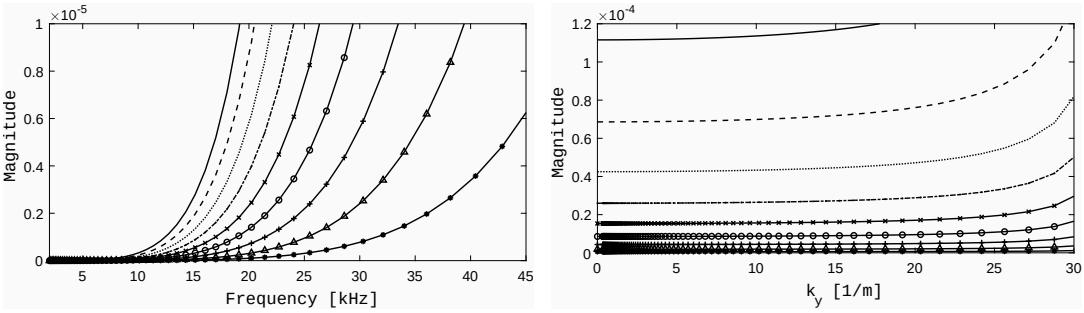


**(a)** w.r.t $\omega$ **(b)** w.r.t. $k_y$

**Figure 7.27:** Longitudinal wave reflection coefficient from the core interlaminar delamination within the sandwich laminate, for various severity ratios of the delamination 0.1 (-*), 0.2 (-Δ), 0.3 (-+), 0.4 (-o), 0.5 (-x), 0.6 (-.), 0.7 (. . . ), 0.8 (- -) and 0.9 (-)

#### 7.4.2.2.5 Comparison of wave interaction coefficient for the different damage modes within the sandwich laminate

Having computed the wave interaction characteristics for different damage modes within the sandwich laminate, it is essential to compare the scattering properties of the damage modes. This provides the basis for establishing optimal parameter for detecting and identifying damage mode based on their wave interaction characteristics.

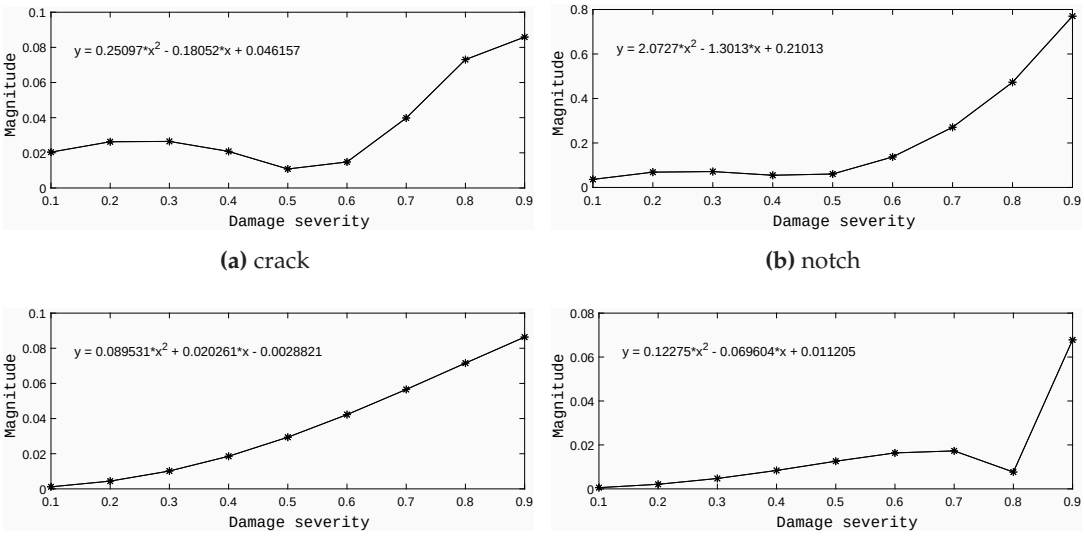


**(a)** crack **(b)** notch

**(c)** core interlaminar delamination **(d)** skin-core interlaminar delamination

**Figure 7.28:** Bending wave reflection coefficient as a function of damage severity (for different damage modes) within the sandwich laminate

Figs. 7.28 and 7.29 present wave reflection coefficient against damage severity for the various damage modes within the sandwich laminate. As observed, crack is much

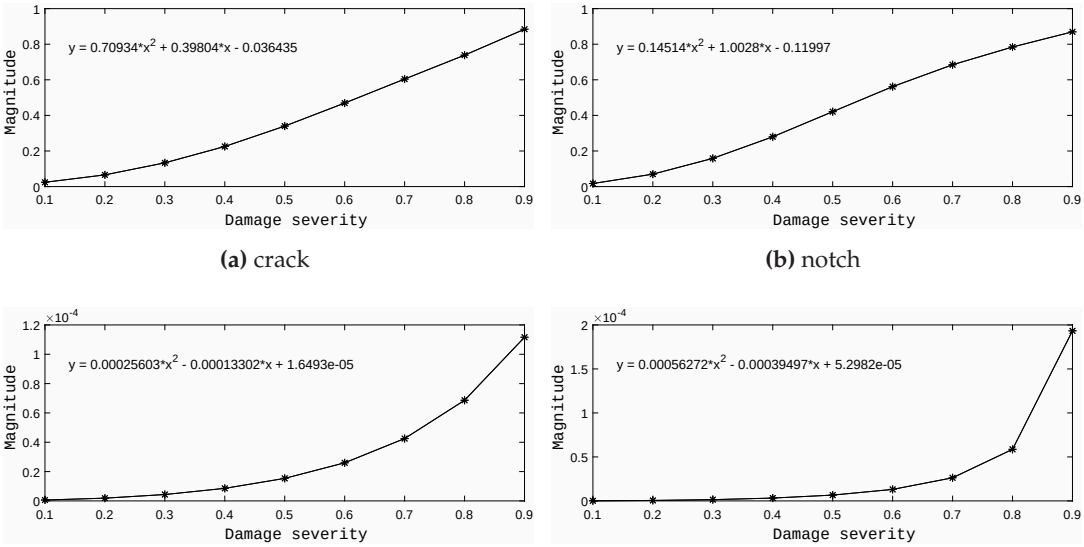


**(a)** crack **(b)** notch

**(c)** core interlaminar delamination **(d)** skin-core interlaminar delamination

**Figure 7.29:** Longitudinal wave reflection coefficient as a function of damage severity (for different damage modes) within the sandwich laminate

more sensitive to longitudinal wave reflection compared to bending wave reflection with an average difference of about 72%. The notch is highly sensitive to both wave modes, but more sensitive to longitudinal wave with an average difference of about 19%. Compared to crack and notch, low reflections are generally observed for the two delamination modes considered. However, the sensitivity of the delaminations to bending wave reflection is much more significant compared to that of longitudinal wave.

From these observations, it therefore follows that bending wave is recommended for detecting interlaminar delaminations within the sandwich laminate while either bending or longitudinal mode is good for detecting crack and notch within the laminate though longitudinal mode is more recommended based on the results. Based on this recommendation and that made for the orthotropic beam, a general recommendation can be reached for horizontally and vertically oriented damage within both composite structural media.

Outcome of this analysis is also applicable for predicting and identifying specific damage type within the structural media using the wave interaction coefficient trend equations.

## 7.5 Conclusions

An FE-based methodology for numerical quantification of wave interaction with damage in two-dimensional periodic structures is presented in this study. The presented

scheme can be applied to structures of arbitrary layering, complexities and material characteristics due to the FE discretisation being employed. The scheme discretises a damaged structural medium into a system of $N$ healthy substructures connected through a joint which bears the structural damage/discontinuity. Wave propagation constants along different propagation directions of the substructures are sought by coupling periodic structure theory with FE. The damaged joint is modelled using standard FE approach, ensuring joint-substructures meshes conformity. This is coupled with the obtained wave propagation constants in order to compute the scattering coefficients of the wave interaction with the damage.

The main outcomes of the work are summarised as:

(i) The scheme is able to quantify wave interaction with damage in arbitrarily multi-layered two-dimensional structures, which may be difficult to solve using the conventional FE method, at a computational time faster than the conventional FE transient approach.

(ii) The presented scheme is validated against theoretical predictions using a cracked aluminium beam. A very good correlation is observed between the two sets of results.

(iii) Wave interaction characteristics for different damage modes and parameters are analysed in order to establish an optimal basis for detecting and identifying damage, as well as assessing the orientation and extent of the damage.

# CHAPTER 8

# General conclusions and future work

## 8.1 General conclusions

In this thesis, computational models for wave propagation as well as interaction phenomena of the wave with damage in periodic layered structures are developed, applied and validated. The principal contributions resulting from this work are:

(i) A wave FE computation scheme is presented for quantifying wave propagation constants for the the waves propagating within one-dimensional periodic structures. Interaction of the waves with damage within the structure is also quantified through the presented scheme. The scheme can be applied to structures of arbitrary complexity, layering and material characteristics as FE discretisation is employed.

(ii) Thermal impact on the wave propagation constants and the wave interaction scattering properties of a sandwich panel is presented. The thermomechanical characteristics of each layer of the panel are separately measured experimentally within a broad temperature range, equivalent to a launch vehicle operating range. The temperature-dependent characteristics are employed to examine thermal impact on the wave propagation and interaction properties. The results exhibited a large divergence in the measured and calculated parameters near and above the glass transition temperature of the sandwich resin. This establishes the significance of temperature (especially at glass transition range) in the design process of aerospace material in order to improve its wave response performance.

(iii) Pre-stress effect on wave interaction with damage within pressurised layered structures is presented and examined. Wave propagation and interaction char-

acteristics in pressurised structures are successfully computed through the developed methodology. It is demonstrated that pressurisation can be employed to enhance damage detection, especially micro defects which may be too insipid to detect under no pressurisation scenario.

(iv) A structural identification technique, based on the wave propagation constants, is developed and applied. The method is able to extract structural layer characteristics which includes thickness, density, elastic and shear moduli and is robust enough to be applied in a broadband frequency range. The exhibited scheme is validated through comparison with experimental results as well as through full FE transient response predictions. Excellent agreement is observed for the identified structural parameters.

(v) A computational scheme for analysing and quantifying wave interaction with nonlinear damage within layered structures is presented. The presented scheme successfully models nonlinear damage using an element birth and death criterion in a commercial FE software, and compute harmonic scattering coefficients for guided wave interaction with the nonlinear structural damage. Results obtained through the developed methodology are validated through comparison with experimental measurements and results presented in open literature for guided wave interaction with damage. Good agreement is generally observed.

(vi) A wave FE methodology for quantifying wave interaction with damage within two-dimensional periodic structures is presented. The scheme is able to quantify wave interaction with damage within arbitrarily multi-layered two-dimensional structures at a computational time faster than the conventional FE transient approach. The presented scheme is validated against theoretical predictions with a very good correlation observed between the two sets of results.

## 8.2 Future work

The exhibited work has shown the potential to serve as a basis to the development and the extension of number of wave propagation and damage detection techniques. However, attempts is made to foresee a number of probable perspective work for continuation of the work presented in this thesis. These include

(i) In this study, wave propagation and interaction phenomena are presented for periodic structures having periodicity in one and two directions respectively. The numerical approach for two-dimensional periodic structures can be improved by

formulating WFE-based superelement models to compute wave properties along the two directions without wave imposition in either direction.

(ii) Impact of two common operating conditions (pressure and temperature) on the acoustic performance of aerospace composite structures are considered in this study. This effort can be extended to other service parameters aerospace structures are subject to during operation.

(iii) The developed wave interaction scheme can be extended for efficient damage identification and structural health diagnosis and prognosis. This will expand the applicability of the presented scheme.

(iv) The scheme can also be extended to model and implement efficient multiscale damage models in order to accurately capture the nonlinear mechanics of advanced damage scenarios, while retaining the size of the FE model and computational effort at acceptable level.

(v) The principal drawback of the presented structural identification approach is the required computational effort. This can range from negligible, when a single structural parameter is sought, to intense, when typically more than three parameters are to be identified and several iterations need to be completed before the Newton's scheme converges to the desired solution. Providing expressions of the wavenumber sensitivity to the investigated structural parameters under investigation can accelerate the convergence process. Drastic computational savings can be attained by solving the WFE model for a fine grid of variables and using a neural-network type approach for extracting the desired parameters.

## 8.3 List of publications

Part of the work presented in this thesis can be found in following publications, which are results of the research conducted during this PhD study:

- Articles in indexed Journals
  - **Apalowo, R.K.** and Chronopoulos, D., 2019. A wave-based numerical scheme for damage detection and identification in two-dimensional composite structures. Composite Structures, 214, pp. 164-182 (Published).
  - **Apalowo, R.K.**, Chronopoulos, D. and Tanner, G., 2018. Wave Interaction with Defects in Pressurised Composite Structures. Journal of Nondestructive Evaluation, 37(3), p.48. (Published).

- **Apalowo, R.K.**, Chronopoulos, D., Ichchou, M., Essa, Y. and Martin De La Escalera, F., 2017. The impact of temperature on wave interaction with damage in composite structures. Proceedings of the Institution of Mechanical Engineers, Part C: Journal of Mechanical Engineering Science, 231(16), pp.3042-3056. (Published).
- Chronopoulos, D., Droz, C., **Apalowo, R.K.**, Ichchou, M. and Yan, W.J., 2017. Accurate structural identification for layered composite structures, through a wave and finite element scheme. Composite Structures, 182, pp.566-578. (Published).
- **Apalowo, R.K.**, Chronopoulos, D. and Cantero-Chinchilla, S. Wave interaction with nonlinear damage and generation of harmonics in composite structures. Composite Structures. (Under review).

• Conference Proceedings

- **Apalowo, R.K.**, Chronopoulos, D. and Malik, M., 2018. A wave and finite element methodology for structural identification in layered composite structures. Proceedings of the 14th International Conference on Vibration Engineering and Technology of Machinery (VETOMAC XIV). 10-13 September 2018, Lisbon Portugal.
- **Apalowo, R.K.**, Chronopoulos, D. and Malik, M., 2018. The influence of temperature on wave scattering of damaged segments within composite structures. Proceedings of the 14th International Conference on Vibration Engineering and Technology of Machinery (VETOMAC XIV). 10-13 September 2018, Lisbon Portugal.
- **Apalowo, R.K.**, Ampatzidis, T., Chronopoulos, D., Ichchou, M., Essa, Y. and De La Escalera, F.M., 2017. Prediction of temperature dependent wave dispersion and interaction properties in composite structures. Proceedings of the 24th International Conference on Sound and Vibration (ICSV24). 23-27 July 2017, London, United Kingdom.
- **Apalowo, R.K.**, Chronopoulos, D. and Thierry, V., Thermal Effect on Wave Interaction in Composite Structures. Proceedings of the 19th International Conference on Aerospace, Mechanical, Automotive and Materials Engineering. January, 19-20, 2017. London, United Kingdom.
- **Apalowo, R.K.**, Chronopoulos, D. and Thierry, V., Wave Interaction with Defects in Pressurized Composite Structures. Proceedings of the 19th International Conference on Aerospace, Mechanical, Automotive and Materials Engineering. 19-20 January 2017, London, United Kingdom.

# Bibliography


[1] M.J.S. Lowe, P. Cawley, J.Y. Kao, and O. Diligent. The low frequency reflection characteristics of the fundamental antisymmetric lamb wave a0 from a rectangular notch in a plate. *The Journal of the Acoustical Society of America*, 112(6):2612–2622, 2002. xvi, 44, 45

[2] D. Chronopoulos, C. Droz, R. Apalowo, M. Ichchou, and W.J. Yan. Accurate structural identification for layered composite structures, through a wave and finite element scheme. *Composite Structures*, 182:566–578, 2017. xvii, 10, 68

[3] J.M. Renno and B.R. Mace. Calculation of reflection and transmission coefficients of joints using a hybrid element/wave and finite element approach. *Journal of Sound and Vibration*, 332:2149–2164, 2013. xviii, 10, 26, 81, 83, 84, 89, 97

[4] W. Hufenbach and C. Holste. Structural-dynamic design of fibre-reinforced structures. *Proceedings of the International SAMPE Europe Conference, Paris*, pages 165–176, 1998. 1

[5] D. S. Forsyth, J.P. Komorowski, R.W. Gould, and A. Marincak. Automation of enhanced visual ndt techniques. *Proceedings 1st Pan-American Conference for NDT, Toronto, Canada*, pages 107–117, 1998. 2

[6] S.J. Vahaviolos. *Acoustic Emission: Standards and Technology Update*. ASTM International, 1999. 2

[7] G. Muravin. *Inspection, Diagnostics and Monitoring of Construction Materials and Structures by the Acoustic Emission Methods*. Minerva Press, London, UK, 2000. 2

[8] G.L. Fitzpatrick, D.K. Thome, R.L. Skaugset, and W.C.L. Shih. Magneto-optic/eddy current imaging of subsurface corrosion and fatigue cracks in aging aircraft. *Review of progress in quantitative NDE, Vol. 15A, D. O. Thompson and D. E. Chimenti (Eds.), Plenum Press, NY*, pages 1159–1166, 1996. 2

[9] B.A. Lepine, B.P. Wallace, D.S. Forsyth, and A. Wyglinski. Pulsed eddy current method developments for hidden corrosion detection in aircraft structures.

*Proceedings 1st Pan-American Conference for NDT, Toronto, Canada*, pages 118–124, 1998. 2

[10] P.D. Wilcox, R.P. Dalton, M.J.S. Lowe, and P. Cawley. Mode transducer selection for long range lamb wave inspection. *Proceedings of the 3rd International Workshop on Damage Assessment Using Advanced Signal Processing-DAMAS, Dublin, Ireland, 28-30 June*, pages 152–161, 1999. 2

[11] B.C. Lee and W.J. Staszewski. Modelling of lamb waves for damage detection in metallic structures, part ii: wave interactions with damage. *Smart Materials and Structures*, 12(5):815–824, 2003. 2

[12] R. E. Green. Emerging technologies for nde of aging aircraft structures. *Proceedings of the Workshop on Intelligent NDE Sciences for Aging and Futuristic Aircraft, C. Ferregut, R. Osegueda and A. Nunez (Eds.), UTEP, El Paso, TX*, pages 267–278, 1997. 2

[13] M. Lasser and G. Harrison. A real time, high resolution imaging system for aging aircraft inspection. *Proceedings of the Workshop on Intelligent NDE Sciences for Aging and Futuristic Aircraft, C. Ferregut, R. Osegueda and A. Nunez (Eds.) UTEP, El Paso, TX*, pages 1–9, 1997. 2

[14] P. Cawley and R.D. Adams. The location of defeats in structures from measurements of natural frequencies. *Journal of Strain Analysis*, 4(2):49–57, 1979. 2

[15] G. Manson, K. Worden, and D.J. Allman. Experimental validation of a structural health monitoring methodology, part iii: Damage location on an aircraft wing. *Journal of Sound and Vibration*, 259(2):365–385, 2003. 2

[16] K.W. Dolan, D.J. Schnebeck, R.D. Albert, and T.M. Albert. Reverse geometry x-ray imaging for ndt applications. *Proceedings of the JANNAF NDE Subcommittee Meeting, CPIA*, 1993. 2

[17] K.Y. Jhang. Nonlinear ultrasonic techniques for non-destructive assessment of micro damage in material: a review. *International Journal of Materials*, 10:123–135, 2009. 2

[18] W. Kruse and A. Zagrai. Investigation of linear and nonlinear electromechanical impendance techniques for detection of fatigue damage in aerospace materials. *7th international workshop on structural health monitoring, Stanford, CA*, 2009. 2

[19] Eleni N Chatzi and Andrew W Smyth. Particle filter scheme with mutation for the estimation of time-invariant parameters in structural health monitoring applications. *Structural Control and Health Monitoring*, 20(7):1081–1095, 2013. 3

[20] Manolis N Chatzis, Eleni N Chatzi, and Andrew W Smyth. On the observability and identifiability of nonlinear structural and mechanical systems. *Structural Control and Health Monitoring*, 22(3):574–593, 2015.

[21] Ka-Veng Yuen and Lambros S Katafygiotis. Bayesian time–domain approach for modal updating using ambient data. *Probabilistic Engineering Mechanics*, 16(3): 219–231, 2001.

[22] Christof Devriendt and Patrick Guillaume. The use of transmissibility measurements in output-only modal analysis. *Mechanical Systems and Signal Processing*, 21(7):2689–2696, 2007.

[23] Wang-Ji Yan and Wei-Xin Ren. Operational modal parameter identification from power spectrum density transmissibility. *Computer-Aided Civil and Infrastructure Engineering*, 27(3):202–217, 2012.

[24] T Kijewski and A Kareem. Wavelet transforms for system identification in civil engineering. *Computer-Aided Civil and Infrastructure Engineering*, 18(5):339–355, 2003.

[25] AN Robertson, KC Park, and KF Alvin. Extraction of impulse response data via wavelet transform for structural system identification. *Journal of vibration and acoustics*, 120(1):252–260, 1998. 3

[26] Jann N Yang, Silian Lin, Hongwei Huang, and Li Zhou. An adaptive extended kalman filter for structural damage identification. *Structural Control and Health Monitoring*, 13(4):849–867, 2006. 3, 58

[27] James L Beck. Bayesian system identification based on probability logic. *Structural Control and Health Monitoring*, 17(7):825–847, 2010. 3, 58

[28] Wang-Ji Yan and Lambros S Katafygiotis. A novel bayesian approach for structural model updating utilizing statistical modal information from multiple setups. *Structural Safety*, 52:260–271, 2015.

[29] Ka-Veng Yuen and Lambros S Katafygiotis. Bayesian fast fourier transform approach for modal updating using ambient data. *Advances in Structural Engineering*, 6(2):81–95, 2003. 3

[30] Marco Matter, Thomas Gmür, Joël Cugnoni, and Alain Schorderet. Identification of the elastic and damping properties in sandwich structures with a low core-to-skin stiffness ratio. *Composite Structures*, 93(2):331–341, 2011. 3

[31] Christophe Droz, Olivier Bareille, and Mohamed N Ichchou. A new procedure for the determination of structural characteristics of sandwich plates in medium frequencies. *Composites Part B: Engineering*, 112:103–111, 2017. 3, 68, 69

[32] I. Newton. *The Principia: mathematical principles of natural philosophy*. Univ of California Press, 1687. 3

[33] G. Floquet. Sur les equations differentielles lineaires. *Ann. ENS [2]*, 12(1883): 47–88, 1883. 4

[34] Daniel Bernoulli. Mixing several species of simple isochronous vibrations that can coexist in the same body system, 1755. 4

[35] C Truesdell. Taylor's analysis of the continuous vibrating string (1713). In *The Rational Mechanics of Flexible or Elastic Bodies 1638–1788*, pages 129–132. Springer, 1960. 4

[36] Leonhard Euler. sharing of motions in the collision of which do not directly brushing. ., pages 50–76, 1744. 4

[37] Joseph-Louis Lagrange. Research on the nature and propagation of sound. *Miscellanea Taurinensia*, 1:39–148, 1759. 4

[38] A. Cauchy. Lecture presented to the french academy of sciences. *Unpublished, Paris Google Scholar*, 1822. 4

[39] Lord Rayleigh. Xvii. on the maintenance of vibrations by forces of double frequency, and on the propagation of waves through a medium endowed with a periodic structure. *The London, Edinburgh, and Dublin Philosophical Magazine and Journal of Science*, 24(147):145–159, 1887. 4

[40] Felix Bloch. Über die quantenmechanik der elektronen in kristallgittern. *Zeitschrift für physik*, 52(7-8):555–600, 1929. 4

[41] L. Brillouin. *Wave propagation in periodic structures*. Dover Publication, Inc. NY, 1953. 4

[42] L Cremer and HO Leilich. Zur theorie der biegekettenleiter. *On Theory of Flexural Periodic Systems), Arch. Elektr. Uebertrag*, 7:261–270, 1953. 6

[43] John W Miles. Vibrations of beams on many supports. *Journal of the Engineering Mechanics Division*, 82(1):1–9, 1956. 6

[44] Manfred A Heckl. Investigations on the vibrations of grillages and other simple beam structures. *The Journal of the Acoustical Society of America*, 36(7):1335–1343, 1964. 6

[45] D.J. Mead. Wave propagation in continuous periodic structures: research contributions from southampton, 1964–1995. *Journal of Sound and Vibration*, 190(3): 495–524, 1996. 6, 8

[46] R. M. Crane and A. L. Santiago. Modal testing of composite cylinders, dynamic characterization of advanced materials. *ASME*, 16:41–49, 1993. 6

[47] D. Chronopoulos, M. Ichchou, B. Troclet, and O. Bareille. Computing the broadband vibroacoustic response of arbitrarily thick layered panels by a wave finite element approach. *Applied Acoustics*, 77:89–98, 2014. 6

[48] G. Kirchhoff. Uber das gleichgewicht und die bewegung einer elastischen schribe. *J. Reine Angew. Math*, 40:51–58, 1850. 7

[49] A.E.H. Love. *The mathematical theory of elasticity*. Cambridge University Press, 1934. 7

[50] S. Timoshenko. *Theory of elasticity*. McGraw-Hill, New York, 1934. 7

[51] R. Rolfes and K. Rohwer. Improved transverse shear stresses in composite finite element base on first order shear deformation theory. *International Journal for Numerical Methods in Engineering*, 40(1):51–60, 1997. 7

[52] E. Reissner. The effect of transverse shear deformation on the bending of elastic plates. *Journal of Applied Mechanics*, 12:69–76, 1945. 7

[53] R.D. Mindlin. Influence of rotatory inertia and shear in flexural motions of isotropic elastic plates. *Journal of Applied Mechanics*, 18:1031–1036, 1951. 7

[54] Y. Stavsky. Bending and stretching of laminated anisotropic plates. *American Society Civil Engineers*, 87:31–56, 1961. 7

[55] J. Whitney and N. Pagano. Shear deformation in heterogeneous anisotropic plates. *Journal of Applied Mechanics*, 37:1031–1036, 1970. 7

[56] G. Kurtze and B.G. Watters. New wall design for high transmission loss or high damping. *Journal of the Acoustical Society of America*, 31:739–748, 1959. 7

[57] C.L. Dym and M.A. Lang. Transmission of sound through sandwich panels. *Journal of the Acoustical Society of America*, 56:1523–1532, 1974. 7

[58] J.A. Moore and R.H. Lyon. Sound transmission loss characteristics of sandwich panel constructions. *Journal of the Acoustical Society of America*, 89:777–791, 1991. 7

[59] S.A. Ambartsumian. On the theory of bending plates. *Izv Otd Tech Nauk AN SSSR*, 5:69–77, 1958. 7

[60] H. Matsunaga. Buckling instabilities of thick elastic plates subjected to in-plane stresses. *Computers and Structures*, 62(1):205–214, 1997. 7

[61] K.P. Soldatos and T. Timarci. A unified formulation of laminated composite, shear deformable, five-degrees-of-freedom cylindrical shell theories. *Computers and Structures*, 25(1–4):165–171, 1993. 7

[62] V. Sokolinsky and S. Nutt. Consistent higher-order dynamic equations for soft-core sandwich beams. *AIAA Journal*, 42:374–382, 2004. 7

[63] K. Swaminathan and S.S. Patil. Analytical solution using a higher order refined computational model with 12 degrees of freedom for the free vibration analysis of antisymmetric angle-ply plates. *Computers and Structures*, 82(2):209–216, 2008. 7

[64] G.W. Swift and R.A. Heller. Layered beam analysis. *Journal of the Engineering Mechanics Division, ASCE*, 100:267–282, 1974. 7

[65] L.L. Durocher and R. Solecki. Bending and vibration of isotropic two-layer plates. *AIAA Journal*, 13:1522–1523, 1975. 7

[66] P. Seide. An improved approximate theory for the bending of laminated plates. *Mechanics Today*, 5:451–466, 1980. 7

[67] R.A. Chaudhuri and P. Seide. Triangular finite element for analysis of thick laminated plates. *International Journal for Numerical Methods in Engineering*, 24:1203–1224, 1987. 7

[68] S. Ghinet and N. Atalla. Vibro-acoustic behaviors of flat sandwich composite panels. *Transactions of the Canadian Society for Mechanical Engineering*, 30(4):473–493, 2006. 7

[69] S. Ghinet, N. Atalla, and H. Osman. The transmission loss of curved laminates and sandwich composite panels. *Journal of the Acoustical Society of America*, 78(2): 774–790, 2005. 61

[70] S. Ghinet and N. Atalla. Modeling thick composite laminate and sandwich structures with linear viscoelastic damping. *Computers and Structures*, 89:15–16, 2011. 7

[71] E.C. Pestel and F.A. Leckie. *Matrix Methods in Elastomechanics*. McGraw-Hill, 1963. 8

[72] W.T. Thompson. Transmission of elastic waves through a stratified solid medium. *Journal of Applied Physics*, 21, 1950. 8

[73] Y.K. Lin and T.J. McDaniel. Dynamics of beam-type periodic structures. *Journal of Manufacturing Science and Engineering*, 91:1133–1141, 1969. 8

[74] H. Nayfeh. The general problem of elastic wave propoagation in multi-layered anisotropic media. *Journal of the Acoustical Society of America*, 89:1521–1531, 1991. 8

[75] Y.K. Lin and J.N. Yang. Free vibration of a disordered periodic beam. *Journal of Applied Mechanics*, 41(2):383–391, 1974. 8

[76] WX Zhong and FW Williams. On the direct solution of wave propagation for repetitive structures. *Journal of Sound and Vibration*, 181(3):485–501, 1995. 8

[77] C.G. Papaleontiou. *Dynamic Analysis of Building Structures under Combined Horizontal and Vertical Vibrations*. PhD thesis, University of Texas, 1992. 8

[78] J. R. Banerjee. Dynamic stiffness formulation for structural elements: a general approach. *Computers & Structures*, 63(1):101–103, 1997. 8

[79] J. R. Banerjee. Free vibration of sandwich beams using the dynamic stiffness method. *Computers & Structures*, 81(18–19):1915–1922, 2003. 8

[80] S. Gopalakrishnan and J. F. Doyle. Wave propagation in connected waveguides of varying cross-section. *Journal of Sound and Vibration*, 175:374–363, 1994. 8

[81] M. Martin, S. Gopalakrishnan, and J.F. Doyle. Wave propagation in multiply connected deep waveguides. *Journal of Sound and Vibration*, 174:521–538, 1993. 8

[82] R.S. Langley. Analysis of power flow in beams and frameworks using the direct-dynamic stiffness matrix method. *Journal of Sound and Vibration*, 136(3):439–452, 1990. 8

[83] J. Lee and D.J. Thompson. Dynamic stiffness formulation, free vibration and wave motion of helical springs. *Journal of Sound and Vibration*, 239(2):297–320, 2001. 8

[84] J. R. Banerjee and F. W. Williams. Vibration of composite beams-an exact method using symbolic computation. *J. Aircraft*, 32:636–642, 1995. 8

[85] J.E. Mottershead and Y.M. Ram. Inverse eigenvalue problems in vibration absorption: passive modification and active control. *Mechanical Systems and Signal Processing*, 20(1):5–44, 2006. 9

[86] B.N. Datta, S. Elhay, and Y. Ram. Orthogonality and partial pole assignment for the symmetric definite quadratic pencil. *Linear Algebra and Its Applications*, 257: 29–48, 1997. 9

[87] M.G. Tehrani, J.E. Mottershead, A.T. Shenton, and Y.M. Ram. Robust pole placement in structures by the method of receptances. *Mechanical Systems and Signal Processing*, 25(1):112–122, 2011. 9

[88] D.J. Mead and S. Markus. Coupled flexural-longitudinal wave motion in a periodic beam. *Journal of Sound and Vibration*, 90:1–24, 1983. 9

[89] D.J. Mead. Wave propagation and natural modes in periodic systems: I. monocoupled systems. *Journal of Sound and Vibration*, 40:1–18, 1975. 9

[90] D.J. Mead. Wave propagation and natural modes in periodic systems: Ii. multicoupled systems, with and without damping. *Journal of Sound and Vibration*, 40: 19–39, 1975. 9

[91] J.F. Doyle. *Wave Propagation in Structures: Spectral Analysis Using Fast Discrete Fourier Transforms*. Springer, 1997. 9, 40, 109, 112

[92] A. Chackraborty and S. Gopalakrishnan. A spectrally formulated finite element for wave propagation analysis in layered composite media. *International Journal of Solid and Structures*, 41:5155–5183, 2004. 9

[93] J. B. Casimir, S. Kevorkian, and T. Vinh. The dynamic stiffness matrix of two-dimensional elements: application to kirchhoff's plate continuous element. *Journal of Sound and Vibration*, 287:571–589, 2005. 9

[94] M. Ruzzene. Vibration and sound radiation of sandwich beams with honeycomb truss core. *Journal of Sound and Vibration*, 277:741–763, 2004. 9

[95] D.R. Mahapatra and S. Gopalakrishnan. A spectral finite element for analysis of wave propagation in uniform composite tubes. *Journal of Sound and Vibration*, 268:429–463, 2003. 9

[96] U. Lee and J. Kim. Dynamics of elastic-piezoelectric two-layer beams using spectral element method. *International Journal of Solids and Structures*, 37:4403–4417, 2000. 9

[97] R. Ruotolo. A spectral element for laminated composite beams: theory and application to pyroshock analysis. *Journal of Sound and Vibration*, 270:149–169, 2004. 9

[98] F. Birgersson. Prediction of random vibration using spectral methods. *KTH, Stockholm*, 2004. 9

[99] L. Gavric. Computation of propagative waves in free rail using a finite element technique. *Journal of Sound and Vibration*, 185:531–543, 1995. 9

[100] S. Finnveden. Evaluation of modal density and group velocity by a finite element method. *Journal of Sound and Vibration*, 273:51–75, 2004. 9

[101] C.M. Nilsson. *Waveguide Finite Elements Applied on a Car Tyre*. PhD thesis, Department of Aeronautical and Vehicle Technology, Royal Institute of Technology, Sweden, 2004. 9

[102] S.B. Dong and K.H. Huang. Edge vibrations in laminated composite plates. *Journal of Applied Mechanics*, 52:433–438, 1985. 9

[103] S.K. Datta, A.H. Shah, R.L. Bratton, and T. Chakraborty. Wave propagation in laminated composite plates. *Journal of the Acoustical Society of America*, 83(6):2020–2026, 1988. 9

[104] D.J. Mead. A general theory of harmonic wave propagation in linear periodic systems with multiple coupling. *Journal of Sound and Vibration*, 27:235–260, 1973. 10, 40, 97

[105] Brian R Mace, Denis Duhamel, Michael J Brennan, and Lars Hinke. Finite element prediction of wave motion in structural waveguides. *The Journal of the Acoustical Society of America*, 117(5):2835–2843, 2005. 10, 14, 16, 26, 40, 97, 103

[106] E. Manconi and B.R. Mace. Modelling wave propagation in two-dimensional structures using a wave/finite element technique. *ISVR Technical Memorandum*, 2007. 10, 97

[107] J.M. Mencik. A wave finite element-based formulation for computing the forced response of structures involving rectangular flat shells. *International Journal for Numerical Methods in Engineering*, 95(2):91–120, 2013. 10

[108] W.J. Zhou and M.N. Ichchou. Wave propagation in mechanical waveguide with curved members using wave finite element solution. *Computer Methods in Applied Mechanics and Engineering*, 199(33-36):2099–2109, 2010. 10

[109] J.M. Renno and B.R. Mace. Calculating the forced response of cylinders and cylindrical shells using the wave and finite element method. *Journal of Sound and Vibration*, 333(21):5340–5355, 2014. 10

[110] J.M. Mencik and M.N. Ichchou. Multi-mode propagation and diffusion in structures through finite elements. *European Journal of Mechanics-A/Solids*, 24(5):877–898, 2005. 10

[111] D. Duhamel, B.R. Mace, and M.J. Brennan. Finite element analysis of the vibrations of waveguides and periodic structures. *Journal of sound and vibration*, 294 (1-2):205–220, 2006. 10

[112] J.M. Renno and B.R. Mace. On the forced response of waveguides using the wave and finite element method. *Journal of Sound and Vibration*, 329(26):5474–5488, 2010.

[113] J.M. Mencik. On the low-and mid-frequency forced response of elastic structures using wave finite elements with one-dimensional propagation. *Computers & Structures*, 88(11-12):674–689, 2010. 10

[114] P.B. Silva and J.R.F. Arruda. Wave spectral finite element analysis of two-dimensional waveguides. *Civil-Comp Press Stirlingshire*, 2012. 10

[115] W.J. Zhou, M.N. Ichchou, and J.M. Mencik. Analysis of wave propagation in cylindrical pipes with local inhomogeneities. *Journal of Sound and Vibration*, 319 (1):335–354, 2009. 10

[116] G. Mitrou, N. Ferguson, and J. Renno. Wave transmission through two-dimensional structures by the hybrid fe/wfe approach. *Journal of Sound and Vibration*, 389:484–501, 2017. 10, 97

[117] M.N. Ichchou, J.M. Mencik, and W. Zhou. Wave finite elements for low and mid-frequency description of coupled structures with damage. *Computer methods in applied mechanics and engineering*, 198(15-16):1311–1326, 2009. 10

[118] T.L. Huang, M.N. Ichchou, and O.A. Bareille. Multi-mode wave propagation in damaged stiffened panels. *Structural Control and Health Monitoring*, 19(5):609–629, 2012. 10

[119] V. Cotoni, R.S. Langley, and P.J. Shorter. A statistical energy analysis subsystem formulation using finite element and periodic structure theory. *Journal of Sound and Vibration*, 318:1077–1088, 2008. 10

[120] D. Chronopoulos, M. Ichchou, B. Troclet, and O. Bareille. Predicting the broadband vibroacoustic response of systems subject to aeroacoustic loads by a krylov subspace reduction. *Applied Acoustics*, 74(12):1394–1405, 2013. 10

[121] R.K. Apalowo, D. Chronopoulos, and G. Tanner. Wave interaction with defects in pressurised composite structures. *Journal of Nondestructive Evaluation*, 37(3):48, 2018. 10

[122] R.K. Apalowo, D. Chronopoulos, M. Ichchou, Y. Essa, and F. Martin De La Escalera. The impact of temperature on wave interaction with damage in composite structures. *Proceedings of the Institution of Mechanical Engineers, Part C: Journal of Mechanical Engineering Science*, 231(16):3042–3056, 2017. 10

[123] R. Talreja and C.V. Singh. *Damage and Failure of Composite Materials*. Damage and Failure of Composite Materials. Cambridge University Press, 2012. 19

[124] R.B. Heslehurst. *Defects and damage in composite materials and structures*. CRC Press, 2014. 19

[125] A. Nag, D.R. Mahapatra, S. Gopalakrishnan, and T.S. Sankar. A spectral finite element with embedded delamination for modeling of wave scattering in composite beams. *Composites science and Technology*, 63(15):2187–2200, 2003. 20

[126] S. S. Kessler, S. M. Spearing, and C. Soutis. Damage detection in composite materials using lamb wave methods. *Smart Materials and Structures*, 11:269–278, 2002. 25, 40, 58

[127] C. Y. Lee, B. S. Thompson, and M. V. Gandhi. Temperature-dependent dynamic mechanical properties of polymeric laminated beams. *J. Eng. Mater. Technol*, 110 (2):174–179, 1988. 25

[128] A. J. Barker and H. Vangerko. Temperature dependent elastic constants of cfrp composites. *Composites*, 14(1):52–56, 1983. 25

[129] A. J. Barker and H. Vangerko. Temperature dependent dynamic shear properties of cfrp composites. *Composites*, 14(2):141–144, 1983. 25

[130] A. K. Noor and U. S. Burton. Computational models for high temperature multilayered composite plates and shells. *Appl Mech Rev*, 45(10):419–446, 1992. 26

[131] Y. I. Dimitrienko. Thermomechanical behaviour of composite materials and structures under high temperature: 1. materials, composites. *Part A. Applied Science and Manufacturing*, 28:463–471, 1997. 26

[132] Y. I. Dimitrienko. Thermomechanical behaviour of composite materials and structures under high temperature: 2. structures, composites. *Part A. Applied Science and Manufacturing*, 28:453–461, 1997. 26

[133] G. M. McNally, M. P. McCourt, and P. L. Spedding. The effect of rapid high temperature excursions on the moisture absorption and dynamic mechanical properties of carbon fibre epoxy composite materials, development in chemical engineering and mineral processing. *Asia-Pacific Journal of Chemical Engineering*, 12 (1):169–178, 2004. 26

[134] O. Putkis, R. P. Dalton, and A. J. Croxford. The influence of temperature variations on ultrasonic guided waves in anisotropic cfrp plates. *Ultrasonic*, 60:109–116, 2015. 26

[135] G. Konstantinidis, P. D. Wilcox, and B. W. Drinkwater. The long-term stability of guided wave structural health monitoring systems. review of progress in quantitative nondestructive evaluation. *American Institute of Physics*, 25B:1702–1709, 2006. 26

[136] G. Konstantinidis, B. W. Drinkwater, and P. D. Wilcox. The temperature stability of guided wave structural health monitoring systems. *Smart Materials and Structures*, 15:967–976, 2006. 26

[137] T. Clarke, P. Cawley, P. D. Wilcox, and A. J. Croxford. Evaluation of the damage detection capability of a sparse-array guided-wave shm system applied to a complex structure under varying thermal conditions. *IEEE Transactions on Ultrasonics Ferroelectrics and Frequency Control*, 56:2666–2678, 2009. 26

[138] T. Clarke, P. D. Wilcox, and P. Cawley. Guided wave health monitoring of complex structures by sparse array systems: influence of temperature changes on performance. *Journal of Sound and Vibration*, 329:2306–2322, 2010. 26

[139] E. Blaise and F. K. Chang. Built-in diagnostics for debonding in sandwich structures under extreme temperatures. *in Proceedings of the Third International Workshop on Structural Health Monitoring, Stanford University*, pages 154–163, 2001. 26

[140] B. C. Lee, G. Manson, and W. J. Staszewski. Environmental effects on lamb wave responses from piezoceramic sensors. *Material Science Forum*, 440–441:195–202, 2003. 26

[141] M. J. Schulz, M. J. Sundaresan, J. Mcmichael, D. Clayton, R. Sadler, and B. Nagel. Piezoelectric materials at elevated temperature. *Journal of Intelligent Material Systems and Structures*, 14:693–705, 2003. 26

[142] F. L. di Scalea and S. Salamone. Temperature effects in ultrasonic lamb wave structural health monitoring systems. *Journal of Acoustical Society of America*, 124: 161–174, 2008. 26

[143] A. Marzani and S. Salamone. Numerical prediction and experimental verification of temperature effect on plate waves generated and received by piezoceramic sensors. *Mechanical Systems and Signal Processing*, 30:204–217, 2012. 26

[144] E. J. Cross and K. Worden. Approaches to nonlinear cointegration with a view towards applications in shm. *Journal of Physics: Conference Series*, 305:12069–12078, 2011. 26

[145] E. J. Cross, K. Worden, and Q. Chen. Cointegration: a novel approach for the removal of environmental trends in structural health monitoring data. *Proceedings of the Royal Society of London*, 467:2712–2732, 2011. 26

[146] K. Worden, E. J. Cross, and A. Kyprianou. Cointegration and nonstationarity in the context of multiresolution analysis. *Journal of Physics: Conference Series*, 305: 12004–12015, 2011. 26

[147] P. B. Dao and W. J. Staszewski. Cointegration approach for temperature effect compensation in lamb-wave-based damage detection. *Smart Materials and Structures*, 22, 2013. 26

[148] R. S. Langley and P. J. Shorter. The wave transmission coefficients and coupling loss factors of point connected structures. *Journal of the Acoustical Society of America*, 113:1947–1964, 2003. 26

[149] R. S. Langley and K. H. Heron. Elastic wave transmission through plate/beam junctions. *Journal of Sound and Vibration*, 143(2):241–253, 1990. 26

[150] I. Bosman and T. Nightingale. modelling vibrational energy transmission at bolted junctions between a plate and a stiffening rib. *Journal of the Acoustical Society of America*, 109(3):999–1010, 2001. 26

[151] S. A. F. M. Ishak, J. M. Horner, and S. J. Walsh. modelling and experimentation of vibration transmission through an angled joint. *42nd International Conference and Exposition on Noise Control Engineering, Innsbruck, Austria*, 2013. 26

[152] S. K. Lee, B. R. Mace, and Brennan M. J. Wave propagation, reflection and transmission in curved beams. *Journal of Sound and Vibration*, 306(3-5):636âĂŞ–656, 2007. 26

[153] M. Rucka, W. Witkowski, J. Chroscielewski, and K. Wilde. Damage detection of a t-shaped panel by wave propagation analysis in the plane stress. *Archives of Civil Engineering*, 58(1):3–24, 2012. 26

[154] M. Rucka. Experimental and numerical study on damage detection in an l-joint using guided wave propagation. *Journal of Sound and Vibration*, 329(10):1760–1779, 2010. 26

[155] S. P. Shone, B. R. Mace, and T. P. Waters. Estimation of reflection and transmission coefficients using the spectral element method: application to crack modelling in beams. In *International Conference on Noise and Vibration Engineering, Leuven 2004*, pages 187–200. ISMA, 2004. 26

[156] C. H. Wang and L. R. F. Rose. Wave reflection and transmission in beams containing delamination and inhomogeneity. *Journal of Sound and Vibration*, 264(4): 851–872, 2003. 26

[157] W. J. Zhou and M. N. Ichchou. Wave scattering by local defect in structural waveguide through wave finite element method. *Structural Health Monitoring*, 10(4):335–349, 2011. 26

[158] J. M. Renno and B. R. Mace. Vibration modelling of structural networks using a hybrid finite element/wave and finite element approach. *Wave Motion*, 51(4): 566–580, 2014.

[159] E. Manconi and B. R. Mace. Modelling wave propagation in two-dimensional structures using finite element analysis. *ISVR Technical Memorandum*, 318(4–5): 884–902, 2008. 26

[160] D.C. Worlton. Ultrasonic testing with lamb waves. *Non-Destructive Testing*, 15: 218–222, 1957. 39

[161] J.L. Rose. *Ultrasonic waves in solid media*. Cambridge University Press, 2004. 39

[162] D.M. Donskoy and A.M. Sutin. Vibro-acoustic modulation nondestructive evaluation technique. *Journal of intelligent material systems and structures*, 9:765–771, 1998.

[163] Z. Su, C. Zhou, M. Hong, L. Cheng, Q. Wang, and X. Qing. Acousto-ultrasonic based fatigue damage characterization: Linear versus nonlinear signal features. *Mechanical Systems and Signal Processing*, 45:225–239, 2014. 39, 73

[164] M.J.S. Lowe. Matrix techniques for modelling ultrasonic waves in multi-layered media. *IEEE Transactions on Ultrasonic, Ferroelectrics and Frequency Control*, 42: 525–542, 1995. 39

[165] Y. Young and Y.K. Lin. Dynamic response analysis of truss-type structural networks: a wave propagation approach. *Journal of Sound and Vibration*, 155:375–381, 1992. 39

[166] R.G. Hutchinson and N.A. Fleck. The structural performance of the periodic truss. *Journal of the Mechanics and Physics of Solids*, 54:756–782, 2006. 39

[167] B.R. Mace. Wave reflection and transmission in beams. *Journal of Sounds and Vibration*, 72:237–246, 1984. 39

[168] B. Chouvion, A.A. Popov, S. McWilliam, and C.H.J. Fox. Vibration modelling of complex waveguide structures. *Computers and Structures*, 89:1253–1263, 2011. 39

[169] WC. Yuana, L. Zhoua, and FG. Yuanb. Wave reflection and transmission in composite beams containing semi-infinite delamination. *Journal of Sounds and Vibration*, 313:676–695, 2007. 39

[170] B. Hosten and M. Castaings. Finite elements methods for modeling the guided waves propagation in structures with weak interfaces. *Journal of Acoustical Society of America*, 117:1108–1113, 2005. 40

[171] T. Pialucha and P. Cawley. The reflection of ultrasound from interface layers in adhesive joints. *Review of Progress in Quantitative Non-destructive Evaluation*, 10B: 1303–1309, 1991. 40

[172] R.C.N. Leung and R.J. Pinnington. Wave propagation through right-angled joints with compliance: Longitudinal incidence wave. *Journal of Sound and Vibration*, 153:223–237, 1992. 40

[173] A. H. Nayfeh and D. E. Chimenti. Ultrasonic wave reflection from liquid-coupled orthotropic plates with application to fibrous composites. *Journal of Applied Mechanics*, 55:863–870, 1988. 40

[174] R. Langley. A note on the force boundary conditions for two-dimensional periodic structures with corner freedoms. *Journal of Sounds and Vibration*, 167:377–381, 1993. 40

[175] Y. Waki, B.R. Mace, and M.J. Brennan. Numerical issues concerning the wave and finite element method for free and forced vibration of waveguides. *Journal of Sound and Vibration*, 327(1-2):92–108, 2009. 40

[176] Michael Bagshaw. Commercial aircraft cabin altitude. *Journal of the Royal Society of Medicine*, 100(2):64–64, 2007. 40

[177] R.D. Cook. *Concepts and Applications of Finite Element Analysis*. John Wiley and Sons. New York., second edition, 1981. 41

[178] ANSYS. *ANSYS 14.0 User's Help*, 2014. 41, 77, 151

[179] Bart Peeters and Guido De Roeck. Reference-based stochastic subspace identification for output-only modal analysis. *Mechanical systems and signal processing*, 13(6):855–878, 1999. 58

[180] Zhongqing Su, Lin Ye, and Ye Lu. Guided lamb waves for identification of damage in composite structures: A review. *Journal of sound and vibration*, 295(3):753–780, 2006. 58

[181] CT Ng, M Veidt, LRF Rose, and CH Wang. Analytical and finite element prediction of lamb wave scattering at delaminations in quasi-isotropic composite laminates. *Journal of Sound and Vibration*, 331(22):4870–4883, 2012. 58

[182] Gang Yan. A bayesian approach for damage localization in plate-like structures using lamb waves. *Smart Materials and Structures*, 22(3):03501–2, 2013. 58

[183] Gary C Cohen and Qing Huo Liu. Higher-order numerical methods for transient wave equations. *The Journal of the Acoustical Society of America*, 114(1):21–21, 2003. 60

[184] Enrico GM Brignoli, Marino Gotti, and Kenneth H Stokoe. Measurement of shear waves in laboratory specimens by means of piezoelectric transducers. *Geotechnical Testing Journal*, 19(4):384–397, 1996. 60

[185] Ian J Collison, Theodosia Stratoudaki, Matt Clark, and Mike G Somekh. Measurement of elastic nonlinearity using remote laser ultrasonics and cheap optical transducers and dual frequency surface acoustic waves. *Ultrasonics*, 48(6):471–477, 2008. 60

[186] D. Chronopoulos. Design optimization of composite structures operating in acoustic environments. *Journal of Sound and Vibration*, 355:322–344, 2015. 62

[187] M. Breazeale and D. Thompson. Finite-amplitude ultrasonic waves in aluminum. *Applied Physics Letters*, 3:77–78, 1963. 73

[188] A. Vakakis. Scattering of structural waves by nonlinear elastic joints. *Journal of Vibration and Acoustics*, 115:403–410, 1993. 73

[189] P.B. Nagy. Fatigue damage assessment by nonlinear ultrasonic materials characterisation. *Ultrasonics*, 36:375–381, 1998. 73

[190] C. Pecorari. Nonlinear interaction of plane ultrasonic waves with an interface between rough surfaces in contact. *The Journal of the Acoustical Society of America*, 113:3065–3072, 2003. 73

[191] A.J. Croxford, P.D. Wilcox, B.W. Drinkwater, and P.B. Nagy. The use of noncollinear mixing for nonlinear ultrasonic dtection of plasticity and fatigue. *The Journal of the Acoustical Society of America*, 126:117–122, 2009. 73

[192] K. Kawashima, R. Omote, T. Ito, H. Fujita, and T. Shima. Nonlinear acoustic response through minute surface cracks: Fem simulation and experimentation. *The Journal of the Acoustical Society of America*, 40:611–615, 2002. 73

[193] H. Soshu and S. Toshihiko. Detection of a closed crack by nonlinear acoustics using ultrasonic transducers. in review of progress in quantitative nondestructive evaluation. *The Journal of the Acoustical Society of America*, 32nd ed.:277–282, 2006. 73

[194] V. Giurgiutiu, M. Gresil, B. Lin, A. Cuc, Y. Shen, and C. Roman. Predictive modelling of piezoelectric wafer active sensors interaction with high frequency structural waves and vibration. *Acta Mechanica*, 223:1681–1691, 2012. 73

[195] T.B. Autrusson, K.G. Sabra, and M.J. Leamy. Reflection of compressional and rayleigh waves on the edges of an elastic plate with quadratic nonlinearity. *The Journal of the Acoustical Society of America*, 131:1928–1937, 2012. 74

[196] G.M. Fierro, F. Ciampa, D. Ginzgurg, E. Onder, and M. Meo. Nonlinear ultrasonic modelling and validation of fatigue damage. *Journal of Sound and Vibration*, 343: 121–130, 2015. 74

[197] F. Ciampa, G. Scarselli, S. Pickering, and M. Meo. Nonlinear elastic wave tomography for the imaging of corrosion damage. *Ultrasonics*, 62:147–155, 2015. 74

[198] Y. Shen and V. Giurgiutiu. Predictive modelling of nonlinear wave propagation for structural health monitoring with piezoelectric wafer active sensors. *Journal of Intelligent Material Systems and Structures*, 25:506–520, 2014. 74

[199] Reza Soleimanpour and Ching-Tai Ng. Locating delaminations in laminated composite beams using nonlinear guided waves. *Engineering Structures*, 131:207–219, 2017. 74

[200] Xiang Wan, Qing Zhang, Guanghua Xu, and Peter W Tse. Numerical simulation of nonlinear lamb waves used in a thin plate for detecting buried micro-cracks. *Sensors*, 14(5):8528–8546, 2014. 74

[201] P Blanloeuil, A Meziane, and C Bacon. Nonlinear interaction of ultrasonic waves with a crack of different orientations. In *AIP Conference Proceedings*, pages 99–106, 2013. 74

[202] F. Moser, L.J. Jacobs, and J. Qu. Modelling elastic wave propagation in waveguides with the finite element method. *NDT&E International*, 32:225–234, 1999. 80

[203] J.H. Nienwenhui, J.J. Neumann, D.W. Greve, and I.J. Oppenheim. Generation and detection of guided waves using pzt wafer transducers. *IEEE transactions on ultrasonics, ferroelectrics, and frequency control*, 52(11):2103–2111, 2005. 81

[204] L. Cremer, M. Heckel, and B.A.T. Petersson. *Structure Borne Sound: Structural Vibrations and Sound Radiation at Audio Frequencies*. Springer, 2005. 109, 112

[205] Carlos A Felippa and Ray W Clough. *The finite element method in solid mechanics*. American Mathematical Society, 1970. 153

# APPENDIX A

# ANSYS and MATLAB codes for extracting model matrices

## A.1 Extracting stiffness, mass and damping matrices text files in ANSYS

```
! After modal solution of the model
! This program extracts stiffness, mass and damping matrices text files in ANSYS®
/AUX2
FILE,'file','full',' '                          ! Title of the structural model: file
HBMAT,'K_mat.txt',' ',' ',ASCII,STIFF,YES,YES     ! extract stiffness matrix
HBMAT,'M_mat.txt',' ',' ',ASCII,MASS,YES,YES      ! extract mass matrix
HBMAT,'C_mat.txt',' ',' ',ASCII,STIFF,YES,YES     ! extract damping matrix
FINISH
```

# APPENDIX B

# Illustration examples for the node duplication method

As an illustration of this method, two different structural segments with through-width damage are considered. The nodes and elements arrangements are based on the nodes and elements connectivities for 2D PLANE182 and 3D SOLID185 elements [178].

## B.1 Case 1: 2D segment

The segment is meshed with six 2D plane strain FEs. Elements and nodes numbering of the segment are as shown Fig. B.1. For the damage depth considered, nodes 6, 7 and 8, which are along the damage axis, are disconnected by adding duplicate nodes 13, 14 and 15 of same respective nodal coordinates.

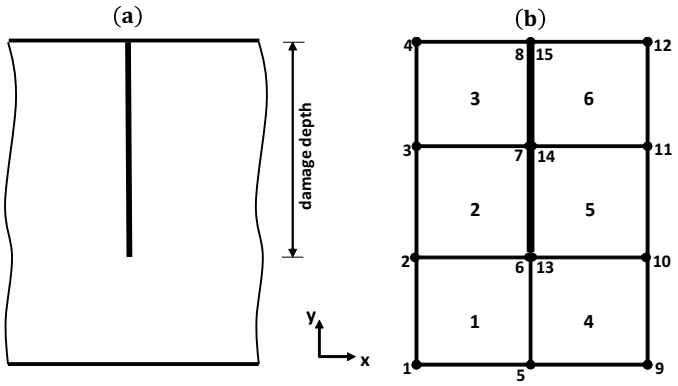


**Figure B.1:** Finite element modelling of damage using node duplication method: (a) damaged 2D structural segment, (b) node duplication model

In a pristine state of the segment, nodal arrangement of finite element 2 is [2, 6, 7, 3] in that order, while that of element 5 is [6, 10, 11, 7]. But, in a damaged state, nodal arrangement of element 2 remains [2, 6, 7, 3] while that of element 5 becomes [13, 10,

11, 14] to model defects at the interface of the two FEs. Similar node ordering holds for elements 3 and 6 with nodal arrangements [3, 7, 8, 4] and [14, 11, 12, 15] respectively in the damaged state of the structural segment.

## B.2 Case 2: 3D segment

The segment is meshed using 80 3D solid FEs as shown in Fig. B.2. Elements and nodes numbering of the segment are as shown in Fig. B.2. For the damage depth considered, nodes 100, 101, 102, 103, 104, 105, 106, 107 and 108, which are along the damage path, are respectively disconnected by adding duplicate nodes 163, 164, 165, 166, 167, 168, 169, 170 and 171 of same respective nodal coordinates.

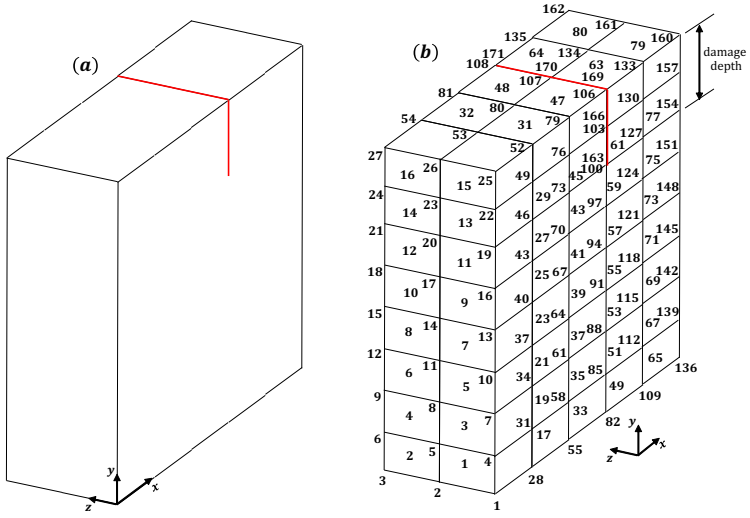


**Figure B.2:** Finite element modelling of damage using the node duplication method: (a) damaged 3D structural segment, (b) node duplication model

In a pristine state of the segment, the nodal connectivities of elements 45, 46, 47 and 48 are [73, 100, 101, 74, 76, 103, 104, 77], [74, 101, 102, 75, 77, 104, 105, 78], [76, 103, 104, 77, 79, 106, 107, 80] and [77, 104, 105, 78, 80, 107, 108, 81] respectively. That of elements 61, 62, 63 and 64 are respectively [100, 127, 128, 101, 103, 130, 131, 104], [101, 128, 129, 102, 104, 131, 132, 105], [103, 130, 131, 104, 106, 133, 134, 107] and [104, 131, 132, 105, 107, 134, 135, 108]. But, in a damaged state, the nodal connectivities of elements 45, 46, 47 and 48 remain unchanged while that of elements 61, 62, 63 and 64 become [163, 127, 128, 164, 166, 130, 131, 167], [164, 128, 129, 165, 167, 131, 132, 168], [166, 130, 131, 167, 169, 133, 134, 170] and [167, 131, 132, 168, 170, 134, 135, 171] respectively. In this sense, the duplicates nodes are attributed to the elements on the right side of the damage axis such that when a tensile force is applied, elements 61, 62, 63 and 64 will be separated from elements 45, 46, 47 and 48 thereby simulating the damage.

# APPENDIX C

# Structural FE matrices expressed directly as a function of layer mechanical characteristics

A linear solid FE is hereby considered as shown in Fig.C.1.

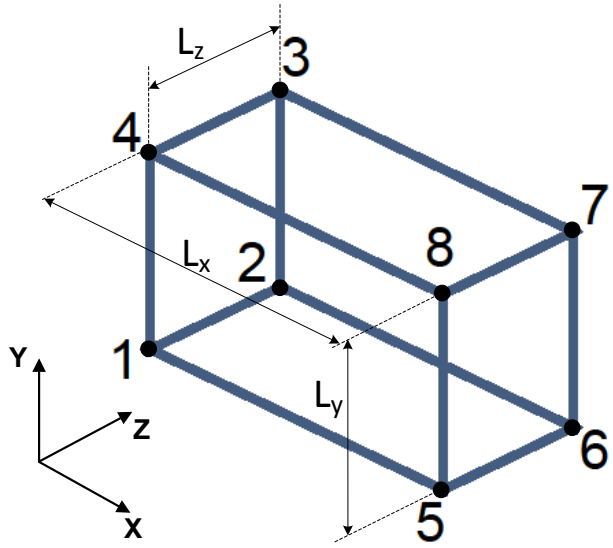


**Figure C.1:** The considered cuboid solid FE

Following the isoparametric notation introduced in [205] the geometry of the element is described as

$$\begin{Bmatrix} x \\ y \\ z \end{Bmatrix} = \begin{bmatrix} x_1 & x_2 & x_3 & x_4 & x_5 & x_6 & x_7 & x_8 \\ y_1 & y_2 & y_3 & y_4 & y_5 & y_6 & y_7 & y_8 \\ z_1 & z_2 & z_3 & z_4 & z_5 & z_6 & z_7 & z_8 \end{bmatrix} \begin{Bmatrix} N_1 \\ N_2 \\ N_3 \\ N_4 \\ N_5 \\ N_6 \\ N_7 \\ N_8 \end{Bmatrix} \tag{C.0.1}$$

The displacement interpolations are expressed as

$$\begin{Bmatrix} u_x \\ u_y \\ u_z \end{Bmatrix} = \begin{bmatrix} u_{x1} & u_{x2} & u_{x3} & u_{x4} & u_{x5} & u_{x6} & u_{x7} & u_{x8} \\ u_{y1} & u_{y2} & u_{y3} & u_{y4} & u_{y5} & u_{y6} & u_{y7} & u_{y8} \\ u_{z1} & u_{z2} & u_{z3} & u_{z4} & u_{z5} & u_{z6} & u_{z7} & u_{z8} \end{bmatrix} \begin{Bmatrix} N_1 \\ N_2 \\ N_3 \\ N_4 \\ N_5 \\ N_6 \\ N_7 \\ N_8 \end{Bmatrix} \tag{C.0.2}$$

Linear shape functions are assumed for the element

$$\begin{aligned} N_1 &= \tfrac{1}{8}(1-\xi)(1-\eta)(1+\mu) \\ N_2 &= \tfrac{1}{8}(1-\xi)(1-\eta)(1-\mu) \\ N_3 &= \tfrac{1}{8}(1-\xi)(1+\eta)(1-\mu) \\ N_4 &= \tfrac{1}{8}(1-\xi)(1+\eta)(1+\mu) \\ N_5 &= \tfrac{1}{8}(1+\xi)(1-\eta)(1+\mu) \\ N_6 &= \tfrac{1}{8}(1+\xi)(1-\eta)(1-\mu) \\ N_7 &= \tfrac{1}{8}(1+\xi)(1+\eta)(1-\mu) \\ N_8 &= \tfrac{1}{8}(1+\xi)(1+\eta)(1+\mu) \end{aligned} \tag{C.0.3}$$

The element stiffness matrix $\mathbf{k}$ is formally given by the volume integral

$$\mathbf{k} = \int_{-1}^{1}\int_{-1}^{1}\int_{-1}^{1} \mathbf{B}^{\top}\mathbf{D}\mathbf{B}|\mathbf{J}|\, \mathrm{d}\eta\mathrm{d}\xi\mathrm{d}\mu \tag{C.0.4}$$

while the element mass and damping matrices $\mathbf{m}$, $\mathbf{c}$ can be determined as

$$\mathbf{m} = \int_{-1}^{1}\int_{-1}^{1}\int_{-1}^{1} \mathbf{N}^{\top}\rho_m\mathbf{N}|\mathbf{J}|\, \mathrm{d}\eta\mathrm{d}\xi\mathrm{d}\mu \tag{C.0.5}$$

$$\mathbf{c} = \int_{-1}^{1}\int_{-1}^{1}\int_{-1}^{1} \mathbf{N}^{\top}\gamma\,\mathbf{N}|\mathbf{J}|\,\mathrm{d}\eta\mathrm{d}\xi\mathrm{d}\mu \tag{C.0.6}$$

with

$$\mathbf{N} = \begin{bmatrix} N_1 & 0 & 0 & \cdots & N_8 & 0 & 0 \\ 0 & N_1 & 0 & \cdots & 0 & N_8 & 0 \\ 0 & 0 & N_1 & \cdots & 0 & 0 & N_8 \end{bmatrix} \tag{C.0.7}$$

while $\rho_m$ is the mass density of the material and $\gamma$ the material damping coefficient. It is also noted that

$$\mathbf{B} = \begin{bmatrix} \frac{\partial N_1}{\partial x} & 0 & 0 & \frac{\partial N_2}{\partial x} & \cdots & \frac{\partial N_8}{\partial x} & 0 & 0 \\ 0 & \frac{\partial N_1}{\partial y} & 0 & 0 & \cdots & 0 & \frac{\partial N_8}{\partial y} & 0 \\ 0 & 0 & \frac{\partial N_1}{\partial z} & 0 & \cdots & 0 & 0 & \frac{\partial N_8}{\partial z} \\ \frac{\partial N_1}{\partial y} & \frac{\partial N_1}{\partial x} & 0 & \frac{\partial N_2}{\partial y} & \cdots & \frac{\partial N_8}{\partial y} & \frac{\partial N_8}{\partial x} & 0 \\ 0 & \frac{\partial N_1}{\partial z} & \frac{\partial N_1}{\partial y} & 0 & \cdots & 0 & \frac{\partial N_8}{\partial z} & \frac{\partial N_8}{\partial y} \\ \frac{\partial N_1}{\partial z} & 0 & \frac{\partial N_1}{\partial x} & \frac{\partial N_2}{\partial z} & \cdots & \frac{\partial N_8}{\partial z} & 0 & \frac{\partial N_8}{\partial x} \end{bmatrix} \begin{Bmatrix} u_{x1} \\ u_{y1} \\ u_{z1} \\ u_{x2} \\ \cdots \\ u_{x8} \\ u_{y8} \\ u_{z8} \end{Bmatrix} \tag{C.0.8}$$

The Jacobian matrix of the element is

$$\mathbf{J} = \begin{bmatrix} \frac{\partial x}{\partial \xi} & \frac{\partial y}{\partial \xi} & \frac{\partial z}{\partial \xi} \\ \frac{\partial x}{\partial \eta} & \frac{\partial y}{\partial \eta} & \frac{\partial z}{\partial \eta} \\ \frac{\partial x}{\partial \mu} & \frac{\partial y}{\partial \mu} & \frac{\partial z}{\partial \mu} \end{bmatrix} \tag{C.0.9}$$

while the the flexibility matrix of the element for an orthotropic material $\mathbf{D}^{-1}$ can generally be written as

$$\mathbf{D}^{-1} = \begin{bmatrix} \frac{1}{E_x} & \frac{-v_{xy}}{E_x} & \frac{-v_{xz}}{E_x} & 0 & 0 & 0 \\ \frac{-v_{yx}}{E_y} & \frac{1}{E_y} & \frac{-v_{yz}}{E_y} & 0 & 0 & 0 \\ \frac{-v_{zx}}{E_z} & \frac{-v_{zy}}{E_z} & \frac{1}{E_z} & 0 & 0 & 0 \\ 0 & 0 & 0 & \frac{1}{G_{xy}} & 0 & 0 \\ 0 & 0 & 0 & 0 & \frac{1}{G_{yz}} & 0 \\ 0 & 0 & 0 & 0 & 0 & \frac{1}{G_{xz}} \end{bmatrix} \tag{C.0.10}$$

The assumption of the undeformed FE being a rectangular parallelepiped is hereby adopted. The coordinates $x_1, x_2, x_3, x_4, x_5, x_6, x_7, x_8$, $y_1, y_2, y_3, y_4, y_5, y_6, y_7, y_8$, and $z_1, z_2, z_3, z_4, z_5, z_6, z_7, z_8$, can then be replaced by $L_x, L_y, L_z$ in the expression of $\mathbf{B}$. The generic expression for $\mathbf{m}$ is thus given as

$$\mathbf{m} = (\rho L_x L_y L_z) \begin{bmatrix}
1/27 & 0 & 0 & 1/54 & 0 & 0 & 1/108 & 0 & 0 & 1/54 & 0 & 0 & 1/54 & 0 & 0 & 1/108 & 0 & 0 & 1/216 & 0 & 0 & 1/108 & 0 & 0 \\
0 & 1/27 & 0 & 0 & 1/54 & 0 & 0 & 1/108 & 0 & 0 & 1/54 & 0 & 0 & 1/54 & 0 & 0 & 1/108 & 0 & 0 & 1/216 & 0 & 0 & 1/108 & 0 \\
0 & 0 & 1/27 & 0 & 0 & 1/54 & 0 & 0 & 1/108 & 0 & 0 & 1/54 & 0 & 0 & 1/54 & 0 & 0 & 1/108 & 0 & 0 & 1/216 & 0 & 0 & 1/108 \\
1/54 & 0 & 0 & 1/27 & 0 & 0 & 1/54 & 0 & 0 & 1/108 & 0 & 0 & 1/108 & 0 & 0 & 1/54 & 0 & 0 & 1/108 & 0 & 0 & 1/216 & 0 & 0 \\
0 & 1/54 & 0 & 0 & 1/27 & 0 & 0 & 1/54 & 0 & 0 & 1/108 & 0 & 0 & 1/108 & 0 & 0 & 1/54 & 0 & 0 & 1/108 & 0 & 0 & 1/216 & 0 \\
0 & 0 & 1/54 & 0 & 0 & 1/27 & 0 & 0 & 1/54 & 0 & 0 & 1/108 & 0 & 0 & 1/108 & 0 & 0 & 1/54 & 0 & 0 & 1/108 & 0 & 0 & 1/216 \\
1/108 & 0 & 0 & 1/54 & 0 & 0 & 1/27 & 0 & 0 & 1/54 & 0 & 0 & 1/216 & 0 & 0 & 1/108 & 0 & 0 & 1/54 & 0 & 0 & 1/108 & 0 & 0 \\
0 & 1/108 & 0 & 0 & 1/54 & 0 & 0 & 1/27 & 0 & 0 & 1/54 & 0 & 0 & 1/216 & 0 & 0 & 1/108 & 0 & 0 & 1/54 & 0 & 0 & 1/108 & 0 \\
0 & 0 & 1/108 & 0 & 0 & 1/54 & 0 & 0 & 1/27 & 0 & 0 & 1/54 & 0 & 0 & 1/216 & 0 & 0 & 1/108 & 0 & 0 & 1/54 & 0 & 0 & 1/108 \\
1/54 & 0 & 0 & 1/108 & 0 & 0 & 1/54 & 0 & 0 & 1/27 & 0 & 0 & 1/108 & 0 & 0 & 1/216 & 0 & 0 & 1/108 & 0 & 0 & 1/54 & 0 & 0 \\
0 & 1/54 & 0 & 0 & 1/108 & 0 & 0 & 1/54 & 0 & 0 & 1/27 & 0 & 0 & 1/108 & 0 & 0 & 1/216 & 0 & 0 & 1/108 & 0 & 0 & 1/54 & 0 \\
0 & 0 & 1/54 & 0 & 0 & 1/108 & 0 & 0 & 1/54 & 0 & 0 & 1/27 & 0 & 0 & 1/108 & 0 & 0 & 1/216 & 0 & 0 & 1/108 & 0 & 0 & 1/54 \\
1/54 & 0 & 0 & 1/108 & 0 & 0 & 1/216 & 0 & 0 & 1/108 & 0 & 0 & 1/27 & 0 & 0 & 1/54 & 0 & 0 & 1/108 & 0 & 0 & 1/54 & 0 & 0 \\
0 & 1/54 & 0 & 0 & 1/108 & 0 & 0 & 1/216 & 0 & 0 & 1/108 & 0 & 0 & 1/27 & 0 & 0 & 1/54 & 0 & 0 & 1/108 & 0 & 0 & 1/54 & 0 \\
0 & 0 & 1/54 & 0 & 0 & 1/108 & 0 & 0 & 1/216 & 0 & 0 & 1/108 & 0 & 0 & 1/27 & 0 & 0 & 1/54 & 0 & 0 & 1/108 & 0 & 0 & 1/54 \\
1/108 & 0 & 0 & 1/54 & 0 & 0 & 1/108 & 0 & 0 & 1/216 & 0 & 0 & 1/54 & 0 & 0 & 1/27 & 0 & 0 & 1/54 & 0 & 0 & 1/108 & 0 & 0 \\
0 & 1/108 & 0 & 0 & 1/54 & 0 & 0 & 1/108 & 0 & 0 & 1/216 & 0 & 0 & 1/54 & 0 & 0 & 1/27 & 0 & 0 & 1/54 & 0 & 0 & 1/108 & 0 \\
0 & 0 & 1/108 & 0 & 0 & 1/54 & 0 & 0 & 1/108 & 0 & 0 & 1/216 & 0 & 0 & 1/54 & 0 & 0 & 1/27 & 0 & 0 & 1/54 & 0 & 0 & 1/108 \\
1/216 & 0 & 0 & 1/108 & 0 & 0 & 1/54 & 0 & 0 & 1/108 & 0 & 0 & 1/108 & 0 & 0 & 1/54 & 0 & 0 & 1/27 & 0 & 0 & 1/54 & 0 & 0 \\
0 & 1/216 & 0 & 0 & 1/108 & 0 & 0 & 1/54 & 0 & 0 & 1/108 & 0 & 0 & 1/108 & 0 & 0 & 1/54 & 0 & 0 & 1/27 & 0 & 0 & 1/54 & 0 \\
0 & 0 & 1/216 & 0 & 0 & 1/108 & 0 & 0 & 1/54 & 0 & 0 & 1/108 & 0 & 0 & 1/108 & 0 & 0 & 1/54 & 0 & 0 & 1/27 & 0 & 0 & 1/54 \\
1/108 & 0 & 0 & 1/216 & 0 & 0 & 1/108 & 0 & 0 & 1/54 & 0 & 0 & 1/54 & 0 & 0 & 1/108 & 0 & 0 & 1/54 & 0 & 0 & 1/27 & 0 & 0 \\
0 & 1/108 & 0 & 0 & 1/216 & 0 & 0 & 1/108 & 0 & 0 & 1/54 & 0 & 0 & 1/54 & 0 & 0 & 1/108 & 0 & 0 & 1/54 & 0 & 0 & 1/27 & 0 \\
0 & 0 & 1/108 & 0 & 0 & 1/216 & 0 & 0 & 1/108 & 0 & 0 & 1/54 & 0 & 0 & 1/54 & 0 & 0 & 1/108 & 0 & 0 & 1/54 & 0 & 0 & 1/27
\end{bmatrix} \tag{C.0.11}$$

a very similar expression is true for $\mathbf{c}$, while the symbolic generic expression of $\mathbf{k}$ can be derived exactly in the same way but is hereby intentionally omitted for the sake of brevity. This implies the very practical fact of the mass, damping and stiffness matrices $\mathbf{m}$ and $\mathbf{k}$ for each independent layer of the structure being a direct expression of the structural and material characteristics $\rho, L_z, E_x, E_y, E_z, G_{xy}, G_{xz}, G_{zy}, v_{xy}, v_{xz}, v_{zy}$. It is obvious that for an isotropic layer, the above expressions are radically simplified, while the stiffness and mass matrices of a multilayer structure can be obtained by assembling the discrete layer matrices. A Newton-like iterative scheme can then be effectively employed for minimising the objective function and solving the system of eigenvalue expressions for recovering the mechanical characteristics of each individual layer.

The generic sensitivity expressions $\frac{\partial \mathbf{k}}{\partial \beta_i}, \frac{\partial \mathbf{m}}{\partial \beta_i}$ as well as $\frac{\partial^2 \mathbf{k}}{\partial \beta_j \partial \beta_i}, \frac{\partial^2 \mathbf{m}}{\partial \beta_j \partial \beta_i}$ with $\beta_i, \beta_j$ being design parameters can therefore be calculated as a function of $E_x, E_y, E_z, v_{xy}, v_{xz}, v_{yz}, G_{xy}, G_{xz}, G_{yz}, L_x, L_y, L_z$ by differentiating over the generic expressions for $\mathbf{k}$, $\mathbf{m}$. The sensitivities of the global matrices $\frac{\partial \mathbf{K}}{\partial \beta_i}, \frac{\partial \mathbf{M}}{\partial \beta_i}$ can then be computed by assembling the individual element sensitivity matrices together.